

Systematic studies, calibration, and
software development for
event reconstruction
and data analysis using the
ANTARES
deep-sea neutrino telescope

Der Naturwissenschaftlichen Fakultät
der Friedrich-Alexander-Universität Erlangen-Nürnberg
zur
Erlangung des Doktorgrades



vorgelegt von
Felix Fehr
aus Köln

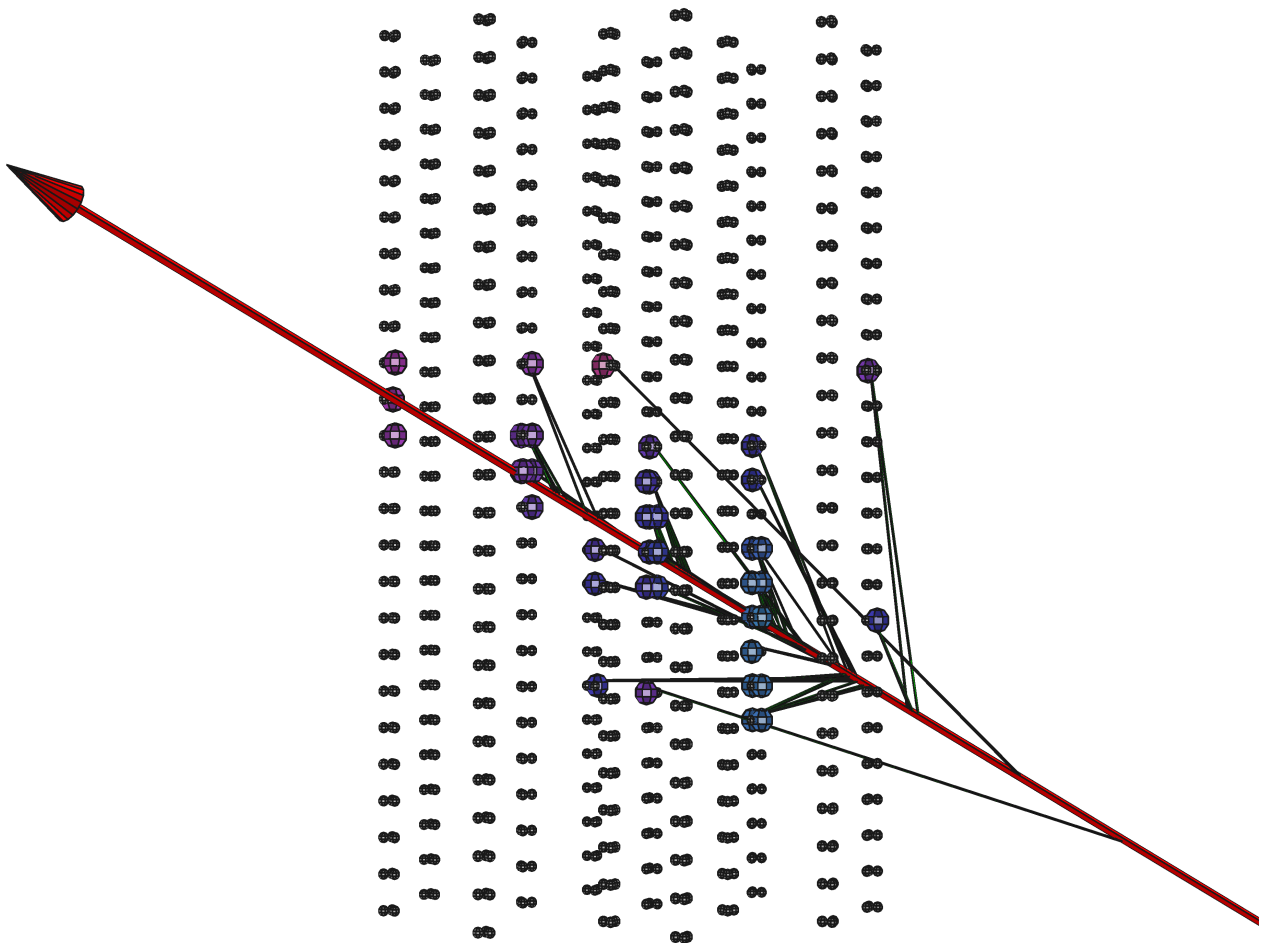
Als Dissertation genehmigt von der Naturwissenschaftlichen Fakultät
der Universität Erlangen-Nürnberg

Tag der mündlichen Prüfung:	7. Januar 2010
Vorsitzender der Promotionskommission:	Prof. Dr. Eberhard Bänsch
Erstberichterstatte:	Prof. Dr. Ulrich F. Katz
Zweitberichterstatte:	Prof. Dr. Christian Stegmann

Systematic studies, calibration, and
software development for
event reconstruction
and data analysis using the
ANTARES
deep-sea neutrino telescope

Felix Fehr

Dissertation



Abstract

The ANTARES neutrino telescope has been constructed in the Mediterranean deep sea in a depth of about 2500 m, 40 km off-shore the city of Toulon at the French coast, in order to detect cosmic neutrino signals. Being the largest apparatus on the Northern hemisphere, with about 900 photo-sensors, in addition to its unique discovery potential, ANTARES represents a benchmark and possible prototype for future neutrino telescope projects. After an introduction into neutrino telescoping and a description of the ANTARES telescope, this dissertation will describe the charge calibration of the front-end electronics. A long-term study of the calibration constants is discussed. Contributions to the software framework will be detailed and systematic studies of the event reconstruction are presented. For a precise telescoping, the absolute orientation of the detector is of utmost importance. A possible verification of the detector pointing relies on the detection of the shadow which is casted by the Moon in cosmic rays. The significance of this effect is evaluated with the help of a detailed Monte Carlo simulation. A first analysis of ANTARES data is performed.

Kurzfassung

Mit dem ANTARES Neutrino-Teleskop, welches im Mittelmeer, 40 km vor der französischen Küste bei Toulon, in einer Tiefe von ca. 2500 m errichtet wurde, sollen kosmische Neutrinos detektiert werden. Mit rund 900 Photosensoren stellt ANTARES derzeit das sensitivste Experiment auf der Nordhalbkugel dar. Neben dem inhärenten Entdeckungspotential können aus Aufbau, Betrieb und Datenanalyse wichtige Erkenntnisse für die nächste Generation von Teleskopen gewonnen werden. Nach einer Einführung in die Neutrinoastronomie und in das ANTARES Experiment stellt diese Dissertation die erarbeiteten Kalibrationsverfahren für die Ausleseelektronik vor. Eine Langzeitstudie der Zeitentwicklung der Kalibrationskonstanten wird präsentiert. Beiträge zur Softwareinfrastruktur (Online-Monitoring, Datenverarbeitung und Rekonstruktion) werden erörtert. Für eine exakte Teleskopie ist die Verifikation der Detektorausrichtung von großer Bedeutung. Eine Kalibrationsmethode besteht in der Beobachtung des Schattens, den der Mond in der kosmischen Strahlung wirft. Die Größe dieses Effektes wird anhand einer detaillierten Simulation quantifiziert. Eine erste Analyse der Daten des komplettierten Teleskopes wird diskutiert.

The image on the cover page shows an event display of a simulated 540 GeV muon-neutrino that interacts via the charged-current process in the vicinity of the ANTARES detector to produce a 130 GeV up-going muon track (red line). The muon traverses the detector and gives rise to Cherenkov light (green lines) which is measured by the optical sensors (enlarged spheres) of the telescope. The image was created with an event-display program developed for this thesis. See Chapter 5 and Appendix A for further information.

This document was typeset using L^AT_EX.

Contents

Introduction	1
I Neutrinos and telescopes	5
1 Astroparticle physics with neutrinos	7
1.1 The cosmic-ray connection	7
1.1.1 The cosmic-ray spectrum	7
1.1.2 Shock acceleration	9
1.1.3 Propagation of cosmic rays	10
1.1.4 Neutrinos and gamma rays	11
1.2 Neutrino sources	13
1.2.1 Candidate sources for hadronic acceleration	13
1.2.2 Other sources	17
1.3 Indications of hadronic accelerators	18
1.3.1 The supernova remnant RX J1713.7-3946	19
1.3.2 Active galactic nuclei	20
2 Neutrino interactions and detection principles	23
2.1 Neutrino interactions	23
2.2 Muon production and propagation	25
2.3 The Cherenkov effect	27
2.4 Neutrino telescope projects	28
2.5 Complementary neutrino detection techniques	32
3 The ANTARES neutrino telescope	35
3.1 The ANTARES project	35
3.2 Layout of the ANTARES detector	37
3.3 Signal and background for ν -telescopes	38
3.4 Data acquisition	41
3.4.1 The off-shore DAQ system	41
3.4.2 Filter algorithms	42
3.5 Calibration	45
3.5.1 Time calibration	45
3.5.2 Alignment of the detector	46

3.5.3	Absolute positioning	47
3.6	Simulation	47
3.6.1	Atmospheric muons	47
3.6.2	Neutrinos	48
3.6.3	Cherenkov light	48
3.7	Status and history of the experiment	49
II	Front-end electronics calibration	53
4	Charge calibration of the front-end electronics	55
4.1	Front-end electronics	55
4.2	The analogue ring sampler	56
4.3	Charge calibration	57
4.3.1	Pedestal and photoelectron peak fit	59
4.3.2	Channel crosstalk correction	61
4.3.3	Automatisation of the calibration procedure	63
4.4	Long-term observation of the PMT gain	66
4.5	Conclusions on charge calibration	66
III	Event reconstruction and software	69
5	The new software framework	71
5.1	Software overview	71
5.2	Offline analysis framework	72
5.2.1	Concepts of the framework	72
5.2.2	Fundamental developments for ANTARES	74
5.2.3	Integration of existing and new algorithms	78
5.2.4	Overview of existing algorithms	82
5.2.5	Event reconstruction chain	83
5.3	Conclusions and outlook	83
6	Event reconstruction	85
6.1	General remarks on event reconstruction	85
6.1.1	Classification - event topologies	85
6.1.2	Track reconstruction algorithms	86
6.2	The likelihood track reconstruction	87
6.3	Linearisation methods	89
6.3.1	Tracking in two dimensions - single line fits	90
6.3.2	Generalisation to 3-dimensional tracking	91
6.3.3	Resolution of ambiguities	92
6.3.4	Application to the reconstruction of showers	92

6.3.5	Conclusions and outlook	92
6.4	Fitting with global optimisation algorithms	96
IV	Pointing verification – Moon-shadow analysis	99
7	Moon-shadow simulation	101
7.1	Detector pointing	101
7.2	The Moon shadow in cosmic rays	102
7.3	Simulation of the Moon-shadow effect	103
7.3.1	The CORSIKA Moon simulation	103
7.3.2	Primary flux	105
7.3.3	Influence of the geomagnetic field	106
7.3.4	The point-spread function and the shape of the shadow	106
7.4	Evaluation of the expected significance	109
7.4.1	Hypothesis tests	109
7.4.2	Definition of the test statistic	110
7.4.3	Expected significance of the shadow effect	112
7.4.4	Optimisation of the analysis cut	115
7.4.5	Comparison with previous analyses	116
7.5	Effect of a misalignment on the Moon shadow	116
7.6	Conclusions and outlook	116
8	Moon-shadow data analysis	117
8.1	Coordinate calculations and transformations	117
8.1.1	Conversion of the event time	118
8.1.2	Calculation of the Moon coordinates in the horizon system	118
8.1.3	Transformation into the detector frame	119
8.2	Reprocessing of raw data	120
8.2.1	Selection of physics data	120
8.2.2	Data reduction and related preparatory work	121
8.3	Data analysis	121
8.3.1	Comparison between data and Monte Carlo	121
8.3.2	The on-source region	123
8.4	Conclusions	126
	Summary and outlook	127
	Zusammenfassung	131
	Appendix	135

A	The ANTARES display program	137
A.1	Installation and start-up	137
A.2	Main functions of the display	137
A.3	Operation modes	138
A.4	Online display	140
B	Derivation of the two dimensional event signatures	143
B.1	Track signal in the (\mathbf{z}, \mathbf{t}) -diagram	143
B.2	Signal of a bright point in the (\mathbf{z}, \mathbf{t}) -diagram	144
C	ANTARES example events	145
	Bibliography	160
	List of Figures	163
	List of Tables	165
	Acknowledgements	167

Introduction

“Non quia difficilia sunt non
audemus, sed quia non audemus
difficilia sunt!” [1]

LUCIUS ANNAEUS SENECA

The night sky with imposing objects visible on the starry firmament and the Universe in general have ever been a stimulus for scientific curiosity and an inspiration for the human mind. However, while light from stars guided man for ages in navigation on the sea and inspired art and science, first evidence of elementary particles of cosmic origin reaching Earth, besides light, did not come until the balloon experiments of V.F. Hess¹ in 1911/12. Originally, these balloon flights were conducted to demonstrate that the radiation known to originate from radioactive elements in the Earth’s crust diminishes with increasing altitude. Using an electrometer, the Austrian physicist recorded the intensity of the radiation during the balloon flights up to heights of 5000 m and was astounded when he discovered that the measured radiation, instead of decreasing, increased with altitude. He then correctly inferred that the observed radiation (dubbed “Höhenstrahlung”) was of extraterrestrial origin [2]. Shortly thereafter, first footprints of cosmic particles were made visible in the cloud chamber, developed in 1912 by C.T.R. Wilson (Nobel prize 1927).

Since then, the cosmic messengers have been studied with more and more refined instruments. Out of these efforts, a modern branch of fundamental physics, nowadays termed astroparticle physics, has evolved. The main aim of modern astroparticle physics is the study of cosmic messenger particles ranging over the electromagnetic spectrum, from the cosmic microwave radiation up to TeV gamma rays, to protons and heavy nuclei. Recently the stage has been extended to neutrinos and also to gravitational waves. Today, astroparticle physics represents a rapidly emerging field using detectors in such outlying places as Antarctica, the Mediterranean deep sea, the Argentinean pampa as well as satellite-borne setups in outer space.

A fascinating aspect of astroparticle physics is its scope, which reaches from sub-atomic structures, fundamental particles, to objects as large as the Universe itself. Its interrelation is really remarkable: while studying cosmic objects with micro-messengers one can learn about the micro cosmos as well as the macro cosmos. Two examples which clearly illustrate

¹Similar experiments have been performed by A. Gockel and later by W. Kohlhörster, however, the discovery of cosmic rays is commonly attributed to V.F. Hess (Nobel prize 1936).

the interdependence of this research branch are the discovery of neutrino oscillations [3] and the direct proof of the existence of non-baryonic dark matter [4]. Further, it deserves to be mentioned that the roots of traditional particle physics lie in the study of particles in the “Höhenstrahlung”. The anti-particle of the electron (the positron) [5], the muon [6], the pion [7, 8, 9], and the kaon [10] all were discovered in cosmic rays long before the advent of suitable man-made accelerators.

One of the long-standing riddles since the discovery of (charged) cosmic rays is their exact origin. Although we know today that cosmic rays are copiously produced and accelerated to macroscopic energies exceeding 10^{20} eV, the sources and concrete production mechanisms remain concealed as charged particles are deflected during their propagation in the intergalactic magnetic field. To shed new light on propagation and production mechanisms of cosmic rays and to reveal the cosmic accelerators, a messenger particle is required which reaches Earth virtually unabsorbed and unperturbed, characteristics perfectly rendered by the neutrino, a weakly interacting, neutral and stable particle with almost vanishing mass. The history of this most elusive particle in the Standard Model is interesting in its own right. In the year 1930, in order to restore the energy and angular momentum conservation that appeared to be violated in the nuclear beta decay, W. Pauli hypothesised the existence of a neutral particle. When he first proposed this concept in an open letter to the community his idea was regarded with suspicion, but was taken up by E. Fermi, who coined the term neutrino and developed a theory for the nuclear beta decay. Another 20 years had to pass till the neutrino was actually directly measured by C.L. Cowan and F. Reines [11] (Nobel prize F. Reines, 1995) in a reactor experiment and thus firmly established.

Besides the artificially produced neutrinos from nuclear reactors or particle accelerators and the neutrinos stemming from interaction processes of cosmic rays in the atmosphere, so far two kinds of low-energy extraterrestrial neutrino signals have been measured from the Sun ([12, 13, 14] and [15, 16]) and from a supernova (SN1987a) [17, 18]. Both discoveries were highly influential on the theoretical picture of elementary particle physics and astrophysics and were awarded with a Nobel prize (2002, R. Davis and M. Koshiba). Albeit being a promising venture, the detection of high-energy cosmogenic neutrinos still poses a challenge to the experimentalists, for the neutrinos² undergo only electroweak interactions and are thus difficult to detect as the actual interaction rates are very small. Therefore large volumes need to be instrumented for the detection (see Chapter 2 for details).

The ANTARES³ collaboration has designed and constructed a large-area water-Cherenkov neutrino detector, a so-called neutrino telescope, at a depth of 2475 metres in the Mediterranean sea, 40 km off the coast of Toulon, France, in order to detect cosmic neutrinos and eventually contribute to the solution of the cosmic-ray puzzle. The University Erlangen (now represented by the Erlangen Centre for Astroparticle Physics, ECAP) joined

²Here and henceforth the term neutrino implicitly includes the anti-neutrino when appropriate.

³Acronym for **A**stronomy with a **N**eutrino **T**elescope and **A**bbyss environmental **R**ESearch.

ANTARES in 2001. Erlangen activities within ANTARES comprise the calibration and data analysis for the optical detector and R&D towards acoustic particle detection.

This work constitutes the first Ph.D. thesis of the ECAP group, devoted to ANTARES optical data analysis after the successful installation of the ANTARES telescope. It is written in an exciting time, when the full potential of the instrument is explored and first results utilising data of the completed detector are established.

This thesis is organised as follows. The treatise commences with an overview of astroparticle physics with neutrinos, which will highlight the physics goals that are pursued with neutrino telescopes. Potential cosmic sources of high-energy neutrinos are discussed and further physics topics are touched upon in Chapter 1. Neutrino interaction mechanisms and detection techniques will be summarised in Chapter 2. A brief account of the history of neutrino astronomy is given and complementary methods will be mentioned. The ANTARES neutrino telescope is described in detail in Chapter 3. This chapter comprises concise descriptions of the layout of the experiment, the data acquisition system and the filtering techniques employed to select the interesting physics events. The simulations that are used to analyse the data are discussed. Calibration systems and methods are presented as well. After the immersion of the detection units in the deep sea, the system is virtually unattainable for direct maintenance, thus reliable in-situ calibration and monitoring procedures are indispensable. Chapter 4 will focus on the in-situ charge calibration procedure developed within the context of this thesis. A precondition for any data analysis is a robust and flexible software environment. Work is currently ongoing to install a new coherent ANTARES framework for data processing and analysis. During the work conducted within this thesis, a first mass reconstruction with the new software framework has been performed and several contributions to the development have been made. The event reconstruction, and here especially the reconstruction of muon tracks, from the recorded raw data will be presented in Chapter 6. For point-source searches of cosmic neutrinos, the precise telescope alignment (detector pointing) is of utmost importance, as any misalignment leads to systematic errors in the analysis. In the final part of this thesis, in Chapter 7 and Chapter 8, a method is presented which allows for verifying the calibration of the absolute pointing of the detector using the shadow of the Moon in cosmic rays. For the first time a detailed account is propounded including all relevant effects. A detailed Monte Carlo simulation is used to quantify the observability of the shadow effect in the ANTARES data. A first systematic look at the Moon-shadow effect is performed utilising first data of the completed ANTARES telescope. Several technical points are consigned to the appendix. Inter alia, the visualisation software developed in this work will be described. A selection of ANTARES events concludes this thesis.

I will summarise the dissertation on pages 127ff. A summary in German is given on pages 131ff.

Apart from the work presented in this dissertation, I had several other responsibilities as a Ph.D. student at ECAP. I contributed to the education of students with regularly held exercise and laboratory courses, I assisted in oral (diploma) examinations and the supervision of diploma students, and helped organising the annual “Schule für Astroteilchenphysik”. I took part in testing of hardware (clock cards) for the ANTARES experiment and maintained the backup server for the local computer cluster for some time. Within ANTARES, I was officially responsible for the coordination of the Moon-shadow analysis and the 3D online event-display service and I have conducted two shifts at the ANTARES control station at La-Seyne-Sur-Mer. I have had the pleasure of representing the ANTARES collaboration at two international conferences.

Part I

Neutrinos and telescopes

The first part of this work provides an introduction into high-energy astroparticle physics with emphasis on one of its recent branches, neutrino telescopes. The connection between high-energy cosmic rays and neutrinos is explained and the search for high-energy cosmic neutrinos is motivated. Candidate sources for high-energy neutrinos are presented in Chapter 1. Techniques for the detection of high-energy neutrinos will be described in Chapter 2. A brief overview of the current status of the field is given. In the final Chapter 3 of this part, the ANTARES neutrino telescope is introduced.

Chapter 1

Astroparticle physics with neutrinos

This chapter provides an introduction to astroparticle physics with neutrinos and a motivation for the construction of high-energy cosmic neutrino detectors which will be described in the following chapter. The cosmic-ray spectrum is discussed and the connection between high-energy charged cosmic rays, neutrinos and gamma rays is explained. A plausible generic cosmic-ray acceleration mechanism is presented along with several candidates for high-energy neutrino sources. Recent measurements of gamma rays and high-energy protons, which have yielded first indications for hadronic accelerators, are discussed.

1.1 The cosmic-ray connection

Deep-sky surveys in the vast range of the electromagnetic spectrum have provided a wealth of knowledge about the structure and the formation of our Universe. A plethora of intriguing objects and phenomena have been localised and studied in the radio, microwave, infrared, visible, x-ray and gamma-ray bands. With respect to charged cosmic rays¹ the situation is significantly different. Albeit many experiments have measured cosmic rays, both their sources and acceleration mechanisms remain speculative, due to the deflection of the charged particles in the (inter-)galactic magnetic field. In this section, the features of the measured cosmic-ray spectrum are discussed and a plausible generic acceleration scenario is presented. In particular, the connection between charged cosmic rays, neutrinos and high-energy photons is pointed out. This provides a main motivation for the construction of high-energy neutrino detectors.

1.1.1 The cosmic-ray spectrum

Evidentially, cosmic accelerators produce high-energy particles with energies exceeding 10^8 TeV, and thus far beyond the scope of any feasible human-designed accelerator on Earth. High-energy cosmic rays can be measured directly on board of satellites and balloons or indirectly by detecting cosmic-ray induced air showers on the ground. Due to the rapid decrease of their flux with energy, the observation at the highest energies requires large apertures and is therefore restricted to the observation of air showers with large surface

¹Usually the term cosmic ray is meant to include only charged particles.

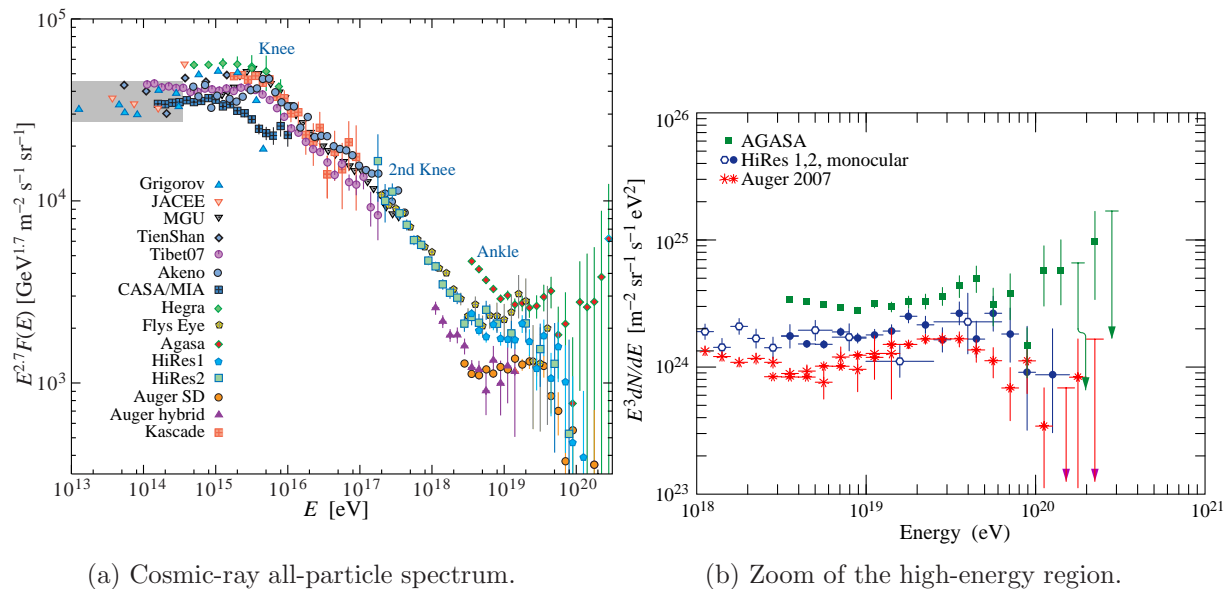


Figure 1.1: Cosmic-ray all-particle spectrum. See text and [19] for further explanation.

arrays and fluorescence telescopes. Combining the results of many different experiments, the all-particle cosmic-ray spectrum has been recorded in a range extending over 13 orders of magnitude in energy and 30 orders of magnitude in flux (see Figure 1.1a). The spectrum follows a broken power law according to

$$\frac{dN(E)}{dE} \propto E^{-\gamma}, \quad (1.1)$$

with an energy dependent spectral index γ . The spectrum falls off steeply ($\gamma \approx 2.7$) with increasing energy to about 1 particle per m² per year at $4 \cdot 10^{15}$ eV, the *knee*, where a transition in the slope to $\gamma \approx 3.0$ is observed and it decreases further with a small change in the slope at about $4 \cdot 10^{17}$ eV, the *second knee*, to about 1 particle per km² and year at $5 \cdot 10^{18}$ eV, the *ankle*, where the spectrum flattens ($\gamma \approx 2.3$) again. At the very high end of the spectrum (see Figure 1.1b) a cut-off is expected to be observed due to the interaction of the cosmic rays with the cosmic microwave background. This is the GZK effect named after Greisen [20], Zatsepin and Kuz'min [21].

The precise cause of the distinct features in the spectrum is still under discussion. The majority of the cosmic rays up to at least an energy of 10^{15} eV is believed to originate from within our galaxy. One plausible explanation of the transition at the knee is that galactic accelerators run out of steam at this point. Phenomenologically, the spectrum can be explained by assigning a charge or mass dependent cut-off energy to the cosmic-ray particles [22]. The transition at the ankle is often interpreted as the crossover from a steeper galactic component to a harder extragalactic component. At this point the Larmor

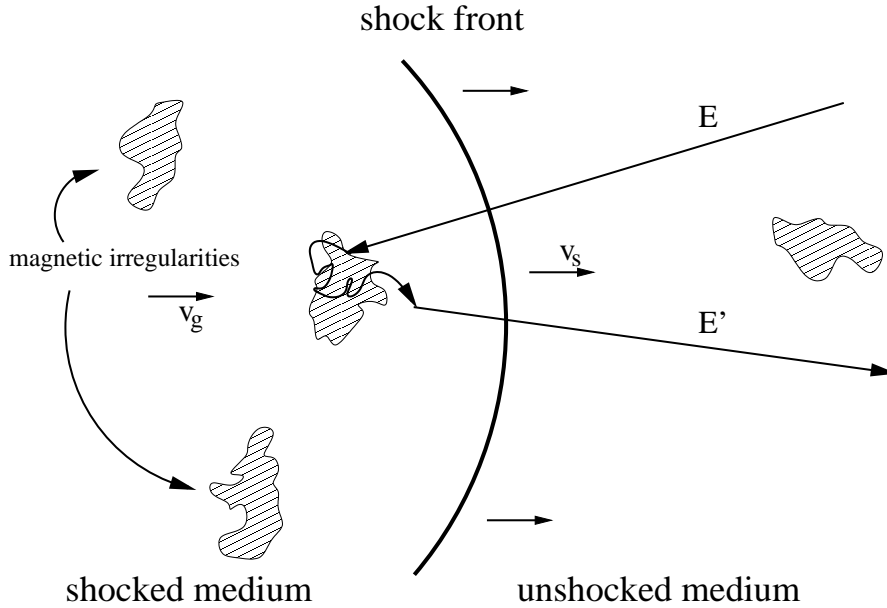


Figure 1.2: Sketch of the shock acceleration mechanism: A shock front propagates with velocity v_s through the medium. A particle of energy E passing the front from the unshocked to the shocked medium is scattered off magnetic irregularities in the gas of the shocked medium and leaves the shocked medium accelerated to an energy E' .

radius of charged particles with charge Ze ,

$$R[\text{kpc}] \approx \frac{E[\text{eV}]}{ZB[\mu\text{G}]} \quad (1.2)$$

starts to exceed the size of the galaxy (assuming an average galactic magnetic field of $\approx 1 \mu\text{G}$ and a galactic radius of 12 kpc). Therefore, charged particles can no longer be confined magnetically to the galaxy at these energies.

1.1.2 Shock acceleration

A plausible generic mechanism for the acceleration of cosmic rays has been proposed by Fermi [23, 24] and is referred to as first-order Fermi mechanism or shock acceleration, as the mechanism involves two colliding plasmas, forming a shock front at the boundary. In this model, particles are magnetically bound to the source and are scattered elastically by magnetic irregularities frozen into the plasma. This mechanism is sketched in Figure 1.2. Based on this mechanism one can derive the spectral index of the accelerated particles. A particle that enters the shocked medium and is scattered off the plasma receding behind the shock front leaves the shocked medium with a fractional energy increase of

$$\frac{\Delta E}{E} \propto \frac{v_g}{c} = \epsilon. \quad (1.3)$$

The particle can be scattered back behind the shock front and the cycle is repeated. Particles starting with an energy E_0 will have acquired an energy $E = E_0(1 + \epsilon)^n$ after passing through this cycle n times. If the escape probability P for a particle to leave the cycle is assumed to remain constant, the number of particles scales as $N = N_0(1 - P)^n$. With this, the number of particles acquiring at least an energy E_n can be calculated to

$$N_{E \geq E_n} = N_0 \left(\frac{E_n}{E} \right)^{\frac{\ln(1-P)}{\ln(1+\epsilon)}}. \quad (1.4)$$

Differentiation with respect to E_n then yields the energy spectrum

$$\frac{dN(E)}{dE} \propto E^{\frac{\ln(1-P)}{\ln(1+\epsilon)} - 1} = E^{-\gamma}, \quad (1.5)$$

which follows a power law with a spectral index of $\gamma \approx 2$ in first approximation. Detailed calculations [25] show that more realistic spectral indices lie in the range between $\gamma = 2.1$ and $\gamma = 2.4$. The maximum energy that can be reached by shock acceleration depends on the lifetime of the shock front and the strength of the confining magnetic field. Although the sketched mechanism nicely reproduces the observed power-law spectrum, it is still subject of theoretical investigations how precisely energies of 10^{20} eV can be reached.

1.1.3 Propagation of cosmic rays

During their propagation in the (inter-)galactic space, high-energy protons as well as high-energy gamma rays are subject to interactions with the ambient stellar light and the cosmic microwave background. The mean free pathlength λ for high-energy protons is determined by the cosmic microwave density $n_{\text{cmb}} = 400 \text{ cm}^{-3}$ and the cross section for the interaction. For a proton with an energy of $5 \cdot 10^{19}$ eV the cross section, averaged over the CMB spectrum, is $\sigma_{p\gamma} = 10^{-28} \text{ cm}^2$ and the mean free pathlength becomes

$$\lambda = \frac{1}{n_{\text{cmb}} \sigma_{p\gamma}} = 10 \text{ Mpc}. \quad (1.6)$$

Figure 1.3 shows the observable distance as a function of the proton energy. The observable distance with photons is also indicated. For high-energy photons the distance is limited by the pair creation process with infra-red or cosmic microwave light. At energies around 1 PeV the mean free pathlength is on the order of 10 kpc, corresponding roughly to the distance from the Earth to the galactic centre. It is therefore impossible to measure photons in this energy range from extragalactic sources.

Charged particles are deflected in the (inter-)galactic magnetic field. Sample trajectories of high-energy protons in the intergalactic field (1 nG) are shown in Figure 1.4 for two different proton energies in order to illustrate the influence of this important effect. As visible from the figure, the deflection of charged particles in the magnetic field becomes smaller at highest energies, however, as we have seen above, the observable pathlength

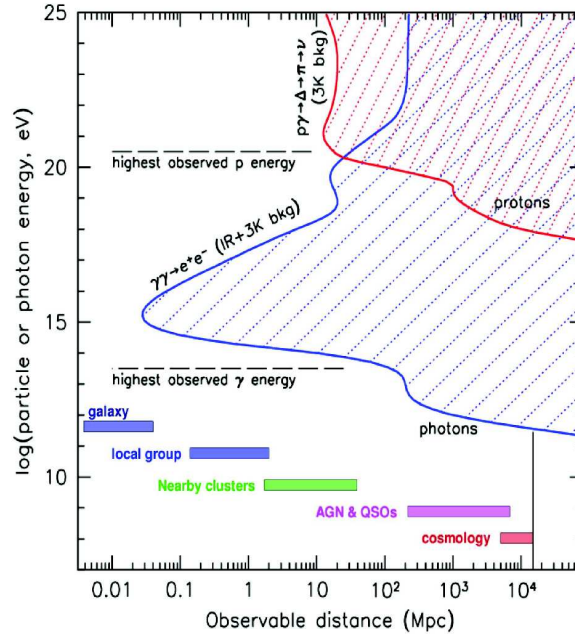


Figure 1.3: Observable distance in Megaparsec as a function of the proton (photon) energy [26]. Typical distances of astrophysical objects are indicated in addition.

also becomes smaller at these energies, which limits the observable region effectively to nearby sources. For charged cosmic rays being absorbed and deflected and photons being absorbed on their way to Earth, the neutrino acquires an important role as a unique cosmic messenger particle.

1.1.4 Neutrinos and gamma rays

This section is devoted to the connection between cosmic rays, gamma rays and neutrinos. As mentioned above, charged particles are deflected during their propagation from the source to the Earth in the (inter-)galactic magnetic field and thus do not provide information about their origin when reaching Earth. At ultra-high energies ($E > 10^{20}$ eV) the deflection becomes smaller; however, at those energies charged particles begin to interact with the cosmic microwave background radiation which limits their range to a few 10 Mpc. Sources within this distance could be detected by cosmic-ray experiments like Auger (see Section 1.3.2), this is nevertheless difficult, as the statistics decreases rapidly at the highest energies. It is thus important to find other means to identify the cosmic accelerators. This can be accomplished as the acceleration of charged particles in a cosmic accelerator is tied to the production of neutrinos and gamma rays. This fact represents a major motivation for neutrino astronomy.

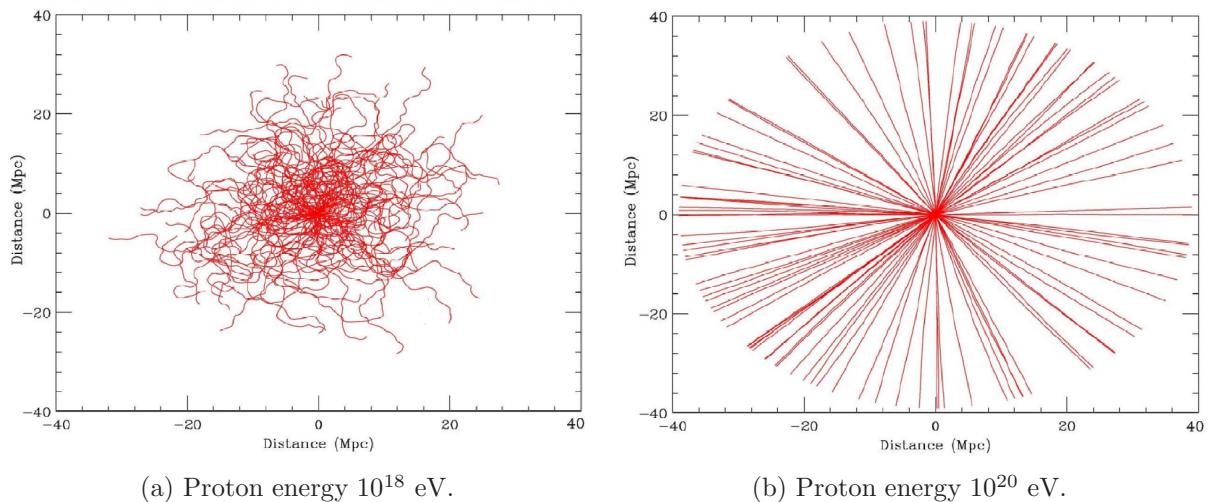
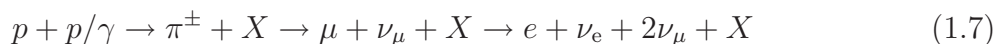
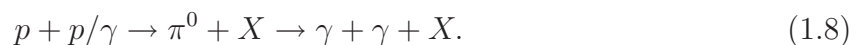


Figure 1.4: Sample trajectories for protons in the intergalactic magnetic field. From [27].

The crucial observation is that in any environment in which hadrons are accelerated to high energies, neutral and charged pions as well as neutrons are inevitably produced along through the interaction of the accelerated particles with both surrounding matter and ambient photon fields. This conception is sometimes referred to as beam dump scenario. The name of this model derives from accelerator physics, where a particle beam is turned off by deflection into a bulk of material, a so-called beam dump. In contrast to the beam dump at accelerators, the cosmic beam dump is less dense and to some extent transparent for neutral particles. This allows the reaction products to escape the acceleration region before being absorbed, and via subsequent decays they give rise to cosmic rays, neutrinos as well as high-energy gamma rays. Neutrinos are generated in the decay of charged pions in the chain



and gamma rays originate from the decay of neutral pions



Since neutrinos and gamma rays reach the Earth undeflectedly, they point back to the accelerators. As photons in the GeV energy region cannot be produced by known thermal astrophysical processes, their detection is direct evidence for non-thermal acceleration processes. However, besides the hadronic production scenario via pion-decay presented above, photons can also be generated in leptonic accelerators via electromagnetic processes such as inverse Compton scattering or synchrotron radiation. A detailed investigation of the photon spectra may lead to a distinction between hadronic and leptonic scenarios, although this is difficult in practice, as important parameters like the magnetic field strength at the source are hard to constrain. This leaves a prominent role for the detection of high-energy neutrinos as messengers from hadronic accelerators in the cosmos.

1.2 Neutrino sources

In this section candidates for astrophysical sources of high-energy neutrinos are presented.

1.2.1 Candidate sources for hadronic acceleration

Having explained the connection between cosmic rays and neutrinos in Section 1.1.4, we will now discuss candidates for hadronic acceleration in the cosmos and hence candidates for neutrino sources. Independent of the concrete acceleration mechanism, the maximum energy to which a particle of a given charge can be accelerated can be derived by the requirement that the Larmor radius of the particle should be smaller than the size of the acceleration region [28]. This argument yields the following relation between energy E , confining magnetic field B and the source extension R ,

$$E \approx \beta ZBR. \quad (1.9)$$

The parameter β in this equation can be interpreted as the acceleration efficiency, which corresponds to the velocity of the shock waves in the Fermi acceleration scheme. Equation 1.9 allows for a classification of astrophysical objects with respect to the “acceleration power”. In Figure 1.5, the magnitude of the magnetic field of candidate sources is plotted against the dimension of the object. As can be seen, good candidates for highest-energy cosmic accelerators are active galactic nuclei or gamma-ray bursts. In the following, the most important candidate objects are discussed.

- **Active galactic nuclei**

Active galactic nuclei (abbreviated AGN) are associated with the centres of galaxies. AGNs are thought to consist of a super-massive black hole ($10^7 - 10^9$ solar masses) residing in the core of a galaxy and accreting matter from its host (see Figure 1.6). Highly relativistic jets are observed perpendicular to the accretion disk. Depending on the orientation of the jet axis relative to the observer, the AGNs are classified as quasars or blazars (jet axis in line of sight). Neutrino production is possible both in the accretion disk, via photomeson production from thermal photons and in the jets where synchrotron photons provide an additional target [29].

- **Gamma-ray bursts**

Phenomenologically, gamma-ray bursts (GRBs) are transient luminous eruptions, which outshine the entire Universe in MeV gamma rays for a duration of typically a few tens of seconds. The thereby released energy per second is estimated to amount to $10^{51} - 10^{54}$ erg/s. In the collapse, a highly relativistic “fireball”, powered by radiation pressure, is produced which punctures through the stellar material, producing intense gamma rays, see Figure 1.7. The emission of gamma rays is followed by an afterglow shifting from x-rays to optical and finally radio emission, which allows for

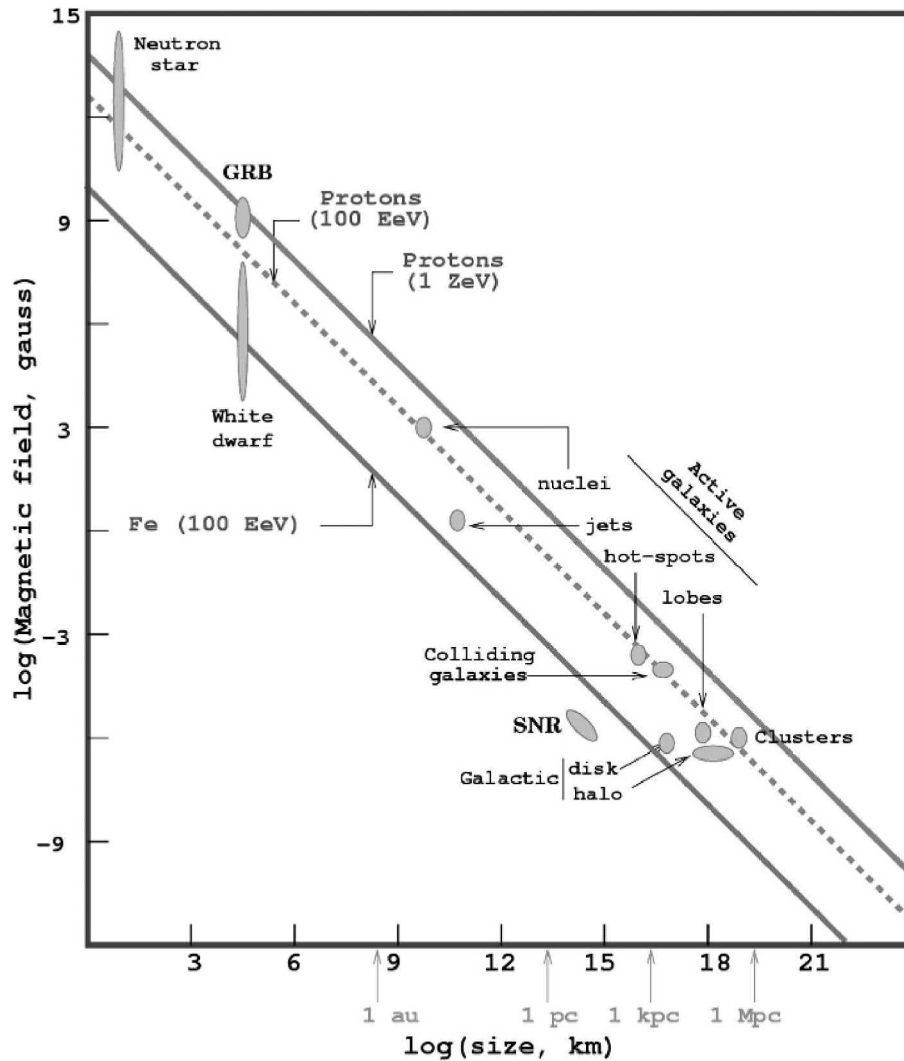


Figure 1.5: Hillas diagram [28]. The magnitude of the confining magnetic field for cosmic-ray accelerator candidates is plotted against the dimension of the objects. Astrophysical objects above the dotted line could be capable of accelerating protons to 10^{20} eV, assuming an efficient shock acceleration mechanism.

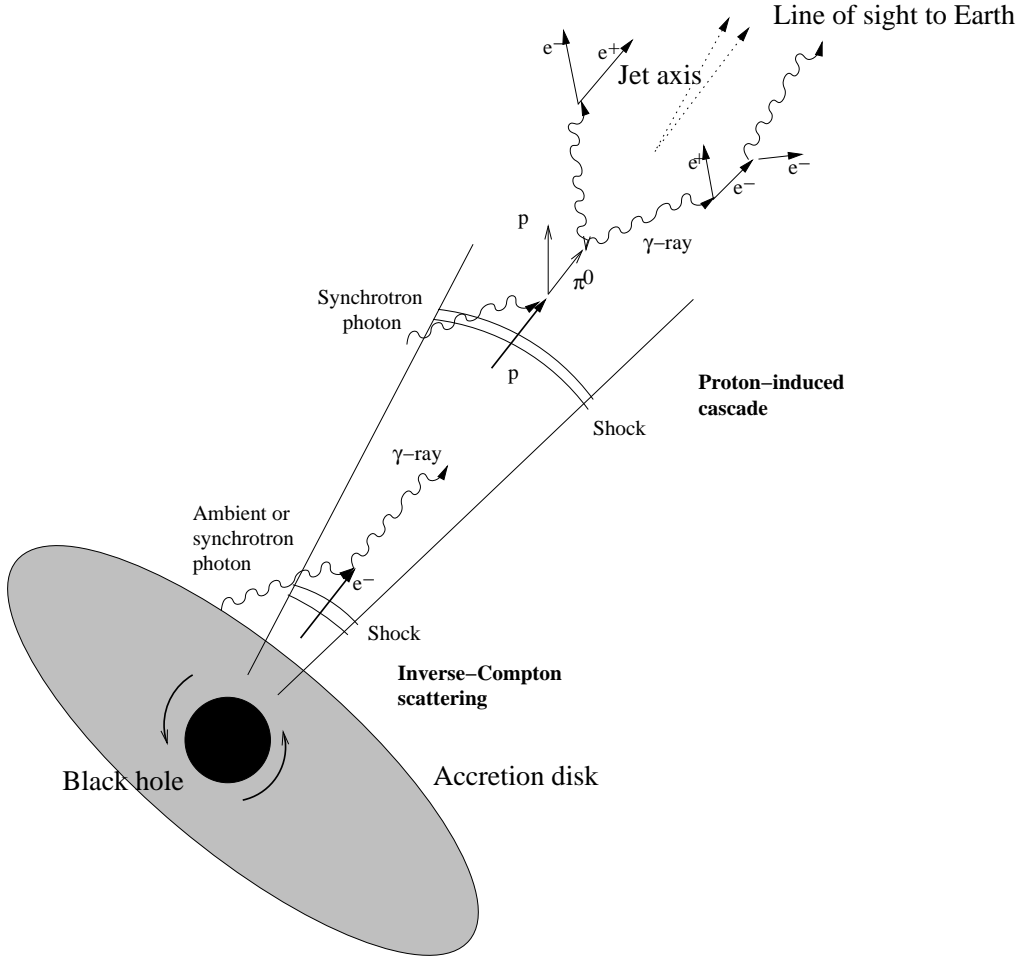


Figure 1.6: *Schematic view of an active galactic nucleus.*

a determination of the redshift and consequently the location of the emission. GRBs are among the best motivated sources of high-energy neutrinos (cf. [30, 31, 32]). It is estimated [30] that about 10% of the energy released in gamma-ray bursts is emitted in form of neutrinos. The multi-messenger observation of gamma-ray bursts, in which satellite observations trigger ν -telescopes, allows for constraining the observation time window and thus reduces the background to a minimum. This is therefore a promising technique for the observation of cosmic neutrino sources.

- **Supernova remnants**

Relics of supernova explosions are prime candidates for hadronic acceleration. In a supernova explosion a massive star collapses to a black hole or neutron star depending on the mass of the progenitor. During this violent process, which can outshine whole galaxies for a short time, parts of the outer shells of the star are ejected into the interstellar medium. In the common shell-type supernova remnants the expanding

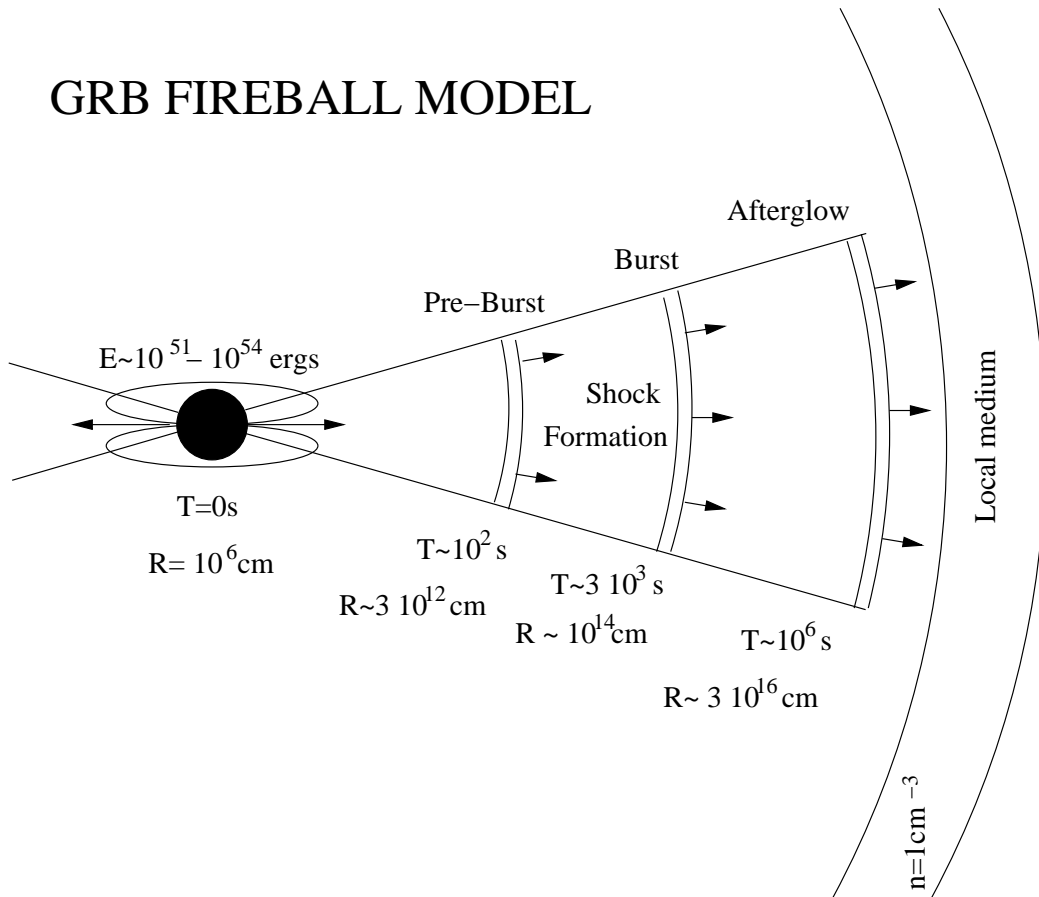


Figure 1.7: Schematic view of the temporal evolution of a GRB according to the fireball model. The evolution of the relativistic fireball during the different phases of the burst is shown together with the corresponding distances R to the origin and times T since the inception of the burst.

shell is a source of high-energy gamma rays. As the recently measured gamma-ray spectra indicate hadronic acceleration processes, supernova remnants are presumably neutrino sources as well. In many cases the supernova explosion results in a pulsar, a spinning neutron star with a strong magnetic field, and a nebula. In this configuration, the central pulsar accelerates particles and emits a wind of highly relativistic jets into the nebula. Pulsars wind nebulae have been identified as sources of high-energy gamma rays, yet the concrete production mechanisms are not fully understood. If the detected gamma rays are of hadronic origin, neutrinos can be expected as well.

- **Microquasars**

Microquasars are binary systems² in which a small black hole or a neutron star of about solar mass accretes matter from a companion star. This configuration resembles the one of a quasar, only on a much smaller scale. Similarly, a relativistic jet perpendicular to the accretion disk is formed, giving rise to cosmic-ray acceleration. The observed pattern of the emitted gamma rays are similar to that of quasars, although the emission is about six magnitudes weaker. Calculations [33, 34] show that microquasars are candidate sources of high-energy neutrinos.

1.2.2 Other sources

The main motivation of neutrino astronomy is the detection of neutrinos from hadronic accelerators in the cosmos to eventually pinpoint the sources of high-energy cosmic rays. Moreover, several other interesting processes exist in which neutrinos could be generated that can be detected with neutrino telescopes. In the following, a selection of the most important other sources of interest for neutrino telescopes is presented.

- **Neutrinos from dark matter annihilation**

Observations have shown that the largest fraction of matter in the Universe is non-baryonic. Since this component is neutral and does not interact electromagnetically, it cannot be directly revealed by optical techniques. Therefore it is referred to as dark matter. The precise nature of this component of our Universe is up to now still speculative. It has been hypothesised that (a fraction of) this component could be made up of WIMPs. WIMPs are weakly interacting massive particles which are postulated in certain supersymmetric extensions of the Standard Model of particle physics. The lightest of these supersymmetric particles plays an important role. If its decay into Standard Model particles is excluded by conservation laws, the lightest supersymmetric particle would be stable and a promising candidate for dark matter. The lightest supersymmetric particle could be the neutralino, a mixture of the supersymmetric partners of the Higgs and the neutral electroweak gauge bosons.

Stable supersymmetric particles originating from the early phase of the Universe can cool down in interactions with ordinary matter and may become gravitationally

²Observed within our galaxy.

bound to massive astrophysical objects like the Earth, the Sun or the galactic centre. The accumulation of such particles leads to a dense population which could facilitate, depending on the exact properties of the particles, annihilation into Standard Model particles. Neutrino telescopes can thus be used to search for neutrino signals originating from the annihilation of dark matter particles by measuring the neutrino flux from massive objects.

- **Neutrinos from the GZK effect**

As discussed above, the highest-energy cosmic rays interact with the cosmic microwave background (GZK effect) which limits their mean free pathlength and the observable distance. The threshold energy for the GZK effect for protons is given by

$$E_p = \frac{m_\pi^2 + 2m_p m_\pi}{4E_{\gamma_{\text{CMB}}}} \approx 6 \cdot 10^{19} \text{ eV} \quad (1.10)$$

In these interactions high-energy neutrinos are generated through pion and neutron decays. Therefore, cosmic rays, produced at cosmological distances, are sources of ultra-high energy neutrinos that can be detected with neutrino telescopes. (See also the discussion in Chapter 2, where alternative methods for the detection of ultra-high energy neutrinos are presented.) Calculations [35] give estimated detection rates of 1 event per km² per year. Since GZK neutrinos are very energetic, they can be well identified and efficiently separated from the background.

- **Neutrinos from the galactic disk**

Cosmic rays propagating through the galactic plane can interact with the interstellar medium to produce gamma rays and neutrinos through the abovementioned interaction channels. As a consequence, a diffuse component of the neutrino flux can be expected to originate from the galactic plane correlated in magnitude with the matter density in the galaxy.

- **Atmospheric neutrinos**

Atmospheric neutrinos are produced in the decay of charged pions, kaons and charmed mesons that are generated in the interaction of cosmic rays with the atmosphere. At energies below several 10 TeV atmospheric neutrinos dominate any expected cosmic neutrino signal.

1.3 Indications of hadronic accelerators

Recently, measurements with gamma-ray telescopes (see Figure 1.8a) and air-shower measurements with the Pierre-Auger experiment (cf. Figure 1.9) have revealed indications of hadronic accelerators. These important measurements shall be briefly discussed in the following. Although the implications of these measurements are still being debated, a detection of neutrino signals from these sources would be a smoking-gun evidence for hadronic acceleration.

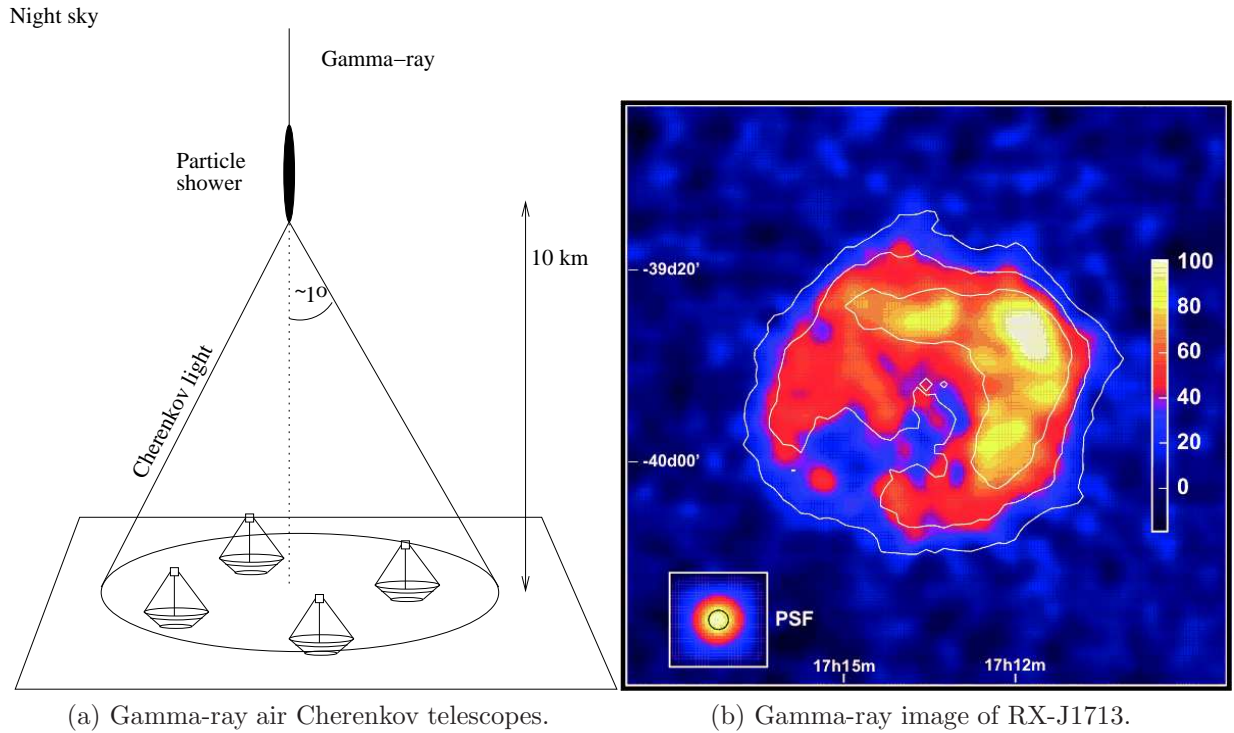


Figure 1.8: (a) Gamma rays interact in the atmosphere in a typical height of 10 km above the ground. The resulting particle cascade emits Cherenkov radiation in a cone with an opening angle of about 1° which is detected on the ground by Cherenkov telescopes. Stereo measurements with two or more telescopes improve the quality of the reconstruction. (b) Gamma-ray image of the supernova remnant RX J1713.7-3946 [37].

1.3.1 The supernova remnant RX J1713.7-3946

An interesting object and a good candidate for hadronic acceleration in our galaxy is the supernova remnant RX J1713.7-3946 which was first observed in TeV gamma rays by the CANGAROO experiment [36] and later also with the H.E.S.S. telescope [37]. The resolved image of the source (see Figure 1.8b) shows TeV gamma-ray emission from the whole object, with a clear increase in flux in the directions of known molecular clouds. This suggests that protons accelerated in the supernova remnant interact with the dense clouds to produce neutral pions which are the source of the observed gamma rays. The high-statistics data exhibits a power-law spectrum over a wide energy range without any indication for the cut-off behaviour expected for synchrotron or inverse-Compton processes. Further, multi-wavelength observations of the object found an insufficient population of electrons for the generation of the TeV photon flux by purely electromagnetic processes.

Interestingly enough, the Super-Kamiokande collaboration has recently reported an intriguing signature (at 97.5 – 99.8% CL) from RX-J1713.7-3946 in neutrinos [38]. In this study, data accumulated between 1996 and 2007, corresponding to a live-time of 2623 days

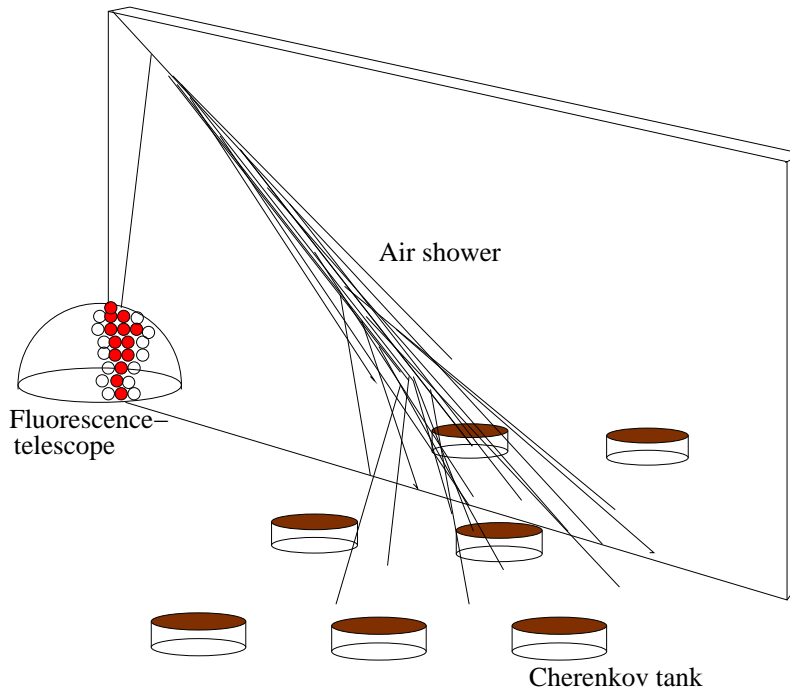


Figure 1.9: Air-shower detection with the Pierre-Auger hybrid detector. A surface array of 1600 water-Cherenkov tanks spread over an area of 3000 km² samples air-shower particles on the ground. In addition, four fluorescence telescopes are installed to detect the fluorescence light from atmospheric nitrogen, excited by air-shower particles.

were analysed. The observed signature, however, still lacks compelling statistical significance and new measurements with improved statistics have to be performed.

1.3.2 Active galactic nuclei

Observations of cosmic-ray induced air showers with the Pierre-Auger Observatory (see Figure 1.9) have revealed an anisotropy in the arrival direction at highest energies ($E \geq 10$ EeV) [39]. The arrival directions of the recorded high-energy events are found to be correlated with the locations of nearby AGNs at distances below 100 Mpc at an angular scale of less than 6° . The correlation is most pronounced at energies $E \geq 57$ EeV, where the measured 27 events (see Figure 1.10) show a correlation with the super-galactic plane. Since no correlation with the galactic plane is found, the events are most likely of extragalactic origin. The favoured interpretation of the measurement is that the observed events originate from AGNs or other (unknown) objects with a similar spatial distribution. A neutrino signal from these objects could help to clarify the issue.

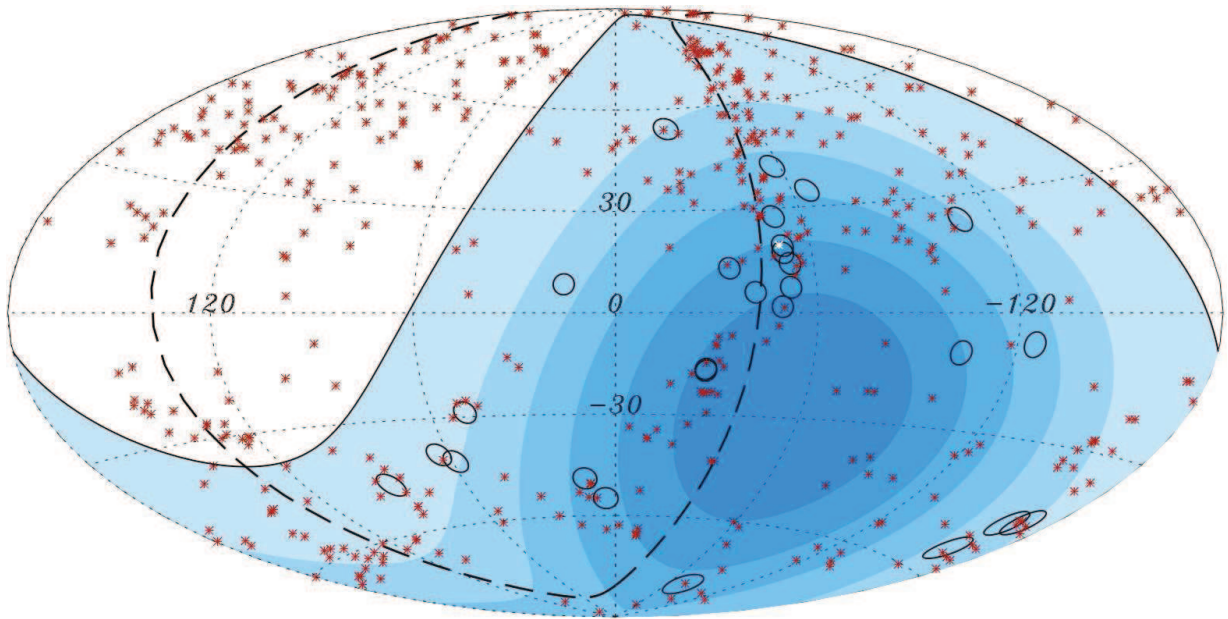


Figure 1.10: Sky map in galactic coordinates of 27 selected high-energy ($E \geq 57$ EeV) cosmic rays (open circles, the size corresponds to the angular resolution of 3.1°) measured by the Pierre Auger experiment. The directions of the closest AGNs (distance smaller than 75 Mpc) are indicated by red asterisks, Centaurus A ($d \approx 7$ Mpc) is drawn in white. The band of the super-galactic plane is given by the dashed line. The different blue-shaded areas denote regions of equal sky exposure time within the field of view (solid line). Figure taken from [39].

Chapter 2

Neutrino interactions and detection principles

This chapter discusses the neutrino interaction processes and the typical event signatures. Emphasis is put on the charged-current interaction channel of the muon neutrino, which is most important for neutrino telescopes. The neutrino detection technique based on the optical Cherenkov effect is explained. An overview of the history and the present status of neutrino detectors aiming at the detection of extraterrestrial neutrinos, commonly referred to as neutrino telescopes, is given. These Cherenkov telescopes reveal secondary muon tracks and electromagnetic and hadronic showers at the interaction vertex in the vicinity of the detector. Complementary, novel detection methods based on the observation of neutrino-induced air showers, acoustic or radio signals are briefly mentioned.

2.1 Neutrino interactions

Interacting only via the weak force, neutrinos represent the most elusive particles in the Standard Model of elementary particle physics. In this highly successful theoretical framework neutrinos are categorised as electrically neutral, stable and almost massless¹ particles which occur in three generations and constitute together with their charged counterparts the leptonic sector of elementary matter. Neutrinos are capable of escaping dense acceleration regions and reach the Earth virtually unattenuated and undeflected. On the one hand, this offers an excellent opportunity for using the neutrinos as unique cosmic messengers, allowing to probe regions inaccessible by other means. However, on the other hand, their detection poses a huge challenge to the experimentalists and requires large volumes to be instrumented. Since there is no direct detection technique available which is purely based on the weak-interaction, the neutrinos can only be detected indirectly, by measuring their interaction products. Hence neutrino detection involves monitoring huge target masses. At energies relevant for cosmic neutrino fluxes, the neutrino interaction cross section is

¹The experimental proof that the neutrinos have a small non-vanishing mass has been adduced only recently. Upper mass limits of 2 eV for all three flavours have been set from a combination of direct and indirect measurements [40].

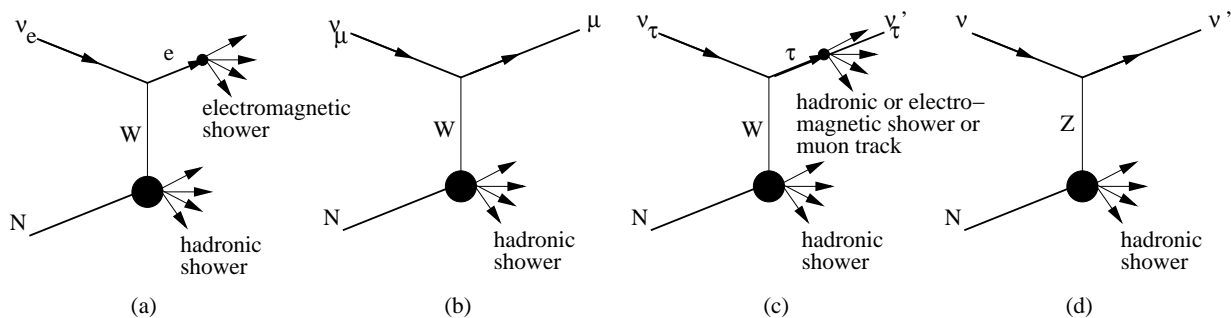


Figure 2.1: Summary of the neutrino nucleon deep-inelastic scattering channels. Charged current reactions (a) (b) (c), neutral-current interaction (d). See text for further explanation.

dominated by deep-inelastic scattering off the target nucleons². The main channels are thus the charged-current deep-inelastic scattering

$$\nu_l + N \longrightarrow l^- + X \quad (2.1)$$

$$\bar{\nu}_l + N \longrightarrow l^+ + X \quad (2.2)$$

where an (anti-)neutrino (of arbitrary flavour) interacts via the exchange of a W^\pm -boson with a nucleon N to produce a hadronic cascade X and an (anti-)lepton (of corresponding flavour), and the neutral-current reaction

$$\nu + N \longrightarrow \nu + X \quad (2.3)$$

where a neutrino exchanges a Z -boson with the target nucleon. In the latter case only the hadronic cascade originating from the interaction vertex can be observed. The Feynman diagrams for the neutral-current process and the charged-current channels for the three different flavours are depicted in Figure 2.1. The phenomenological signatures that are observed by a neutrino telescope are showers which, to a good approximation, are confined to a localised point (the extension of a shower is typically a few metres, which has to be compared to the spacing the sensors) and the signature of a long track. If the interaction happens outside the instrumented volume, only the track signatures of muons or taus can be seen. Electrons produce electromagnetic showers that are unlikely to reach the detector. In practice, it will not be possible to distinguish the neutral-current reaction of electron neutrinos from their charged-current reaction as one cannot disentangle electromagnetic showers at the interaction vertex from hadronic showers. Similarly, it is impossible to identify the flavour type of the neutrino in the neutral-current reaction. However, the charged-current channels for the different flavours differ in their event topologies. The electron neutrino will produce an electron that initiates an electromagnetic shower. In the interaction of the muon neutrino a long-range muon track is produced. Interesting signatures are created by the charged-current interaction of tau neutrinos. If the high-energy neutrino-nucleon interaction takes place inside the instrumented volume and the

²The only exception is the resonant W^- production via the $\bar{\nu}_e e \rightarrow W^-$ channel at 6.4 PeV (Glashow resonance).

decay of the emerging tau (via a semileptonic or the electron channel) happens within the detector, two distinct showers connected by a track will be visible. This is the famous “double bang” signature [41], cf. Figure 2.2. In the case that the interaction happens outside the detector and the emerging tau decays inside the detector, a “lollipop-like” event signature with a track, ending in a cascade will be produced. Detection of these intriguing events will probably be reserved for km³-scale instruments, where the detection of showers will play an important role. For smaller telescopes, the charged-current interaction of muon neutrinos, in which long muon tracks are produced, is of special importance. In comparison to the other channels the effective volume for the detection is largely enhanced.

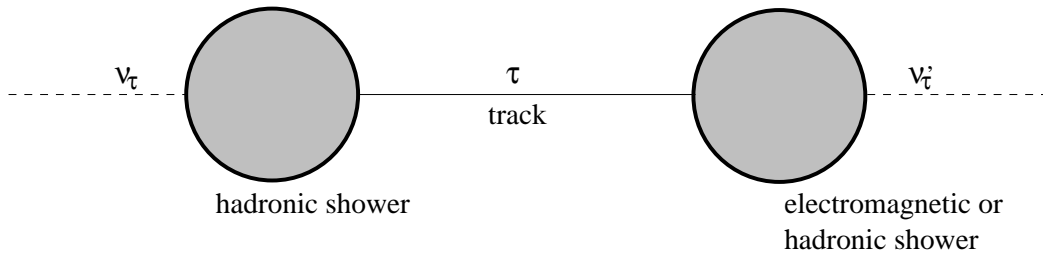


Figure 2.2: Topology of the “double-bang” event. A tau neutrino interacts to produce a hadronic cascade and a tau which gives rise to a track signature. The subsequent hadronic decay of the tau then initiates a second cascade.

2.2 Muon production and propagation

The charged-current neutrino nucleon deep-inelastic scattering cross section [42] is given in leading order by

$$\frac{d^2\sigma^{cc}}{dx dy} = \frac{2G_F^2 M E_\nu}{\pi} \left(\frac{M_W^2}{Q^2 + M_W^2} \right)^2 [xq(x, Q^2) + x\bar{q}(x, Q^2)(1-y)^2] \quad (2.4)$$

where $x = Q^2/2M(E_\nu - E_1)$ and $y = (E_\nu - E_1)/E_\nu$ are the Feynman-Bjorken scaling variables, which correspond to the momentum fraction of the nucleon carried by the struck quark in the quark-parton model and the momentum fraction transferred to the out-going hadronic state in the rest frame of the nucleon. The variable Q^2 denotes the negative squared four-momentum transfer between incoming and outgoing lepton. Furthermore, $G_F = 0.117 \cdot 10^{-4} \text{ GeV}^{-2}$ is the Fermi coupling constant, M the mass of the nucleon, E_ν the initial neutrino energy, M_W the mass of the W -boson and $q(x, Q^2)$ and $\bar{q}(x, Q^2)$ are the parton distribution functions for quarks and anti-quarks respectively. Figure 2.3 gives the cross section as a function of the neutrino energy. At low and intermediate neutrino energies $E_\nu \ll M_W^2/2M \approx 5 \text{ TeV}$ the cross section rises linearly with energy. At higher energies $E_\nu \gg 5 \text{ TeV}$, the cross section is determined by the parton distribution functions at small x . In this region, the sea-quark distributions of the nucleon are probed by the

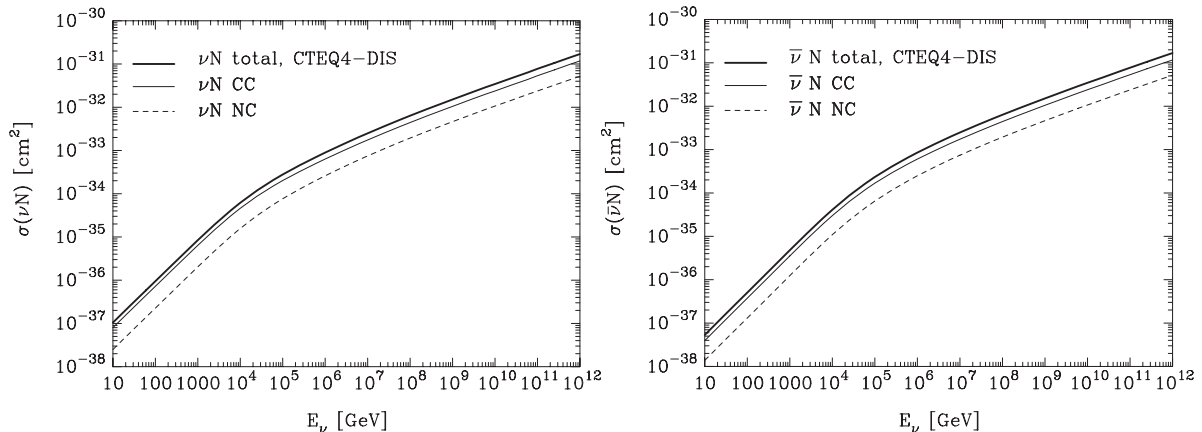


Figure 2.3: Neutrino isoscalar nucleon cross section as function of the neutrino energy. The neutrino-nucleon interaction cross section is depicted in the left plot, whereas the plot on the right shows the cross section for the antineutrino-nucleon reaction.

electro-weak interaction with the neutrino mediated by the W^\pm -bosons.

The angle between the direction of the initial neutrino and the out-going muon in the charged-current channel is very small, the muon track and the parent neutrino are almost collinear. A parameterisation of the median angle between muon and neutrino is given by

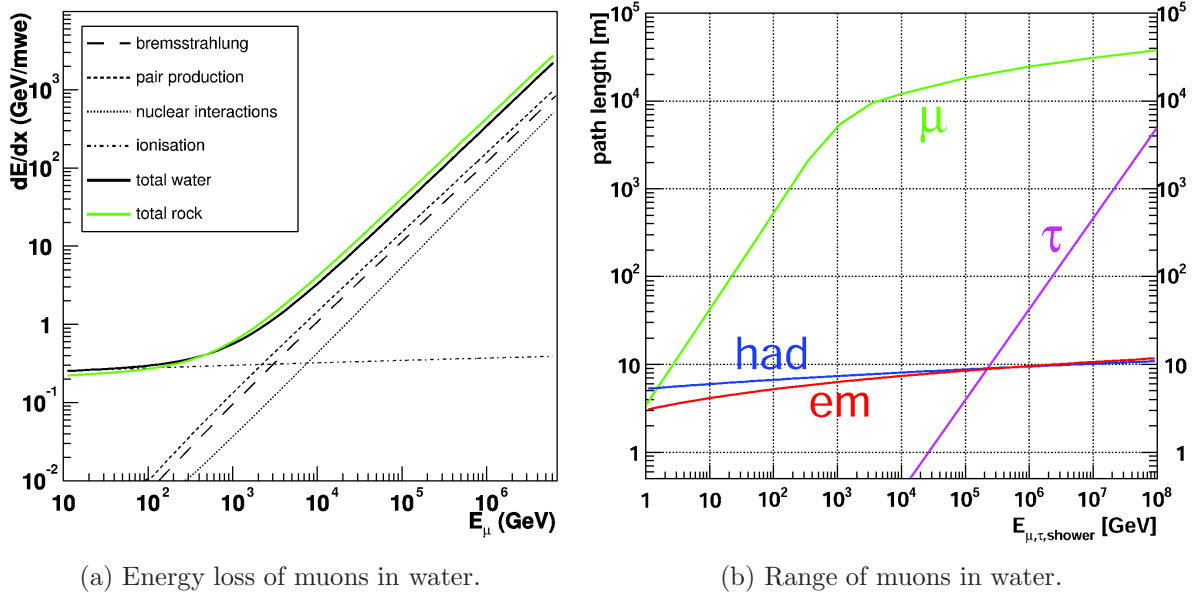
$$\Delta\theta_{\text{scat}} = \frac{0.7^\circ}{(E[\text{TeV}])^{0.6}}. \quad (2.5)$$

During the propagation in the medium (in our case sea water or rock) the muon track is further deflected as the muon undergoes multiple scattering. The mean angular deviation between the initial muon direction and the direction after passing a distance x in the medium is described by [43]

$$\Delta\theta_{\text{ms}} = \frac{13.6\text{MeV}}{E_\mu} \sqrt{x/X_0} [1 + 0.0038 \ln(x/X_0)], \quad (2.6)$$

where X_0 is the radiation length of the medium and $\Delta\theta_{\text{ms}}$ is given in radians. The deviations due to multiple scattering described by Equation 2.6 are generally smaller than the scattering angle in Equation 2.5. As a result, the muon produced in the charged-current interaction of the ν_μ retains the original direction of the neutrino to a very good approximation. By measuring the direction of the muon one can therefore infer with a good precision the original neutrino direction and hence the location of the neutrino source in the sky. This fact legitimates the term neutrino astronomy.

During the propagation, the relativistic muon produced in the charged-current interaction loses energy due to ionisation and radiative processes (bremsstrahlung, pair production



(a) Energy loss of muons in water.

(b) Range of muons in water.

Figure 2.4: (a) Average energy loss per metre water equivalent (mwe) for muons in rock and water as a function of the muon energy. The different contributions are detailed. Figure from [45]. (b) Range of the muons, taus, hadronic and electromagnetic showers in water. Figure taken from [46].

and photo-nuclear interactions) [44]. For energies below 1 TeV the main contribution comes from ionisation and is roughly constant at about 0.3 GeV per metre of water. At higher energies radiative losses dominate. The different contributions to the energy loss in dependence on the muon energy are detailed in the left plot of Figure 2.4. The resulting muon range is shown in the right plot of Figure 2.4. In this plot, the muon range is compared with the range of taus and electromagnetic and hadronic showers. A 10^7 GeV muon can traverse tens of kilometres of water before it stops. Due to the long range of high-energy muons, neutrino telescopes are most sensitive to the muon neutrino.

2.3 The Cherenkov effect

If a charged particle traverses a dielectric medium with a velocity greater than the speed of light in the medium, a characteristic radiation is emitted. This phenomenon, first observed in the 1930s, is called Cherenkov effect [47]. Along the particle track electric dipoles are polarised. If the particle moves slowly compared to the speed of light, the configuration of the dipoles is almost symmetric and no radiation is produced. If the particle velocity exceeds the speed of light a net dipole moment is produced and radiation is emitted in a cone with a characteristic angle θ_C . An illustration of the effect is given in Figure 2.5. The angle under which the Cherenkov radiation is emitted is determined by the velocity β of the particle and the refraction index n of the medium. From the geometry sketched in

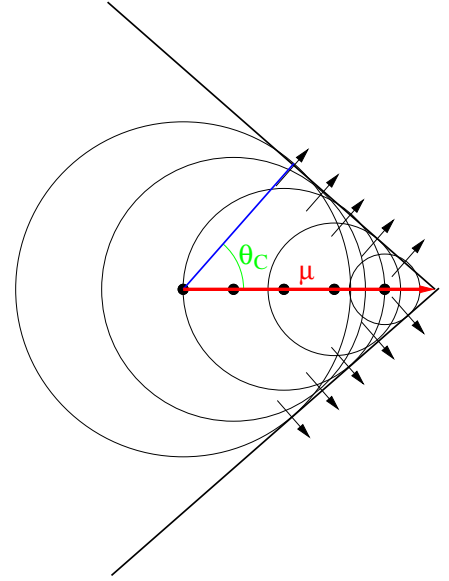


Figure 2.5: *Illustration of the Cherenkov effect. Local distortions of the charge configuration in the medium lead to the emission of electromagnetic waves. The individual contributions along the track (red line) interfere constructively on their envelope which forms a cone. Cherenkov photons (blue line) are emitted under a characteristic angle θ_C . The situation is in analogy to the supersonic bang.*

Figure 2.5 one can deduce that

$$\cos \theta_C = \frac{1}{n\beta}. \quad (2.7)$$

The typical Cherenkov angle for sea water is $\theta = 42^\circ$. The number N of emitted Cherenkov photons per distance x and wavelength λ can be calculated (Frank-Tamm equation, see e.g. [48]) to be

$$\frac{d^2 N}{dx d\lambda} = \frac{2\pi\alpha}{\lambda^2} \left(1 - \frac{1}{\beta^2 n^2} \right). \quad (2.8)$$

This equation can be reformulated with the help of Equation 2.7 and by integrating over the wavelength in the sensitive region of the PMTs (300–600 nm) to

$$\frac{dN}{dx} = 76500 \sin^2 \theta_{Ch} m^{-1}. \quad (2.9)$$

Thus, the number of emitted Cherenkov photons per metre amounts to about 35000. From Equation 2.8 it is visible that the number of emitted photons is (almost) independent of the particle energy. The emission of Cherenkov radiation only gives a small contribution to the energy loss of the particle.

2.4 Neutrino telescope projects

Today's large-scale neutrino telescope experiments, which aim at the detection of high-energy cosmic neutrinos, are preceded by smaller instruments which have successfully measured extraterrestrial neutrinos from the Sun and from a supernova (SN 1987a) and have further establish neutrino oscillations through the study of the angular distribution of atmospheric neutrinos. These instruments differ from the telescopes in their size and observable

energy range. Whereas the neutrinos emitted in nuclear fusion processes in the Sun or from supernovae have energies of keV–MeV, neutrinos from high-energy cosmic accelerators are presumably in the TeV–PeV region; thus different detection concepts are necessary.

The concept of exploiting natural abundances of deep-sea water or ice for high-energy neutrino telescopes has been discussed already about 50 years ago (e.g. [49, 50]). As the technical challenges to equip such hostile (high pressure, corrosive sea water) and difficult to access environments with optical sensors and electronics are tremendous, a long phase of preparatory work bringing along some difficulties and setbacks was unavoidable before mature technical concepts could be devised and the first successful installations were performed. The detection principle is based on the instrumentation of large volumes of water or ice with photomultipliers (PMTs), optical sensors, which are immersed in large depths to detect the Cherenkov light induced by neutrino interaction products. This approach mainly addresses the detection of cosmic neutrinos in the TeV to PeV energy region. In the following, present and past neutrino telescope projects are presented.

- **DUMAND**

The Deep Underwater Muon and Neutrino Detection (DUMAND) project [51] was started around 1976 to construct a neutrino telescope at a depth of 4800 m on a deep-sea site in the Pacific ocean off Keyhole Point on the Big Island of Hawaii. After several years of preparatory work, a prototype string was deployed in order to validate the design for the telescope. In 1993, a string with photosensors and a second one with monitoring devices were installed together with a junction box to connect the setup to the shore. Regrettably, the instrument did not perform as expected; after a while, short-circuits occurred and the connection to the shore was cut. In 1996 the funding was ceased and the project was cancelled. Although DUMAND ended unsuccessfully, the fundamental work and the technical know-how gained during this project was important for subsequent projects.

- **BAIKAL**

The first working setup which proved the feasibility of the optical detection technique by detecting several neutrinos in the year 1996 has been deployed in the Siberian Lake Baikal [52, 53]. The experiment has been running since 1993, when three detection strings with 36 PMTs embedded in pressure-resistant glass spheres were immersed to a depth of 1 km and put into operation. The detector was later expanded to 18 strings with a total of 192 PMTs, the NT-200 setup. The detector is arranged around a central unit with the main electronic block and a calibration laser on the top of the layout that provides the support structures for the 18 strings which are distributed on a circular geometry with a radius of 22 m. Each of the strings measures 68.5 m. This setup was extended in 2005 by three additional strings of 200 m length with 36 PMTs at a distance of 100 m (NT-200+) to the detector centre in order to increase the effective area for showers. Compared to neutrino telescopes in the deep sea, the Baikal setup offers several advantages. Firstly, the operation in fresh water naturally

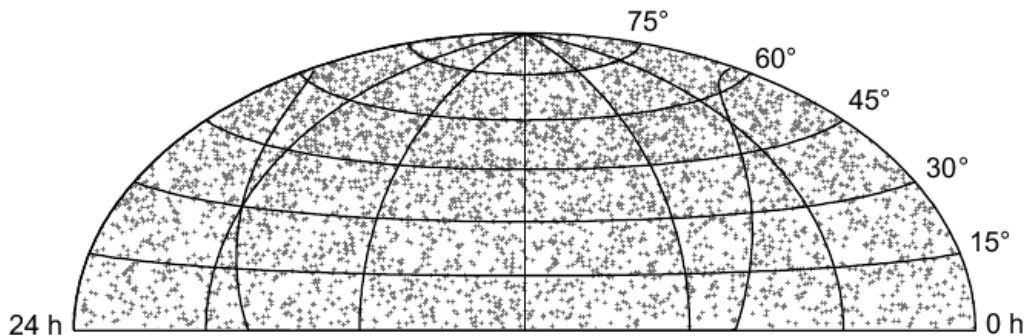


Figure 2.6: A sky map of 4282 reconstructed up-going neutrino candidate events recorded by AMANDA-II during the years 2000 to 2004 [54]. The remaining background from mis-reconstructed atmospheric muons is estimated to be less than 5%. The total number of events is in agreement with the prediction (4600) derived from a simulation of atmospheric-neutrino events. A detailed analysis of the measured sky map could not reveal any neutrino-point sources.

reduces the background contributions from ^{40}K decays. Secondly, the maintenance of the detector is greatly alleviated by the possibility to use the frozen sea surface as a basis for deployment and recovery operations. Disadvantages are the reduced absorption length of the water in Lake Baikal and the relatively low depth which leads to a larger atmospheric muon background compared to deep-sea telescopes.

- **AMANDA**

The Antarctic Muon And Neutrino Detection Array (AMANDA) is located near the Scott-Amundsen South Pole station in the Antarctic Ice. In 1997 the AMANDA B-10 detector was completed. It consists of 10 strings immersed in the glacial ice at a depth of 1500 m to 2000 m, carrying 302 PMTs of 8 inch diameter. In the year 2000, the setup has been enhanced to its final configuration (AMANDA-II) by adding 9 strings to a total of 677 PMTs. The analogue signals of the PMTs are read out by copper cables connecting the PMTs to the control station. AMANDA has been switched off in early 2009. In Figure 2.6 a map of neutrino candidates recorded during the years 2000-2004 is shown [54]. Unfortunately, despite the good statistics, analyses of AMANDA data have not found any point-source signals.

- **ICECUBE**

IceCube [55] is the km^3 -sized successor of the AMANDA neutrino telescope currently under construction in the Antarctic ice. The final configuration will consist of 80 strings of over 1000 m length separated by 125 m, with 4800 PMTs in total. On the surface, the instrument is complemented by an air-shower array, IceTop, which will serve as a calibration device and as a veto for atmospheric muons. Part of the detector is already operating and taking data. Figure 2.7 shows a sky map of neutrino events detected with 9 strings. As of today no signals of cosmic neutrino sources could be detected with this, currently, most sensitive instrument.

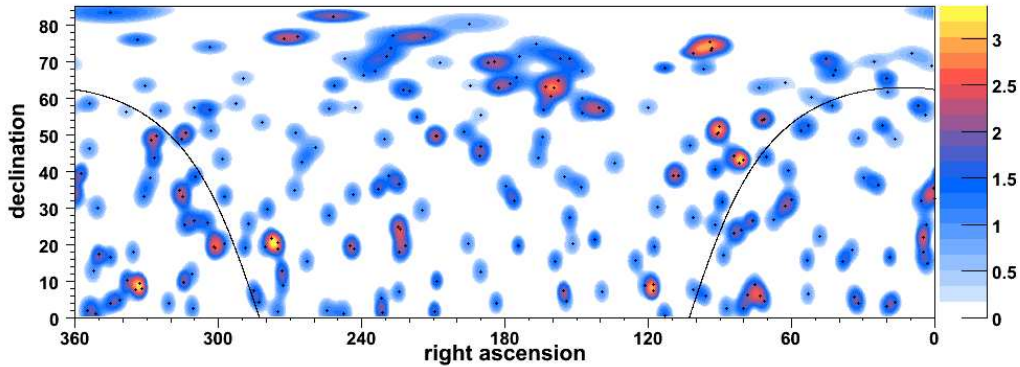


Figure 2.7: A sky map in Equatorial coordinates, showing the excess above the atmospheric neutrino background in units of standard deviations as recorded with the IceCube 9-string detector [56]. The maximal observed excess of 3.35 standard deviations is found at a right ascension of 276.6° and a declination of 20.4° . This spot is not correlated to any promising candidate object, and furthermore the magnitude of the deviation is not significant. The probability (p -value) of finding such a deviation (or an even higher one) caused by random fluctuations of the background only has been evaluated to be 60%.

- **NESTOR**

The Greek NESTOR (Neutrino Extended Submarine Telescope with Oceanographic Research) collaboration [57, 58] initiated the first project for a neutrino telescope in the Mediterranean sea at a site located 18 km off the coast of Pylos at a depth of 4000 m. The chosen telescope design uses tower-like rigid support structures instead of flexible mooring strings. These towers consist of 12 layers made up of six arms each, which are laid out in a star-shaped form. On each of these arms one upward and one downward looking $13''$ PMT are mounted. The final detector is planned to comprise seven towers. A prototype version of the detector has been tested in 2003, and first atmospheric muon data were recorded [59].

- **ANTARES**

Located in the Mediterranean sea offshore Toulon, ANTARES is the largest neutrino telescope on the northern hemisphere currently operated. The ANTARES telescope is subject of this thesis and will be described in detail in Chapter 3.

- **NEMO**

The Italian NEMO (Neutrino Mediterranean Observatory) project [60, 61] has focused on research and design for a future km^3 -scale detector in the Mediterranean sea. The NEMO design concept features a flexible tower structure of horizontal bars of 15 m length which are connected by ropes. At each end of the bars two PMTs are mounted, one looking downwards, the other one in the horizontal direction. The detection towers can be deployed as a compact object together with a socket and

self unfurl in the sea. After the unfolding, adjacent bars are aligned perpendicular to each other.

- **KM3NeT**

The KM3NeT project [62, 63, 64] is a joint effort of the ANTARES, NEMO and NESTOR collaborations to construct a cost-effective next generation telescope of cubic-kilometre size which will succeed the current generation of instruments in the Mediterranean sea and complement the IceCube detector on the northern hemisphere. A conceptual design report has already been formulated and the technical design report is expected to become available in early 2010.

2.5 Complementary neutrino detection techniques

In addition to the optical neutrino detection in water or ice relying on the Cherenkov effect described above, novel methods for neutrino detection are investigated as well. Experiments are designed and performed aiming at the detection of neutrino induced radio emission, for instance in ice or the Moon’s crust, the measurement of fluorescence light of neutrino induced air showers in the atmosphere, or acoustic detection of bipolar pressure waves caused by the local heating of the medium at the neutrino interaction vertex. Despite being based on entirely different techniques, these new methods all have in common to focus on the detection of ultra-high energy neutrinos ($E > 100\text{PeV}$), an energy regime where the predicted fluxes become too small for the “traditional” optical technique, which would require the instrumentation of exceedingly large volumes with optical sensors, bearing in mind that the maximal sensor distance is to a large extent determined by the attenuation length of light in the medium. We will now briefly discuss these novel techniques in turn.

- **Radio detection**

In an electromagnetic cascade propagating through a dense medium, energetic electrons are accumulated, created by Compton scattering and knock-on processes. These effects lead to a net negative charge traversing the material, which in turn gives rise to Cherenkov radiation [65]. The emitted radiation will be polarised and coherent in case the cascade dimensions are smaller than the emitted wavelength. For typical extensions of electromagnetic cascades of several metres the emission will be in the radio band. Hence, this effect allows for the detection of neutrino induced showers with radio antennas. This method is very appealing, since large volumes can be monitored cost-efficiently. Ground based, balloon and satellite experiments are conducted to measure the radio emission in the polar ice or, at even higher energies, in the Moon’s crust.

- **Acoustic detection**

The acoustic detection of neutrinos relies on the hydrodynamic radiation in form of ultrasonic pressure waves described by the thermo-acoustic model [66]. The energy deposition of particles interacting in fluid media leads to a local heating of the

medium and subsequently to an expansion or contraction according to the volume expansion coefficient. Therefore a pressure pulse is created which propagates through the medium and can be detected by acoustic sensors. Acoustic detection is also studied within the ANTARES project (see Chapter 3).

- **Neutrino-induced extended-air-shower detection**

Extended air-shower array detectors are chiefly designed to detect particle cascades induced by interactions of cosmic rays with the atmosphere. The two main techniques which are employed for this purpose rely on the sampling of the cascade on the ground via an array of water-Cherenkov counters or on the measurement of the fluorescence light emitted by excited nitrogen molecules in the atmosphere. In the Pierre Auger Observatory (see Chapter 1) both methods are combined into a hybrid setup. The aperture is large enough for the observatory to be sensitive to rare neutrino-induced cascades. Whilst the interaction of hadrons takes place in the top layers of the atmosphere (at an altitude between 10 and 20 km for a vertically down-going primary), the weakly interacting neutrinos can give rise to showers in much deeper layers. A gold plated neutrino candidate event would therefore be a young inclined air shower which could be well separated from ordinary hadron induced events.

The following table summarises the different methods and gives rough estimates of the respective energy thresholds and attenuation lengths.

Detection type	Medium	E_ν threshold	Attenuation length
Cherenkov	Ultra clean H_2O	$> \text{GeV}$	$\approx 70 \text{ m}$
	Natural lake	$> \text{GeV}$	$\approx 20 \text{ m}$
	Deep-sea	$> \text{GeV}$	$\approx 40 \text{ m}$
	Polar ice	$> \text{GeV}$	$\approx 20 \text{ m}$
Radio Cherenkov	Polar ice	$> 5 \text{ PeV}$	$\approx 1 \text{ km}$
	Moon	$> 100 \text{ EeV}$	$\approx 10 \text{ m}$
	Salt	$> \text{PeV}$	$\approx 1 \text{ km}$
Acoustic	Water	$> \text{PeV}$	$\approx 5 \text{ km}$
	Ice	$> \text{PeV}$	$\approx 1 \text{ km}$
Air shower particles	Air	$> 10 \text{ PeV}$	$\approx 1 \text{ km}$
N_2 fluorescence	Air	$> \text{EeV}$	$\approx 10 \text{ km}$
Air shower radar	Air	$> \text{EeV}$	$\approx 100 \text{ km}$

Table 2.1: Comparison of different high-energy neutrino detection techniques. Based on [25].

Chapter 3

The ANTARES neutrino telescope

This chapter introduces the ANTARES neutrino telescope and deals with the data acquisition chain from the recorded light signals to the mass storage system. Thus, this chapter provides a basis for the disquisition in the following chapters. Subsequent to the description of the technical layout of the ANTARES telescope, signal and background processes as well as their signatures are presented. The methods to efficiently select the relevant physics data are described. The ANTARES telescope is equipped with several systems to monitor environmental parameters and to calibrate the instrument. The calibration systems and methods that are used to ensure high reconstruction accuracy are discussed. Detailed Monte Carlo simulations are used in order to understand the response of the instrument to various relevant processes. The ANTARES simulation chain, used in the analysis in Chapter 7 is described. The chapter closes with a glimpse at the history of the construction of the instrument.

3.1 The ANTARES project

The ANTARES collaboration was formed in 1996 as a European effort with the objective of conducting design, construction and operation of a large-area water Cherenkov neutrino detector in the Mediterranean sea, optimised for the detection of muons from high-energy cosmic neutrinos. Presently, the ANTARES collaboration counts more than 150 active physicists and engineers from 7 European countries. The rationale and the physics motivation of the experiment are detailed in the conceptual design report [67], whilst the technical aspects are described in the technical design report [68]. For technical details beyond the scope of this work the reader is referred to these documents.

In 2006 the first detection unit of the final detector configuration has been deployed. Since then data has been taken continuously with a growing detector configuration. The construction of the telescope has been finished end of May 2008 with the connection and commissioning of the last two detection units. Being the largest apparatus in the Northern hemisphere, in addition to its unique discovery potential, ANTARES represents a benchmark and possible prototype for the next generation KM3NeT detector [69], envisaged for construction in the Mediterranean sea.

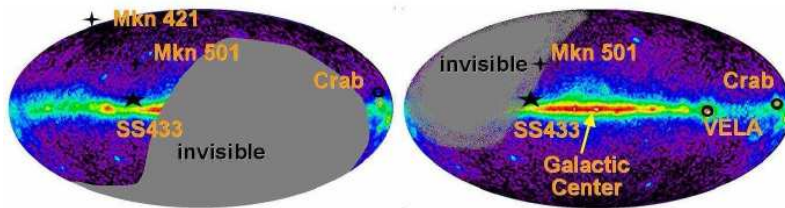


Figure 3.1: Comparison of the field of view of a neutrino telescope at the South Pole (left) to that of ANTARES (right). A few neutrino source candidates are indicated as well.

The installation of the detector on the Northern hemisphere warrants a direct view on the galactic centre (in 67% of the observation time) inasmuch as neutrino telescopes use the Earth as a shield against background and distinguish their signal as up-going neutrino-induced tracks or showers from down-going atmospheric muons. Figure 3.1 shows a comparison of the field of view to an installation at the South Pole.

The precise geographical position of ANTARES in the Ligurian sea at $42^{\circ}50'N$ and $6^{\circ}10'E$ in a depth of 2475 metres, approximately 40 km off Toulon at the French coast, is indicated in Figure 3.2, where the sea-depth levels and the coast line (in grey) are given in addition. The site benefits from the proximity to the sea infrastructure available in the harbour of Toulon, which facilitates the installation and maintenance of the detector. From its position, ANTARES has an annualised sky coverage of 3.5π sr, sharing an instantaneous field of view of 0.5π sr and an integrated common view of 1.5π sr with the IceCube telescope at the South Pole.

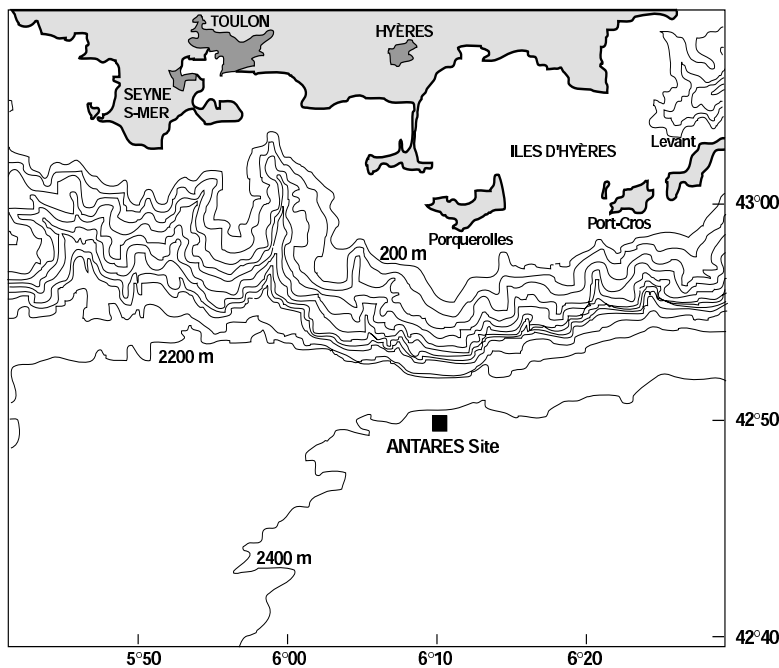
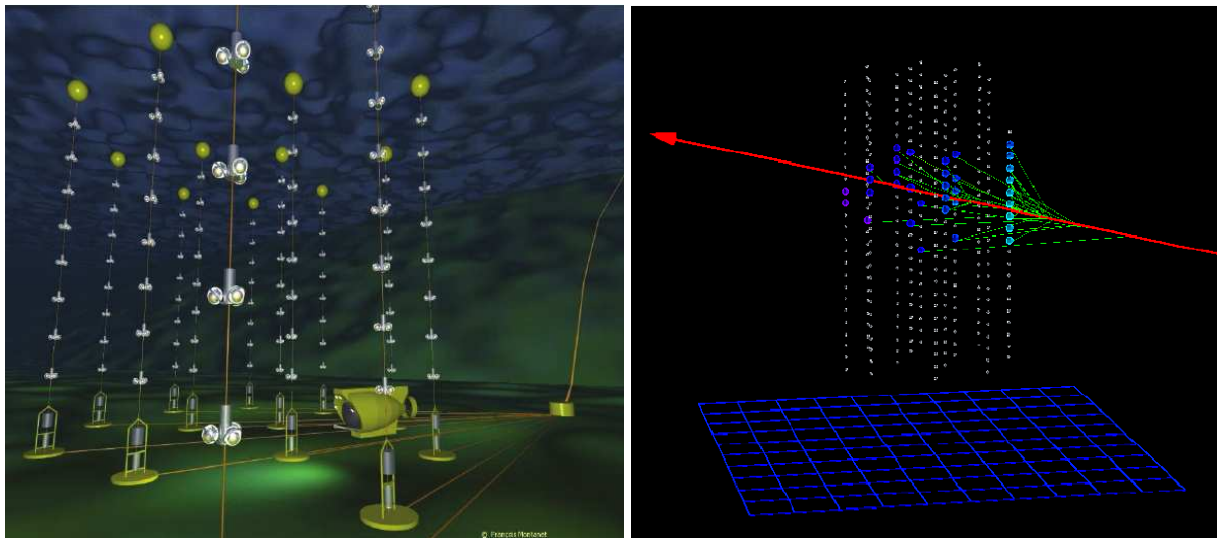


Figure 3.2: A map of the ANTARES site. The detector is installed at a depth of 2475 metres at $42^{\circ}50' N$ and $6^{\circ}10' E$. Indicated are the depth levels and the coast line. The telescope is connected via a deep-sea cable to the shore-station at La-Seyne-Sur-Mer, where the transmitted data are filtered and archived at a computer farm. The telescope is operated by a shift crew either from the shore-station or remotely from the home institute via the network.



(a) Artist's view of the ANTARES detector.

(b) Display of a neutrino candidate event.

Figure 3.4: *The ANTARES detector – from vision to reality. (a) An artist's view of the telescope [70] in which only 8 of the 25 storeys per string are drawn. (b) A computer graphic [71] of a real neutrino candidate event recorded with the ANTARES detector. In this view only the storeys of the ANTARES detector are visible and not the OMs. Hit storeys are enlarged. The reconstructed muon track is shown in red, the Cherenkov photon trajectories are indicated in green.*

3.2 Layout of the ANTARES detector

The ANTARES detector is conceived as a three-dimensional array of about 900 photo-multipliers arranged on 12 mooring detection units, so called lines or strings. Each line consists of an electro-optical-mechanical cable (EMC) which measures 450 metres and is anchored on the sea floor by a dead weight and hold upright by a buoy. The mechanical support structures (frames) for the 25 storeys holding the sensors and the electronics are mounted with a spacing of 14.5 m on the EMC, which provides the connection to the bottom string socket (BSS) for readout and power supply. The first storey of each line is located at a height of 100 m above the sea floor. On each of the storeys three optical modules (OMs), consisting of 10" photo-multiplier tubes (PMTs) housed in pressure-resistant glass spheres, are mounted radially on a rigid titanium frame looking downwards at an angle of 45° with respect to the horizontal. A cylindrical titanium container for the front-end electronics is mounted at the centre of the frame. The selected Hamamatsu R7081-20 PMTs are most sensitive at 400 nm, where the quantum efficiency peaks at about 23%. For a typical high-voltage of 1800 V the PMT gain is about

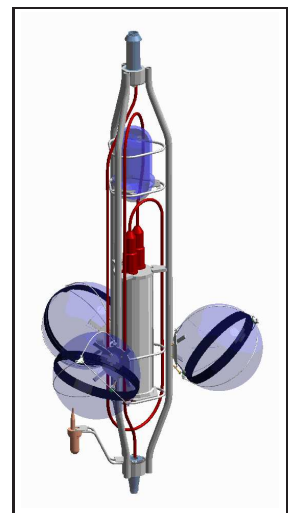


Figure 3.3: *Storey with 3 OMs.*

$5 \cdot 10^7$. The time and charge resolution is 2.6 ns and 40%, respectively [72]. With respect to readout and power supply each line is organised in five independent units (sectors), each of which comprises five storeys. One storey (the second, counting from the bottom) of the sector is equipped with a master local control module (MLCM) which gathers the information collected in the local control modules (LCMs) of the other storeys. The MLCMs are connected via the string control module (SCM) in the BSS to the junction box (JB) which in turn is connected to the shore-station by a standard deep-sea communication cable. The data flow in the ANTARES detector is further discussed in Section 3.4. The connections of the individual lines to the junction box are performed after the deployment by a submersible. For this operation an unmanned, remotely operated vehicle (ROV) can be used. The interline spacing is about 65 m – 70 m and the 12 lines are arranged in an octagonal structure (see Figure 3.6), covering an area of about 180 m \times 180 m on the sea bed. The detector layout is depicted in Figure 3.5. The ANTARES detector is supplemented by a set of devices for calibration and monitoring purposes. LED and laser devices are used for time calibration. Hydrophones, compasses and tiltmeters are employed for the positioning of the detector elements. The calibration of the instrument is described in Section 3.5. In addition to the optical part of the detector, an acoustic setup, AMADEUS¹, has been implemented in ANTARES to perform R&D for acoustic detection. Acoustic detection units are housed on Line 12 and on an additional string with monitoring and calibration devices, the Instrumentation Line, IL07 for short. A detailed description of the acoustical components can be found in [73].

3.3 Signal and background for ν -telescopes

The ANTARES telescope is installed at a depth to which no sunlight penetrates. The sensitive PMTs can thus detect the faint light that is emitted by neutrino-induced muons or showers. Unfortunately, not only reaction products of cosmic neutrino interactions emit detectable light, but also charged particles produced by the interaction of atmospheric neutrinos and muons originating from cosmic-ray-induced air showers, see Figure 3.7. These additional signals represent a blessing and a curse. Atmospheric muons can reach the detector only from above and they can therefore be differentiated from up-going neutrino events, even though a down-going muon can be occasionally incorrectly reconstructed as up-going. A

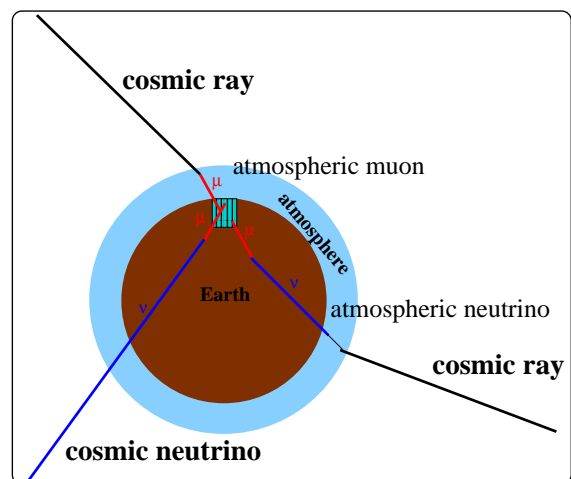


Figure 3.7: Physics signals in ANTARES.

¹Acronym for Antares Modules for Acoustic DEtection Under the Sea.

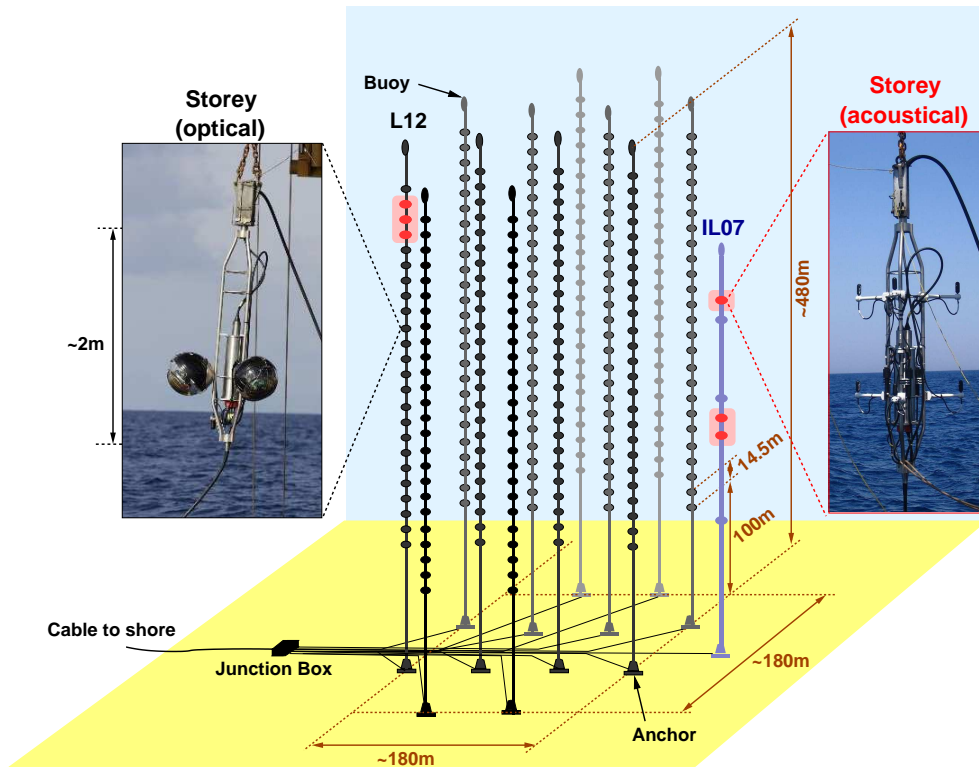


Figure 3.5: Layout of the ANTARES detector. The 12 detection lines (black) and the instrumentation line (blue) are shown. The positions of the storeys are indicated by full circles. Optical storeys are drawn in black, acoustical storeys in red. The insets show pictures of the optical and acoustical storeys taken during the deployment operation. Line anchors, buoys, interconnection cables and the junction box are also indicated, as is the dimension of the detector. This figure has been adapted from [73].

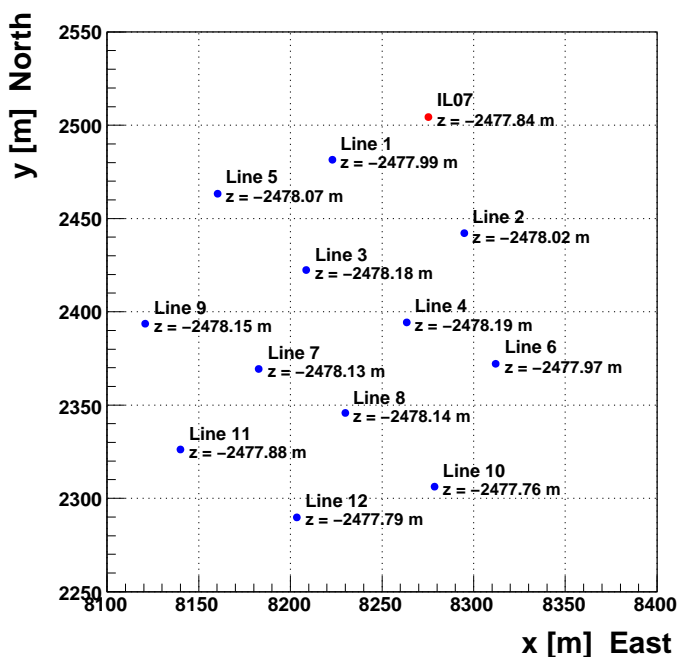


Figure 3.6: Triangulated anchor positions (see Section 3.5.3) of the ANTARES detection strings Line 1 – 12 (marked by blue points) and the instrumentation line IL07 (indicated in red) on the sea floor end of 2009. The horizontal axis (x) points towards East, the vertical axis (y) towards North. Distances are given in metres. The lines are arranged in an octagonal structure. The depth (z -coordinate) of each anchor is also stated, confirming that the sea floor at the installation site is almost flat.

much harder task is to differentiate between cosmic and atmospheric neutrinos. To some extent the atmospheric neutrinos represent an irreducible background. Methods for identifying cosmic neutrinos therefore rely on statistical methods such as the search for event clusters from a certain celestial direction on top of the atmospheric neutrino background. For certain source candidates (e.g. GRBs) independent observations of transient photon signals help to restrict the search window (i.e. time and celestial direction) for neutrino events, reducing the atmospheric neutrino background to a negligible minimum. At very high energies the cosmic neutrino flux is predicted to dominate the flux of atmospheric neutrinos, therefore the detection of ultra-high-energy events represents a third method. While being a marring background for the cosmic neutrino search, atmospheric neutrinos and muons are, on the other hand, a valuable tool for calibration and reconstruction fine-tuning. For instance, in Chapter 7 and Chapter 8, a method will be presented to calibrate the detector pointing by observing the depletion of the atmospheric muon flux from the direction of the Moon. The atmospheric neutrino data can be used to optimise the track reconstruction for neutrino events. Recent analyses also indicate that neutrino oscillations are visible with ANTARES. Exploiting the energy dependence of this effect, the atmospheric neutrino data could provide valuable information to understand the response of the detector for different neutrino energies in the low-to-intermediate energy regime.

Further background light is produced by the decay of radioactive potassium (^{40}K) and by bioluminescence. The background light from radioactive decays is constant in time. The electron, produced in the main channel of the potassium-40 decay, emits about 43 Cherenkov-photons [74] on average. Simulations [75] predict a background rate contribution of 30 kHz for the ANTARES PMTs. The measured ^{40}K coincidence rate between two neighbouring PMTs is on the order of 10 Hz. The rate of bioluminescence light produced by micro-organisms varies in time, depending on environmental conditions like deep-sea current and weather conditions on the sea surface. The observed overall mean rates are between 40 kHz and 200 kHz with a long-term average of about 60 – 70 kHz. Fortunately, these processes mainly lead to single, uncorrelated photon signals in individual PMTs and can therefore be efficiently filtered out. More disturbing, aperiodic, localised optical bursts which lead to counting rates of more than a few MHz can be produced by larger, multicellular organisms like fluorescent squids, crustaceans or fish. During phases of high optical activity the detector has to be switched off preventively to avoid degradation of the PMT sensitivity due to ageing effects.

The data quality, in terms of contamination with background hits, can be assessed by the mean baseline (defined to be the mean of a Gaussian, fitted to the counting rate distribution obtained from a time interval of 5 min) and the fraction of bursts (being defined as the fraction of time in a 5 minute interval in which the counting rate is 20% or more above the baseline). This separation permits to describe the long term, slowly varying part as well as the localised, burst-like part of the counting rates [76]. The median background rate during four years of detector operation is shown in Figure 3.8. Extreme optical activity has been observed in spring 2006 and spring 2009, when temporary counting rates of several

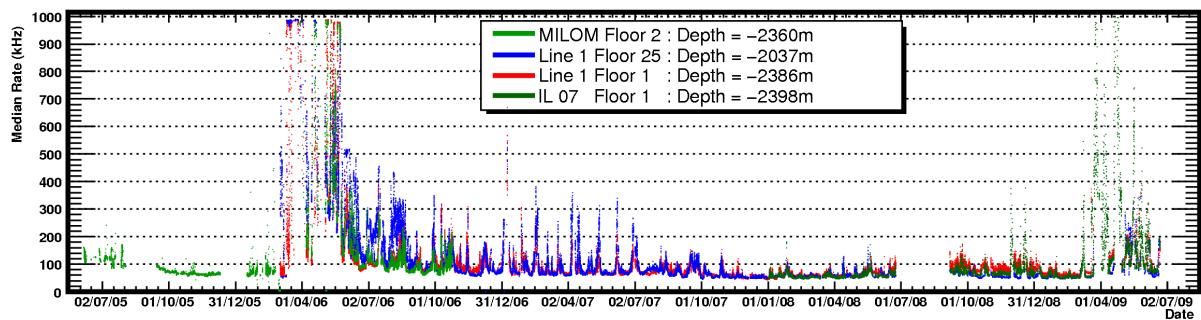


Figure 3.8: Median single PMT background rates at different depth levels, monitored over four years of operation. Temporary counting rates of several 100 kHz were observed in spring 2006 and 2009.

100 kHz were measured. These periods are followed by tranquil phases with counting rates as low as 50 kHz.

3.4 Data acquisition

The readout of the PMT signals and the communication with the off-shore units of the ANTARES detector are performed by the ANTARES data acquisition (DAQ) system [77]. The different on- and off-shore DAQ software processes are synchronised in a distributed network based on the TCP/IP protocol by a finite state machine implemented in the CHSM language [78]. By the use of the TCP/IP protocol each of the DAQ processes can be addressed via its unique IP. The transfer of data and control messages, organised by the Ligier software package [79] based on ControlHost [80], is thus fully transparent. The RunControl [81] program serves as the interface between the instrument and the operator and permits managing state transitions and the distribution of configuration and initialisation data.

3.4.1 The off-shore DAQ system

Off-shore, the analogue PMT signals are read out in the LCMs by a custom designed electronic front-end chip, the analogue ring sampler, ARS for short (see also Chapter 4). The ARS enables physics data to be recorded in two different modes. In the single photoelectron (SPE) mode every PMT pulse that exceeds a predefined threshold (typically 0.3 pe) is integrated over a predefined time window (typically 25 ns) and the resulting charge is digitised. At the moment of the threshold crossing the ARS assigns a timestamp to the PMT signal. Timing information is provided by the local clock-system in the LCM which is synchronised with a 20 MHz master clock on shore. In order to improve the timing resolution to about 0.2 ns accuracy, the ARS uses a time-to-voltage converter (TVC) to

interpolate between two clock signals. The combined digital information of the charge and the time of a PMT pulse is referred to as a hit. After the integration of the pulse, the ARS has a dead time of about 200 ns. Every PMT is connected to two ARS chips arranged in a token-ring scheme in order to minimise dead-time losses during data taking. Alternatively to the SPE mode, the PMT pulse can be sampled in the waveform mode. In this mode the pulse shape of a signal can be recorded.

The ARS data are collected in an adjustable time window (of typically 104.858 ms) by a field programmable gate array (FPGA) and buffered as a so-called data frame into a 64 MB memory. Inside the LCM two DAQ processes are running on a central processing unit (CPU). The DAQHarness manages the ARS data and the SCHarness controls compass and tiltmeter devices. The DAQ system is designed for a maximum data throughput corresponding to a hit rate of 300 kHz per PMT. The bi-directional 100 MB/s data stream of the LCMs is linked in the MLCM into a 1 GB/s ethernet connection to shore using two uni-directional optical fibres for incoming and outgoing data. In the SCM the data stream from the MLCMs of the string are combined into a single pair of optical fibres and transferred to the junction box from where the data are sent further to shore via the main electro-optical cable (MEOC), a standard deep-sea telecommunication cable.

Every PMT signal (so-called L0 hit) that exceeds a predefined threshold (typically 0.3 photoelectrons) is transferred to shore. This is commonly referred to as the “all data to shore” concept. Whilst the bandwidth is sufficient to transmit every PMT signal to shore, it is not attempted to archive the complete data. On-shore the ARS data frames from a given time slice are buffered, thus allowing for delays in the network, and collected into a so-called data time slice. Once all frames have been collected or a time-out has been reached, the time-slice data are passed to the filter algorithms discussed in the next section. After filtering, the selected data are written to disk by the DataWriter program.

3.4.2 Filter algorithms

The data stream of about 9 Gb/s transmitted to shore has to be reduced before being archived. For that purpose a software algorithm [82] running in a PC farm at the shore station analyses the incoming data in real time and selects relevant physics candidate signals. To handle the huge data rate transferred to shore in real time, the filter algorithm has to be optimised in terms of speed and while reducing the amount of data by a factor of at least 10^4 , a good efficiency for reconstructible muon tracks has to be kept.

The first step in the filter process scans for hits related in time and position. Since the algorithm mimics the features of common hardware triggers implemented in high-energy physics detectors, it is often referred to as trigger algorithm. Background caused by bioluminescence or ^{40}K decay mostly leads to single, uncorrelated hits. Therefore, coincident hits that arrive within a common short time window (of typically 20 ns) at adjacent PMTs or hits with large amplitudes are good indicators of muon tracks or showers. A minimal

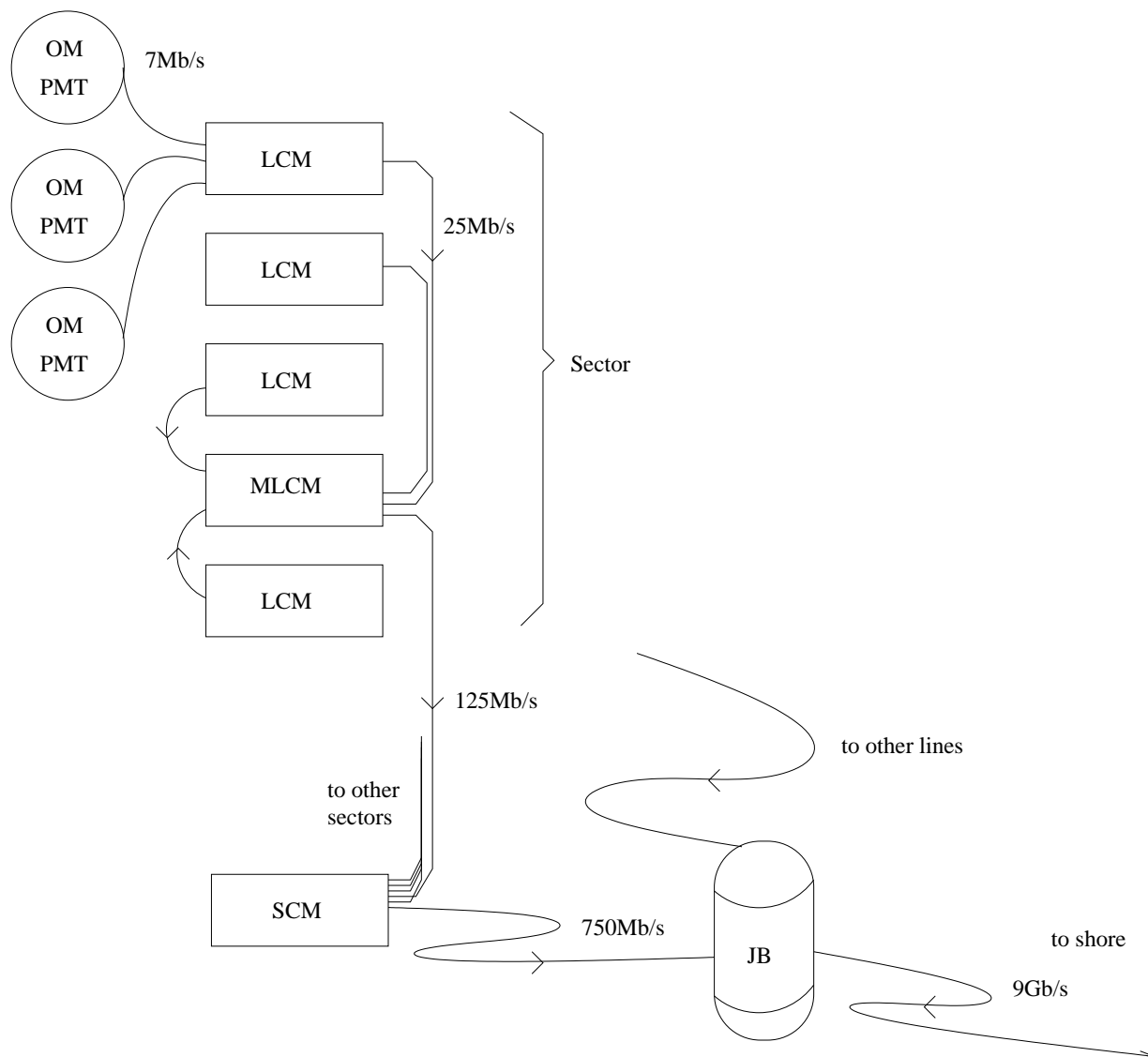


Figure 3.9: Data flow in the ANTARES detector. The PMTs, that are housed in the optical modules (OMs), are read out by the front-end electronics installed in the local control modules (LCMs). The LCM data are combined in the master local control module (MLCM) and sent to the string control module (SCM) from where they are routed to the junction box (JB) and finally to the shore station. The transferred data rate in the main electro-optical cable to shore amounts to 9 Gb/s.

number of such coincident or large-amplitude hits, summarily named L1 hits, is required for a trigger. This requirement allows one to reduce the data rate by a factor of about 10^4 . The selected L1 hits form the basis for several more elaborate algorithms that are used to reduce the data rate further.

One of these higher-level filters is the clustering algorithm. Since L1 hits can be occasionally produced by background processes, this algorithm checks if the L1 hits selected in the first step are causally connected. Assuming that the L1 hits are due to Cherenkov photons propagating with a group velocity $v_g = c/n_g$, with a refraction index n_g , the arrival time difference Δt and distance d between two PMT hits have to fulfill

$$|\Delta t| \leq \frac{n_g}{c} d. \quad (3.1)$$

The causality criterion Equation 3.1 is then used to group the L1 hits in clusters of causally connected hits. At least one such cluster with a minimal number of L1 hits (typically 5) is required. As Equation 3.1 does not take the special geometry of muon tracks into account, the causality relation is constrained further a final step, which verifies that the selected clusters are compatible with a muon track. A predefined number of track directions is generated uniformly in the solid angle and the preselected hits have to fulfill a stricter causality criterion with respect to a certain direction. For single-PMT background rates of 100 kHz the clustering algorithm allows for suppressing the background event rate to about 0.1 Hz [83].

Another important trigger simply scans for simultaneous L1 hits in adjacent storeys of the same string [84, 85]. The so-called T2 trigger requires a set of two L1 hits on adjacent storeys, a weaker version, the T3 trigger requires the two L1 hits to be on adjacent or next-adjacent storey. A certain number of these T hits is usually required for a full trigger. The 2T3 trigger for instance requires two T3 hit combinations in every event. This method, based on locally coincident L1s, permits increasing the sensitivity in the low-energy region and is important for some analyses; however, not all of the triggered events are easily reconstructible with good quality. The hit selection for the online reconstruction [86] is also based on the T hits.

If the recording of an event candidate is triggered, not only the L1 hits are saved for analyses but also all of the initial L0 hits in a certain time window. This time window is defined by the first and the last L1 hit as explained in Figure 3.10. Typical trigger rates are about 3 Hz for the clustering algorithm and about 10 Hz for the 2T3 trigger for data periods with moderate background rates (70 kHz for each PMT). In order to improve the sensitivity for certain source candidates and analyses, specialised triggers have been developed. These include a trigger with an improved sensitivity for tracks from the direction of the galactic centre as well as special calibration triggers used for the time calibration of the detector.

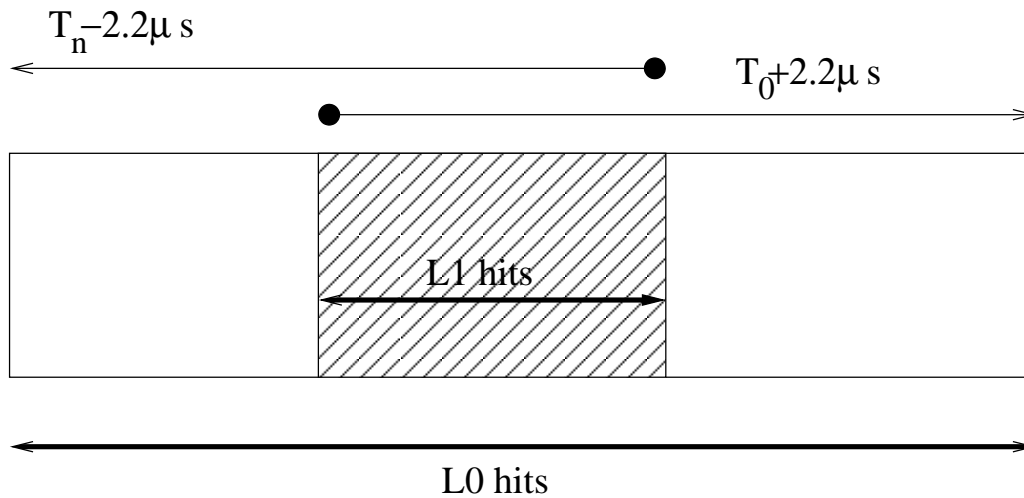


Figure 3.10: *The physics event is built from the L1 hits that caused the physics trigger and the snapshot hits in a time window of $\pm 2.2 \mu s$ with respect to the last, respectively the first, L1 hit. The $2.2 \mu s$ corresponds to the maximal time a relativistic muon needs to traverse the detector.*

3.5 Calibration

The ANTARES detector is equipped with several calibration systems [87] in order to reach a high angular resolution, which is intimately related to a precise resolution of the relative arrival times of Cherenkov photons at the PMTs. The time resolution is intrinsically limited by the transit time spread of the signal in the PMTs ($\sigma \approx 1.3$ ns) and the optical properties of the sea water [88] such as light scattering and chromatic dispersion ($\sigma \approx 1.5$ ns at a distance of 40 metres). The ANTARES readout electronics and calibration instruments are designed to contribute less than 0.5 ns to the overall timing resolution. In addition, a measurement of the relative positions of the OMs, with an accuracy of 10 – 20 cm is required. Another important calibration is that of the charge, which is discussed in Chapter 4 in detail and is therefore omitted here.

3.5.1 Time calibration

The time calibration of the optical sensors in the ANTARES telescope is performed using several systems which provide complementary information on the propagation of the signals in the detector. A precise time reference clock system has been implemented in the ANTARES detector. This system consists of an on-shore 20 MHz clock generator connected to the clock signal transceiver boards integrated in each storey. This setup allows one to measure time offsets using an echo-based time calibration whereby each storey sends back a return signal through the same optical path as the outgoing clock signal. In-situ measurements yield an excellent resolution of ≈ 0.1 ns. The internal clock system facilitates an absolute event time measurement with a precision of about 100 ns by assigning a GPS

time stamp to the data. This absolute precision is more than sufficient to attribute possible (transient) astrophysical sources to the recorded neutrino events.

An internal LED is mounted in each optical module on the back of the PMT. The LED light intensity peaks at 470 nm with a FWHM of 15 nm. The LEDs are used to measure the relative variation of the PMT transit time.

The relative time calibration including the optical properties of the sea water at the ANTARES site is accomplished using inter-storey illumination by LED and laser devices, so-called beacons [89]. Four LED beacons are distributed along every string. The beacon LEDs have been synchronised in the laboratory to better than 0.1 ns. The light pulse emitted by the LED beacons has a rise time of about 2.8 ns. The laser beacon located at the bottom of selected lines uses a diode-pumped Q-switched Nd-YAG laser to produce pulses of $\approx 1 \mu\text{J}$ with a FWHM of ≈ 0.8 ns at a central wavelength of 532 nm. The laser beam is widened by a diffuser which spreads the light out according to a cosine angular distribution. This permits the beacon to illuminate adjacent lines for time calibration purposes.

3.5.2 Alignment of the detector

Being exposed to the sea current, the ANTARES strings undergo movements depending on the sea current velocity. Even relatively small water currents of about 5 cm/s can result in displacements of the top storeys of a few metres. Therefore an essential element of the calibration of the detector is a real-time measurement of the optical sensor positions. To achieve this task, the strings are equipped with acoustic receivers (hydrophones) which measure high-frequency acoustic signals (40 – 60 kHz) emitted by transceivers located at the line anchors. The precision of the positioning is improved by the use of autonomous emitters (termed pyramids) located at a distance of about 150 metres from the detector. The propagation time of the acoustic signals can be translated into distances, provided the sound velocity is known. The determination of the positions is done by acoustic triangulation every two minutes. Triggered by the ANTARES clock system, the acoustic emitters alternately send signals to other modules in listening mode. Complementary information on the orientation of the storeys is provided by a set of tiltmeters and compasses located in the LCMs of the storeys.

The full alignment of the detector is finally obtained based on a line-shape model that includes the information from the acoustic system, the compasses and tiltmeter measurements as well as the known line geometry. The line shape is determined by the drag force due to the sea current and the known buoyancies and weights of the detector elements. The single free parameter in this fit is the sea current velocity which is obtained as a by-product of the calibration. Comparisons of the sea current velocity with independent measurements show good agreement. The accuracy with which relative optical sensor positions are constrained by the calibration has been found to be better than 10 cm [90].

3.5.3 Absolute positioning

The determination of the precise geodetic position and the absolute orientation of the ANTARES detector is accomplished by acoustic triangulation of the line anchor positions with an acoustic sensor on a ship equipped with a differential GPS system. The measurement can be repeated from different ship positions which allows constraining the error of the absolute positioning. Accuracies of 1 m on the anchored line elements are reached by this method. An even more precise calibration can be achieved by combining the results of the anchor triangulation with the acoustic relative positioning. This requires the knowledge of the line anchor geometries which are, for this purpose, individually measured in the laboratory prior to deployment as well as the orientation of the anchors on the sea bed, measured by the submarine during the connection operation. Systematic studies show that the combination of these measurements translate into an absolute pointing accuracy of better than 0.2° [91].

3.6 Simulation

Detailed Monte Carlo simulations are used to investigate the response of the ANTARES detector to various relevant physics processes. Simulations help to develop reconstruction algorithms and are also used as a tool for the data analysis. The simulations generally consist of several steps. First, the underlying physics of the interaction processes of primary particles (high-energy neutrinos, or cosmic rays) is used to simulate the generation of secondary charged particles. The resulting particles are propagated through the medium (atmosphere, rock, sea water) to the detector. In the final step the emission, propagation and detection of Cherenkov light is simulated. As a result of the simulation the detector response to the input signal is obtained as sets of hits with well determined amplitudes, positions and arrival times. Depending on the nature of the primary particle different programs are used for the first step in the simulation chain.

3.6.1 Atmospheric muons

Since ANTARES is installed in the deep sea, cosmic rays cannot reach the detector directly. However, muons generated in cosmic-ray-induced air showers can be observed. Two approaches are adopted to simulate the detector response to cosmic-ray induced muons [92]. The full simulation chain is based on the CORSIKA program [93, 94] that describes the evolution of cosmic-ray-induced air showers in the atmosphere. The muons from these showers reaching the sea-surface are then propagated to the detector by the MUSIC [95] program. In this way, it is possible to evaluate the response of the detector to a given cosmic-ray flux. Alternatively, the muons can be generated according to a parameterisation of the under-water muon flux derived from a full simulation; this is done with the MUPAGE program [96, 97, 98]. In contrast to the full simulation, this ansatz does not require repeating the detailed tracking of the muons to the detector for every event. Therefore this approach is much faster than the full simulation. On the downside, it does not

offer the possibility of adjusting the input cosmic-ray flux and provides less handles on the simulation characteristics.

3.6.2 Neutrinos

Interactions of neutrinos in the energy range of $10 - 10^8$ GeV in a large volume around the detector are simulated with the GENHEN package [99, 100, 101]. The size of the volume is determined by the maximal muon range associated with the given energy interval. The simulation includes deep-inelastic scattering simulated using the LEPTO [102] package and resonant and quasi-elastic interactions using RSQ [103]. The CTEQ parton distribution functions are used as default [104]. The hadronisation is done using PYTHIA/JETSET [105]. The neutrino events are typically only generated in the hemisphere below the detector. If the interaction takes place within the vicinity of the detector, all secondary particles are used in the Cherenkov light simulation. Otherwise (for charged-current reactions of the muon neutrino) only the high-energy muon is propagated to the detector and passed to the Cherenkov light simulation.

3.6.3 Cherenkov light

The KM3 package [106] is used to simulate the response of the ANTARES detector to through-going muons. In view of their large number, it is not feasible to track the emitted Cherenkov photons individually. Therefore, an alternative approach is adopted, which relies on a parameterisation of the distributions of the intensities and arrival times of the light emitted by a muon track or an electromagnetic shower at different distances and orientations to the PMTs. KM3 uses MUSIC for the propagation of the muons through the detector. The propagation and light emission of other particles than muons is simulated by the GEASIM software [107] based on the GEANT3 package [108]. This software provides a full tracking of the generated particles and their secondaries including all relevant physics processes. The treatment of the Cherenkov light is similar to KM3, except that the light scattering in the sea water is not included in the simulation. The simulation depends heavily on the optical properties of the sea water at the ANTARES site as well as the response of the optical modules. The dependence of the absorption length on the wavelength is taken from a fit to in-situ measurements [109]. Elaborate models are used to describe the light scattering [110]. A very important factor in the simulation of the optical modules is the angular detection efficiency of the photomultipliers which can be measured in the laboratory [111].

The final result of a simulated physics event which fully describes the detector response is a set of registered hits with given positions, amplitudes and arrival times. This set does not only include hits due to signal photons but also incorporates photons due to random background processes. Realistic background rates are incorporated from real data runs via a dedicated program [112].

3.7 Status and history of the experiment

The history and the milestones of the construction of the ANTARES telescope from the first site evaluations to the installation of the instrument are summarised in the following overview.

- 1996 – 1999: During this period several site evaluation campaigns were conducted. The site properties have been evaluated in terms of refraction index, scattering and absorption length, and background rates.
- November 1999 – June 2000: The demonstrator line, a 350 m long string equipped with 7 photodetectors was immersed to a depth of 1200 m allowing for a test of the acoustic positioning system and the measurement of first atmospheric muon data. With this operation the feasibility of the deployment of a large structure was proven.
- March 2001: The sea site was studied with the submarine “Cyana” in order to map out possible large-scale obstacles on the sea bed. Within the deployment zone only one large object was found. Thus, taking a deployment accuracy of ≈ 5 m for granted, any problems for future installation operations due to uneven spots on the sea floor could be safely ruled out.
- October 2001: The main-electro-optical cable (MEOC) was laid out from the shore station to the sea site.
- December 2002: The junction box and the prototype sector line (PSL) were deployed. The PSL represented a miniature version of a full ANTARES line with only one basic detection unit (sector) holding 15 PMTs, one LED beacon, a sound velocimeter, a pressure sensor, hydrophones and an acoustic transceiver. This setup allowed to test all features of the complete design.
- February 2003: The MIL (mini instrumentation line) containing time calibration (laser and LED beacons), positioning (hydrophones and acoustic transceiver) and monitoring (seismometer, sound velocimeter, pressure sensor, conductivity-temperature-density probe) devices was deployed.
- March 2003: In a sea operation using the manned submarine “Nautile”, the PSL and the MIL were successfully connected to the junction box. However, in the course of data taking some problems were revealed. Due to a damage of the optical fibre distributing the clock signal a nano-second time resolution could not be reached. Furthermore, a water leak in an electronics container of the MIL was discovered. These problems were thoroughly studied and the deficiencies were remedied by appropriate design modifications.
- May 2003: The MIL was successfully retrieved from the deep sea about two months after the connection.

- July 2003: The PSL was recovered and analysed.
- March 2005: In order to validate the final design a further test was performed. A mechanical test line (Line 0) with the mechanical elements of the full string but without electronics and an improved MIL, the MILOM, were built and immersed.
- May 2005: The mechanical test line was recovered. Investigations of the containers did not show any water leaks.
- February 2006: The first complete ANTARES string (Line 1) was deployed.
- March 2nd, 2006: After the connection, the first string proved fully functional right from the power-up and down-going muon data were taken immediately.
- July 2006: The second full line was deployed.
- September 2006: The second line was put into operation.
- January 2007: The lines 3,4,5 were connected. With the commissioning of the new strings ANTARES became not only a full-fledged telescope but also already the most sensitive instrument on the Northern hemisphere.
- December 2007: With the connection of the lines 6–10 the ANTARES telescope was doubled in size enhancing the sensitivity of the instrument significantly.
- May 28th, 2008: With the connection of the lines 11 and 12 the construction phase of ANTARES was successfully finished.

Since the commissioning of the first string the ANTARES detector has continuously taken data in a growing configuration. The active time of the instrument is shown in Figure 3.11. On June 24th, 2008 a fault occurred in the cable powering the junction box from the shore station and interrupted the power supply of the detector. In a sea operation on September 6th, 2008 the cable was repaired and data taking was resumed without problems after the operation.

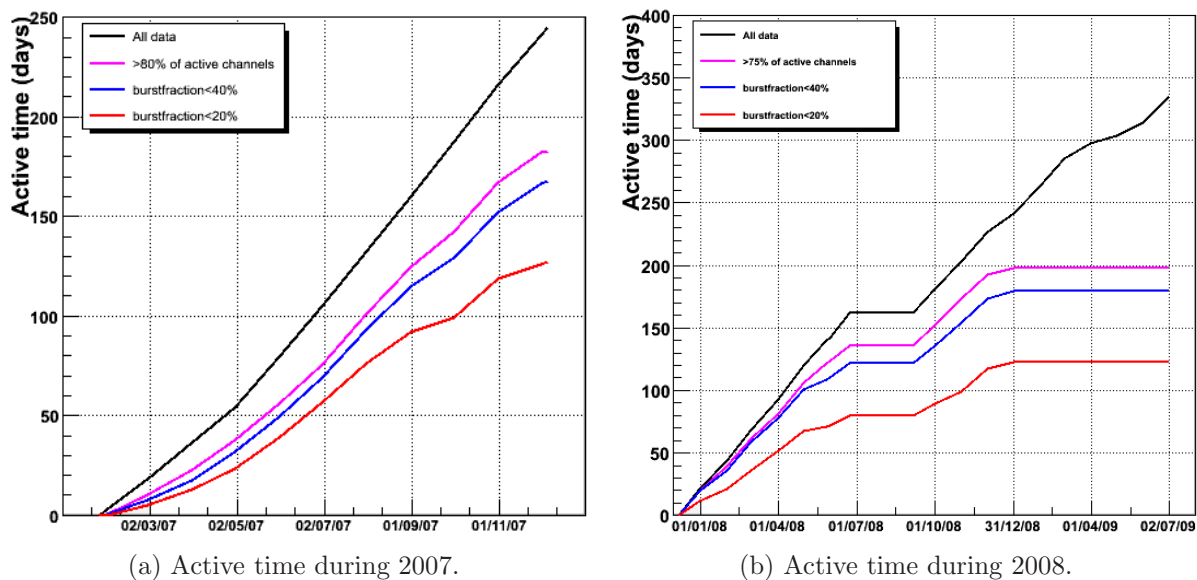


Figure 3.11: Active time of the instrument during the years 2007 (mainly 5 lines) and 2008 (10 and 12 lines). The effect of data quality cuts is indicated.

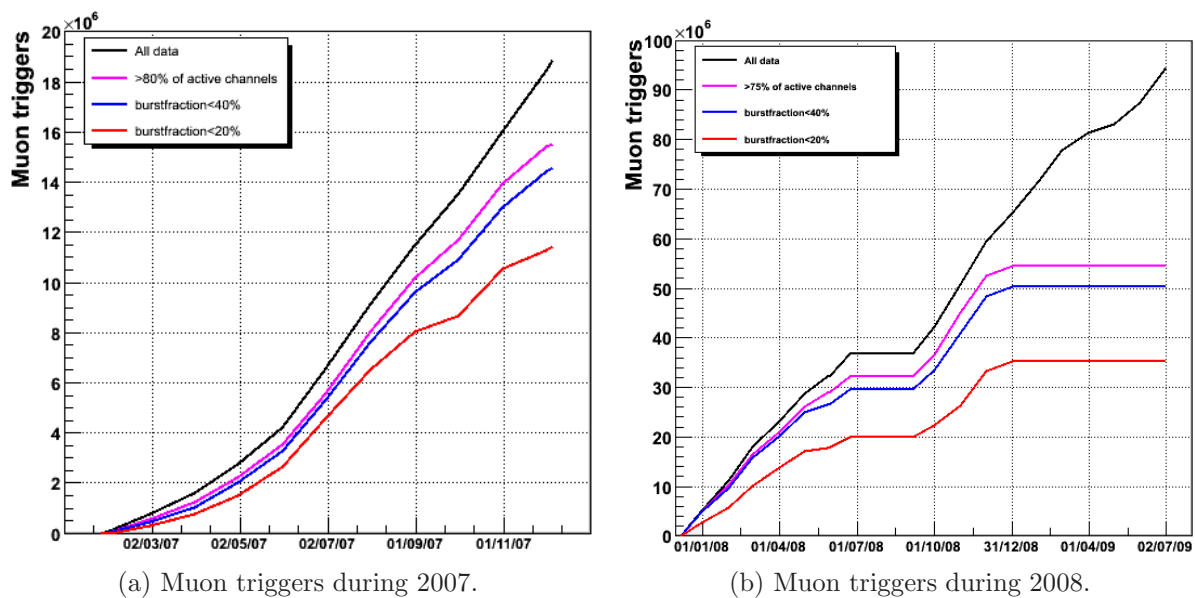


Figure 3.12: Number of muon triggers for the years 2007 (5 lines) and 2008 (10 and 12 lines). The effect of data quality cuts is indicated.

Part II

Front-end electronics calibration

In this part the charge calibration of the custom-designed analogue ring sampler (ARS) front-end chip which performs the readout of the photomultipliers is presented. The calibration procedure as well as calibration results including a long-term survey of the PMT gain are discussed.

Chapter 4

Charge calibration of the front-end electronics

In ANTARES, the Cherenkov light is detected by photomultiplier tubes (PMTs). The Cherenkov photons hit the photocathode of the PMT and release electrons which are then amplified. The integrated PMT output pulse has an intrinsic spread of about 30% – 40% and the average total charge increases linearly with the number of photoelectrons. The front-end electronics records the analogue PMT signal and converts the integrated charge into a digital signal. The charge calibration is required to determine the number of photoelectrons from this digital information. For this purpose a robust, automatised calibration scheme has been developed which is presented in this chapter. Imperfections of the electronics (differential-non-linearities of analogue-to-digital converters, channel crosstalk) are corrected for or mitigated in their impact. Prior to the deployment, calibration parameters for the detector lines are obtained in dedicated dark-room measurements. However, since calibration parameters are expected to change with time, in-situ calibrations have to be performed regularly and the time evolution has to be studied carefully. Tools have been devised to monitor the time evolution of the calibration constants. A long-term study of the PMT gain has also been performed and is discussed in this chapter.

4.1 Front-end electronics

As explained in Chapter 3 the PMT readout is performed in the local control module (LCM) of the storeys where the DAQ boards are mounted in a titanium cylinder. Here the signal is processed, digitised and finally sent to shore. A schematic of the front-end electronics responsible for the readout is given in Figure 4.1. Each PMT is connected to two fully custom-designed chips (ARS, cf. the following section). In total there are 6 ARS chips integrated in the LCM for the readout of the three PMTs of the storey. The ARS chips in the LCM of one storey are conventionally numbered from 0 to 5. This number, together with the unique LCM index, allows for identifying individual chips unambiguously. The ARSes communicate with a field programmable gate array (FPGA) in the LCM which buffers and converts the data stream into a dedicated data format. From there, the signals are retrieved and sent to shore by the central processing unit of the LCM.

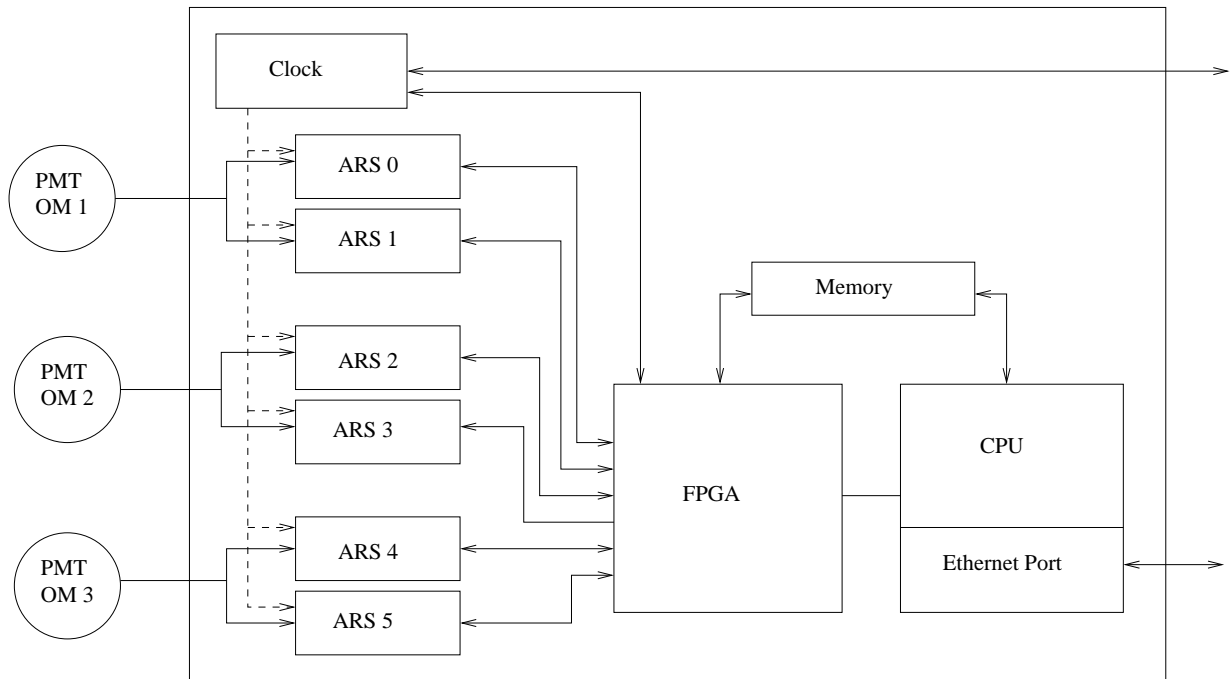


Figure 4.1: Schematic of the PMT readout in the off-shore DAQ electronics. Each of the three PMTs of one storey, labelled from 1 to 3, is connected to two ARS chips. A common clock signal synchronises the individual chips. The data are collected in the FPGA and finally sent to shore by the integrated central processing unit (CPU).

4.2 The analogue ring sampler

The custom-designed analogue ring sampler chip [113] has been developed for the ANTARES experiment to perform the complex front-end operation needed for the readout of the PMT signals. The ARS allows for digitising the analogue PMT signals off-shore in the LCM. The chip has been devised to handle high counting rates and to ensure fast processing of the data. By default, the ARS chip processes the PMT anode signal. Optionally, the PMT signal can be read out from the last dynode allowing for an increase in the dynamic range. In order to reduce the dead time during the processing of the signals, each PMT is connected to two ARS chips which are arranged in a “token ring”. The ARS enables the recording of the PMT signals in two different operation modes. In the waveform mode the PMT anode signal is sampled with a tunable frequency of up to 2 GHz. In the standard single photoelectron (SPE) data taking mode, every PMT pulse which exceeds a configurable threshold is integrated. At the time of threshold crossing a timestamp is assigned to the pulse. The high-precision timing information is provided by two TVCs which are alternately used to interpolate between two pulses of the external clock signal. A circuit diagram of the ARS is shown in Figure 4.2.

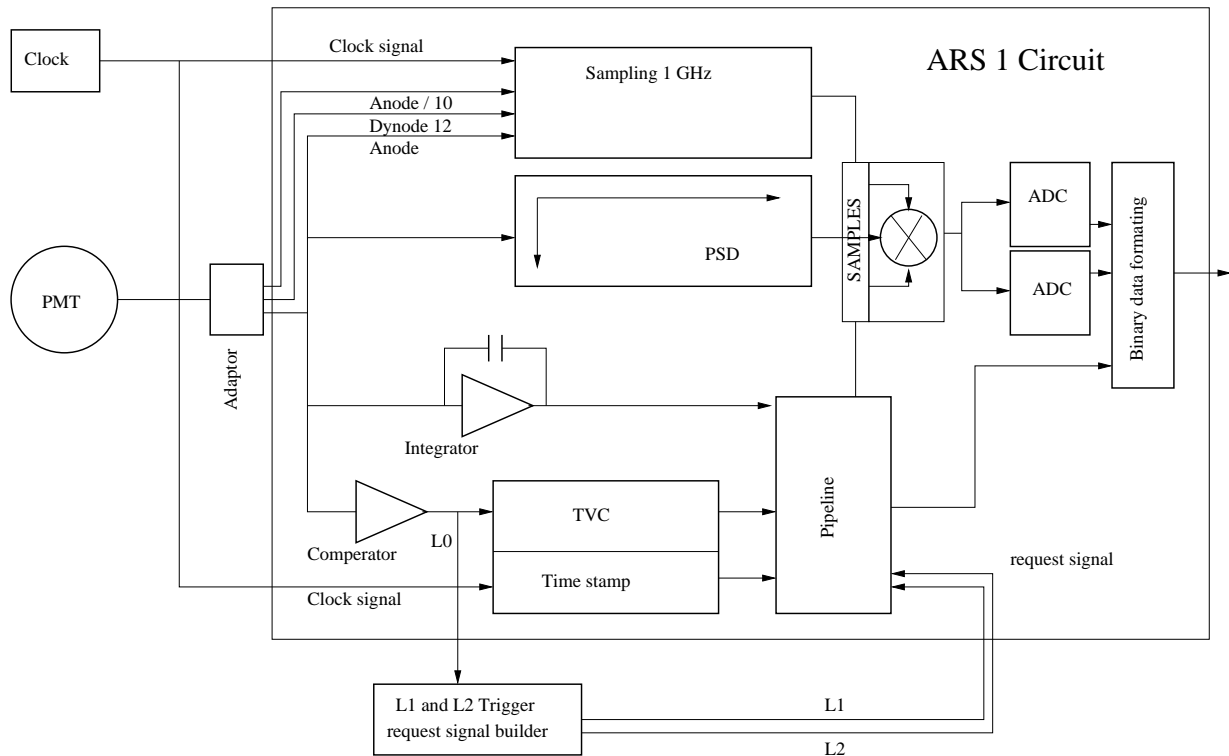


Figure 4.2: Architecture of the ANTARES ARS chip [114].

4.3 Charge calibration

Introduction

As described in the previous section, the default ARS operation mode for physics data taking is the SPE mode, in which the pulse of the photomultiplier is integrated for typically 30 ns if a given threshold is passed (typically one third of the 1pe value) and the total charge is digitised by means of an analogue-to-digital converter (ADC) to an integral representation (8bit AVC channel) which is then transmitted to shore. The aim of the charge calibration is to convert the integrated charge of the PMT signal Q in its integral representation, as recorded by the DAQ system, into the number of initial photoelectrons n that caused the PMT pulse. The final result (n) is given as a real number and can be interpreted as the average count of photoelectrons that corresponds to a given integrated charge. Due to the inherent dispersion of the ARS chips it is not possible to apply the same global calibration to every module, rather it is mandatory to calibrate each of the ARS chips individually. As the charge calibration parameters are expected to vary with time, for instance due to PMT ageing, it is important to develop a robust in-situ charge calibration procedure and to monitor the calibration values with a period of a few weeks. The algorithms needed to realise this task have been implemented in the calibration framework,

(CALIBFW, [115]) maintained in the `tools/Analysis/CalibFW` directory of the ANTARES DAQ software repository. This framework provides the mechanisms to process ANTARES data and contains several useful algorithms and functions for calibration purposes.

Application

Once an accurate calibration set has been obtained, the knowledge of the exact number of photoelectrons allows one to reconstruct the energy of the recorded events and can be used to improve the reconstruction quality of tracks and showers when used as an independent information in the fitting procedures which complements the measured time residuals. The information obtained by the charge calibration can help to distinguish signal hits from random background hits. Most of the hits due to background processes are caused by single photons whereas hits with a large amplitude are most likely signal hits. Furthermore, a precise charge calibration is important for the timing of the PMT hits, since the time measurement is affected by the shape (amplitude) of the pulse due to the time walk effect. Finally, important parameters like the charge (L0) and the pulse shape discriminator thresholds as well as the PMT gains can be monitored and adjusted with the help of the charge calibration.

Calibration procedure

Technically, the relation between the digitised total charge Q of the integrated PMT pulse and the (mean) number of photoelectrons n is described by the transfer function $n = f(Q)$. Thus the determination of the transfer function allows inferring the number of photoelectrons from the digitised charge. In a wide range the system (integrator and ADC) behaves linear as could be verified with test-bench measurements [116], although small deviations from the linearity caused by saturation effects and local non-linearities (see section on DNL below) are present. Assuming a linear response of the system, the transfer function is linear as well and hence two parameters are sufficient to specify the calibration prescription completely over the full dynamic range. The two most convenient reference points are the charge pedestal, the offset AVC value corresponding to the null point (0 pe) of the ADC, the AVC_{0PE} , and the photoelectron peak (1 pe), corresponding to single photon hits. Due to the intrinsic spread of the PMT gain the photoelectron peak is not a narrow spike but rather an extended distribution which is well described by a Gaussian function with mean AVC_{1PE} . Based on these two reference points the transfer function can be expressed by the following relation:

$$n = f(AVC) = \frac{AVC - AVC_{0PE}}{AVC_{1PE} - AVC_{0PE}}. \quad (4.1)$$

A modified version of this equation will be presented in Section 4.3.2 where a small correction is applied to the input AVC channel. By measuring the positions of the pedestal and the photoelectron peak the transfer function can be determined. These procedures are explained in the next section.

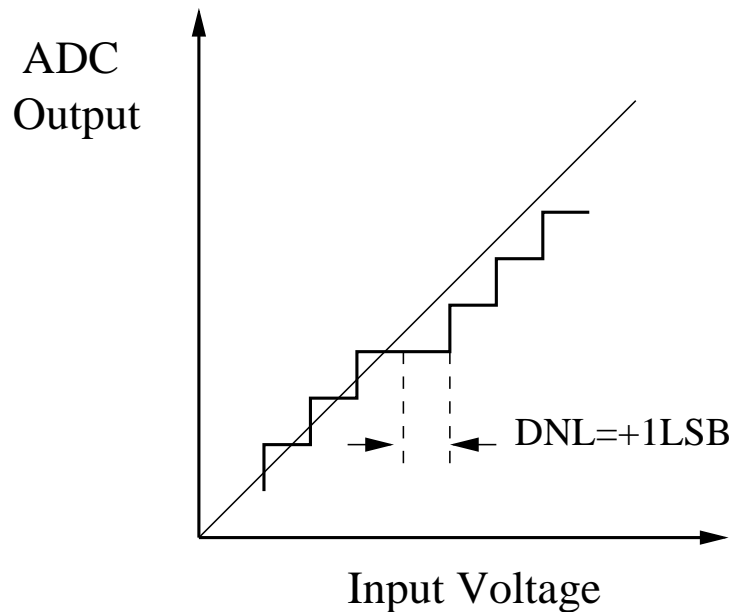


Figure 4.3: *Illustration of the differential non-linearity.*

4.3.1 Pedestal and photoelectron peak fit

The charge pedestal is extracted from special runs with a dedicated setup where the PMT current is read out at random times. This allows for the determination of the offset channel of the ADC which is the null point of the measurement corresponding to 0 pe. The photoelectron peak is studied with minimum-bias events taken during regular physics runs. The analysis is restricted to background events which mostly contain PMT hits due to ^{40}K -decay and bioluminescence, since these processes produce mainly single-photons at the photocathode level. Alternatively, the photoelectron peak data can be obtained from the timeslice data, recorded by the GRB trigger system, which also represent an unbiased data snapshot. The charge spectra are histogrammed and fitted individually for each ARS chip.

Influence of differential non-linearities

The conversion from the analogue value to the integral digital number performed by the ADC is not perfect. In the conversion process the analogue input signal is compared to a reference signal by a comparator. A certain time is needed to set up a stable and well defined reference signal. Occasionally the comparison is done when the reference signal has not yet fully reached its gauge level and thus assignments to wrong ADC channels are made. This effect leads to inhomogeneous ADC bin sizes, so-called differential non-linearities (DNL), cf. Figure 4.3. The deviations from the nominal bin width for a given bin can be quantified by comparing the size of this particular bin to the average bin width. Analysis of the ARS chips designed for ANTARES has revealed DNLs as high as 5, which

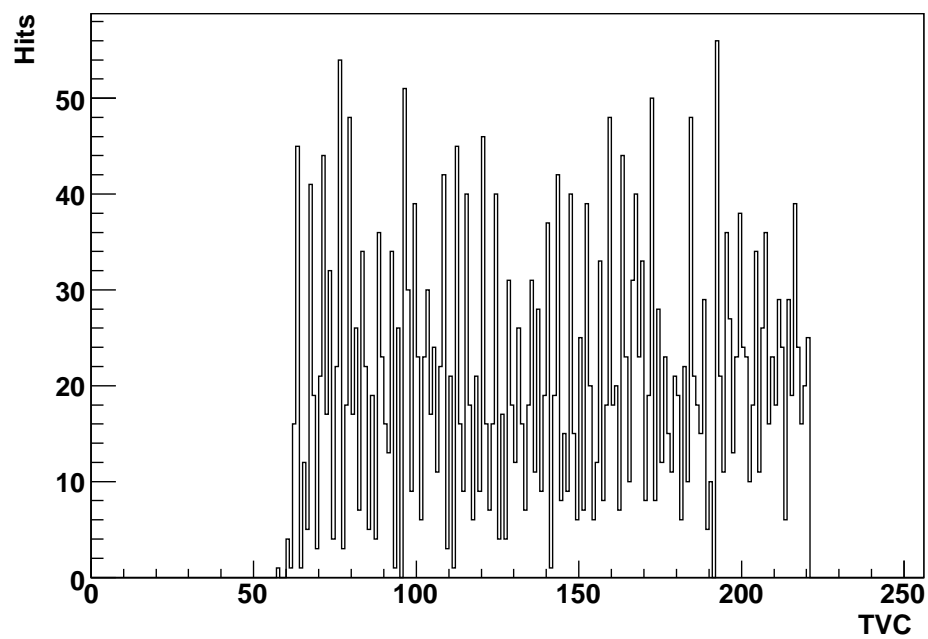


Figure 4.4: *Illustration of the DNL effect. This figure shows a TVC spectrum which is per-se uniform. Due to the inhomogeneous bin size of the TVC the spectrum gets a comb-like structure.*

means that certain bins can have 5 times more than the average width and some may have only 1/5 of the average bin width. Strategies to correct for the DNL effect can be found in [117]. Investigation have shown that a global DNL correction is not feasible.

Photoelectron peak fit

If contributions from the second and higher photoelectron peaks can be neglected, the charge spectrum can be described by the following distribution [118]

$$A \exp(-\alpha(x - x_{\text{th}})) + B \exp\left(-\frac{(x - x_1)^2}{2\sigma^2}\right). \quad (4.2)$$

The first term in Equation 4.2 describes the contribution of the dark current and the second term is the photoelectron peak which follows a Gaussian distribution (with mean x_1).

In order to render the fitting procedure less sensitive to the DNL effects, the integral of the spectrum is analysed instead of the differential form Equation 4.2. The integral of Equation 4.2 is given by

$$\frac{A}{-\alpha} [\exp(-\alpha(x - x_{\text{th}}))] + \frac{B}{\sqrt{\pi}} \Gamma\left(\frac{1}{2}, \frac{(x - x_1)^2}{2\sigma^2}\right) \quad (4.3)$$

where Γ is the incomplete Gamma function. Since the dark current term gives only a small contribution in the region of the 1pe peak the fits in the current version of the calibration program are performed with $A = 0$. This removes two degrees of freedom from the fit and improves the fit stability considerably. An example fit to an integrated AVC photoelectron spectrum is shown in Figure 4.5.

Pedestal fit

As for the photoelectron peak fit, the integrated charge spectrum is analysed to obtain the pedestal parameter. The algorithm scans the histograms to identify the pedestal region which is used to constrain the initial fit parameters. Then a fit is performed according to the following function

$$\frac{C}{\sqrt{\pi}} \Gamma\left(\frac{1}{2}, \frac{(x - x_0)^2}{2\sigma_0^2}\right) \quad (4.4)$$

to obtain the charge pedestal x_0 . An example of a charge spectrum obtained with the pedestal run setup and the corresponding fit is depicted in Figure 4.6.

4.3.2 Channel crosstalk correction

Analysis of the TVC and AVC distributions have revealed that the charge measurements in the AVC channel are influenced by the time measurements in the TVC channel. This effect is presumably caused by a crosstalk of the capacitors inside the ARS SPE pipeline. An example of the crosstalk effect is shown in Figure 4.7. In Figure 4.7a, the AVC channel in the 1pe region is plotted vs. the TVC channel for SPE hits recorded by a particular ARS. A profile plot of this distribution is given in Figure 4.7b. The shift of the AVC channel appears

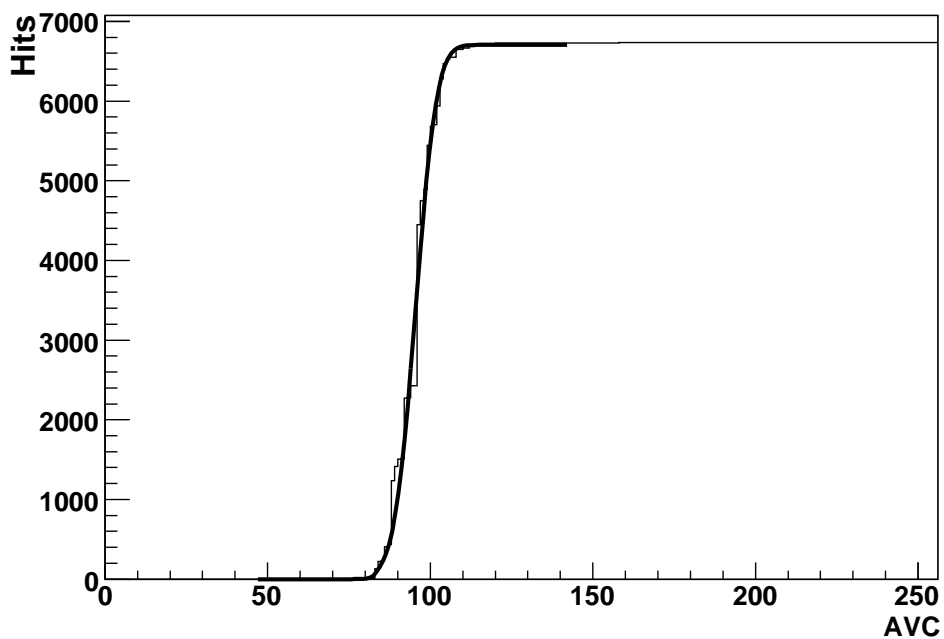


Figure 4.5: Example of an integrated photoelectron peak spectrum. The fit is indicated in addition.

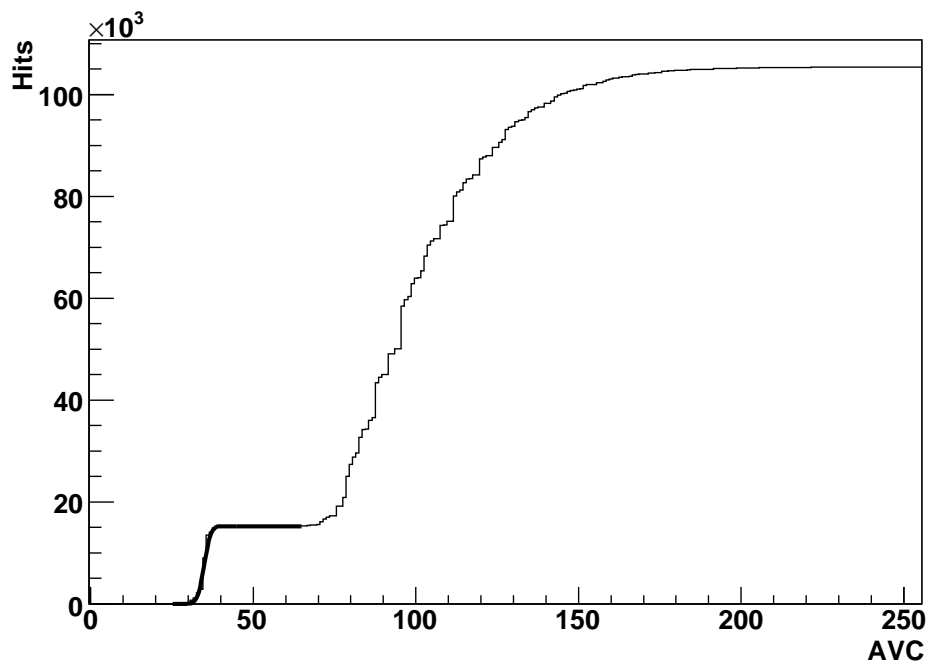


Figure 4.6: Example of an integrated pedestal spectrum. The fit is indicated in addition.

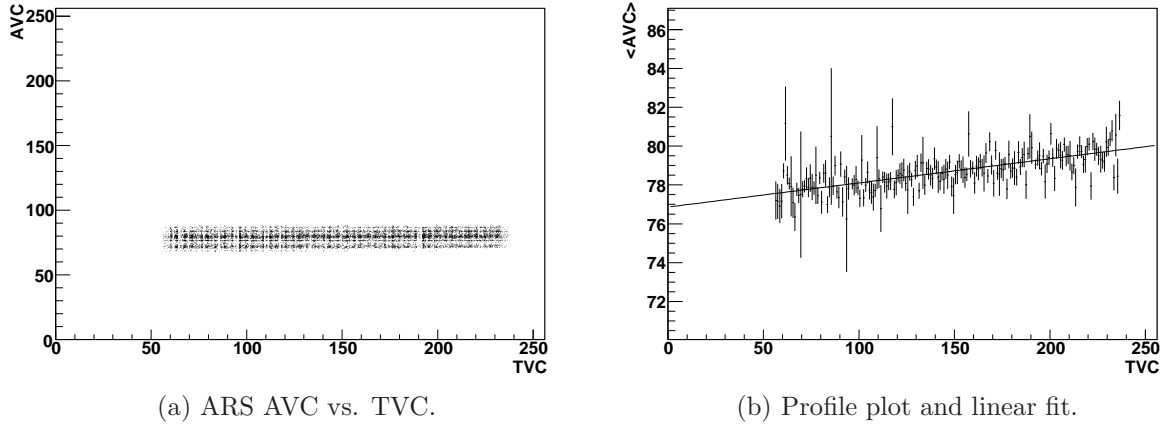


Figure 4.7: Example of the crosstalk effect. The scatter plot on the left shows the AVC channel plotted versus the TVC channel. The plot on the right shows a profile of the AVC versus the TVC and a linear fit.

to be linear in the TVC channel to a good approximation. The linear fit is indicated in the example distribution. Over the full TVC range the differences in the measured charge due to the crosstalk effect can reach up to 0.2 pe. Therefore absolute deviations on the order of 10% can be caused by the channel crosstalk. It is thus important to correct for this effect.

For the correction, the TVC range (given by the start (TVC_{\min}) and end (TVC_{\max}) points in the TVC spectrum) is extracted from the (AVC, TVC) distribution. The XT_{range} parameter which gives the deviation due to the crosstalk effect over this range is calculated from the linear fit. The influence of the crosstalk can then be determined and removed using the following prescription:

$$AVC_{\text{corr}} = AVC - XT_{\text{range}} \frac{TVC - \frac{TVC_{\max} + TVC_{\min}}{2}}{TVC_{\max} - TVC_{\min}}. \quad (4.5)$$

For the correction using this formula, one has to consider that the time interpolation between the clock pulses is performed alternately by two TVCs (for more information see e.g. [119]) and the corresponding TVC parameters can differ slightly. The correction is therefore obtained for the two TVCs individually. The final and complete version of the transfer function is then given by Equation 4.1 with the input AVC channel corrected by Equation 4.5.

4.3.3 Automatisation of the calibration procedure

The algorithms to extract the AVC channels corresponding to the charge pedestal and the photoelectron have been implemented in separate modules in the calibration framework software. The crosstalk effect is evaluated together with the photoelectron peak. In order

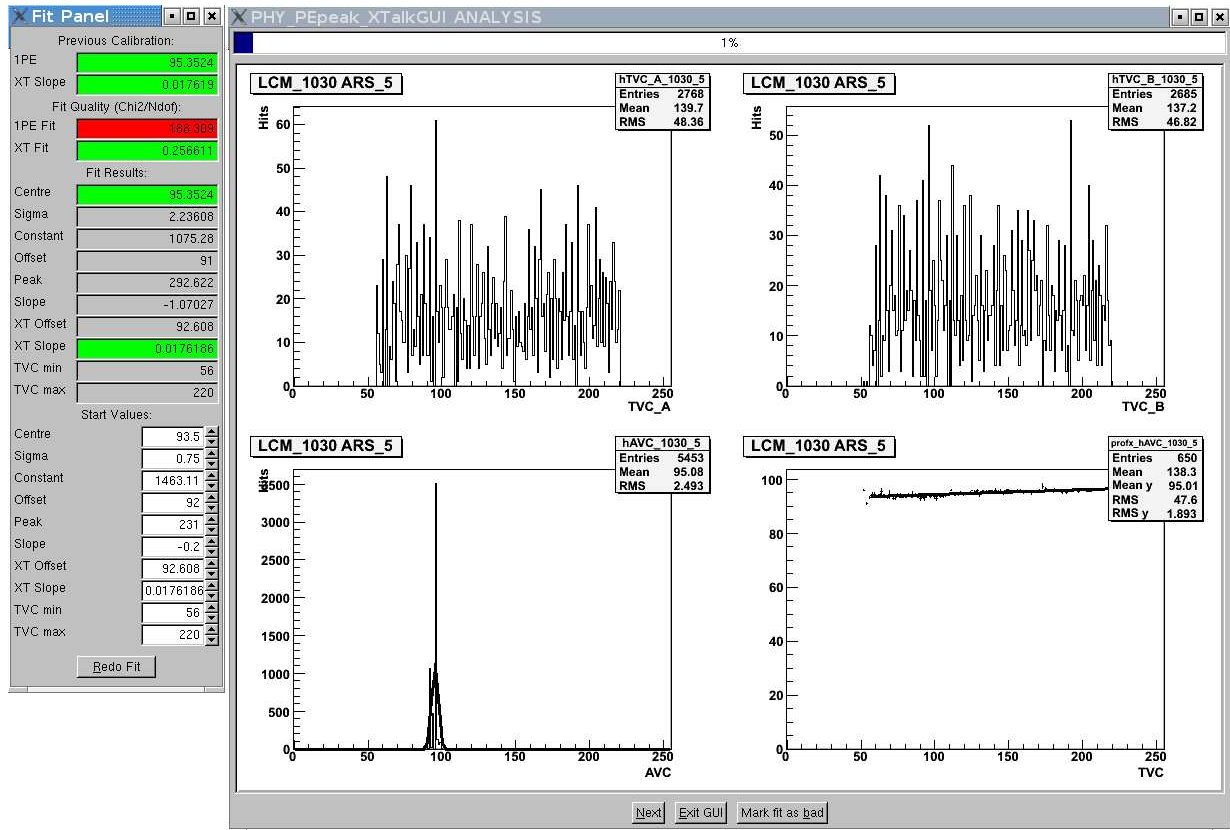


Figure 4.8: Example of the calibration user interface for the photoelectron and crosstalk fit. In the main window are shown counter-clockwise starting from the right top, the TVC distributions, a profile plot of the AVC vs. the TVC channel, the photoelectron peak fit. In the auxiliary window, the user can check the fit results and repeat the fitting with modified starting parameters, if necessary.

to facilitate the calibration procedure and especially the monitoring of the quality of the fits a simple graphical user interface (GUI) has been devised. An example of the interface for the photoelectron peak fit is shown in Figure 4.8. During the calibration procedure the application checks the fit quality and compares the calibration parameters with previously obtained parameters, which are retrieved from the database. In case the fit quality is suspicious or the deviation from the previous value becomes too large the fit procedure is stopped and the user can decide whether the fit is appropriate or has to be redone with new initial parameters. If the distribution is ill-behaved due to other problems (PMT not active, etc..) the calibration of this particular ARS can be marked as failed. The quality required for the fit as well as the deviations with respect to previous parameters can be adjusted in configuration files. After the calibration has been performed the result is stored in a well defined output file. The data can then be written into the database. Another small GUI has been programmed to monitor the quality of the calibration. A snapshot of this program is shown in Figure 4.9. This program generates control distributions for

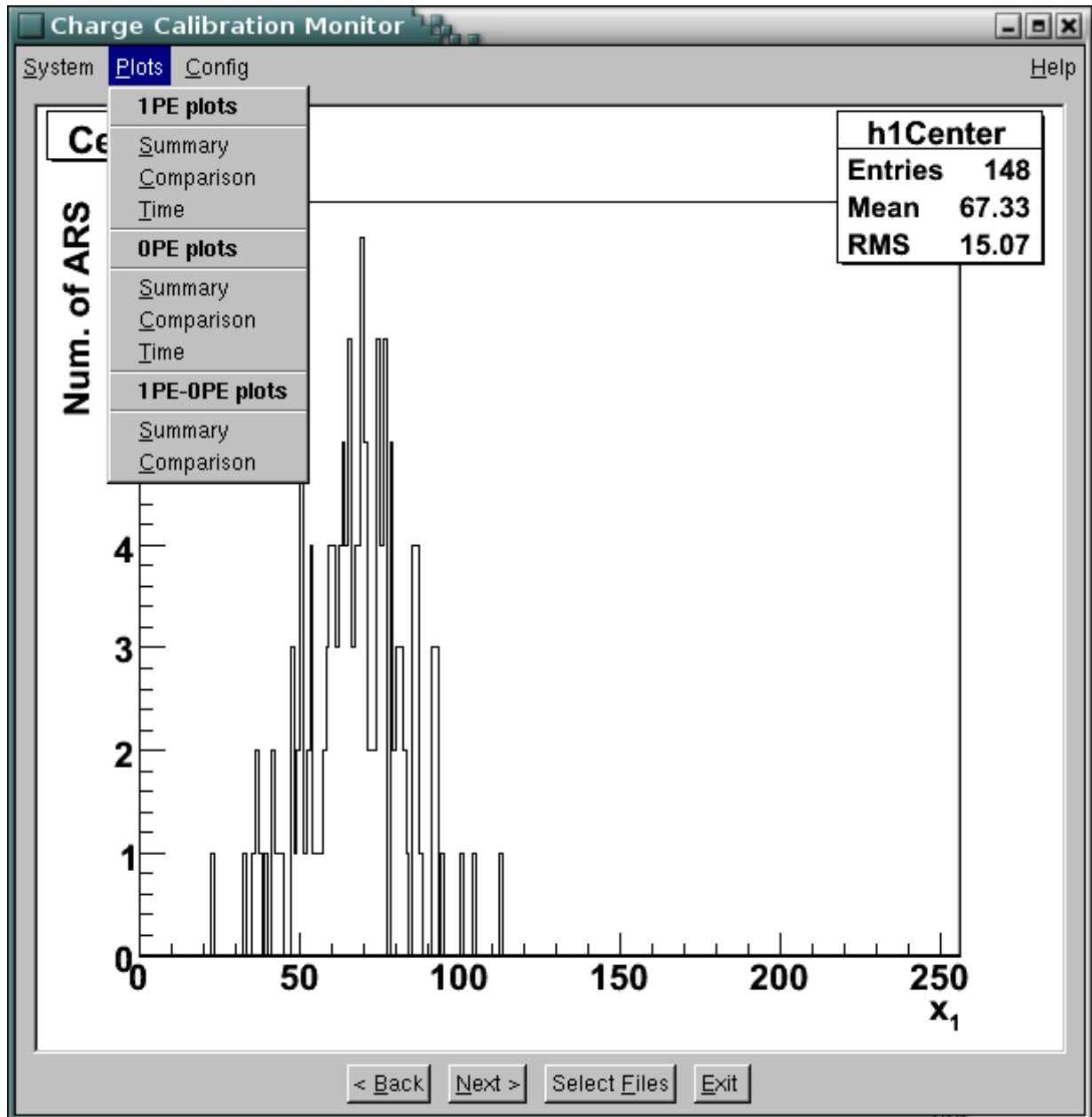


Figure 4.9: The calibration monitor program. This program has been developed to generate control distributions for the charge calibration sets. It can be used to read the calibration parameters from the calibration file or alternatively from the database. Differences in two calibration sets can be visualised. The program can also be used to study the time evolution of the calibration parameters.

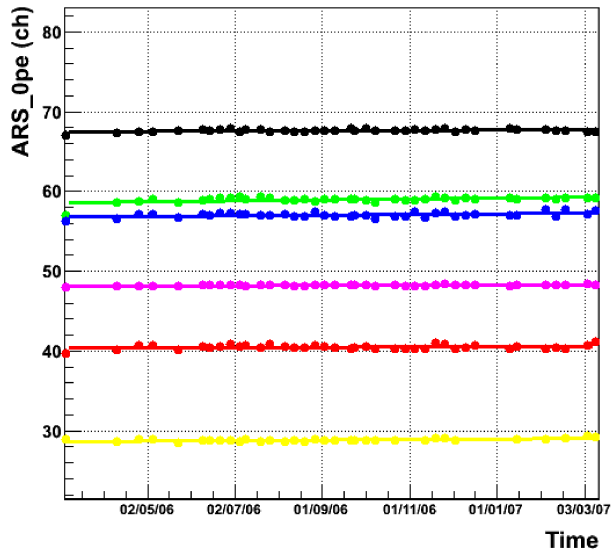
the calibration and allows comparing different calibration sets. The time evolution of calibration parameters (see Section 4.4) can be monitored too. The presented software has been used (and is used) to perform dark-room and in-situ calibrations. A long-term study of the stability of the calibration parameters is presented in the next section.

4.4 Long-term observation of the PMT gain

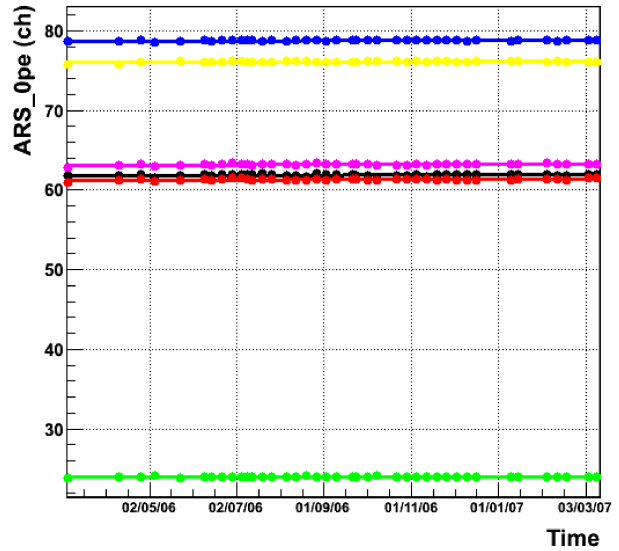
Since the PMTs are exposed to ambient light produced by radioactive decay and in particular bioluminescence (see Chapter 3) which can lead to temporary counting rates exceeding 1 MHz, it is important to monitor the PMT parameters as ageing effects can occur and necessitate reconfiguration of the DAQ settings (HV, thresholds etc.). Therefore long-term observations of the calibration parameters have been conducted. For this study Line 1 data from the connection in March 2006 to March 2007 have been used. Examples for the evolution of the charge pedestal are shown in Figure 4.10. The charge pedestal is almost constant in time. The individual fluctuations are rather small. A linear fit was applied to the evolution of the pedestal. The fits are indicated in the figure. The slope of the fits for Line 1 is summarised in Figure 4.13a. In Figure 4.11 examples for the time evolution of photoelectron peak positions are shown. Again linear fits are indicated in the figure. The evolution shows a clear drop in the photoelectron peak channel for most of the modules. However, in individual cases the drift can also be positive, which is exemplified in Figure 4.12. In Figure 4.13b the fitted slope of the drift is depicted. On average the photoelectron peak drop amounts to about -0.02 pe per month. The drop of the photoelectron peak corresponds directly to a drop in the PMT gain ($1\text{pe} - 0\text{pe}$) as the pedestal is stable. The observed drift is presumably due to ageing effects of the photocathode, although further studies are necessary for definite conclusions.

4.5 Conclusions on charge calibration

A robust, automatised charge calibration scheme has been developed. The calibration is based on integrated spectra in order to reduce the influence of the DNL effects. A correction for the channel crosstalk effect, which influences the charge measurement in some extreme cases up to 10%, has been implemented. Prior to deployment, calibration parameters are obtained in the laboratory in dedicated dark-room measurements. In-situ charge calibrations have been performed regularly. The systematic error of the calibration is estimated to be 30%, which is of the same order as the intrinsic PMT spread. Further improvements in the precision of the charge calibration will involve a solution to the DNL problem. A long-term observation of the PMT gain has been made. The study revealed a small drift of the PMT gain of about 0.2 channels per month. Presumably the observed drift is due to PMT ageing effects. This phenomenon needs further studies.

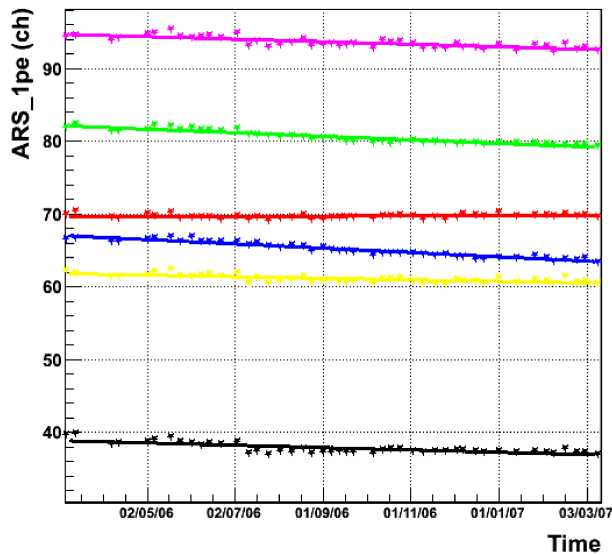


(a) Evolution for LCM 1621 on Line 1.

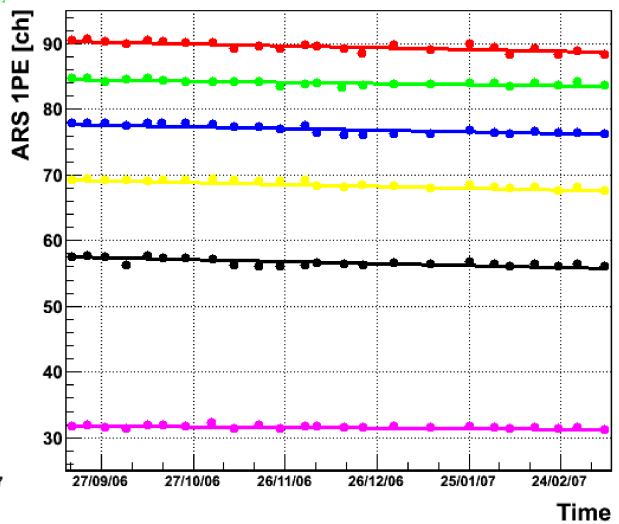


(b) Evolution for LCM 1624 on Line 1.

Figure 4.10: Evolution of the charge pedestal. See Figure 4.12 for an explanation of the colours.



(a) Evolution for LCM 1626 on Line 1.



(b) Evolution for LCM 1645 on Line 1.

Figure 4.11: Evolution of the photoelectron peak. See Figure 4.12 for an explanation of the colours.

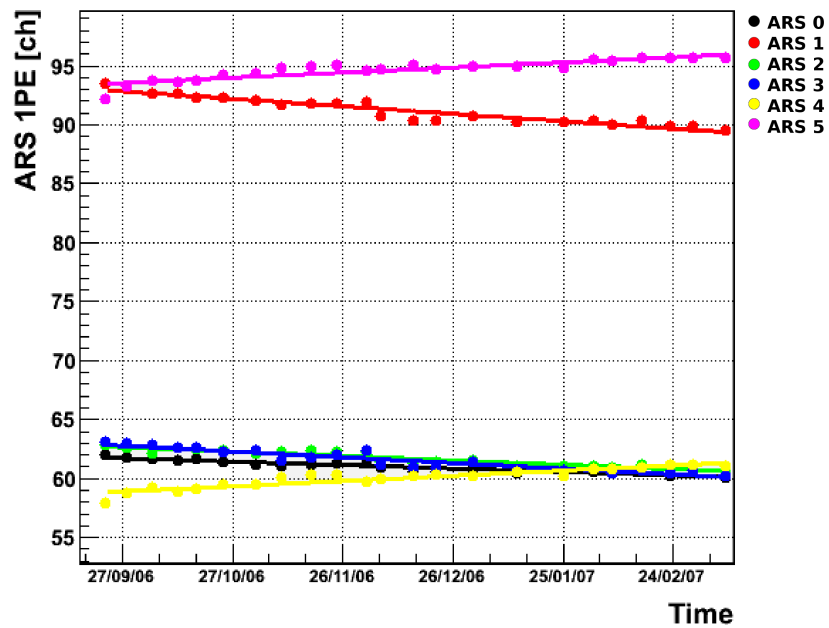


Figure 4.12: Example of a positive drift of the photoelectron peak calibration parameter from Line 2 LCM 1037, where ARS 4 (yellow curve) and ARS 5 (magenta curve), both connected to OM 3, show a positive drift in the AVC value over time.

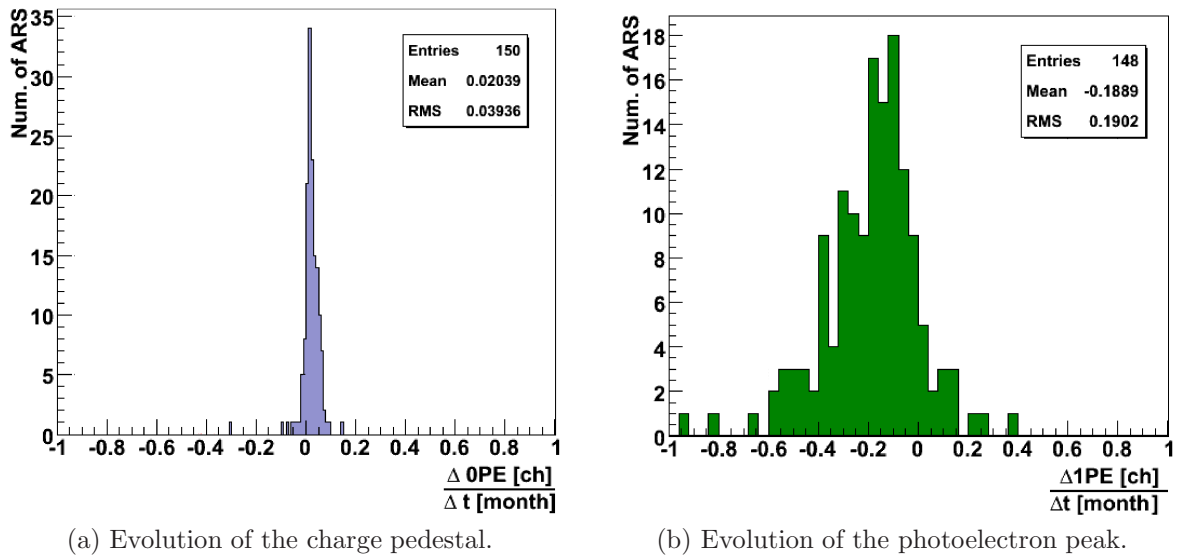


Figure 4.13: Summary of the time evolution of the charge calibration parameters. In this plot the fitted slope (change per month) is shown for the charge pedestal (left) and the photoelectron peak (right) of Line 1 as extracted from the long-term observation.

Part III

Event reconstruction and software

This part deals with the new ANTARES software framework and details the contributions which have been made during the work for this thesis (Chapter 5). The algorithms that are used to reconstruct physics events are described in Chapter 6 with focus on the reconstruction of muon tracks.

Chapter 5

The new software framework

Large-scale experiments in high-energy physics do not only involve high-end state-of-the-art electronics and detection hardware, but in addition call for complex algorithms for the processing of recorded data. The software of today's experiments typically includes physics and detector response simulations, calibration procedures, monitoring tools, and reconstruction as well as high-level analysis algorithms. The intrinsic complexity necessitates organising the diverse algorithms into a well conceived framework which enforces a coherent, pertinent design and ensures high quality standards. In this chapter, the new ANTARES offline analysis framework is described along with the contributions made in this thesis. The analysis chain is presented which is used to process the ANTARES data in a first mass reconstruction for the following analysis in Chapter 7 and Chapter 8. Within the framework, a web based monitoring tool has been developed which enables observation of the ANTARES data acquisition in real time and provides information about the detector status.

5.1 Software overview

Presently, the ANTARES software can be divided into the algorithms used for the data acquisition, which run off-shore and on-shore at the control station in La-Seyne, the simulation software, and the offline analysis programs. This classification is not fully unambiguous as, for instance, the DAQ software repository comprises algorithms which are used in other places as well. For instance, an important ingredient of the DAQ software is the data-filter described in Section 3.4.2. This algorithm is also applied to simulated data in order to evaluate efficiencies of the trigger [120] for signal and background. The ANTARES simulation chain has been briefly discussed in Section 3.6. The RECO package [121, 122, 123], which was developed in the past and mainly used for Monte Carlo studies, has been superseded by the CalReal/Physics [124] software which includes raw data calibration, event reconstruction, and some high-level analysis tools. However, inserting new algorithms into this package is not easy. Clearly, it is desirable to establish a coherent software framework. Work has been started to set up such a general framework, which can also be used for other neutrino telescope projects. This framework, presently mostly used for offline analysis and for online monitoring purposes is described in the following sections.

5.2 Offline analysis framework

Owing to the persistently increasing complexity of physics experiments, it has become general practice to gather algorithms, used to process, calibrate, and analyse data, in a common software framework. The key feature of the framework is to provide a set of rules, interfaces and services to the working physicist. Due to the particular layout of the interfaces and service classes, the framework defines a specific data flow and enforces a predefined programming logic. As a result, it becomes easier to exchange, re-use and expand existing algorithms. The ANTARES collaboration has recently decided to introduce such a general software framework in which existing algorithms are now gathered and new procedures are implemented. This software (KM3Tray¹, described in detailed in [125]) has been adopted from the IceCube collaboration, where the core of the framework was developed by a group of computer scientists, and has been modified with respect to the needs of water Cherenkov neutrino telescopes. The decision of introducing a shared code basis will clearly help collaborating not only in the ANTARES project, but will also support and abet next generation projects like KM3NeT.

In the context of this thesis several modification and specialisations for the ANTARES experiments have been made. In addition, new algorithms have been devised. In particular, the data structures for Monte Carlo simulation and real data reconstruction and the calibration services for geometry, charge, and time calibration have been implemented, respectively extended, tested and modified for a first data mass reprocessing. Tools for analysing and visualising ANTARES data were integrated. This section will first describe the gross overall structure of the framework in order to give an insight into the layout of the software and to provide an orientation for the reader and then detail the modifications, which have been made during this work. The aim of these descriptions is twofold. First of all, the developed algorithms should become transparent and easy to use. Furthermore, the explanations should allow developers to assess the modifications based on the design specifications and thus facilitate further developments.

5.2.1 Concepts of the framework

The KM3Tray framework consists of a coherent set of code (algorithms and data structures) bundled together with third party software (for instance ROOT [126]) needed to build the executables and libraries. The build process is automatised based on the CMAKE build system [127]. The code can be retrieved from the SVN [128] repository at Erlangen. A detailed conceptual description is also available [129].

The framework follows a modular approach in which several small functional units (modules) are chained together in a dedicated steering script to perform a specific task. Data

¹Within ANTARES, the project has been renamed to SeaTray. The original IceCube name is IceTray.

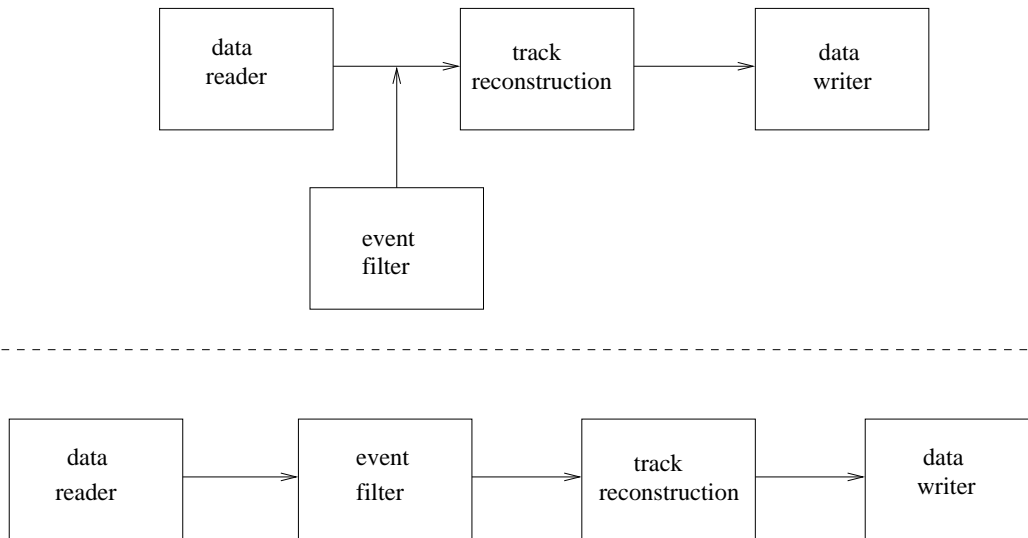


Figure 5.1: Illustration of the modular approach adopted in the KM3Tray software framework. The modules for a specific task (e.g. reading, writing, track reconstruction, etc.) are chained together to a full application. After the processing of data in a module is finished, the data are passed to the next module in the chain. This approach facilitates the expansion of existing programs by simply inserting additional, new modules. In this illustrative case, a module for event-filtering is inserted into the chain. The resulting chain could be expanded further, e.g. by the insertion of monitoring modules (generating event-displays or other control plots). This example has been adopted from [129].

are passed from module to module in a generic container (a so-called frame). In addition, service units, aiding the modules in performing their tasks, can be instantiated. Most of the modules and services are coded using the C++ object oriented programming language [130], whereas the steering scripts which chain the different modules together to a meaningful application are written in Python [131]. This mixture of programming languages combines the speed of a compiled language (C++) with the advantages with respect to flexibility and utilisation of an interpreted scripting language like Python. Whereas modifications of the framework’s core require considerable experience in programming and a profound knowledge of C++ design patterns, the software is intended to be easily usable for performing daily tasks, i.e. the insertion of new modules or implementation and execution of steering scripts.

The KM3Tray framework is designed such that after a first processing of the raw data has been performed and a certain reduction of the data volume has been achieved, the high-level data tables are stored in HDF5 format [132] and the final analysis can be realised with the fast and flexible Python language. Optionally, the possibility of using the ROOT format for data summary tables (DSTs) and the ROOT scripting facility for the final analysis is also supported.

5.2.2 Fundamental developments for ANTARES

During the adaption of the software [133, 134] for water Cherenkov telescopes, several algorithms developed and used for ANTARES were transferred to the framework. The possibility of reading and calibrating ANTARES raw data has been incorporated into the framework. An interface was developed to collect calibration sets (for time and charge calibration as well as for the detector alignment) from the ANTARES database. Furthermore, a version of the ANTARES trigger (data filter) simulation has been implemented. The functionality of reading simulated data in text format (ASCII) was provided. Several reconstruction algorithms have been ported from previous work. Summa summarum, most of the fundamental algorithms needed for ANTARES were already present, although not fully perfected for large-scale data (re-)processing.

In order to use the framework for a first mass reprocessing of ANTARES data and to evaluate Monte Carlo simulations for the Moon-shadow analysis, described later in this thesis, several modifications and specialisations for the ANTARES experiment have been made. This work has been conducted with emphasis on general usability, and a considerable amount of time has been spent to ensure a convenient design and implementation, hence the applicability of this work is not restricted to the analysis at hand, but provides a sound basis for future analyses as well. The developments, which have been made in the framework, are described in the following sections.

Interface to Monte Carlo files

The native file format of the ANTARES DAQ software is the ROOT format [135]. ANTARES raw data as well as Monte Carlo simulations on trigger level are stored in this format. The output of the detector response simulation is stored in ASCII-format and is converted (using the `MonteCarloEventWriter` program) into the ROOT format, in which the relevant information is stored in a dedicated data structure (ROOT tree). The information is then processed by the trigger simulation. The reading of this Monte Carlo ROOT tree structure was not supported by the framework. A version of the ANTARES trigger simulation has already been ported to the framework [133], which processes the simulation files in ASCII-format and generates the output in the KM3Tray “i3” XML [136] based file format. However, at the moment the possibility of inserting realistic background from real data runs is not implemented in the framework. Besides, the official ANTARES productions are currently still done with the trigger simulation code implemented in the DAQ-software and are thus only available as ROOT files.

So as to process the simulation for the Moon-shadow analysis (see Chapter 7, Chapter 8) the necessary functionality for reading the Monte Carlo ROOT structures has been programmed and added to the KM3Tray framework. During the integration, two key points have been accounted for. These are

- already existing data structures should be (re-)used. And,
- future changes in the DAQ software should be (conceptually) easily accommodated.

The implementation uses the structures [134] defined for the reading of the ASCII format. The new code has been separated into several already existing or newly developed functional units (services/modules) to facilitate the usage and to allow for straightforward possible future modification. The integration of the functionality implies the following changes to existing code and new services:

- The code generating the data class dictionaries (used to process the information) has been ported to (respectively updated in) the framework.
- A Monte Carlo run information service (`I3AntMCRunInformation`, which collects information about the MC production has been derived from the existing abstract run information service class.
- A calibration service (`I3AntMCCalibrationService`) has been devised. This service installs a calibration set (at the moment a fixed default MC calibration set, but foreseen future generalisations can be integrated easily) used for the calibration of the simulated data. This service is then available and used in the modified reader code. The calibration service is instantiated by a service factory, which can be configured in the Python scripts.
- A mapping of the Monte Carlo PMT numbering scheme to the concrete string and storey numbers has been defined in the `I3AntMCOMKey2LCM` service. Again, any modifications in the numbering scheme can be easily accounted for.
- The existing code, which reads the raw-data files, has been extended to read the MC structures. This module (`AntReader`) makes use of the abovementioned service classes.
- The existing service factory for the reader module has been adapted to incorporate the new functionality. The same syntax as introduced for the reading of raw-data files can be used in the Python steering scripts to read the simulated data. In case no specific calibration, run information or PMT mapping services are instantiated by the user, convenient default services are automatically initialised and used during the processing of the data.

The modifications detailed above were performed coherently with the already existing code and inserted into the *antares-reader* project.

The standard ANTARES data class (`Event`) implemented in the DAQ software permits users to store additional variables based on a template container approach. (Technically this is accomplished by inserting the variables into a `std::map<std::string, std::string>`.) This conception has been translated to the KM3Tray framework. User defined variables stored in the DAQ format are read out and saved in an instance of the `I3StringStringMap`, which has been added to the basic data classes for this purpose.

Interface to SPE time-slice data

Similar to the organisation of the Monte Carlo information, a special tree-like structure is used to store the unfiltered raw data (SPE time slices) which are recorded by special run setups or the GRB flash-back trigger [137]. If a GRB alert is reported by the GRB-alert-network, the unfiltered (pre-buffered) data stream is saved to disk in order to increase the sensitivity for GRB data analysis. Beside the GRB analysis, this time-slice data represents an unbiased snapshot data set and is valuable for calibration purposes and other systematic studies. To complete the interface to the ANTARES data structures and to forward the analysis of the sensitivity to supernova neutrinos performed in Erlangen [138] the functionality of reading SPE time-slice data has been integrated. The complete data, taken during one time slice (typically 104 ms) are converted into a vector of hits and are stored into the generic data stream (frame). The implementation has been added to the *antares-reader* project.

Nominal geometry

As described in Chapter 4, the accurate positioning is done offline based on the line shape model in which the hydrophone, tiltmeter and compass data as well as the known cable lengths are combined in a global fit. This procedure consists of several steps and as of this writing requires still a considerable time. Since the precise alignment information is not available during data-taking and filtering, a nominal geometry is used instead, in which the detection strings are assumed to be straight and strictly vertical. In order to process online data (e.g. for data quality tests, online event-displays and preliminary productions) with KM3Tray it is necessary to retrieve the nominal geometry of the detector which has been used during the data acquisition. Basically the geometry is fixed, but may change with updated data of the string anchor positions, the insertion of new lines during the construction phase of the telescope, or when recovered strings are re-deployed. It is thus desirable to obtain the nominal geometry at the discretion of the user

- based on a given run number,
- by specifying a certain time (corresponding to the start time of the data-taking run),
- by a calibration label which encodes the version of the nominal geometry,
- or automatically [139], based on the acquisition time of the processed data file and the configuration setup used during data-taking.

On that score, a service class (`I3AntaresDbTriggerGeometryService`), which provides the nominal geometry, has been written and integrated into the framework. The class is instantiated by a factory class (a well know C++ design pattern, see e.g. [140]). The source code and illustrative example scripts can be found in the *antares-db-interface* directory of the KM3Tray distribution.

Offline calibration tables

Since the calibration parameters (for time and charge calibration) can change with time, the configuration used during the data acquisition may not be optimal. Time and charge

calibrations are performed on a regular basis. Offline, an expert reviewed calibration set is determined, which is valid for a specified period and recommended for physics analysis. The information is stored in a dedicated offline calibration table in the ANTARES database [141]. The already present calibration service, which used the trigger configuration (that is retrieved from the database) has been modified to accommodate the offline calibration.

In order to facilitate the maintenance of the code, the shared functionality has been gathered in an abstract base class, `I3AntaresDbCalibrationServiceBase`, from which the two classes `I3AntaresDbOnlineCalibrationService` and `I3AntaresDbOfflineCalibrationService` inherit. The first class is a restructured version of the previously existing class, which can be utilised to obtain the configuration used during the data-taking by the data-filter algorithm. The latter class provides the functionality for reading the calibration sets from the offline calibration table. A service factory class implementation, `I3AntaresDbCalibrationServiceFactory`, decides via an option, specified in the steering script, which of the two service classes is instantiated. Again, source code and examples are available in the *antares-db-interface* directory of the KM3Tray framework.

Reconstruction data classes

In the original IceTray framework, the reconstruction information is stored in a dedicated data class (`I3Particle`). However, this class provides only a minimalistic, incomplete, set of variables. Therefore additional supplementary information has to be stored independently into the generic container (`Frame`). This approach has several shortcomings. Firstly, no coherent data structure is defined, which means that every reconstruction module has to be equipped with its own special data class and the additional information is left cluttered amongst several classes which renders further processing in subsequent analysis stages difficult. Furthermore, the original data class (`I3Particle`) does not allow for single line tracks (being fitted only at a single string the azimuth angle remains undetermined, for instance the track fit will only have four free parameters). A basic data class for single-line fits would have to be added. Therefore, the original data class in IceTray has been adapted to the needs of ANTARES according to the following specifications:

- Canonical variables, for instance the reconstruction quality parameter, the error matrix and an array of hit identifiers should be stored in well defined fields without creating huge overhead in case the information (e.g. the covariance matrix) is not present.
- The existing class should be naturally extended, allowing for single as well as multiple-line fits.
- The data class should be equipped with Python bindings, which extend the already present bindings of the `I3Particle` class.
- Besides the canonical variables, it should be possible to store reconstruction specific information in additional fields of the class, again without creating any overhead.

Based on these specifications, the data class `AntaresRecoParticle` has been implemented by inheriting from the `I3Particle` class. Inheritance models the “is-a” relationship in a natural way [142] and allows exploiting the built-in polymorphism feature of C++. This facilitates using the new data class with already existing code written for the `I3Particle` base class. The Python bindings have been inserted using the Boost-Python library [143] which allows extending the existing bindings of the base class in a natural and non-conflicting way. The class has been equipped with a template mechanism which allows for storing additional, more specific variables. The implementation resides in the *antares-common* source directory, where several example scripts can be found in addition. All of the standard ANTARES reconstruction algorithms have been modified to comply with the new data format specification implemented by the `AntaresRecoParticle` class and write this structure (optionally) into the frame. Tools like `dataio-shovel` (data visualisation) and `gl-shovel` (event visualisation) have been made aware of the new data class. Thanks to the construction (implementation via public inheritance), only minor modifications were necessary. The ANTARES display program described in the following section and further in Appendix A supports the functions of the new class as well.

5.2.3 Integration of existing and new algorithms

ScanFit reconstruction

The reconstruction algorithm developed in [144] has been ported to the new framework based on the implementation described in [124]. The source code can be found in the *antares-scanfit-reco* folder. Only minor modifications of technical nature have been made to the core algorithm. The calls to the old Fortran based minimisation algorithms (`Minuit`) have been replaced by an interface to the newer C++ version (`TMinuit`) available in ROOT. The original ScanFit structures for PMT signals (hits) are initialised with the corresponding `KM3Tray` objects in the frame. The result of the reconstruction is converted to the `AntaresRecoParticle` class and stored in the frame.

ANTARES display

In addition to the contributions described above, an event visualisation software developed during this work has been integrated into the framework. The implementation was ported [145] from a preliminary version of the program [146] for the `CalReal` package. This program offers:

- A two dimensional (z, t) control plot (see Appendix B) for each line, showing the PMT hits and the expected arrival time of the Cherenkov light cone emitted by a track or a shower.
- A simple (animated) 3D representation of hit OMs, tracks, showers and Cherenkov photons. The 3D scene is set up with the GL [147] functions available in ROOT. Both the 3D image and the 2D (z, t) -plot can be stored in an image file.

- Summary tables with event data and reconstruction information are displayed, and
- browsing and searching functions are available which allow skimming through a data file and which can be used to look up selected events (e.g. neutrino candidates).

The program can be utilised as a module in interactive- or in batch mode as instantiated inside the usual steering script or simply as a standalone program. The source-code is available in the *antares-display* directory together with illustrative scripts. The functions of the display program are described further in greater detail in Appendix A.

Online event-display service

Based on the ANTARES display program, an online event-display service has been installed which allows viewing the data acquisition and reconstruction in KM3Tray in real time, with a very short delay of only a few seconds. Information about the detector status and operation (for instance current run setup, run number, start time, operator, etc.) is fetched from the live stream, respectively from the database, and is passed to a web server together with an image-stream of online reconstructed events. The stream of reconstructed events is reduced by certain quality cuts to about one event per five seconds, corresponding to the polling frequency of the web client. Special events (neutrino candidates, etc.) are archived on the web server and are retrievable via the web application. The service on the server side was implemented mainly using PHP [148], the client application running in the web browser of the user was written using AJAX [149]. The online event-display service is depicted in Figure 5.2.

Further developments

Further improvements, most of which are related to the work on the analysis presented in Chapter 7 and Chapter 8 and on the online display service, but not limited to that, are listed below.

- A trigger rate monitor tool has been integrated into the framework in order to monitor event rates in the ANTARES live data stream as well as in archived runs on disk. The rate display of the live stream is exported to a web server and is then available via the online-display service.
- The `I3AntDbRunInformationService` has been extended to supply further information like run setup and operator to the analysis chain. A run info module was written which dumps the information related to a certain run into an XML-file.
- A mechanism for marking selected hits in the BBFit [86] reconstruction algorithm implemented in KM3Tray has been integrated. This information is useful for the assessment of reconstruction quality and is used in the event display.
- A simple selection module (`I3OnlineSelection`) enables reduction of the data stream in the live display to events with a certain reconstruction quality and selects special events (neutrino candidates).

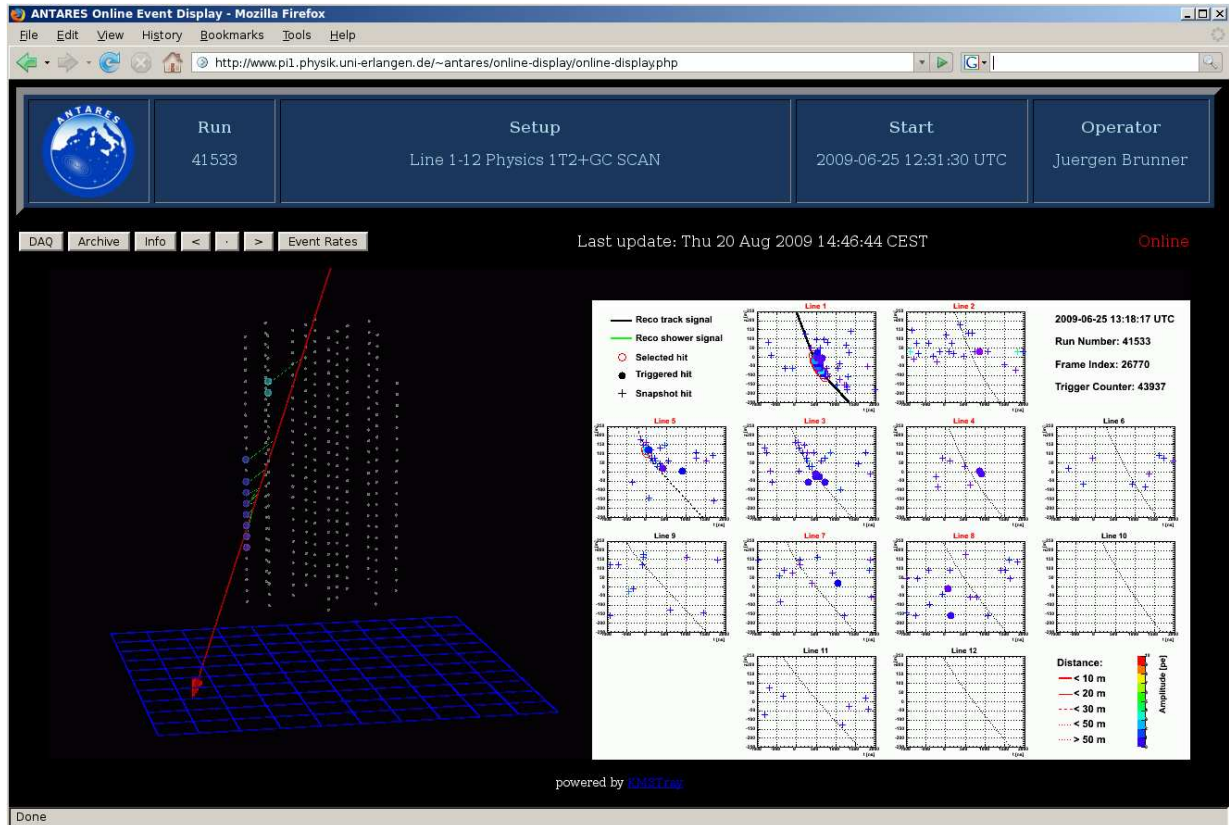


Figure 5.2: The ANTARES online event-display service. This figure shows a screen shot of the client application of the online event-display service running in a web browser. The application provides access to the live stream of ANTARES data, information of the detector status (e.g. run number, run setup, data acquisition time, and operator) an event archive with neutrino candidates and an event-rate monitor. The browser application was written using AJAX [149].

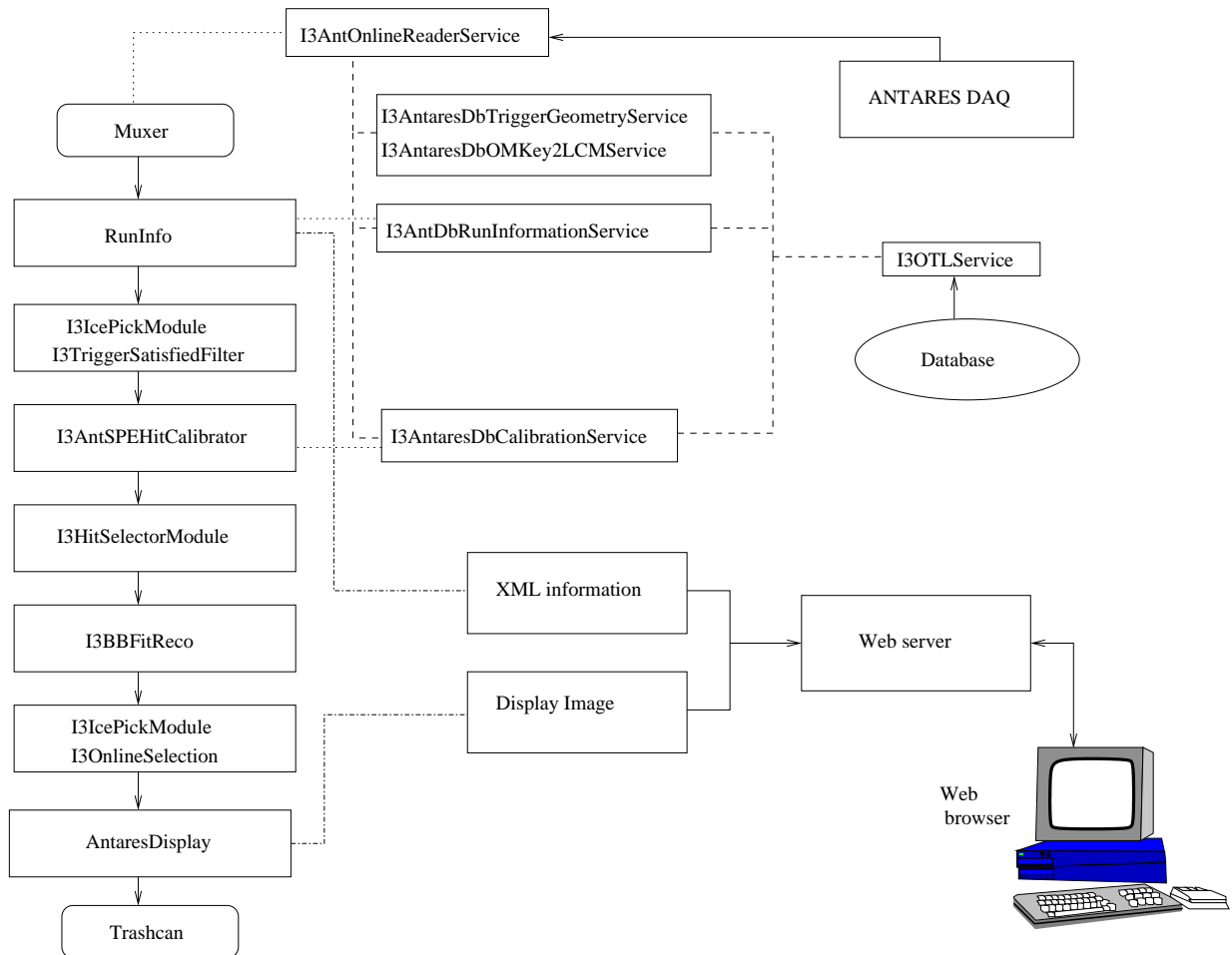


Figure 5.3: The data flow from the deep sea to the browser application of the web client in the *KM3Tray* online event display. The *KM3Tray* modules which are chained together are given on the left. The *RunInfo* module updates the XML information exported by the web server. The data stream is filtered by the *IcePickModule*, and only physics events are passed on to the calibration module. A list of hits triggering the event is stored in a separate vector in the *HitSelectorModule*. The fast online reconstruction is then used to reconstruct the events. The reconstruction information is evaluated in the *I3OnlineSelection* module and passed on to the *AntaresDisplay*, which generates an image of the reconstructed event. The information is transferred to a web server, processed by PHP scripts and exported to the web browser application, where an AJAX script polls every five seconds for information updates.

- A C++ version of the simulated annealing algorithm, used in the shower reconstruction [134], was implemented into the framework. This minimiser class provides callbacks to arbitrary C++ class member functions via a dedicated mechanism.

5.2.4 Overview of existing algorithms

At the time of this writing all of the essential algorithms needed to process ANTARES data and most of the existing reconstruction code developed in the past outside the framework has been integrated into KM3Tray.

The framework supports the readout of ANTARES raw data from ROOT files and simulated data from both text (ASCII) and ROOT files. It is further possible to connect directly to the live stream of ANTARES data provided by the ANTARES DAQ in order to monitor the data acquisition. The functionality for accessing ANTARES data is implemented in the antares-reader project.

A full calibration including all relevant effects, like time-walk correction, channel crosstalk correction, precise detector alignment, etc., can be obtained from the database. The user can refer to the offline reviewed calibration tables to automatically retrieve the optimal detector calibration sets for a given run period.

The ANTARES likelihood reconstruction and a robust online reconstruction are present in the antares-aart-reco, respectively the antares-bbfit-reco projects. Tools like AntaresDisplay in the antares-display project or the IceTray glshovel program allow users to monitor the event reconstruction quality. Visualisation of complex data structures is also possible with the data-io-shovel program.

The algorithms which are utilised for the processing of the ANTARES data and simulation in this thesis are summarised in Table 5.1.

Project	Description
antares-aart-reco	full likelihood reconstruction
antares-bbfit-reco	robust online reconstruction
antares-scanfit-reco	reconstruction algorithm
antares-display	event display
antares-reader	data input (file, live-stream)
antares-db-interface	DB interface and data calibration
icepick	event selection and filtering
hit-selector	hit selection algorithms
antares-common	data structures

Table 5.1: *Non-exhaustive list of KM3Tray projects, used in this work.*

5.2.5 Event reconstruction chain

In addition to the abovementioned developments in the framework, a set of steering scripts for data processing including the reconstruction of recorded events on a batch farm (running the Sun Grid engine) have been set up and a first mass reprocessing (with a data volume of several tera bytes) of ANTARES data with KM3Tray has been performed. The reconstruction chain is explained in Figure 5.4. A list of suitable runs with a physics setup has been compiled using run information from the database. After the processing, jobs are checked for a successful completion and if necessary redone. A few technical problems had to be solved, like the restriction of simultaneously running processes, copying data from the file server to the worker machine. (This was achieved by implementing a semaphore for the communication of the batch jobs.) The technical details have been (partly) documented [150].

5.3 Conclusions and outlook

The KM3Tray framework represents a robust and flexible software package which eases processing and analysis of simulated as well as real data. Thanks to the modular approach, it is easy to expand existing code and to incorporate new algorithms. A considerable amount of time has been spent to adapt the IceTray framework for ANTARES and to port existing algorithms. The software development performed in the context of this thesis is not restricted to the specific analysis in this thesis, but can be used by other analyses in the future as well. Several sanity tests and a first mass reconstruction were performed, demonstrating the functionality for ANTARES. However, it should be emphasised that the development of a coherent ANTARES software framework is not yet fully finished and further modifications will have to be made in a collaborative effort. An important point which remains to be solved is the seamless integration of the code in the DAQ software.

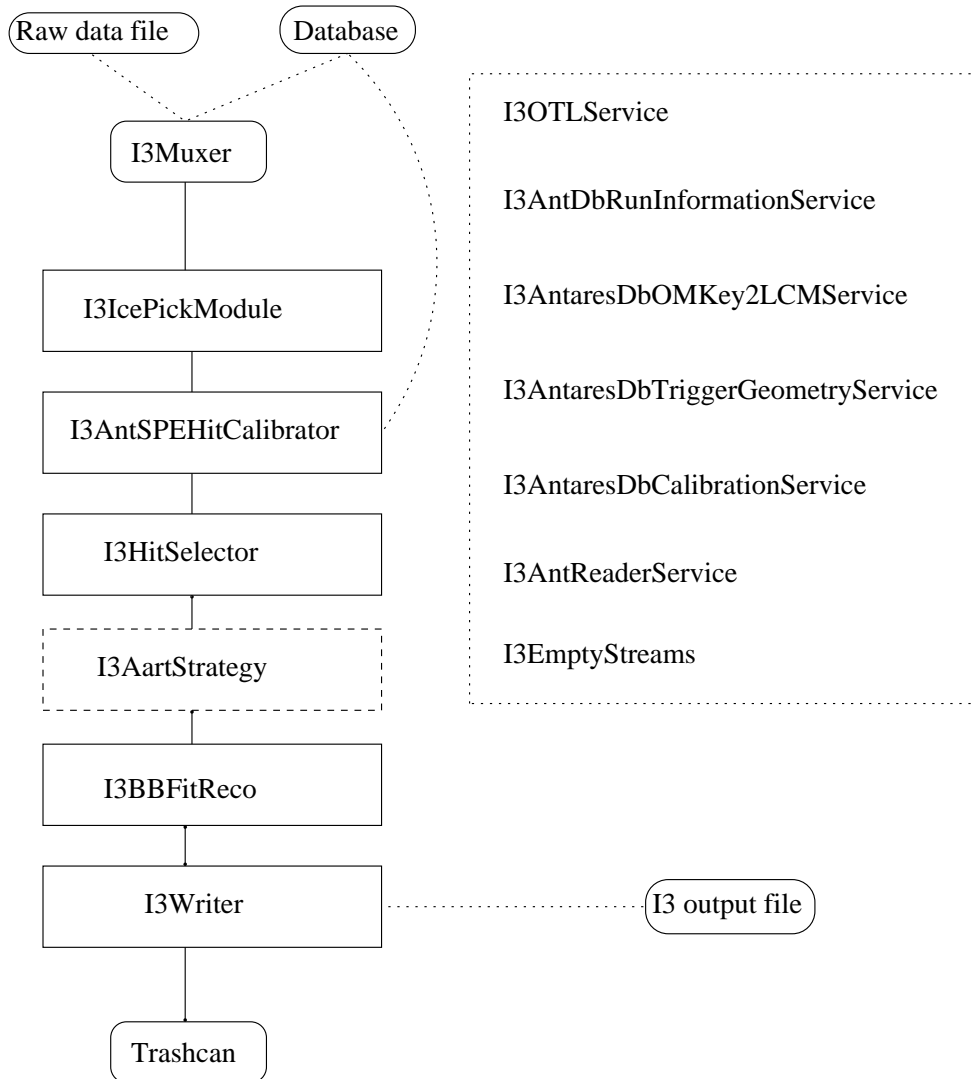


Figure 5.4: Schematic of the *KM3Tray* reconstruction chain used for data analysis in this work. The boxes represent modules in the chain. The dotted box “*I3AartStrategy*” is itself composed of several sub-modules which are not listed here. The services which are used throughout the chain are listed separately in the dotted frame. The ANTARES raw data are read out from a *ROOT* file by the reader service. Several modules make use of the database interface provided by the “*I3OTLService*” class and use the listed database service classes to retrieve the alignment, charge and time calibration sets as well as supplementary run information from the database. At the end of the processing chain the reconstruction results are stored in an *I3* file.

Chapter 6

Event reconstruction

This chapter briefly describes the strategies which are used to reconstruct muon tracks from the measured PMT signals in the following analysis. A novel prescription is presented which allows us to reduce the complexity of the track-fit problem on the pre-fit level. Implications of this reduction are discussed. In the last section of this chapter, we comment on the usage of global optimisation algorithms for the track-fit problem.

6.1 General remarks on event reconstruction

6.1.1 Classification - event topologies

As described in Chapter 2, the two characteristic signatures of physics processes relevant for neutrino telescopes are showers of electromagnetic or hadronic origin in which the Cherenkov light emanates from a well-localised region (bright point) and the extended signature of a long (muon) track. Figure 6.1 illustrates the two different event topologies. An example visualisation of a real track-like event measured with ANTARES can be found in the Appendix C in Figure C.1 and an example of a real shower-type event recorded with ANTARES is given in Figure C.3. In practice, the separation is not clear cut, since an event can have a track and also several showers originating from the interaction vertex and, respectively or, from bremsstrahlung processes occurring along the track. (Cf. the discussion in Chapter 2.) Although hybrid reconstruction algorithms are in preparation, most of the current reconstruction algorithms based on pattern matching assume a certain event type (shower or track) and try to maximise a likelihood function for the specific signature by varying the reconstruction parameters. Afterwards, quality cuts are applied in order to constrain the influence of wrongly classified events. Due to the characteristic topology of a long track the direction can (usually) be reconstructed with a high precision in track-like events. Contrariwise, the resolution of the direction in the shower reconstruction is rather poor. With respect to the energy of the events, showers are easier to reconstruct, since the energy scales to a good approximation linearly with the measured charge for contained showers, if corrections for light propagation are applied. The following discussion concentrates on the track reconstruction which will be used in the analysis in Chapter 7 and Chapter 8. Comprehensive descriptions of algorithms for the shower reconstruction can be found in [151].

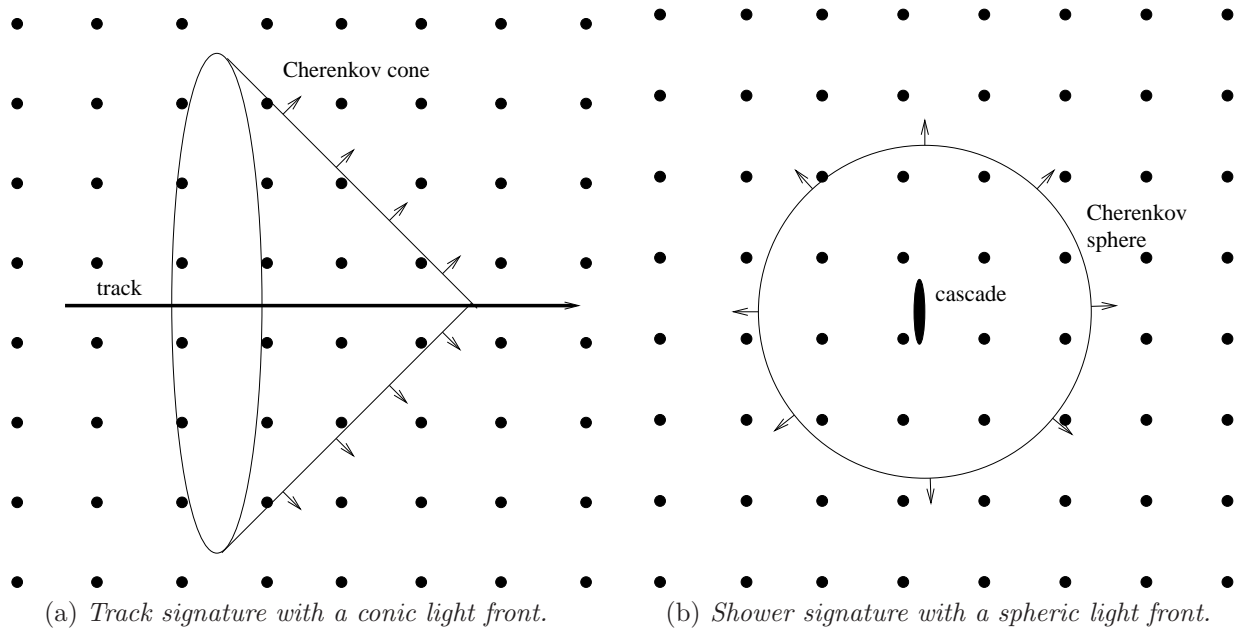


Figure 6.1: (a) Track- and (b) shower-like events in ANTARES. In case of the track the Cherenkov light is emitted into a cone. In case of the shower event the Cherenkov light front has a spheric shape.

6.1.2 Track reconstruction algorithms

Muon tracking in a Cherenkov PMT array is a difficult non-linear 5-dimensional optimisation problem. For a given time (e.g. the time of the first L1 hit, see Chapter 3), the position of the muon (i.e. three Cartesian coordinates) and the direction (given by two angles) are to be determined. For ANTARES, noise rates at the level of 100 kHz, light scattering and absorption in the sea water limit the resolution of the reconstruction. Thus track reconstruction schemes are based on iterative procedures with several steps reaching from a robust pre-fit based on a reliable hit selection with mediocre resolution to a final high precision fit which depends on a good starting point and a good understanding of the detector properties in terms of angular acceptance, light scattering, precise alignment, et cetera. In the following Section 6.2, the standard ANTARES likelihood track reconstruction will be briefly described, as this algorithm is used in the Moon-shadow analysis presented in Chapter 7 and Chapter 8. The reader is referred to [86] for a description of the online reconstruction algorithm, which is used in the event-display service. A compelling method to reduce the complexity of the tracking problem to a one-dimensional optimisation problem is described in Section 6.3 and some remarks on attempts to improve the tracking by employing global optimisation algorithms are documented in Section 6.4. The explanations in these two sections are rather intended to provide some insight and guidance for future studies than to represent the last word on a difficult problem.

6.2 The likelihood track reconstruction

A flow chart of the likelihood track reconstruction algorithm [45] is given in Figure 6.2. After an initial hit selection in which hits with large amplitudes and coincident hits are selected, an analytic pre-fit is performed to provide a robust starting point for further fits. This pre-fit basically assumes that the hits (with measured amplitude A_i) occur along the track and derives the starting point analytically from the minimisation of the following χ^2 function:

$$\chi^2 = \sum_{i=1}^N A_i (\mathbf{x}_i - \mathbf{x}_0 - \mathbf{v}t_i)^2. \quad (6.1)$$

In this equation, \mathbf{x}_i is the measured hit position at time t_i , \mathbf{x}_0 denotes the track position at time $t = 0$, \mathbf{v} is the velocity vector of the track and N corresponds to the number of selected hits. See [45] for details, where a small refinement is discussed. This pre-fit is used as a starting point for subsequent fits. At the next level of the reconstruction, the time residuals $\delta t = t_{\text{meas}} - t_{\text{exp}}$, defined as the difference between measured and expected light arrival times, are evaluated. For this calculation, the Cherenkov photons are assumed to be emitted under the Cherenkov angle with respect to the track. The time residuals of the selected hits are combined into a so-called M-estimator function which is *approximately* given by the sum

$$M \approx \sum_{i=1}^N 2\sqrt{1 + \delta t_i^2/2} \quad (6.2)$$

of the individual residuals δt_i . It has been found that this function is less sensitive to outliers (hits with large residuals, caused by background processes) than the traditional χ^2 - estimator, $\chi^2 \propto \sum \delta t_i^2$. The result of the optimisation of the M-estimator is used as input for the next step which is based on a likelihood fit with a p.d.f. (so-called *original* p.d.f. for historic reasons) depending on time residuals only. This function contains some artificial unphysical features (tail at negative time residuals), which are introduced to improve the convergence of the fitting algorithm. The hits that are used in this p.d.f. fit are selected by the requirement of small time residuals with respect to the result of the M-estimator fit. The M-estimator fit and the original p.d.f. fit are repeated starting with transformed input tracks (with in total nine different transformations) in order to ensure that a large part of the parameter space is scanned for the global optimum. The final step uses the best original p.d.f. fit as starting point and includes amplitude information of the hits as well as background hits (with rate R^{bg}). The detailed p.d.f., $p(\delta t_i, a_i, b_i | A_i, R^{\text{bg}})$, which is used in the final fit has been extracted from Monte Carlo simulations. It is a function of the time residuals δt_i , the incident angle a_i , and the photon pathlength b_i . In the fit, the likelihood function

$$\mathcal{L} = \prod_{i=1}^N p(\delta t_i, a_i, b_i | A_i, R^{\text{bg}}) \quad (6.3)$$

is then maximised. This function includes the hits with small time residuals with respect to the preceding p.d.f. fit. The quality of the reconstruction can be assessed by the logarithm of the likelihood function normalised to the degree of freedom $\frac{\log(\mathcal{L})}{N_{\text{dof}}}$. However, it was found [45] that the number of starting tracks N_{comp} in the iteration which lead to results comparable to the preferred solution (within 1° in direction) can be used as an independent quality indicator. Therefore, these two parameters are combined into a test statistic

$$\Lambda = \frac{\log(\mathcal{L})}{N_{\text{dof}}} + 0.1(N_{\text{comp}} - 1). \quad (6.4)$$

This variable is used to tune the angular resolution of the final event sample in the Moon-shadow analysis presented in Chapter 7 and Chapter 8.

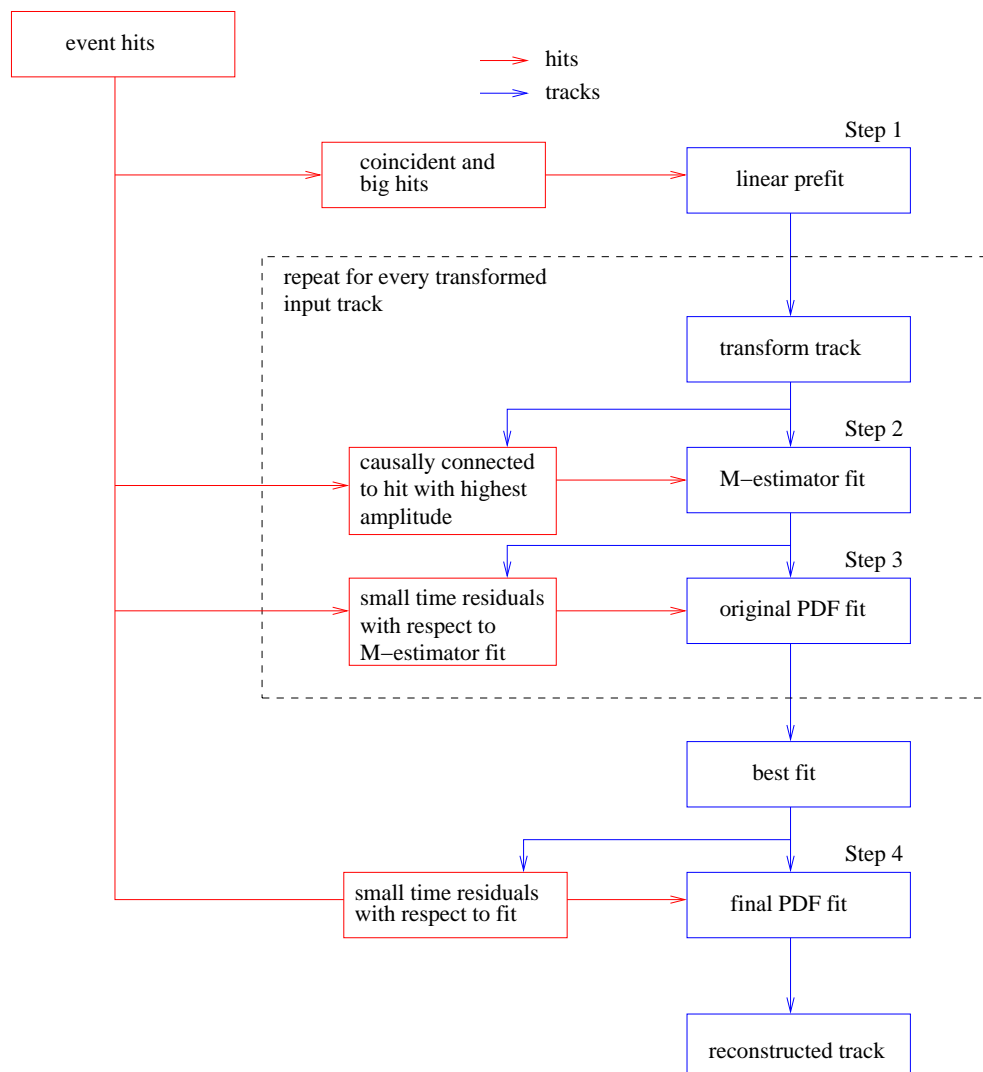


Figure 6.2: Schematic [152] of the full likelihood fit. See text for further information.

6.3 Linearisation methods

The relation between registered hit coordinates, arrival times, and track parameters is non-linear. This non-linearity considerably complicates the reconstruction of the track parameters, as it is difficult to find robust and accurate starting points for the optimisation algorithms. In [153] a method has been described to reduce the general 5-dimensional least squares track fit problem to a minimisation problem of a 2-dimensional χ^2 function depending on the direction of the track only. The remaining spacial parameters are obtained together with the χ^2 by solving a system of linear equations. A similar method has been used as a pre-fit in [154]. An example of such a two-dimensional χ^2 function after the reduction is shown in Figure 6.3. As one can see, the directional χ^2 function is still complicated and it is difficult to find the global minimum. The arguments leading to the reduction will not be repeated here. For more information on the method, the reader is referred to [155, 156, 157]. Instead, it is shown in this section that the problem can be reduced further, i.e., the directional χ^2 function can be factorised into two one-dimensional functions depending merely on the track zenith angle and the track azimuth angle respectively. This fact greatly simplifies the optimisation problem, since a one-dimensional space can be scanned easily. After the discussion of the mathematical basis it is described how this approach can be embedded into the full 3-dimensional tracking.

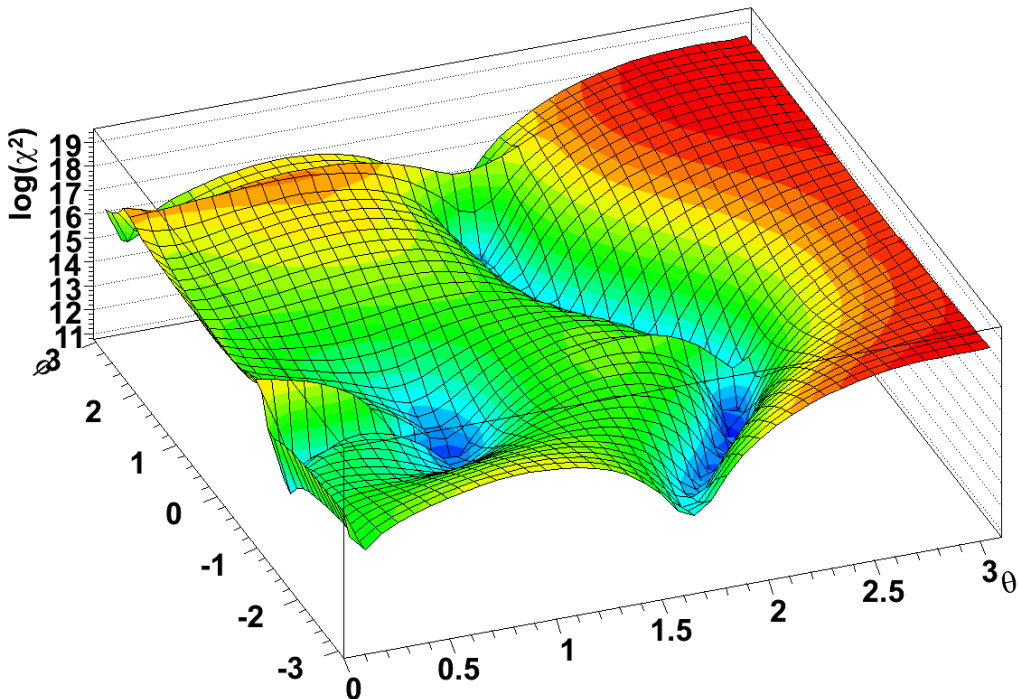


Figure 6.3: Example of a χ^2 -landscape. In this plot the directional χ^2 function (see text) is shown (in arbitrary units) as a function of the track direction. The global minimum is difficult to identify in this complex structure.

6.3.1 Tracking in two dimensions - single line fits

In order to reduce the problem further a few simplifying assumptions have to be made. First, the optical modules are assumed to be fixed on a straight line (string). This is a common premise for a first level fit. One can then consider the hit signature on a single string first and generalise the treatment later to the full detector. For a given track with zenith angle θ , velocity v , distance of closest approach to the line d_0 at a corresponding height z_0 and time t_0 , the relation between light arrival time t and altitude z on the line is given by

$$t = t_0 + \frac{1}{v}(z - z_0) \cdot \cos \theta + \frac{\tan \theta_C}{v} \cdot \sqrt{d_0^2 + \sin^2 \theta (z - z_0)^2}. \quad (6.5)$$

This equation is derived in Appendix B. One can now consider a fixed direction ($x = \cos \theta$) and introduce the shorthands $T = t - t_0$ and $Z = z - z_0$. This permits us to rewrite Equation 6.5 for a given hit at Z, T :

$$\begin{aligned} vT - Zx &= \tan \theta_C \sqrt{d_0^2 + (1 - x^2)Z^2}. \\ v^2T^2 - 2vTZx + Z^2x^2 &= \tan^2 \theta_C (d_0^2 + (1 - x^2)Z^2) \\ v^2T^2 - 2vTZx + Z^2(x^2 + \tan^2 \theta_C(x^2 - 1)) &= \tan^2 \theta_C d_0^2 \\ v^2T^2 - 2vTZx + Z^2K &= D^2. \end{aligned}$$

Here we have set $K = x^2 + \tan^2 \theta_C(x^2 - 1)$ and $D^2 = \tan^2 \theta_C d_0^2$. For a pair of hits $\{(T_i, Z_i) \mid i \in \{1, 2\}\}$, we can subtract the corresponding equations to obtain

$$v^2(T_2^2 - T_1^2) + K(Z_2^2 - Z_1^2) = 2vx(T_2Z_2 - T_1Z_1). \quad (6.6)$$

After expanding we are left with

$$\begin{aligned} (-2v^2(t_2 - t_1) - 2vx(z_1 - z_2))t_0 + (-2k(z_2 - z_1) - 2vx(-t_2 + t_1))z_0 &= \\ -v^2(t_2^2 - t_1^2) - k(z_2^2 - z_1^2) + 2vx(t_2z_2 - t_1z_1). \end{aligned}$$

At this point, the equation is *linear* in the remaining track parameters t_0 and z_0 . This equation can thus be solved using the method of least squares [158]. The following treatment uses the nomenclature of the general discussion in [159]. The equations for hit pairs can be written in a compact form with the response matrix R , the track parameter (or solution) vector \mathbf{a} and the measurement vector \mathbf{y} :

$$R\mathbf{a} = \mathbf{y} \quad (6.7)$$

with

$$R = \begin{pmatrix} -2v^2(t_2 - t_1) - 2vx(z_1 - z_2) & -2k(z_2 - z_1) - 2vx(-t_2 + t_1) \\ \ddots & \ddots \\ -2v^2(t_n - t_{n-1}) - 2vx(z_{n-1} - z_n) & -2k(z_n - z_{n-1}) - 2vx(-t_n + t_{n-1}) \end{pmatrix} \quad (6.8)$$

and

$$\mathbf{a} = (t_0, z_0), \quad \mathbf{y} = \begin{pmatrix} -v^2(t_2^2 - t_1^2) - k(z_2^2 - z_1^2) + 2vx(t_2z_2 - t_1z_1) \\ \dots \\ -v^2(t_n^2 - t_{n-1}^2) - k(z_n^2 - z_{n-1}^2) + 2vx(t_nz_n - t_{n-1}z_{n-1}) \end{pmatrix}. \quad (6.9)$$

In general, Equation 6.7 is overdetermined and has no well-defined solution. However, a well-defined solution vector \mathbf{a} in terms of least squares exists, provided a non-singular $R^T N^{-1} R$, minimising

$$\chi^2(\mathbf{a}) = (\mathbf{y} - R\mathbf{a})^T N^{-1} (\mathbf{y} - R\mathbf{a}), \quad (6.10)$$

where N is the covariance matrix. Under this condition the unique solution for the estimator is given by

$$\mathbf{a} = (R^T N^{-1} R)^{-1} R^T N^{-1} \mathbf{y} = S\mathbf{y}. \quad (6.11)$$

The quality of this solution can be judged by the covariance matrix of the estimator which is determined by

$$\text{Cov}[\mathbf{a}_i, \mathbf{a}_j] = \text{SNS}^T = (R^T N^{-1} R)^{-1}. \quad (6.12)$$

It is advisable to rearrange the hits for the numerical evaluation of Equation 6.11 in order to obtain entries of similar magnitude in the response matrix R . This resorting of hits improves the numerical stability of the algorithm. For practical purposes the covariance matrix N can be set to the unit matrix. This has little impact on the shape of the χ^2 distribution and improves the stability further.

6.3.2 Generalisation to 3-dimensional tracking

After having solved the minimisation problem of the one-dimensional χ^2 function for each line, there are two different strategies to obtain the full solution of the track fit problem. The alternatives are:

- Combining the individual χ^2 functions for the single lines into a cumulative χ^2 function for the global event. This method yields a global θ_{opt} value, which can be inserted into the 2-dimensional directional χ^2 function. The remaining azimuth angle can then be obtained by a further one-dimensional scan.
- Using the individual χ^2 functions to determine the individual optimal θ_{opt} solutions and to probe the two dimensional χ^2 function with these individual solutions. The best (θ, ϕ) combination then determines the solution of the full track fit problem.

The first approach is naturally faster than the second one, however, the latter method has the benefit that wrongly fitted lines (due to background hits or delayed scattered hits) do not influence the solutions of correctly fitted lines. The performance with respect to angular resolution of the second approach is therefore in general better. An illustrative example of the procedure is given in Figure 6.5. This figure displays the one-dimensional χ^2 functions for the simulated muon-neutrino event in Figure 6.4. The cumulative $\chi^2(\theta)$ function is

shown together with true track zenith angle value. The $\chi^2(\phi)$ function is subsequently obtained by inserting the optimal θ value, found by scanning the zenith angle, into the 2-dimensional $\chi^2(\theta, \phi)$ function. This function is shown in the bottom plot of Figure 6.5. The pair of optimal zenith and azimuth angles then corresponds to the solution of the global track fit problem.

6.3.3 Resolution of ambiguities

The novel prescription of reducing the track-fit problem can be used to analyse difficult hit pattern which lead to ambiguities in the reconstruction. An example of such a pattern is given in Figure 6.6. In this case, the one-dimensional $\chi^2(\theta)$ function allows us to identify the correct solution and resolves the ambiguity.

6.3.4 Application to the reconstruction of showers

It is noteworthy that the linearisation prescription of the track-fit problem can also be applied to shower events. A 3-dimensional method has already been described [151]. The 2-dimensional signature produced by a bright point is given by the time t_0 , the altitude z_0 and the distance to the string d_0 of the shower:

$$v(t - t_0) = \sqrt{(z - z_0)^2 + d_0^2}. \quad (6.13)$$

After introducing the short-hands $T = t - t_0$ and $Z = z - z_0$ and subtracting pairs ($i = 1, 2$) of hits one obtains

$$v^2(T_2^2 - T_1^2) - (Z_2^2 - Z_1^2) = 0, \quad (6.14)$$

which can be expanded to

$$-2v^2t_0(t_2 - t_1) + 2z_0(z_2 - z_1) = -v^2(t_2^2 - t_1^2) + (z_2^2 - z_1^2). \quad (6.15)$$

This equation is again *linear* in the parameters t_0 and z_0 , so that the machinery described above can be readily applied. By comparing the different χ^2 values for the track and the shower signature, one can directly classify the event (or hit pattern) type. This allows extracting showers (from the interaction vertex and, respectively or, from bremsstrahlung processes along the track) from track-like events and could thus considerably improve the reconstruction quality.

6.3.5 Conclusions and outlook

The linearisation prescription described in this section is a very promising technique which allows reducing the complexity of the track fit problem at the first stage (pre-fit level) effectively to a one-dimensional minimisation problem. In order to integrate this technique fully into the reconstruction chain, a detailed analysis of the hit selection (possibly in combination with an iterative algorithm) and a deeper study of the performance for different

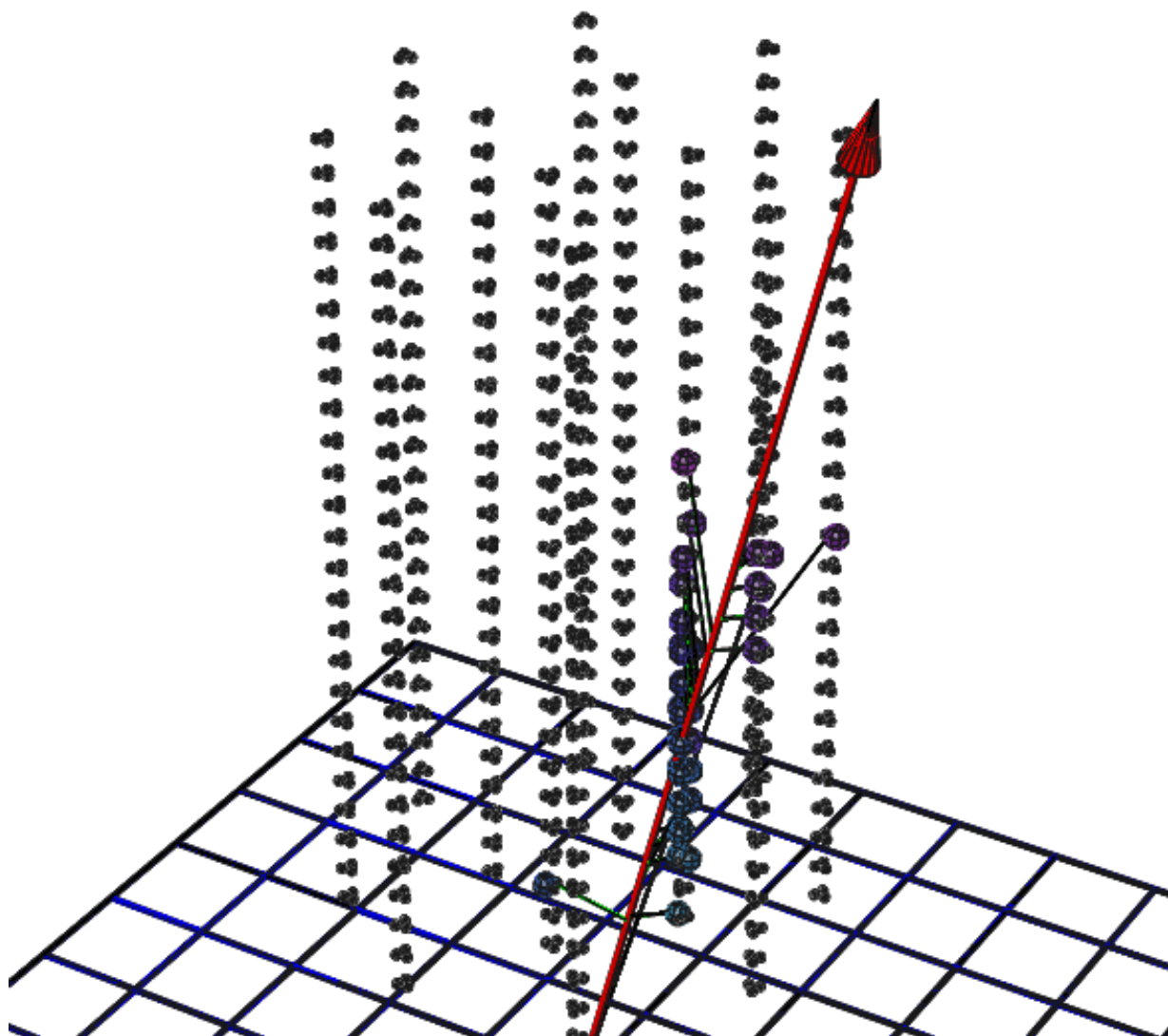


Figure 6.4: Visualisation of a simulated (muon-)neutrino event. The muon track traversing the detector is indicated by the red line. The optical modules with hits are enlarged in this view. The measured Cherenkov photons are drawn in green. The χ^2 distributions for this example event are shown in Figure 6.5.

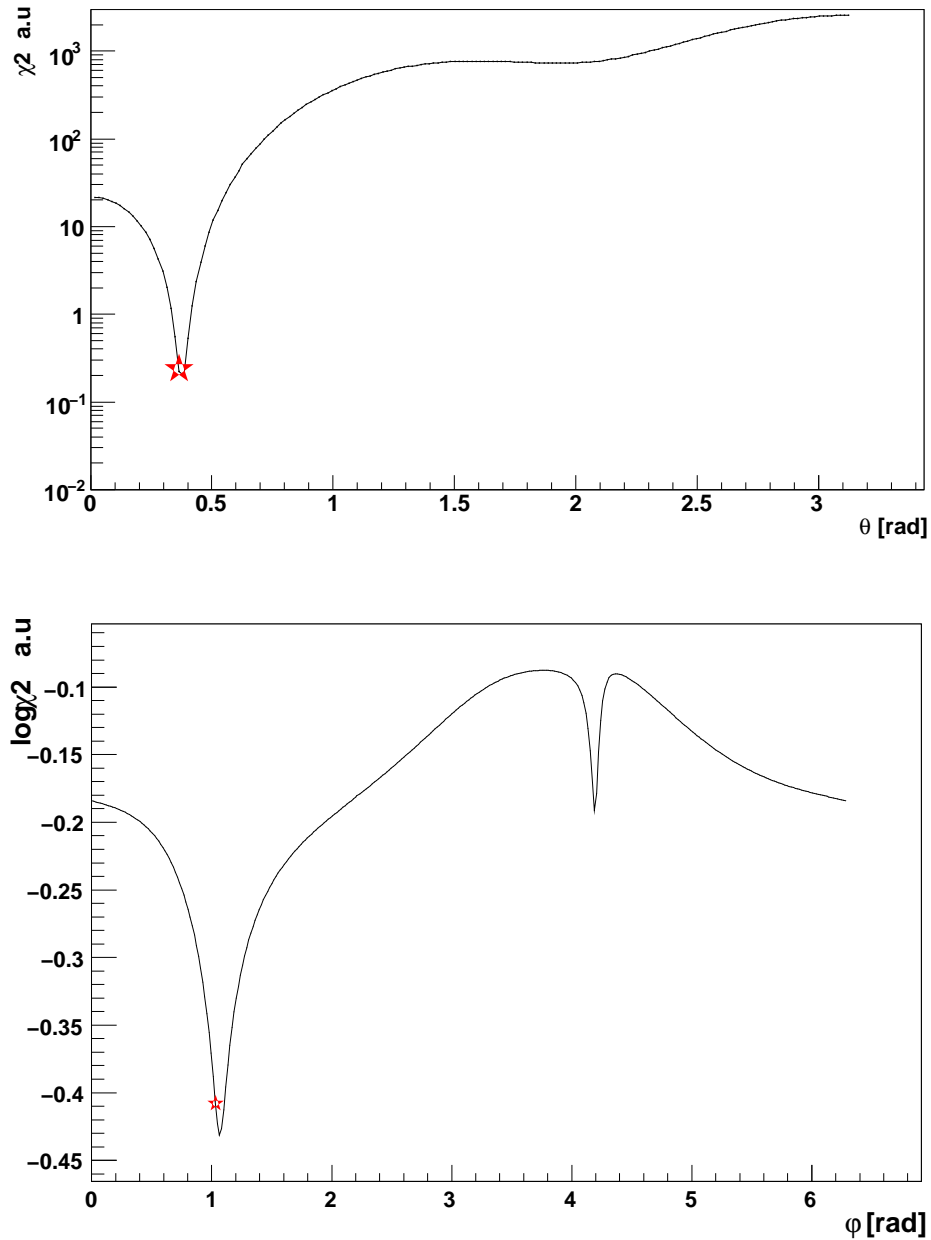


Figure 6.5: One-dimensional χ^2 distributions for the event depicted in Figure 6.4. The cumulative $\chi^2(\theta)$ function is shown together with the true zenith angle (θ_{true}), red asterisk (top). The global minimum θ_{opt} can be identified easily. The $\chi^2(\phi, \theta = \theta_{\text{opt}})$ function obtained by fixing the θ angle in the full directional χ^2 function is given in the bottom figure. Again the global minimum ϕ_{opt} (red asterisk) is immediately visible.

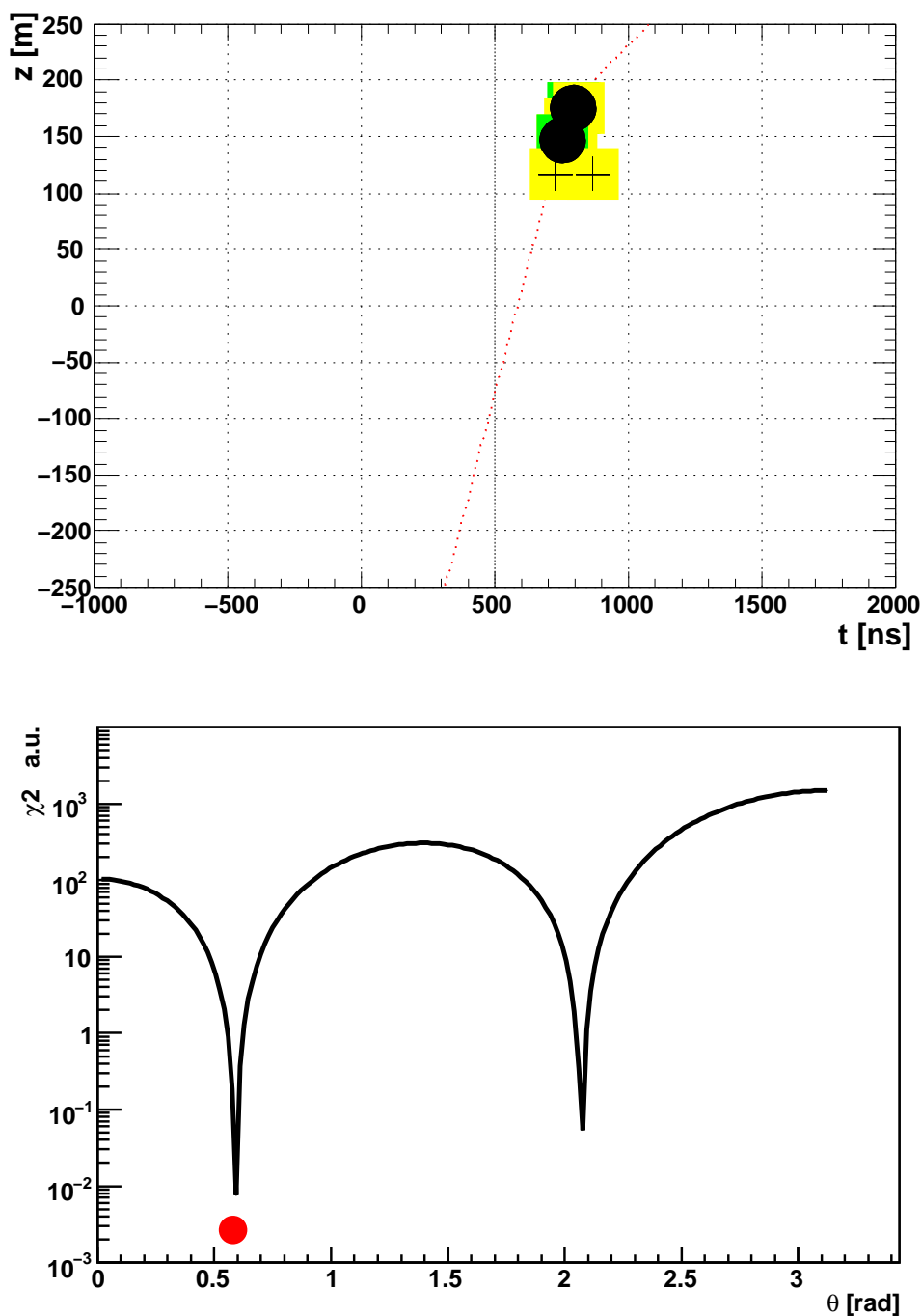


Figure 6.6: Illustration of ghost solutions to the fit problem. The linearisation allows analysing difficult hit pattern and can resolve ambiguities. The top figure gives an example of a hit pattern on a single string which is difficult to reconstruct. In the bottom plot, the one-dimensional $\chi^2(\theta)$ function for the example signature is shown. A second minimum (so-called ghost solution) is visible, located at a distance of twice the Cherenkov angle with respect to the true solution (red circle).

event topologies has still to be made. Since the same procedure can be applied to track and shower type events, an event or hit pattern classification based on this method seems feasible and deserves further attention. The method can also be used to filter hits for subsequent fitting stages.

6.4 Fitting with global optimisation algorithms

As described above, even relatively simple track quality estimators (as the χ^2 -function or the M-estimator) can create very complicated structures in the parameter space. This is especially true in case one includes models for background hits and light scattering into the track-estimator. The transformation of initial track-seeds and the iteration of the fitting in the likelihood algorithm ensure that a large part of the parameter space is scanned. In the standard likelihood fit, described in Section 6.2, the minimisation for each step is done using a standard gradient descend algorithm which makes use of the (analytically obtained) function derivatives. This procedure is therefore limited to the regions nearby the initial (transformed) track, and hence, despite the iteration over the transformed input tracks, there are still cases in which the fit does not converge to the global optimum.

Several alternative approaches to optimisation problems have been discussed in the literature. In particular, several algorithms have been proposed to scan the parameter space for the *global* optimum. These algorithms have been successfully applied to a large variety of problems. It is therefore interesting to study the performance of global optimisation algorithms applied to the event reconstruction for neutrino telescopes.

One powerful global minimisation algorithm is the simulated annealing [160] prescription. In this algorithm, stochastic elements are introduced by not only accepting *downhill* steps leading to an improvement of the objective function f , but also *uphill* steps with a probability given by $\exp(-\Delta f/T)$ (Metropolis criterion) where T is the *temperature* parameter. This gives the algorithm the chance to escape from local minima regions and allows for scanning the full parameter space. The temperature is decreased slowly during the iteration, which leaves the system time to converge to the global minimum. In this way, the algorithm resembles the annealing process of a hot metal, which is cooled out slowly to reach the ground state at the end of the process. In fact, one can prove by using the theory of Markov processes that the simulated annealing algorithm converges to the global optimum for finite problems in infinite time, if an appropriate cooling scheme is used [161].

Another popular global optimisation method is the particle swarm algorithm [162]. Here the parameter space is scanned by an ensemble of *particles* which move through the space according to a specific propagation law. A certain inertia weight is attributed to the particles, so that the initial particle velocity (step-length vector) is retained to some degree. Further components are added, which drive the particles towards the best individual positions they have encountered during their propagation and also towards the best global

position of the ensemble. This so-called standard particle swarm optimisation (SPSO) has been further refined by adding dissipative elements in order to prevent the system from stagnation at local extrema. The refined dissipative particle swarm (DPS) [162] introduces random shifts of the particles' locations and velocities occurring with a certain probability during the minimisation.

Studies have been conducted during this work in order to employ the simulated annealing as well as the dissipative particle swarm for the track reconstruction. As shown in [163], the simulated annealing algorithm implemented after Goffe et al. [164] leads to good results at the M-estimator level. However, it was observed [155] that the quality parameter for the fitted track tends to be better than for the true simulated Monte Carlo track. This clearly indicates the insufficient modelling of the track by the M-estimator. One has to bear in mind that this function does not include a detailed physics model, but is rather designed to provide a robust estimate for subsequent higher level fits. Without a detailed description of the underlying physics, it is difficult to remove the inherent ambiguities and a second step with a high level p.d.f. is therefore mandatory to reach a good resolution. In principle, one could use the result of the M-estimator fitted with a global optimisation algorithm plus a set of transformed tracks for the next reconstruction step. This ansatz, however, contradicts the spirit of global optimisation methods and is therefore not very attractive. On the other hand, a direct minimisation of the full likelihood is also feasible even though very time-consuming, since the computation of the likelihood function is rather expensive with respect to the consumption of CPU time. Compared to the standard track-fit, described in Section 6.2, in which the final likelihood function is evaluated only a few hundred times, the global optimisation requires much more function evaluations to raster the parameter space completely. The application of the simulated annealing algorithm in the final minimisation step in the standard likelihood function has been investigated but was found to lead only to marginal improvements in the fit quality. The particle swarm algorithm exhibits a similar performance. Here it was found that the algorithm can be improved by adjusting the weights of the global and individual extrema in the propagation law (see above) during the minimisation, such that at the end of the iteration the influence of the individual best function value vanishes and the contribution from the global extremum dominates.

The observed minimal improvements in the fit resolution are expected to depend on the Monte Carlo description of the input parameters for the probability density function. Since the level of agreement between Monte Carlo and data has not yet reached a completing state, it was refrained from using global minimisation algorithms in this study. Instead, the standard algorithm, described above, which performs the reconstruction much faster, has been used. It is however thinkable to refit samples of selected events with global algorithms in the future to improve the resolution of the track reconstruction further.

Part IV

Pointing verification

—

Moon-shadow analysis

The final part of this thesis is devoted to the verification of the detector pointing by measuring the Moon shadow in cosmic rays. A motivation for the study as well as a panorama on related methods is provided in Chapter 7. A detailed Monte Carlo simulation including all relevant effects is evaluated in order to derive the expected significance of the shadow effect. First data of the completed ANTARES telescope are analysed and the results are discussed in Chapter 8.

Chapter 7

Moon-shadow simulation

The calibration of the absolute orientation of the ANTARES telescope is performed by long-baseline low-frequency acoustic triangulation of the line anchors with a DGPS reference on the sea surface with a precision of about 0.2° . This procedure is complicated and involves transformations between several coordinate systems. Any misalignment of the ANTARES telescope represents a systematic error for point-source searches. Therefore, it is important to establish an independent method which allows for verifying the absolute pointing of the instrument. One possible method relies on the detection of the shadow that is casted by the Moon in cosmic rays. Another possibility, which is under discussion, would require the installation of a dedicated sea-surface detector array. In this chapter, the Moon-shadow effect will be investigated with the help of a detailed Monte Carlo simulation. Especially in view of the expenses necessary for the installation of a large-area sea-surface detector, it is important to quantify the potential of the Moon-shadow method thoroughly.

7.1 Detector pointing

For any optical telescope, knowledge of the exact pointing is crucial, needless to say, same holds true for neutrino telescopes. A precise pointing improves the angular resolution of the telescope by limiting systematic errors. This allows suppressing background by narrowing the search region as well as it facilitates attributing signals correctly to known objects, which is important, e.g. for point-source searches based on predefined candidate source catalogues derived from independent observations. ANTARES adopts a complicated global alignment procedure, described in Section 3.5.3, which involves many coordinate systems and corresponding transformations between them. Systematic studies indicate a precision of about 0.2° , which is of the same order as the angular resolution of the telescope for high-energy up-going neutrino-induced muons. A verification of the detector pointing by an independent method is thus very important. Unfortunately, neutrino telescopes cannot yet resort to a standard “neutrino candle” for the calibration of the detector pointing. However, the absolute orientation of the detector can be independently checked by looking at a deficit in the flux of down-going atmospheric muons in the direction of the Moon (the “Moon shadow”), or by searching coincidences between atmospheric shower events in a detector at the sea surface and down-going muons in the telescope. The latter method would require the installation of a dedicated detector at the sea surface, which is currently

under discussion for ANTARES [165]. A third alternative method is based on the study of the angular modulation in the down-going muon flux due to the rock slope of the coast (“cliff shadow”). Simulations have been performed, indicating that the effect should be visible in the data [166]. However, as of this writing, a precise assessment of the capability of this method has not been undertaken. If successfully conducted, all three methods allow for the verification of the detector pointing up to the very final analysis stage, thereby ensuring that all the different transformation have been done correctly. In the following, the potential of the Moon-shadow method will be quantified based on a detailed simulation which determines the significance of the effect in the ANTARES data.

7.2 The Moon shadow in cosmic rays

In 1957, G.W. Clark pointed out that the Moon casts a shadow in the isotropic flux of cosmic rays [167]. The Moon is opaque to cosmic rays, therefore a deficit should occur in the direction of the Moon. In ANTARES only muonic remnants of cosmic-ray-induced air showers are seen, therefore this translates into a deficit of muon events from the direction of the Moon. The detection of the Moon shadow has by now become a standard measurement for cosmic-ray experiments. A summary of observations of the Moon shadow by different experiments is given in Table 7.1. However, it has to be mentioned that the observation is still a difficult task, since the Moon, with an average angular diameter of 0.52° , covers only a tiny fraction ($\approx 10^{-5}$) of the sky and the angular resolution of the experiments is typically larger than the angular size of the Moon disk, thus the measurement requires careful scrutinisation of the data. Actually, the shadow effect was only observed in the 90s when experiments reached a certain angular resolution.

For a first assessment it might be helpful to consider a simplified model of the shadow effect. A more elaborate definition of the significance for the detection of the effect is presented below, here we assume the case that the angular resolution σ_{ang} is of the order of $\approx 1^\circ$ which is larger than the radius R_{Moon} of the Moon disk. Then, we simply define the significance to be the number of missing events $d = \rho\pi R_{\text{Moon}}^2$, where ρ denotes the number of events per solid angle, divided by the statistical fluctuations in the measurement bin determined by the angular resolution. A measure of these fluctuations is given by the variance $\sigma = \sqrt{\rho\pi\sigma_{\text{ang}}^2}$, therefore

$$\mathcal{S} = \frac{d}{\sigma} \approx \frac{\rho\pi R_{\text{Moon}}^2}{\sqrt{\rho\pi\sigma_{\text{ang}}^2}} = \sqrt{\rho\pi} \frac{R_{\text{Moon}}^2}{\sigma_{\text{ang}}} = \sqrt{\rho_0\pi} \frac{R_{\text{Moon}}^2}{\sigma_{\text{ang}}} \sqrt{T}, \quad (7.1)$$

where we have introduced the event density per unit time ρ_0 and the observation time T . From Equation 7.1, one can see that

- the effect scales with the square root of the live time. And,
- is inversely proportional to the angular resolution.

An important point, which becomes obvious from Equation 7.1, is that the significance has to be optimised as a trade-off between statistics and angular resolution. Any quality cut that will improve the angular resolution will reduce the statistics, therefore the analysis cut has to be optimised carefully. This point is addressed in Section 7.4.4.

7.3 Simulation of the Moon-shadow effect

In this section, a detailed simulation will be presented which includes the interaction of the cosmic-ray primaries with the atmosphere, the air-shower development, in particular the angle between primary and secondary muon(s), the impact of the geomagnetic field during the propagation of primaries and secondary muons as well as the resolution of the reconstruction after optimised analysis cuts are applied. From the sample of reconstructed muon events generated by the simulation, the point-spread function (see Section 7.3.4 for a definition) will be extracted. The point-spread function can be used to derive the expected distribution of muon events around the direction of the Moon centre.

The analysis presented in this chapter is restricted to simulations for the complete ANTARES 12-string detector and makes use of the detailed likelihood reconstruction described in Chapter 6. Studies of smaller geometries [179] as well as of other reconstruction algorithms [180] have shown that in other cases only marginal effects can be expected.

7.3.1 The CORSIKA Moon simulation

The detailed simulation of the Moon-shadow effect comprises several parts. In the first part, a full simulation of the cosmic-ray-induced air shower is performed. This simulation is based on the CORSIKA algorithm, see Section 3.6. This algorithm has been modified for the generation of events in a circular bin around the Moon centre. Additionally, the cosmic primary particles are tracked through the magnetic field of the Earth to the interaction point. In the subsequent evolution of the air shower, the geomagnetic field is taken into account by the CORSIKA program. The simulation chain then follows the path described in Chapter 3 up to the detector response simulation. Thereafter, a simulation of the data-filter (trigger) efficiency is performed. Finally, the selected events are reconstructed using the KM3Tray framework presented in Chapter 5.

The CORSIKA Moon program [181] generates the primary particles in a circular bin around the Moon centre with a 10° radius. In this way, the simulation allows for a slight dependence of the reconstruction quality on the direction of the incident events caused by the particular detector geometry. In addition, CORSIKA Moon calculates the deviation of the primary particles in the geomagnetic field before the interaction point. The number of generated primary air showers for different zenith angles, primary nucleons and energies is given in Table 7.2.

Experiment	Technique	Altitude /depth	Threshold [TeV]	Rate [Hz]	Total events	Area	Density	σ	Resolution
CYGNUS [168]	EAS	2100 m	50	4	238389	$\pm 5^\circ$	2400	4.9	0.8° (+0.17°, -0.12°)
CASA [169]	EAS	1220 m	100	12	$4.7 \cdot 10^6$	$\pm 12^\circ$	2820	4.7	0.77° (+0.14°, -0.10°)
Tibet [170]	EAS	4300 m	7(mode)	20	$1.09 \cdot 10^6$	$\pm 8^\circ$	5750	5.8	0.87° (+0.13°, -0.10°) pointing err < 0.2°
Tibet As γ [171]	EAS	4300 m	3	640	$1.5 \cdot 10^{10}$	$\pm 5^\circ$		40	0.9° pointing err < 0.2°
ARGO-YBJ [172]	EAS	4300 m	5(median)	4000	$2.2 \cdot 10^5$	$\pm 6^\circ$		10	0.51°
HEGRA [173]	EAS	2200 m	50	8.5		$\pm 5^\circ$	1400	6	0.82° \pm 0.1°
	Cherenkov			(12 - 14)			/10 ⁻⁴ sr		
L3+C [174]	Underg μ	72 mwe	0.065 - 0.1	400	$6.71 \cdot 10^5$	$\pm 10^\circ$	2366	5.5	0.3 \pm 0.07
			> 0.1				2956	8.3	0.22 \pm 0.05
Soudan2 [175]	Underg μ	2200 mwe	6 - 15	0.24	$33.5 \cdot 10^6$	$\pm 10^\circ$	2444	5	0.29° alignment < 0.15°
MINOS-far [176]	Underg μ	2070 mwe	≈ 10	0.5			970	4.3	0.41 \pm 0.06 pointing 0.3 \pm 0.07
MACRO1 [177]	Underg μ	3140 mwe	10	0.22	$2.3 \cdot 10^5$	$\pm 10^\circ$	730	3.6	0.9° \pm 0.3°
MACRO2 [178]	Underg μ	3140 mwe	10	0.25	$4.1 \cdot 10^5$	$\pm 10^\circ$	1300	6.5	0.55° \pm 0.05°

Table 7.1: Observation of the Moon shadow by different experiments.

$0^\circ < \theta < 60^\circ$			
primary nucleus	1 – 10 TeV/nucleon	10 – 100 TeV/nucleon	100 – 10^5 TeV/nucleon
p	$6.0 \cdot 10^9$	$2.0 \cdot 10^8$	$5.0 \cdot 10^6$
He	$2.0 \cdot 10^8$	$5.0 \cdot 10^6$	$2.5 \cdot 10^5$
N	$3.0 \cdot 10^7$	$5.0 \cdot 10^5$	$5.0 \cdot 10^4$
Mg	$1.27 \cdot 10^7$	$5.0 \cdot 10^5$	$1.0 \cdot 10^4$
Fe	$5.0 \cdot 10^6$	$2.0 \cdot 10^5$	$1.0 \cdot 10^4$

$60^\circ < \theta < 85^\circ$			
primary nucleus	1 – 10 TeV/nucleon	10 – 100 TeV/nucleon	100 – 10^5 TeV/nucleon
p	$6.0 \cdot 10^9$	$2.0 \cdot 10^8$	$5.0 \cdot 10^6$
He	$4.0 \cdot 10^6$	$2.0 \cdot 10^7$	$5.0 \cdot 10^5$
N	$3.0 \cdot 10^7$	$1.0 \cdot 10^6$	$5.0 \cdot 10^4$
Mg	$1.25 \cdot 10^7$	$5.0 \cdot 10^5$	$2.5 \cdot 10^4$
Fe	$5.0 \cdot 10^6$	$2.5 \cdot 10^5$	$1.0 \cdot 10^4$

Table 7.2: Number of generated air showers in the CORSIKA Moon simulation.

7.3.2 Primary flux

The absolute normalisation of the muon flux can be obtained from the Hörandel model [182] which provides a parameterisation of the cosmic-ray flux for different cosmic-ray primaries. In the simulation a simplified model with only five mass groups is used [92]. The flux for each group can be expressed by

$$\frac{d\Phi_Z}{dE} = \Phi_Z^0 E_0^{\gamma_Z} \left[1 + \left(\frac{E}{\bar{E}_Z} \right) \right]^{(\gamma_c - \gamma_Z)/\epsilon_c}, \quad (7.2)$$

where the parameters Φ_Z^0 , γ_Z and \bar{E}_Z are the absolute flux at 1 TeV/nucleon, the spectral index and the cut-off energy (knee) respectively, depending on the specific mass group. The variables $\gamma_c = -4.7$ and $\epsilon_c = 1.87$ characterise the change in the spectrum at the cut-off energy \bar{E}_Z and are identical for all primary particles. The values of the parameters are detailed in Table 7.3.

	γ_Z	Φ_Z^0 [m ² sr s TeV ⁻¹]	E_Z [GeV]
p	-2.71	$8.73 \cdot 10^{-2}$	$4.5 \cdot 10^6$
He	-2.64	$5.71 \cdot 10^{-2}$	$9.0 \cdot 10^6$
CNO	-2.68	$3.24 \cdot 10^{-2}$	$3.06 \cdot 10^7$
Mg-Si	-2.67	$3.16 \cdot 10^{-2}$	$6.48 \cdot 10^7$
Fe	-2.58	$2.18 \cdot 10^{-2}$	$1.17 \cdot 10^8$

Table 7.3: Parameters of the Hörandel model used in the CORSIKA Moon simulation.

7.3.3 Influence of the geomagnetic field

Charged particles are deflected in the magnetic field of the Earth. The deflection angle $d\alpha$ of a particle with momentum \mathbf{p} after having passed a short distance dl in the magnetic field \mathbf{B} is given by

$$d\alpha = Z \frac{|\mathbf{p} \times \mathbf{B}|}{p^2} dl. \quad (7.3)$$

In the simulation, this relation is used to evaluate the deflection of the cosmic primary on the trajectory from the Moon to the interaction point in the atmosphere [183]. The distance between the Moon and the interaction vertex is divided in small intervals where the magnetic field is computed by the International Geomagnetic Reference Field (IGRF) model [184]. The partial deflection angles, given by Equation 7.3, are then added to obtain the total deflection of the particle. Figure 7.1 shows the angular deflection of primary protons in the geomagnetic field depending on the energy of the incident proton. The influence of the geomagnetic field on a 10 TeV proton is rather small, the average deflection angle is less than 0.1° . The overall impact of the magnetic field on the point-spread function for muons detected with ANTARES is therefore also small.

7.3.4 The point-spread function and the shape of the shadow

This section deals with the calculation of the shape of the Moon shadow based on the simulation presented in the previous section. This function is of central importance for the following analysis. First, the point-spread function (abbreviated p.s.f.) $f(\delta\theta, \delta\psi)$ is extracted at the final analysis level. The point-spread function describes the distribution of the differences in direction between the reconstructed muon track and the initial primary. It is a function of the differences in the zenith angle θ and the differences in ψ , where $\psi = \phi \sin \theta_{\text{primary}}$. The angle ψ is used rather than the azimuth ϕ , since the solid angle $d\Omega$ can be approximated by $d\Omega = \sin \theta d\theta d\phi = d\psi d\theta$. Therefore, the distribution of the point-spread function becomes symmetric in ψ and θ , provided that the reconstruction error is not too large and not too much biased by the detector geometry. By construction, the point-spread function contains information about the scattering angle between primary and the muon produced in the air shower, the geomagnetic field effect, propagation effects, and the angular resolution of the reconstruction after analysis cuts have been applied. Figure 7.2

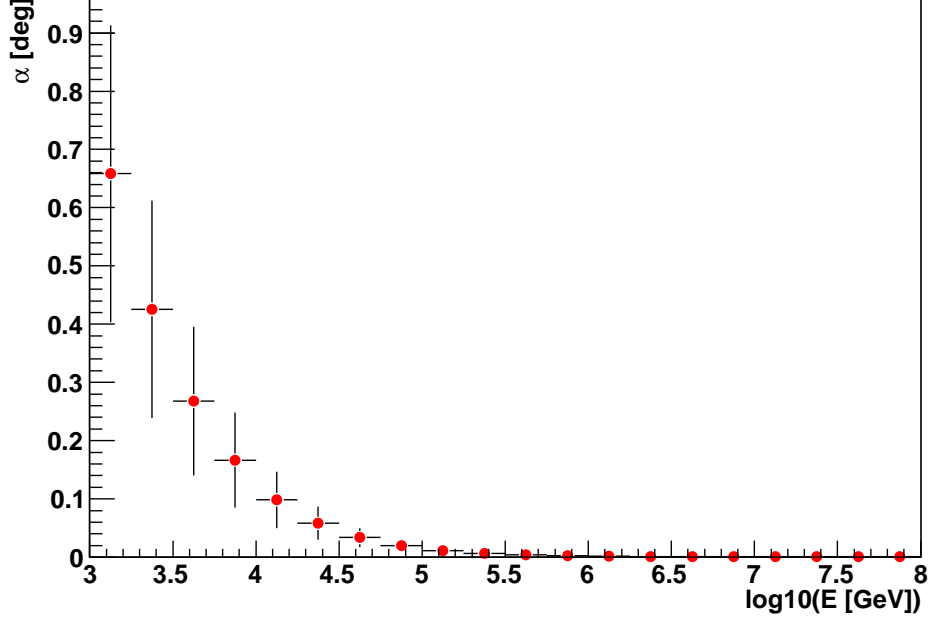


Figure 7.1: Deflection of the primary proton in the geomagnetic field versus energy. The error bars indicate the spread of the deflection.

shows the p.s.f. at the final analysis level after the cut discussed in Section 7.4.4. The shape of the Moon shadow is defined as the ratio of the muon density n^{H_1} with the shadow effect and the muon density n^{H_0} for the full flux without the shadow effect at the coordinates $(\delta\theta, \delta\psi)$ with respect to the Moon centre,

$$s(\delta\theta, \delta\psi) = \frac{n^{\text{H}_1}}{n^{\text{H}_0}} = \frac{n^{\text{H}_0} - n^{\text{shadow}}}{n^{\text{H}_0}} = 1 - \frac{n^{\text{shadow}}}{n^{\text{H}_0}}. \quad (7.4)$$

The shape function s is related to the point-spread function since

$$n^{\text{shadow}}(\theta, \psi) = N_0 \frac{1}{C} \int f(\theta - \theta', \psi - \psi') \chi_{\text{Moon}}(\theta', \psi') d\Omega', \quad (7.5)$$

with $\chi_{\text{Moon}} = 1$ on the Moon and $\chi_{\text{Moon}} = 0$ elsewhere. The normalisation is given by

$$C = \int \int f(\theta - \theta', \psi - \psi') \chi_{\text{Moon}}(\theta', \psi') d\Omega' d\Omega \quad (7.6)$$

and

$$N_0 = \rho \Omega_{\text{Moon}} = \rho \pi R_{\text{Moon}}^2, \quad (7.7)$$

with the event density ρ . As can be seen in Figure 7.3, the distribution exhibits a sharp dip at the Moon centre.

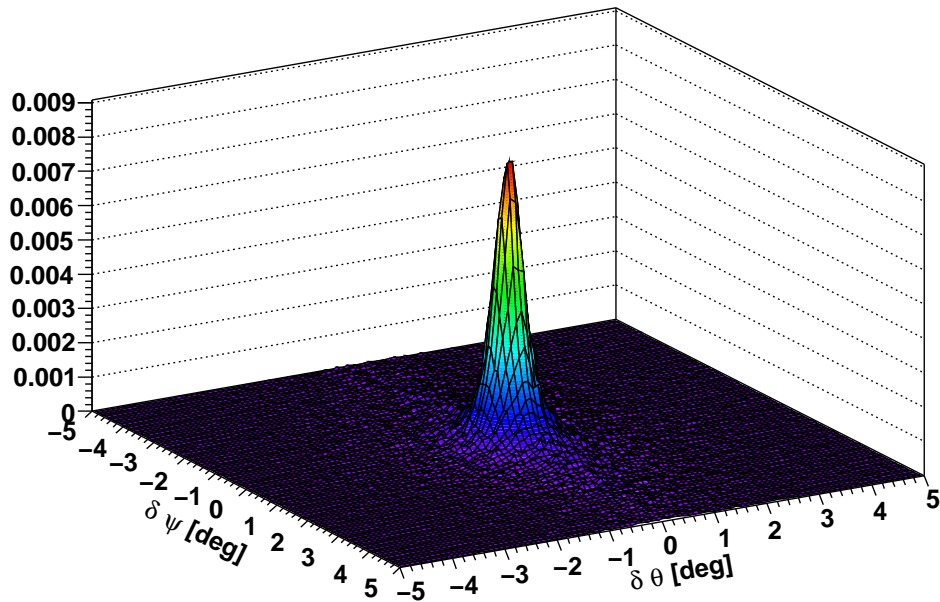


Figure 7.2: Point-spread function at the final analysis level.

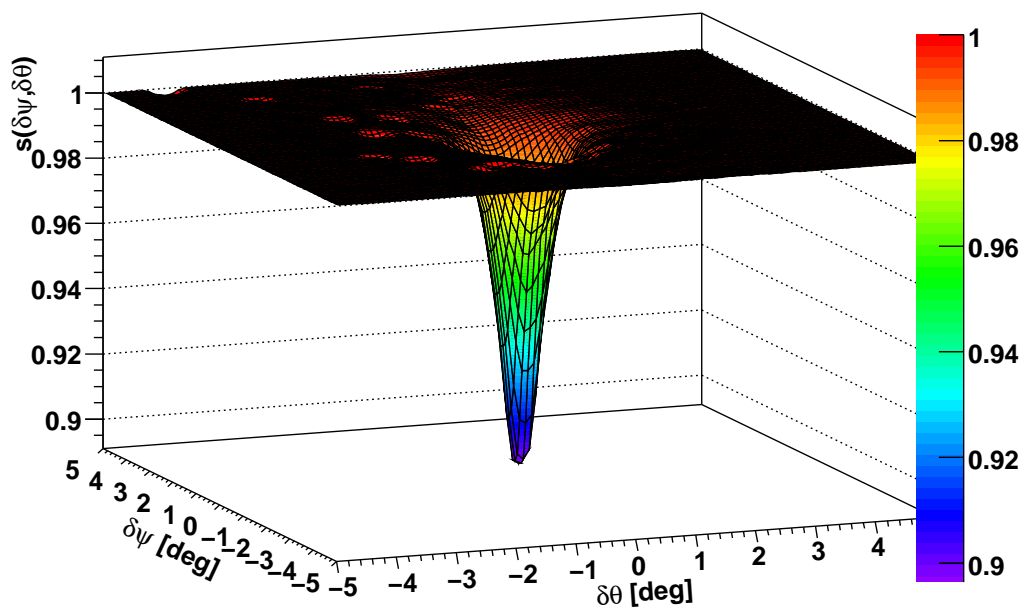


Figure 7.3: Shape of the Moon shadow. Calculated from the above p.s.f..

7.4 Evaluation of the expected significance

In this section, the expected significance is calculated from the shape function extracted from the simulation. The following calculations performed to estimate the expected significance of the shadow effect rely on the theory of hypothesis tests. The relevant concepts of this subject are therefore briefly summarised (based on the review [185]) and the terminology that is used throughout the discussion is introduced.

7.4.1 Hypothesis tests

In general, a hypothesis test provides a rule to distinguish between several possible hypotheses depending on the outcome of a measurement by defining acceptance or rejection criteria. In this context, a hypothesis is a statement about the distribution of the data. A *simple* hypothesis specifies the distribution completely without remaining free parameters, whereas in the more general case of a *composite* hypothesis several parameters might be present. The decision whether to accept or to reject a given hypothesis is made in a statistical test, which is a rule (or a set of cuts) specifying precisely when to accept or rejected a given hypothesis. During this decision process two different errors can occur. Rejecting the hypothesis H_0 if it is true is called an *error of the first kind*. The corresponding probability is called the significance level α of the test. Conversely, if H_0 is accepted although it is false, this is called an *error of the second kind*. The probability β for this to occur depends on the alternative hypothesis H_1 , and $1 - \beta$ is called the power of the test to reject H_1 . It is of course desirable to avoid both kind of errors, thus α and β are preferably to be kept small. However, in general minimising one kind of error results in accepting a larger probability for the other kind. In practice, a compromise has to be found and commonly the significance level is set to a predefined accuracy. Often rather than using the full data sample one tries to condense the relevant information into a convenient scalar parameter which defines a so-called test statistic t . Then the acceptance region for a certain hypothesis corresponds to a specific range of values of t .

In order to apply the above formalism to the Moon-shadow analysis we define:

- H_0 (null hypothesis): The detector is badly misaligned, no shadow is visible.
- H_1 (alternative): The detector is perfectly aligned, the Moon shadow is visible.

The probability distributions are specified completely for the two hypotheses without remaining free parameters. Therefore this is a simple test. In the following an appropriate test statistic is defined. The expected significance will then be extracted from the separation of the distributions of the test statistic for the two hypotheses. The probability for measuring at least a certain significance α for the shadow effect is given by the power $1 - \beta$ of the hypothesis test as can be seen from Figure 7.4.

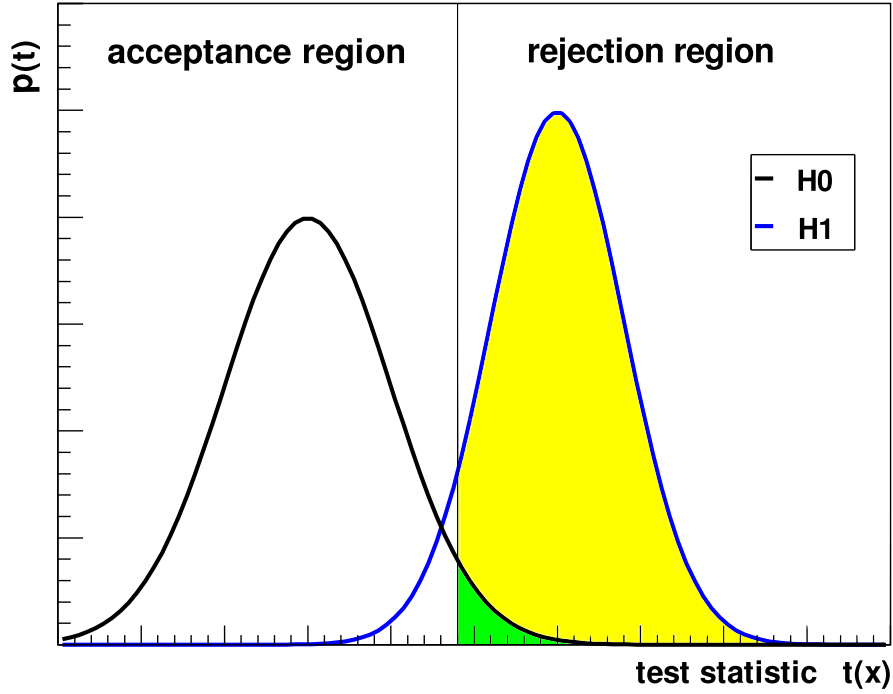


Figure 7.4: Interpretation of the significance α (green) and the power $1-\beta$ (yellow) as areas in the rejection region under the probability distribution $p(t|H_0)$ (black) and $p(t|H_1)$ (blue) respectively.

7.4.2 Definition of the test statistic

In this paragraph, a test statistic based on an unbinned approach will be defined, which can be proven to be optimal under certain assumptions as explained below. This test statistic has the additional benefit that it allows for asymmetric p.s.f.s. For a start, let $p(\delta\theta, \delta\psi|H_0)$ be the probability density function (p.d.f.) for observing an event within a view region Ω_{View} at coordinates $(\delta\theta, \delta\psi)$ in case hypothesis H_0 is true and $p(\delta\theta, \delta\psi|H_1)$ be the probability density for observing an event at the same coordinates in case of H_1 . Then, the joint p.d.f.s (also commonly called likelihood functions) of n independent measurements are given by the product of the individual p.d.f.s:

$$P(x|H_1) = \prod_{i=1}^N p(\delta\theta_i, \delta\psi_i|H_1), \quad (7.8)$$

and

$$P(x|H_0) = \prod_{i=1}^N p(\delta\theta_i, \delta\psi_i|H_0) \quad (7.9)$$

respectively. According to the Neyman-Pearson lemma [186] the optimal test statistic is given by the likelihood ratio

$$\lambda(x) = \frac{P(x|H_1)}{P(x|H_0)}. \quad (7.10)$$

For technical reasons given below we will use the logarithm of Equation 7.10 rather than λ directly. The test statistic can be expressed in terms of the shape function $s(\delta\theta, \delta\psi)$ introduced in Section 7.3.4:

$$\begin{aligned} t(x) &= \log \frac{P(x|H_1)}{P(x|H_0)} = \log \prod_{i=1}^N \frac{p(\delta\theta_i, \delta\psi_i|H_1)}{p(\delta\theta_i, \delta\psi_i|H_0)} \\ &= \sum_{i=1}^N \log s(\delta\theta_i, \delta\psi_i) - N \log\left(1 - \frac{\Omega_{\text{Moon}}}{\Omega_{\text{View}}}\right). \end{aligned} \quad (7.11)$$

This equation is central for the following discussions. The last term in Equation 7.11 ensures a proper normalisation of the test statistic. It reflects the fact that the expected number of events in case of no shadowing is higher than in case of shadowing. By construction, the last term gives an overall positive contribution to the test statistic, as the logarithm is always negative. Thus an increase in the number of events favours hypothesis H_1 whereas a lack of events favours H_0 and disfavors H_1 as expected.

In order to prove the last step in Equation 7.11, we consider the p.d.f.s for the hypotheses H_0 and H_1 in a region around the Moon centre with a solid angle Ω_{view} . The p.d.f.s can be obtained from the event densities n^{H_0} and n^{H_1} respectively. For $k = (0, 1)$

$$p(\delta\theta, \delta\psi|H_k) = \frac{n^{H_k}(\delta\theta, \delta\psi)}{N^{H_k}}. \quad (7.12)$$

Where $N^{H_0} = \rho\Omega_{\text{view}}$ and $N^{H_1} = \rho(\Omega_{\text{view}} - \Omega_{\text{Moon}})$. With these definitions, one can calculate

$$\begin{aligned} \log \frac{p(\delta\theta, \delta\psi|H_1)}{p(\delta\theta, \delta\psi|H_0)} &= \log \frac{n^{H_1}/N^{H_1}}{n^{H_0}/N^{H_0}} = \log \frac{n^{H_1}}{n^{H_0}} \frac{N^{H_0}}{N^{H_1}} \\ &= \log \frac{n^{H_1}}{n^{H_0}} + \log \frac{N^{H_0}}{N^{H_1}} = \log s + \log \frac{\rho\Omega_{\text{View}}}{\rho(\Omega_{\text{View}} - \Omega_{\text{Moon}})} \\ &= \log s - \log\left(1 - \frac{\Omega_{\text{Moon}}}{\Omega_{\text{View}}}\right). \end{aligned} \quad (7.13)$$

Incidentally, we note that the use of the logarithm in Equation 7.10 allows for the approximation of the test statistic distribution with a Gaussian distribution by virtue of the central limit theorem (see e.g. [187, 188]): If independent random variables x_1, x_2, \dots are distributed according to any p.d.f.s with finite means and variances, then the sum $y = \sum_i^n x_i$ will have a p.d.f. that approaches a Gaussian for large n . The mean and variance of y are given by the sums of corresponding terms from the individual x_i .

7.4.3 Expected significance of the shadow effect

The probability of observing the shadow effect is now calculated using a hypothesis test in which the two hypotheses H_0 and H_1 are examined. A sample of measurements for each of the two hypotheses is simulated for a fixed observation time in order to derive the corresponding probability distributions of the test statistic, which are then used to calculate the probability for observing the shadow effect at a predefined significance level and the expected significance for a given observation duration. The simulations are performed for live times in the range from 1 year to 5 years at twenty different equidistant interval points starting at 1 year. A sample of 2000 measurements is generated according to the hypotheses H_0 and H_1 . For each measurement the test statistic is evaluated and histogrammed. Example distributions of the test statistic and a corresponding Gaussian fits for an observation time of 1 year are shown in Figure 7.5. From the separation of the two probability density functions of the test statistic $p(t|H_0)$ and $p(t|H_1)$ with means $\mu(H_0)$, $\mu(H_1)$ and standard deviations $\sigma(H_0)$, $\sigma(H_1)$ respectively, the expected significance and the test characteristic can be extracted. The expected significance corresponding to a probability of 50% is given in units of standard deviations by

$$\mathcal{S}_{\text{exp}} = \frac{\mu(H_1) - \mu(H_0)}{\sigma(H_0)}. \quad (7.14)$$

The results for the simulated measurements for different live times are shown in Figure 7.6. A few small fluctuations due to numerical issues are visible, however, the measurements follow the expected $\propto \sqrt{T}$ behaviour very well as indicated by the fit. The parameterised form of the test characteristics is given by

$$\text{TC}(t) = \begin{pmatrix} \alpha \\ 1 - \beta \end{pmatrix} (t) = \begin{pmatrix} \int_t^{+\infty} p(t'|H_0)dt' \\ \int_t^{+\infty} p(t'|H_1)dt' \end{pmatrix}. \quad (7.15)$$

The test characteristics describes the probability for measuring the shadow effect at least with a certain significance, see also Figure 7.4. The final result of the analysis is summarised in Figure 7.7 and Figure 7.8. From the intersection of the test characteristics with the 3σ -line, one can derive the probabilities for a 3σ (or higher) detection after different live times, detailed in Table 7.4. After a live time of 2 years the expected significance (see Figure 7.8) reaches about 3 standard deviations. One can therefore conclude that the Moon-shadow effect is observable with ANTARES, although a certain statistics has to be accumulated first.

observation time	1 a	2 a	3 a	4 a	5 a
probability	15%	55%	78%	94%	98%

Table 7.4: Probabilities for a 3σ (or higher) detection of the Moon-shadow effect with ANTARES after different observation times.

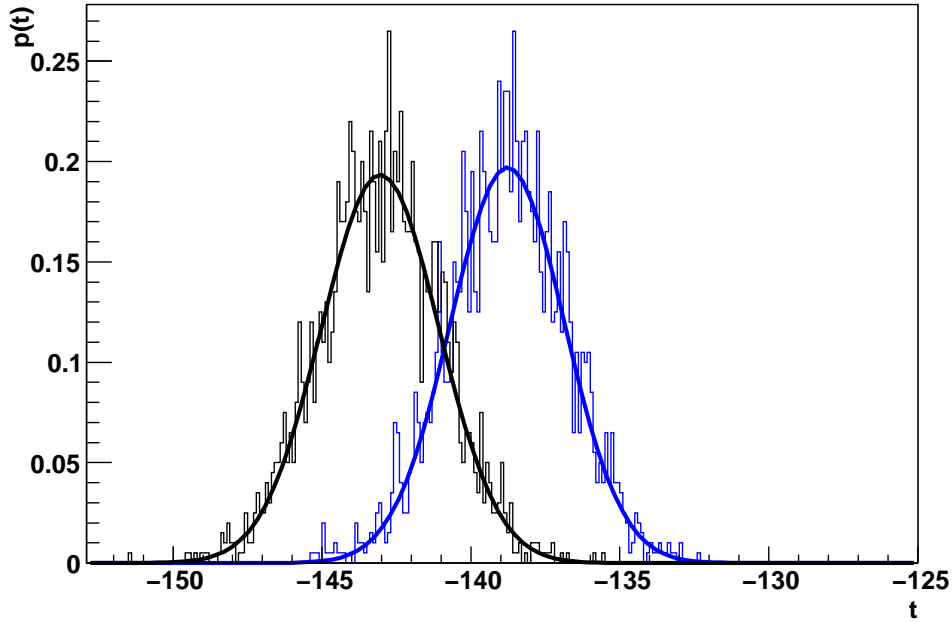


Figure 7.5: Simulated distributions of the test statistic for the hypotheses H_0 (black) and H_1 (blue) after one year of observation. The fitted Gaussians (see text) are indicated in addition.

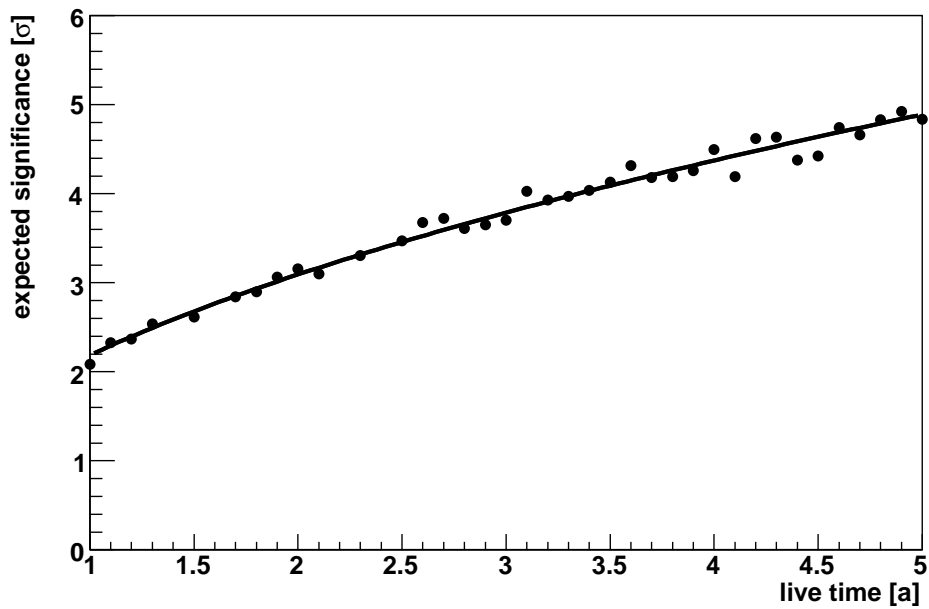


Figure 7.6: Expected significance for the detection of the Moon-shadow effect vs. live time. Each point represents a simulation result for a given observation time. A fit $\propto \sqrt{T}$ of the expected significance is indicated.

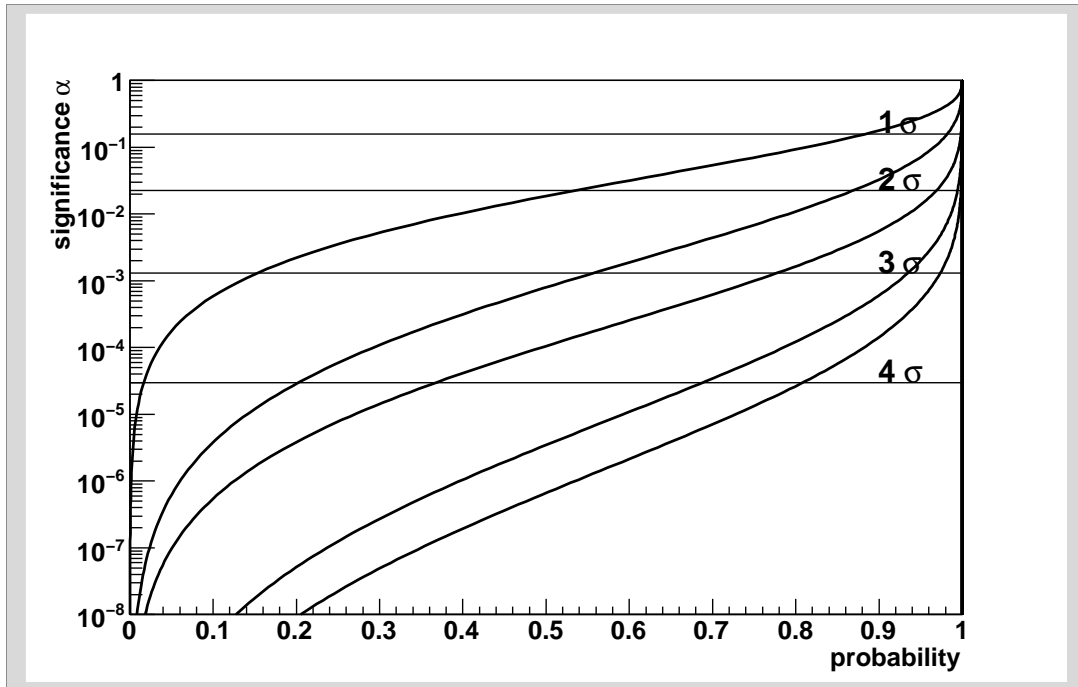


Figure 7.7: Probability of measuring at least a certain significance after 1 (top), 2, 3, 4 and 5 (bottom) years. Horizontal lines indicate the significance level in units of standard deviations.

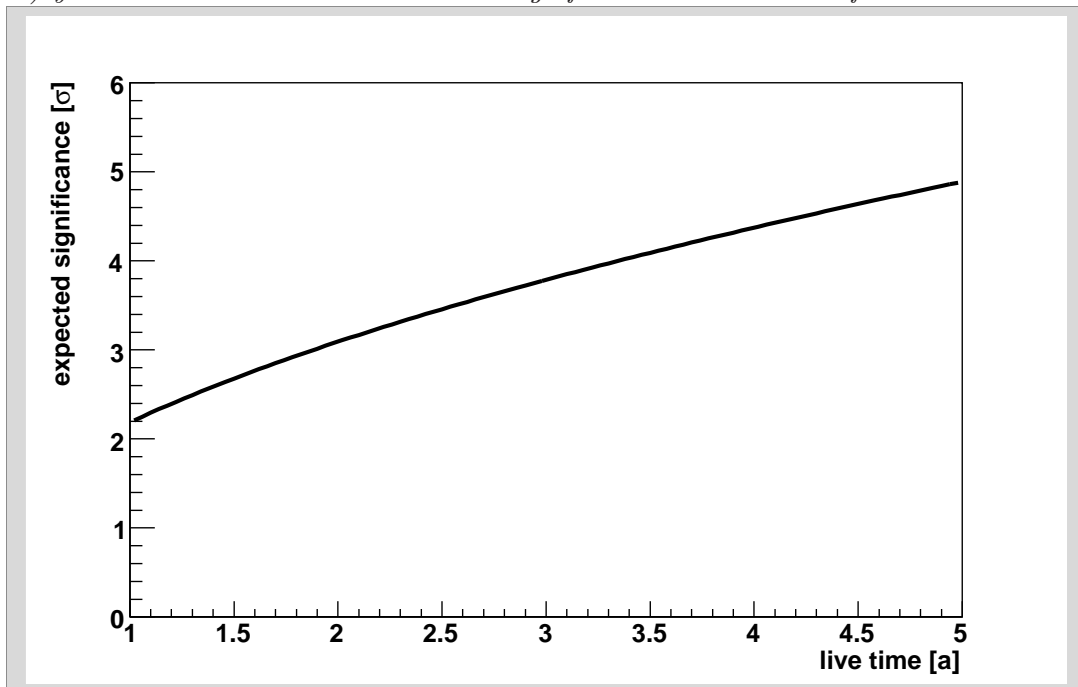


Figure 7.8: Expected significance (in units of standard deviations) for the observation of the Moon-shadow effect with ANTARES as a function of the data-taking time. The effect scales with the square root of the observation time, after 2 years the 3σ level is reached.

7.4.4 Optimisation of the analysis cut

As we have already mentioned, the significance for the detection of the Moon shadow depends on the angular resolution and on the available statistics. Quality cuts can be used to improve the angular resolution of the reconstruction, however, they will also reduce the statistics N of the data sample. For a Gaussian point-spread function with angular resolution σ , we expect that the significance \mathcal{S} scales according to $\mathcal{S} \propto \sqrt{N}/\sigma$. A direct handle on the reconstruction quality is given by the Λ parameter described in Chapter 6. The point-spread function for a given quality cut on the Λ parameter and the number of events passing the cut were evaluated for several cut values in the range from -7.0 to -5.2 . The results are shown in Figure 7.9, where the expected significance is plotted against the cut parameter. The optimal cut which maximises the expected significance of the detection is found to be

$$\Lambda \geq -5.8. \quad (7.16)$$

For looser quality cuts the angular resolution gets worse, for stricter cuts the statistics deteriorates. The optimal cut value has been used to obtain the results presented in the previous section.

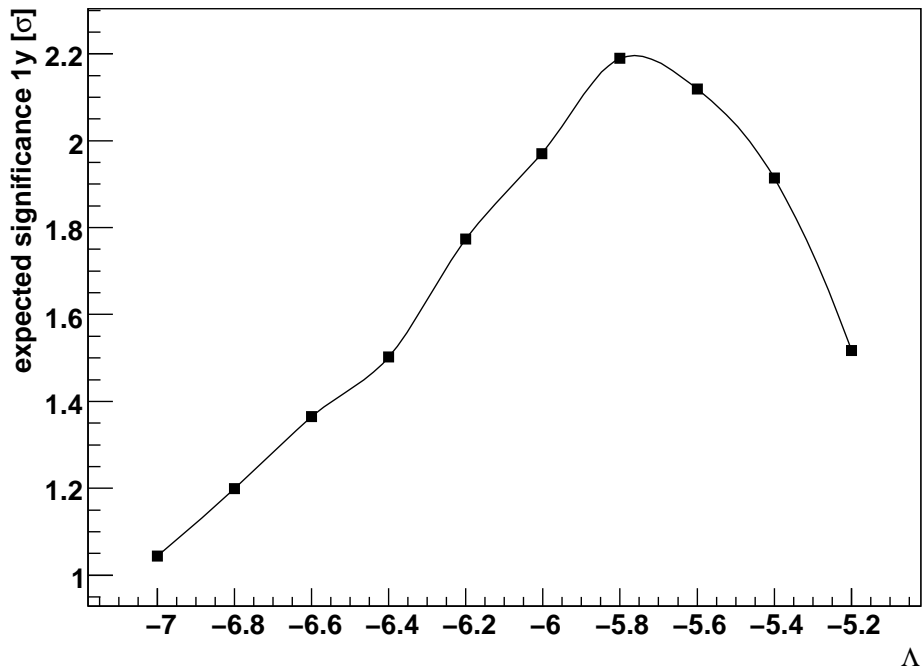


Figure 7.9: Optimisation of the quality parameter cut. The expected significance is computed as a function of the Λ parameter cut from -7.0 to -5.2 in steps of 0.2 . The line is drawn to guide the eye. The optimal value is found at $\Lambda = -5.8$.

7.4.5 Comparison with previous analyses

The Moon-shadow effect has been subject to investigations before in ANTARES. In the first discussions in [189] and [190], a Gaussian point-spread function with an angular resolution of 1° has been assumed and the result for the expected significance is a factor of two smaller compared to the result in the present analysis. The expected significance evaluated in this thesis is comparable with the result obtained in the study [191] in which a binned test statistic has been used and which did neither include trigger inefficiencies nor the geomagnetic field effect. Further an unoptimised quality cut of $\Lambda \geq -6.0$ was used.

7.5 Effect of a misalignment on the Moon shadow

Any misalignment of the telescope will result in a distortion of the shadow effect. The impact of a 0.5° misalignment on a point source (e.g. the Moon-centre position) over the course of one year is illustrated in Figure 7.10. It is important to note that the point source is not merely shifted in the misaligned detector frame, but instead follows a time dependent path. The reason for this phenomenon lies in the non-commutativity of the involved coordinate transformations. To take account of possible misalignments, an additional transformation of the measured event coordinates has to be included in the analysis. This transformation maps from the misaligned frame onto the correct frame and can be found by optimising the measured significance of the shadow effect.

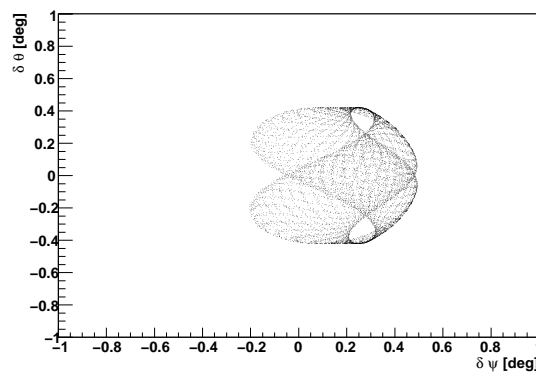


Figure 7.10: *This figure shows the impact of a 0.5° -misalignment on a point source. The deviations $(\delta\theta, \delta\psi)$ from the (time-dependent) nominal coordinates in the detector frame are recorded over a period of one year.*

7.6 Conclusions and outlook

The performed calculations indicate that the Moon-shadow effect is visible with ANTARES. The simulation predicts an expected significance for the effect of about 3σ after a live time of 2 years. These values are derived under the assumption of a perfectly orientated detector. If the shadow effect is not visible after 2 years a detailed study including the correction for misalignments has to be performed. The impact of any misalignment is beyond the scope of this work and has to be addressed in further studies. The study can also be extended to include the effect of the Sun shadow. The Sun covers about the same angular region on the sky as the Moon. However, the influence of the magnetic field is much more difficult to calculate for the Sun.

Chapter 8

Moon-shadow data analysis

In the analysis described in this chapter, in a figurative sense, the ANTARES telescope will be pointed at the Moon, and the first months of data taken since the completion of the instrument in May 2008 will be scrutinised for a deficit of muon tracks from the direction of the Moon. The analysis chain presented in Chapter 5 is used to reconstruct muon tracks from the raw data recored by the telescope. The coordinate calculations for the determination of the Moon position in the detector frame are expounded. The relevant on-source data, defined by the sample of muon tracks coming from a circular region around the Moon's centre, are analysed. Differences between the Monte Carlo simulation and the conditions in the data processing are addressed.

8.1 Coordinate calculations and transformations

In the following analysis, the Moon position on the sky is first calculated in Equatorial coordinates at the time of every registered event, then transformed into the detector coordinate system, and finally compared to the direction of the reconstructed event in order to extract the distribution of events coming from the direction of the Moon. This method is reciprocal to the procedure adopted in point-source searches, in which the direction of the reconstructed track or shower is transformed to the Equatorial coordinate system and then compared with the coordinates of objects in a predefined catalogue or analysed in terms of correlation and clustering.

Since only theoretical Moon coordinates are transformed and event coordinates are left untouched in the detector frame, any accidental unblinding¹ of data, which might be relevant for other analyses, is excluded at the outset. With respect to the low statistics for point-source searches, blinding policies are to be strictly obeyed. For the Moon-shadow analysis, however, a blinding of event coordinates is not necessary, as the shadow is localised at a well-defined unique place. The verification of the correctness of the detection can be proven afterwards by evaluating the significance of the effect and by comparing with the prediction of the Monte Carlo simulation presented in the previous chapter.

¹A blind analysis is a measurement performed without looking at the answer in order to reduce any experimental bias. See [192, 193] for more information.

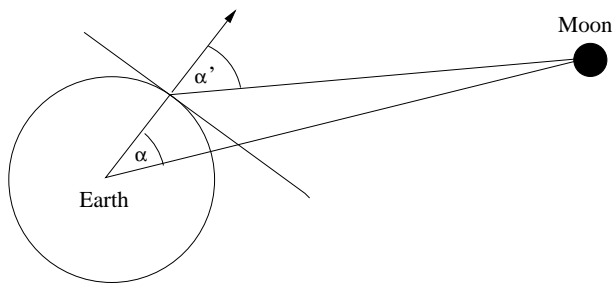


Figure 8.1: *The geocentric parallax. The Moon appears under a different angle in the topocentric horizon system as in the geocentric system. The mean difference between the angles α and α' is about 0.95° .*

Another advantage of transforming the Moon coordinates into the detector frame is that any misalignment of the detector frame can be conceptually easier corrected for in the analysis by a simple additional transformation.

8.1.1 Conversion of the event time

Every event registered in the ANTARES detector is assigned a UTC time. The UTC time is the coordinated civil time derived from the revolution of the Earth and due to irregularities in the movement of the Earth not fully synchronised to the dynamical timescale (Barycentric Dynamical Time, TDB) used in the computation of ephemerides of solar system bodies (planets and satellites). In fact, the UTC time differs from the dynamic time by several leap seconds. Currently, the difference amounts to about 1 min. This effect is important for the precise calculation of the Moon position as the Moon moves with $0.5''/s$ in the Equatorial system and due to the rotation of the Earth the Moon coordinates move in the detector frame with an angular velocity of

$$\omega = \frac{\delta\phi}{\delta t} = \frac{360^\circ}{24 \cdot 60 \text{ min}} = 0.25^\circ \text{ min}^{-1}, \quad (8.1)$$

which is an even larger effect, corresponding to about the size of the Moon's radius per minute. Therefore, it is important to account for the difference of the time scales.

8.1.2 Calculation of the Moon coordinates in the horizon system

The geocentric positions of the Moon are calculated with the Meeus algorithm [194] provided by the SLALIB package [195]. This algorithm reaches accuracies of $10''$ in longitude, $3''$ in latitude and 20 km in distance which is more than sufficient for the needs of the present analysis. The SLALIB function DTT can be used to obtain the difference between the UTC time and the dynamic time. This does not include the latest leap seconds, but is sufficient for the needs of the present analysis.

The SLALIB package offers functions to convert from the geocentric equatorial coordinates into the topocentric horizon system². The conversion allows for the geocentric

²In the present analysis the SLALIB function RD_PLAN has been used which gives the Moon coordinates directly in the horizon system.

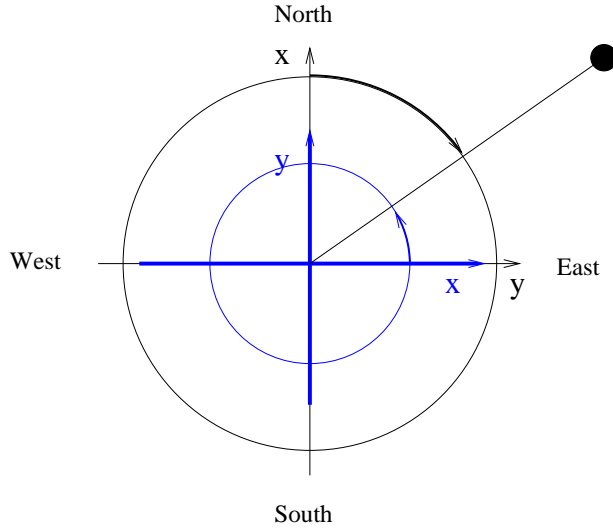


Figure 8.2: The conventional topocentric horizon system (black) used in the SLALIB package differs from the detector coordinate system (blue). The azimuth angle ϕ in the conventional system is measured from North, counted clock-wise, the corresponding angle in the detector system is counted counter-clock-wise with respect to East. The additional UTM meridian convergence correction is **not** indicated, see text for further details.

parallax, an important effect, as the mean geocentric parallax for the Moon corresponds to about 0.95° . The effect is explained in Figure 8.1.

8.1.3 Transformation into the detector frame

In the final step, the topocentric coordinates (azimuth and elevation) are transformed into the detector frame. The detector coordinate system is based on the UTM system [196] which differs from the topocentric system by the orientation of the x and y axes as illustrated in Figure 8.2. The definitions of the coordinate axes with respect to the point of the compass are

- SLALIB: $(x, y, z) = (\text{North}, \text{East}, \text{Up})$. And,
- ANTARES = UTM: $(x, y, z) = (\text{Easting} \approx \text{East}, \text{Northing} \approx \text{North}, \text{Up})$.

Since the UTM coordinate system is obtained by a projection of the coordinates on the Geoid onto a cylinder the transformation is not fully isogonic and (in general) the UTM northing (y -axis) does not exactly point towards North. In the transformation from the SLALIB to the UTM system a (constant) angular correction on the azimuth angle depending on the exact location of the detector has to be applied. This angle is commonly termed meridian convergence and is calculated to be 1.93° at the ANTARES site [197]. Hence the full transformation of the azimuth angle from the conventional horizon system to the ANTARES UTM detector frame is given by

$$\phi_{\text{UTM}} = 90^\circ - \phi_{\text{SLALIB}} - 1.93^\circ \quad (8.2)$$

This conversion is reverse to the conversion needed for the point-source search analyses. The distribution of the azimuth and zenith angles of the Moon in the detector system at the ANTARES site for the year 2008 are shown in Figure 8.3. For other time spans the distributions look only slightly different.

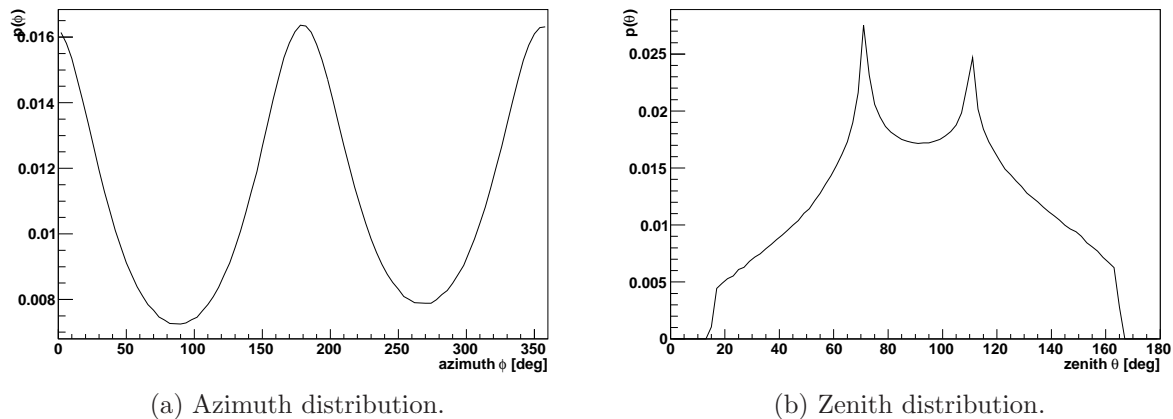


Figure 8.3: Distribution of the Moon position (azimuth and zenith distance) in the detector system for the year 2008 calculated with the SLALIB package [195]. For other time spans the distributions look only slightly different.

8.2 Reprocessing of raw data

The raw data recorded by the ANTARES DAQ system has to be reprocessed before any high-level analysis can be performed. The reprocessing includes the calibration of the low-level raw data based on optimised calibration sets and the reconstruction of the events using high-level reconstruction algorithms.

8.2.1 Selection of physics data

The ANTARES data from the completion of the instrument in May 2008 till March 2009 have been calibrated and reconstructed using the reconstruction chain in the KM3Tray software framework described in Chapter 5. The mass reconstruction was performed at the Erlangen computer cluster. Due to the cable fault in June 2008, which caused a down-time of approximately two months, the accumulated statistics is lower than expected. Periods with high optical noise and a few calibration and test runs reduce the on-time of the instrument further. The total live time of the data accumulated in the selected physics runs from May 28th, 2008 till March 22nd, 2009 amounts to 132 days.

In the selected period, all of the available physics runs have been reconstructed and included in the analysis. On the one hand, the reconstruction quality will be degraded in runs with high optical background. On the other hand, excluding such runs will reduce the statistics further, which means a trade-off between statistics and reconstruction quality needs to be made in order to optimise the run selection. This, however, is a difficult general issue and cannot be addressed in this thesis. The reconstruction makes use of dedicated calibration sets (so-called offline calibration, see Section 5.2.2 in Chapter 5) and is therefore

conducted with optimal charge and time calibration. Unfortunately the precise alignment information was not available in due time and could therefore not be used during the reconstruction. Instead, the nominal geometry that is assumed by the data filter (where the strings are assumed to be strictly vertical) had to be used. The results presented in this chapter are therefore preliminary and a full agreement with the Monte Carlo simulation presented in Chapter 7 cannot be expected. Differences between data and simulation are addressed in Section 8.3.1.

8.2.2 Data reduction and related preparatory work

In this section, the technical details of the final analysis are briefly discussed. This section can serve as an illustration of the data processing at the final analysis level in KM3Tray and might be helpful when the Moon-shadow analysis is repeated in the future with better statistics.

After the processing of the raw data with the KM3Tray software chain described in Chapter 5 the low-level maxi-DST data are stored in an “i3” file. (XML based file format.) The whole production consumes several TBytes of disk space. Therefore, efficient reduction of the reconstructed data is necessary for further analysis. In a first step, important variables relevant for the Moon-shadow analysis are extracted. This includes the reconstruction information as well as the calculated Moon coordinates. The information is then stored in a compact form in a HDF5 file. The following programs are utilised in the final analysis.

- An n-tuple builder implemented in `moon_ntuple.py` reads the low-level data and extracts the relevant parameters for the analysis into a HDF5 file. This program is an example of a KM3Tray module written in Python. (See Chapter 5.)
- The Python class implemented in `moon_coordinates.py` provides the Moon coordinates in the detector frame used by the n-tuple builder script.
- The final analysis module `moon_analysis.py` reads the high-level data and executes the analysis.

The same n-tuple builder program has also been used to extract the information from the Monte Carlo production analysed in Chapter 7.

8.3 Data analysis

8.3.1 Comparison between data and Monte Carlo

Since the analysis presented in this chapter is the very first one based on the 12-line data, a full agreement between data and simulation cannot be expected. The differences between

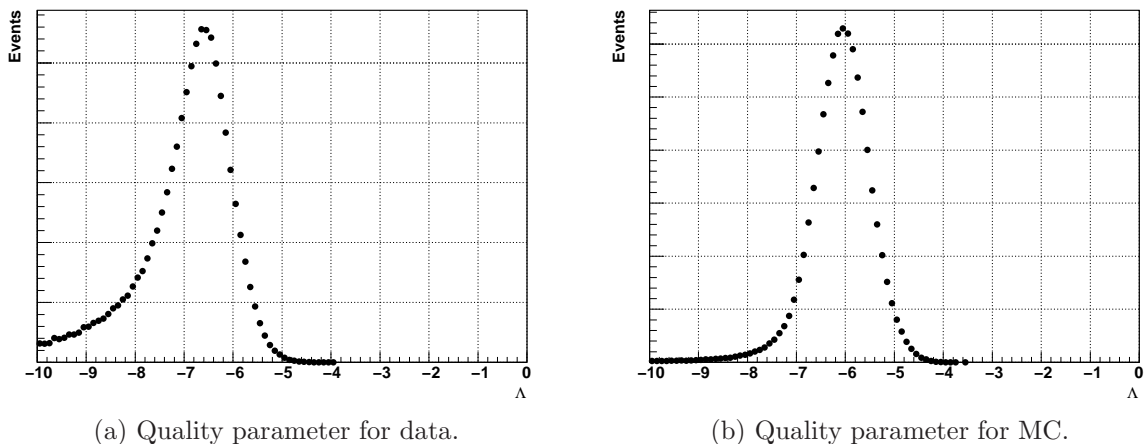


Figure 8.4: Comparison between the quality parameter distributions for data and simulation.

the Monte Carlo simulation and the data reconstruction which cannot be resolved at the moment are:

- Missing alignment information: The full alignment of the detector was not available for the reprocessing and the reconstruction was performed based on the assumption of strictly vertical lines. The assumption of a nominal geometry is sufficient for the data filter and the online reconstruction algorithm, but clearly limits the reconstruction quality in the full likelihood fit.
- Dead channels (defunct optical modules, inoperable lines) are not simulated. This can be accomplished by removing hits from the full Monte Carlo simulation. A detailed list of dead channels reflecting the real data taking conditions has still to be worked out.
- Although the background rates have been inserted according to observed background rates in real data runs, the conditions in data and simulation are slightly different. More faithful background rates have to be evaluated for the data period used in the production.

The impact of these effects needs careful study. The most important variable which is used to control the reconstruction quality is the Λ parameter described in Chapter 6. A comparison of this parameter between data and Monte Carlo is shown in Figure 8.4. As the alignment information is not available, the reconstruction quality for the data sample is degraded compared to the Monte Carlo and a clear shift between the two distributions is visible. The analysis has to be redone once the full alignment information and a more detailed Monte Carlo simulation which includes the missing channels and the faithful single PMT background rates is available and the differences can be better understood.

8.3.2 The on-source region

The on-source region is defined as the circular region comprising points with angular distance to the Moon centre smaller than 3° . The following analysis cuts are applied to the data sample:

- The Moon should be visible above the horizon in the detector frame at the time of the event.
- The event should be reconstructed as down-going.
- A reconstruction quality of $\Lambda > -5.8$ is required.

The first two requirements are obvious and almost equivalent for events in the on-region. The quality cut has been tuned with the Monte Carlo in Chapter 7, distributions for other cuts have been studied as well, but the results presented in the following are obtained with the abovementioned cut. After the cuts are applied, 2578 events survive in the on-source region.

The distribution of the azimuth and zenith angle for events in the on-region in the detector frame is shown in Figure 8.5. As a consistency check, the calculated Moon coordinates are shown in addition in the graphs (blue histogram). The azimuth angle distribution exhibits the expected shape. The Moon rises in the East ($\phi = 0^\circ$), culminates in the South ($\phi = 270^\circ$), the Moonset is located in the West ($\phi = 180^\circ$) and the Moon is invisible below the horizon in the North ($\phi = 90^\circ$). The modulation in the azimuth angle is due to the variations in the telescope acceptance caused by the detector geometry. The zenith angle distribution is influenced by the distribution Figure 8.3b, but is dominated by the zenith angle dependence of the atmospheric muon flux. One should note that the Moon never fully reaches the zenith (see Figure 8.3b).

In order to visualise the muon flux from the direction of the Moon the number of observed events is plotted against the solid angle in a circular region around the Moon centre. The distribution is shown in Figure 8.6. The bin size has been chosen to roughly correspond to the angular resolution. The expected distributions for the two hypotheses H_0 and H_1 are evaluated with the Monte Carlo simulation and are depicted in addition. In the case that the shadow is invisible, the expected event density is flat. (Straight line in Figure 8.6.) The black histogram shows the expected distribution for the alternative. The statistics is not yet sufficient and a shadow effect cannot be observed at the moment.

The distributions of the test statistic for the two hypotheses have been computed for the observed event density and are shown in Figure 8.7. At the moment, as expected, the two hypotheses are hardly distinguishable.

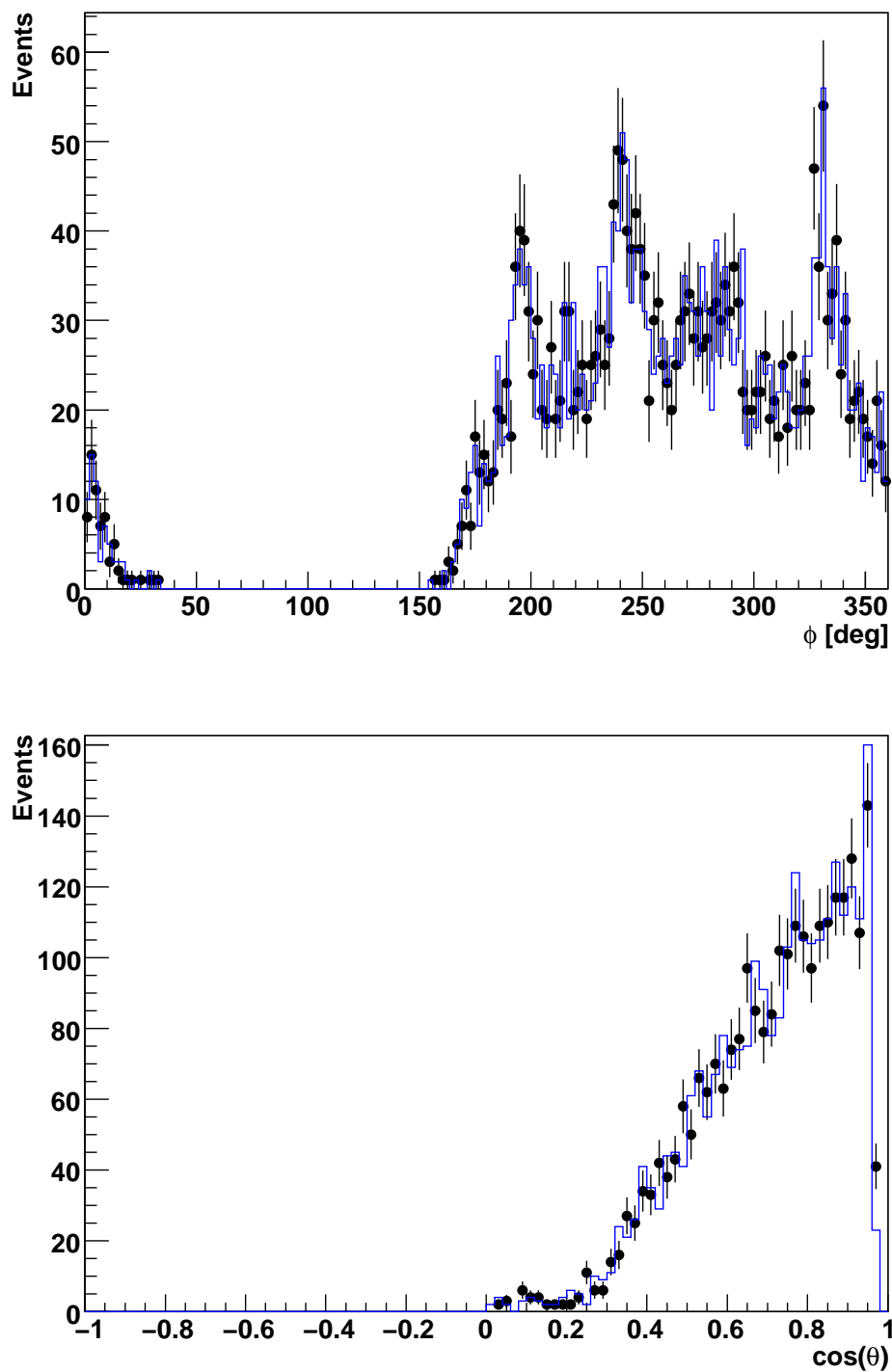


Figure 8.5: Azimuth (top) and zenith angle (bottom) distributions (black data points) for events in the on-region. As a consistency check, the corresponding calculated Moon coordinate distributions are shown in addition.

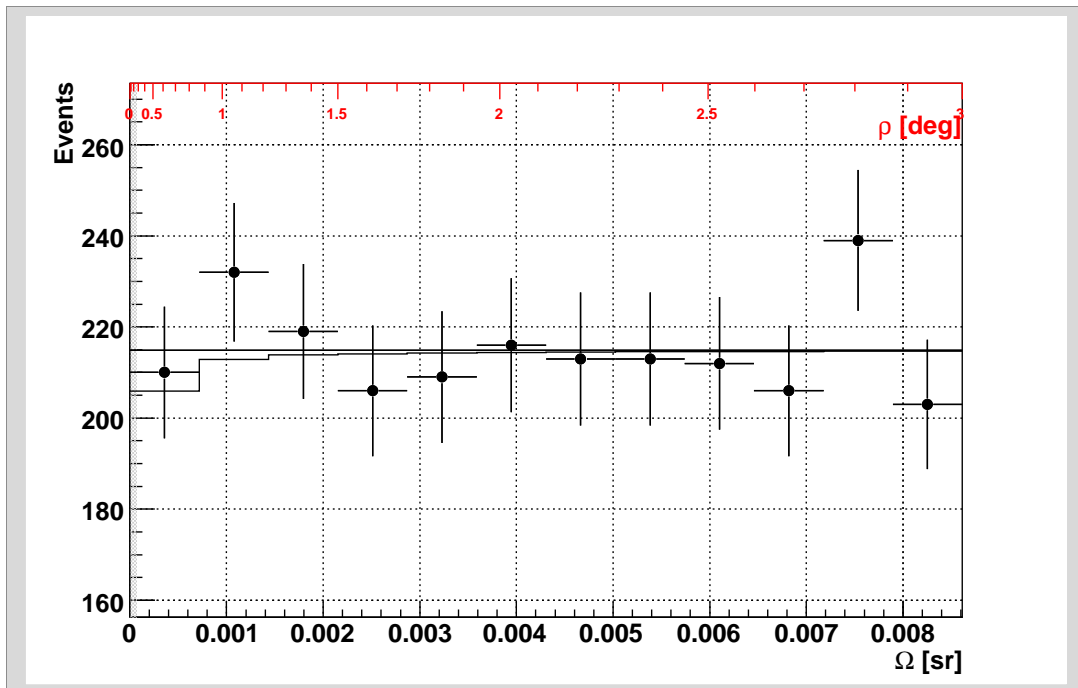


Figure 8.6: Number of events versus solid angle Ω (bottom scale) in a circular region with radius ρ (top scale) around the Moon centre. In addition, the expected event numbers for the two hypotheses are shown. The horizontal line gives the expected event density for H_0 , which is constant. The solid histogram represents the expectation for the alternative H_1 .

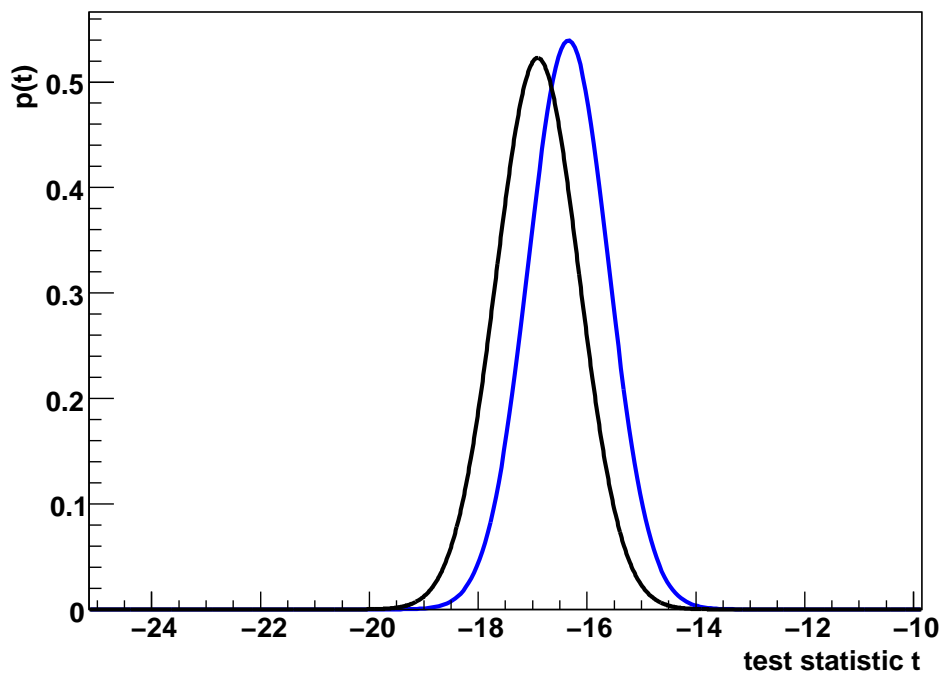


Figure 8.7: Test statistic for the two hypotheses H_0 (black), no shadow visible, and H_1 (blue), shadow visible, corresponding to the observed event density after 132 days. At this stage the two hypotheses are hardly distinguishable.

8.4 Conclusions

A first mass reconstruction with the data taken by the completed ANTARES detector has been done based on the preparatory work presented in Chapter 5. From a technical standpoint, it was demonstrated that all of the essential algorithms are present and the new software framework is well adapted for ANTARES data processing and analysis. The performed reconstruction is not limited to the Moon-shadow study presented in this chapter, but can be used for other analyses as well.

In the Moon-shadow analysis, physics data taken by the ANTARES telescope since the connection of the last string in May 2008 to March 2009, corresponding to a total live time of 132 days, have been used. At the current stage the analysis is still preliminary, as the full detector alignment information is missing (since not available in due time) and an idealistic nominal detector geometry had to be assumed instead. Therefore the reconstruction quality in the data sample is degraded compared to the Monte Carlo. Furthermore, the impact of dead channels and inoperable lines could not be addressed in the presented study. A more realistic simulation including the dead channels and more faithful background rates is necessary and (partly) already in preparation.

A first look at the on-region did not reveal the shadow effect yet. The present statistics does not allow for an observation of the effect. However, the fundamental analysis chain for the Moon-shadow analysis has been set up and can be used in the future to detect the Moon shadow once sufficient statistics has been accumulated.

Once a fully reliable reconstruction is available and a good agreement between Monte Carlo simulation and data is reached, it is worthwhile to include the Sun-shadow effect into the analysis. This can be done without any additional work; and by combining the two effects, a significant observation could be reached in a considerably shorter time. It has also been proposed to design a specialised trigger in order to improve the efficiency for events coming from the direction of the Moon and the Sun. Taking into account that the optimisation of the analysis in Section 7.4.4 has lead to a rather strict quality cut, it is however questionable that a dedicated trigger can improve the expected significance of the shadow effect any further.

Summary and outlook

As we have seen in Chapter 1 and Chapter 2, neutrino telescopes are an emerging field that may provide important clues to solutions of fundamental problems in astroparticle physics in the near future. The main goal is to address the question of the origin of charged cosmic rays and to reveal the so far well-concealed cosmic accelerators, which are presumably sources of high-energy neutrino beams as well. In the most promising TeV – PeV energy range for the detection of neutrino point sources, the concept of optical-Cherenkov telescopes immersed in the deep sea or in the glacial polar ice represents the designated technique. Moreover, complementary methods aiming at the detection of ultra-high energy neutrinos, above the EeV scale, based on radio, air-shower, or acoustic techniques are studied in addition.

Albeit a significant excess above the atmospheric neutrino background could not yet be observed by the current generation of instruments, there are first vague indications [38] of possible point sources reported recently by the Super-Kamiokande collaboration, which of course have to be verified with new data and improved statistics. More importantly, instruments, which are currently under construction as IceCube or the envisaged KM3NeT project in the Mediterranean, reach sensitivities which are in the range of the predicted neutrino fluxes. Hence, a very exciting hunt for the first high-energy cosmic neutrino is already initiated and within the forthcoming years the sky will be probed deeply for cosmic neutrino sources.

This thesis has been conducted in the context of the ANTARES project (described in Chapter 3), featuring a neutrino telescope of 0.03 km³ size with about 900 photosensors in the Mediterranean, 40 km off the city of Toulon at the French coast in a depth of 2475 m and currently the most sensitive instrument to observe the Southern hemisphere of the sky with direct view on the galactic centre. As it started during the construction phase of ANTARES, the main focus of this thesis has been on calibration and development work.

In Chapter 4, the charge calibration studies for the ANTARES front-end chip (ARS) conducted during this work have been described. The charge calibration permits translating the measured charge of a PMT pulse into the number of photoelectrons released at the photocathode and thus to (indirectly) deduce the energy of the recorded physics event. Since the time measurement depends to some extent on the amplitude of the PMT pulse (time-walk effect), a reliable charge calibration helps improving the time measurement as well. A robust, automatised calibration procedure for dark-room and in-situ calibration was integrated into the calibration framework. The fitting procedures used to extract the

photoelectron peak and the charge pedestal treat integrated charge spectra in order to render the fitting less sensitive to the observed differential non-linearities of the ADCs. A graphical user interface has been devised which allows for monitoring the quality of the charge calibration procedure as well as the time evolution of the calibration constants. The charge measurement in the AVC channel of the front-end electronics has been found to be slightly influenced by the time measurement in the TVC channel. This effect is presumably due to a crosstalk of the capacitors inside the ARS pipeline. The effect is to a good approximation linear in the TVC signal and can reach up to 0.2 pe. A correction for the observed crosstalk was implemented. With the algorithms developed, dark-room and several in-situ calibrations have been performed. A long-term study, monitoring the stability of the calibration parameters was conducted, utilising data from the first complete ANTARES strings and the MILOM instrumentation line. The charge pedestal was found to be stable with a minimal average positive drift of 0.02 channels per month. The average photoelectron peak position and thus the average PMT gain is subject to a drift of about -0.2 channels per month corresponding to roughly 2% of the average difference between pedestal and photoelectron peak per month. The observed drift is presumably due to ageing effects of the PMT photocathode and requires constant monitoring and regular adjustment of the high-voltage settings. Further studies of this important effect should be performed.

A fully functional data reduction scheme has been set up in the KM3Tray framework allowing for the (re-)processing of ANTARES data and simulations. In this pioneering work, data classes as well as supporting algorithms have been devised. These efforts are described in Chapter 5. During the development emphasis has been put on general usability, hence the work performed for this thesis is not limited to the analysis at hand, but can provide a sound basis for other analyses in the future. The complete analysis chain has been used to process the ANTARES data for the analysis presented in Chapter 7 and Chapter 8. In addition, monitoring tools allowing for the observation of data quality and performance of reconstruction algorithms have been implemented. A web-based, online observation tool has been set up and was fed with a live stream of ANTARES data.

In Chapter 6 the algorithms used for the reconstruction of muon tracks have been described briefly. A novel prescription was presented, which permits reducing the complicated track fitting problem to the much simpler task of minimising a one-dimensional function. This may have profound implications on the track fitting procedure and deserves further attention. It was reported on studies which have been made in order to improve the standard fitting procedures by employing global optimisation algorithms, namely the simulated annealing and the dissipative particle swarm algorithms.

Taking the delicately low statistics of expected signal events in neutrino point-source searches into account and the fact that no high-energy cosmic neutrino signal could be observed up to now, in case of a positive result one is obliged to demonstrate that the response of the detector and the systematic errors of the analysis are well understood and

under control. An important task is to verify the absolute pointing of the instrument. Lacking a “standard candle” in neutrinos one has to revert to other means. One possible method of verifying the detector pointing relies on the study of the shadow of the Moon in cosmic rays by measuring the number of muon events from the direction of the Moon. In Chapter 7, this method has been discussed and evaluated by means of a detailed Monte Carlo simulation. The expected significance is found to scale with the square root of the observation time and calculated to be 3σ after 2 years. A first look at the data (Chapter 8) of the completed detector has been taken with the algorithms developed and described in Chapter 5. Although the analysis is preliminary, as it does not include the full detector alignment (which was not available in due time) and the statistics of the analysed data is not yet sufficient for an observation of the effect, all the relevant intricacies have been disclosed and the analysis can be repeated easily with a better statistics in the future. In any case, the results of the calculations presented in this thesis suggest that the observation of the Moon shadow will be a promising method for the calibration of large-scale next generation telescopes¹.

¹While this work was redacted for publication, the IceCube collaboration has reported the detection of the shadow effect with a significance of 5.0σ [198].

Zusammenfassung

Knapp hundert Jahre nach der Entdeckung der kosmischen Strahlung durch V.F. Hess fehlen noch immer die letzten Puzzlesteine, um ihre Quellen zu sondieren und die zugrundeliegenden Beschleunigungsmechanismen endgültig zu verstehen. Die Suche nach den Quellen der kosmischen Strahlung gestaltet sich schwierig, da elektrisch geladene Teilchen im (inter-)galaktischen Magnetfeld auf dem Weg von der Quelle zur Erde eine Ablenkung erfahren und folglich jegliche Richtungsinformation, die Aufschlüsse über die Position und damit letztlich der Art der Quelle liefern könnte, verloren geht. Aus diesem Grunde ist die gegenwärtige Forschung bemüht Methoden aufzuzeigen, die die fehlenden Mosaiksteine zu liefern vermögen.

Eine Möglichkeit die Quellen der kosmischen Strahlung dingfest zu machen, besteht im Nachweis von hoch-energetischen Neutrinos, die in den kosmischen Beschleunigern einhergehend mit den Hadronen erzeugt werden. Neutrinos können als ungeladene und nur schwach wechselwirkende Teilchen direkte Richtungsinformation liefern und eignen sich damit vorzüglich als "Botschafterteilchen", die Auskunft über nicht-thermische Prozesse im Universum geben können. Die Erforschung der Quellen der kosmischen Strahlung bildet denn auch eine wesentliche Motivation für einen jungen Zweig der Astroteilchenphysik, der Neutrinoteleskopie. Die designierte experimentelle Technik zur Detektion hoch-energetischer kosmischer Neutrinos im TeV – PeV Energiebereich basiert auf dem Nachweis der von Reaktionsprodukten der Neutrinowechselwirkung emittierten Cherenkov-Strahlung. Dabei ist die Wechselwirkung von Myon-Neutrinos über den Geladenen-Strom-Prozess aufgrund der großen Reichweite der dabei entstehenden Myonen von besonderer Bedeutung. Alternative Methoden zum Nachweis von ultra-hoch energetischen Neutrinos werden ebenfalls exploriert. Diese komplementären Methoden beruhen auf dem Nachweis von neutrino-induzierten Radiosignalen oder neutrino-induzierten Teilchenkaskaden in der Atmosphäre. Des Weiteren können Neutrinos durch den Nachweis von akustischen Signalen, die infolge der lokalen Energiedeposition am Wechselwirkungsvertex entstehen, detektiert werden.

Die schwache Wechselwirkung der Neutrinos ermöglicht es, einzigartige Informationen über sonst unzugängliche Bereiche zu erhalten, bedingt auf der anderen Seite aber auch geringe Reaktionsraten und erfordert daher in der optischen Cherenkov-Methode die Instrumentation großer Detektionsvolumina mit Photosensoren. Trotz aller experimenteller Anstrengungen und der sorgfältigen Analyse der aufgezeichneten Daten konnte bislang kein hoch-energetisches kosmisches Neutrinosignal gemessen werden. Hinweise auf mögliche Quellen wurden vor kurzem von der Superkamiokande-Kollaboration berichtet [38], erfordern allerdings die Überprüfung durch genauere Messungen mit besserer Statistik. Mit

Experimenten wie IceCube und dem geplanten KM3NeT-Projekt werden zukünftig Sensitivitäten erreicht, die eine Entdeckung von Neutrinoquellen erwarten lassen und eine gründliche Musterung des Himmels auf Neutrinoquellen gestatten werden.

Die vorliegende Arbeit wurde im Rahmen des ANTARES Projektes durchgeführt, welches den Aufbau und den Betrieb eines Tiefsee Wasser-Cherenkov Neutrino-Teleskops zum Gegenstand hat. Mit der kürzlich vollendeten Installation von gut 900 Photosensoren in einer Tiefe von 2475 m im Mittelmeer, 40 km vor der französischen Küste in der Nähe von Toulon, stellt ANTARES derzeit das sensitivste Experiment auf der Nordhalbkugel mit direktem Blick auf das galaktische Zentrum dar. (Vgl. auch Kapitel 3.) Neben dem inhärenten Entdeckungspotential des Teleskops können aus Aufbau, Betrieb und Datenanalyse wichtige Erkenntnisse für die zukünftige Generation von Instrumenten gewonnen werden. Da die Arbeit für diese Promotion während des Aufbaus des Teleskops durchgeführt wurde, ist der Schwerpunkt dieser Dissertation in der Erarbeitung von Kalibrationsmethoden, effizienten Datenanalysestrukturen und Algorithmen zu sehen.

Nach eingehender Erörterung des theoretischen und experimentellen Hintergrundes der Astroteilchenphysik mit Neutrinos im Teil I, nebst ausführlicher Beschreibung des ANTARES Teleskopes im Kapitel 3, wurden im Kapitel 4 Studien zur Ladungskalibration der Ausleseelektronik beschrieben. Vermöge der Ladungskalibration kann die genaue Anzahl der registrierten Cherenkov Photonen aus den digitalisierten Photomultiplierdaten ermittelt werden und damit letztlich die Energie der aufgezeichneten Ereignisse bestimmt werden. Des Weiteren hilft eine genaue Ladungskalibration die Zeitauflösung zu verbessern, da die Messung der Ankunftszeiten zu einem gewissen Grade abhängig von der Amplitude des gemessenen Pulses ist. (Diese Abhängigkeit ist in der Literatur als sogenannter “Time-Walk Effekt” beschrieben.) Ein automatisches Kalibrationsverfahren für den Analogue-Ring-Sampler (ARS) Chip wurde entwickelt und für die Ladungskalibration eingesetzt. Hierbei wurde der Nichtlinearität der Analog-Digital-Wandler durch entsprechende Behandlung (Integration der gemessenen Spektren) Rechnung getragen. Eine nähere Analyse der gemessenen Amplituden zeigt eine, wenn auch geringe, Abhängigkeit von der gemessenen Zeit der Signale. Dieses Artefakt wird durch Übersprecher (“Crosstalk”), parasitäre kapazitive Kopplungen, im ARS Elektronikschaltkreis verursacht. Der Effekt ist in guter Näherung linear und kann durch eine lineare Korrektur hinreichend gut korrigiert werden. Langzeitstudien der Photomultiplier-Verstärkung wurden durchgeführt. Hierbei wurde ein mittlerer Abfall der Verstärkung um 0.2 AVC Kanäle, entsprechend 2% des Photoelektronensignals, pro Monat festgestellt, welcher vermutlich auf Alterungseffekte zurückzuführen ist. Weitere Studien zum genaueren Verständnis dieses Effektes sind notwendig und bereits in Planung bzw. Ausführung begriffen.

Zur effizienten Verarbeitung und Analyse der Daten einschließlich der Steuerung und Überwachung des Detektorbetriebs ist eine Softwareinfrastruktur im Sinne eines kohärenten Paketes (in der vorliegenden Arbeit als “Framework” bezeichnet) unabdingbar. Im Rahmen dieser Arbeit sind wesentliche allgemeine Strukturen für die Analyse von ANTARES Daten

erarbeitet bzw. bereits bestehende erweitert und in das Softwareframework eingepflegt worden. Eine vollständige Datenverarbeitungs- und Reduktionskette wurde entwickelt, welche sowohl auf simulierte als auch auf reale Daten angewendet werden kann. Das vollständige Verfahren wurde erstmalig im Sinne einer Massenproduktion auf ANTARES Daten angewendet. Im Verlauf der Entwicklungsarbeit wurde ein besonderes Augenmerk auf die universelle Verwendbarkeit der neuen Strukturen gelegt. Ausführliche Darlegungen der im Rahmen dieser Arbeit vorgenommenen Implementierungen und deren zugrundeliegenden Spezifikationen sind im Kapitel 5 zu finden. Ein Ereignisvisualisierungsprogramm, das u.a. die Möglichkeit bietet im Internet in Echtzeit Daten des Teleskopes zu visualisieren und es gestattet, die Datennahme zu überwachen, wurde entworfen und als Dienstleistung für die ANTARES Kollaboration betrieben.

Im Anschluss an die Beschreibung der Softwareinfrastruktur sind in Kapitel 6 die Verfahren zur Ereignisrekonstruktion mit Schwerpunkt auf der Spurrekonstruktion geschildert worden. Ein neues Verfahren, welches es gestattet, das komplizierte 5-dimensionale nicht-lineare Problem der Spurrekonstruktion auf ein einfaches 1-dimensionales Minimierungsproblem zu reduzieren, wurde vorgestellt und die sich daraus ergebenden Möglichkeiten und Konsequenzen wurden diskutiert. Abschließend wurde die Möglichkeit der Verwendung von globalen Optimierungsalgorithmen in der Ereignisrekonstruktion erläutert und die gewonnenen Erfahrungen mit dem Simulated Annealing und dem Teichenschwarm Algorithmus erörtert.

Aufgrund der Tatsache, dass bislang noch keine hoch-energetischen kosmischen Neutrinos nachgewiesen worden sind und auch in Zukunft die verfügbare Statistik begrenzt bleiben wird, ist es von großer Wichtigkeit, dass alle systematischen Fehlerquellen in der Analyse kontrolliert und optimal eingeschränkt werden können. Ein wichtiger Punkt bei der Rekonstruktion und Analyse der Daten ist die globale Ausrichtung des Detektors. Die verwendeten Kalibrationsverfahren, die für das ANTARES Teleskop eingesetzt werden (siehe Beschreibungen im Kapitel 3), ermöglichen eine absolute Ausrichtung mit einer Genauigkeit bis auf 0.2 Grad. Dies entspricht in etwa der erreichbaren Richtungsauflösung für hoch-energetische Myon-Neutrinos, die über den Geladenen-Strom-Prozess wechselwirken. Für eine exakte Teleskopie ist es daher wünschenswert, die Detektorausrichtung mittels unabhängiger Methoden zu verifizieren bzw. gegebenenfalls auch korrigieren zu können. Die Entwicklung eines probaten Verfahrens zur Verifizierung der Kalibration ist daher von großer Bedeutung. Eine Möglichkeit besteht im Nachweis des Schattens, den der Mond in der kosmischen Strahlung auf die Erde wirft. Der Mond ist undurchlässig für die primäre kosmische Strahlung, daher ist aus der Richtung des Mondes ein Ereignisdefizit (hier als Schatten bezeichnet) zu erwarten. Da ANTARES nur Myonen als Überreste der Interaktion der kosmischen Strahlung in der Atmosphäre nachweisen kann, überträgt sich ein Defizit an Primärstrahlung direkt in ein entsprechendes Defizit an Myonereignissen aus der Richtung des Mondes. Im Rahmen dieser Arbeit wurde eine detaillierte Monte Carlo Simulation ausgewertet, um die Nachweisbarkeit des Mondschatten Effektes quantifizieren zu können. Diese Studie ist im Kapitel 7 ausführlich beschrieben. Als Resultat der statis-

tischen Analyse ergibt sich, dass der Mondschatteneffekt mit einer erwarteten Signifikanz von 3σ nach einer Beobachtungszeit von etwa zwei Jahren nachgewiesen werden kann. Die Simulation zeigt, dass der Effekt mit der Wurzel aus der Beobachtungszeit skaliert. Eine erste Analyse der Daten des komplettierten ANTARES Teleskopes wurde vorgenommen und in Kapitel 8 diskutiert. Hierbei wurden die entwickelten Verfahren und Strukturen zur Datenanalyse verwendet und einer ersten praktischen Prüfung unterzogen. Wichtige systematische Punkte, wie die erforderlichen Zeit- und Koordinatentransformationen, die in der Analyse Berücksichtigung finden müssen, wurden beschrieben. Aufgrund der limitierten Statistik konnte der Mondschatteneffekt in Übereinstimmung mit dem Resultat aus Kapitel 7 noch nicht nachgewiesen werden. Die Analyse kann zu einem späteren Zeitpunkt mit besserer Statistik und unter Einbeziehung von bislang noch nicht verfügbaren Kalibrationsinformationen (siehe Kapitel 8 für Details) erneut ausgeführt werden. In Anbetracht der Resultate der ausgeführten Berechnungen kann abschließend bemerkt werden, dass der Nachweis des Mondschattens eine wichtige Kalibrationsmethode für Neutrinoobservatorien der nächsten Generation, wie IceCube¹ oder KM3NeT, darstellen wird.

¹Während die Druckfahnen dieser Arbeit redigiert wurden, hat die IceCube Kollaboration über den Nachweis des Mondschatten-Effektes mit einer Signifikanz von 5.0σ berichtet [198].

Appendix

This appendix contains a description of the ANTARES display program developed during the work for this thesis. A derivation of the (z, t) -relations is provided. This thesis concludes with a selection of ANTARES events.

Appendix A

The ANTARES display program

In the context of this work, an event-visualisation software has been developed which allows browsing, viewing and monitoring of ANTARES data. This appendix details the most important features of the program and provides some usage instructions.

A.1 Installation and start-up

The display program is part of the KM3Tray distribution. It should be available in the

```
antares-display
```

folder in the KM3Tray installation. Compilation and installation of the program are done automatically via the CMAKE build system. Provided the KM3Tray environment is loaded and the sources have been compiled, the standalone version of the display can be invoked from the terminal prompt by

```
antares-display-standalone <i3-filename>
```

to view any KM3Tray native “i3” file.

A.2 Main functions of the display

The main window of the program is shown in Figure A.2. The main screen of the program provides a (z, t) -diagram (see Appendix B) for each detection line. The layout of the (z, t) -diagrams on the screen corresponds to the location of the detection lines on the sea floor, see Figure 3.6. In addition, information about the run and a legend explaining the marker and colour conventions are (optionally) shown. The time range of the (z, t) -plots can be adjusted around $t = 0$, which corresponds to the time of the first L1 hit in the triggered event. The (z, t) -graphs for the measured hits and the expected light arrival times for reconstructed tracks allow assessing the quality of the event reconstruction and thus help monitoring data quality and facilitate the development of reconstruction algorithms. The full plot with the (z, t) -diagrams can be saved into an image file. Detailed information about hits and visualised track signals can be obtained by moving the mouse pointer to the corresponding object. The information is then displayed in the status bar

of the main window. Information about the selected run and the event trigger status is also indicated in the status bar. Via the tool bar, located at the right top of the main window, the user can browse through the file (in the standalone-mode only, see below) by using the up-down arrows or the input dialogue, in which the number of the event in the selected file can be entered. A popup window provides information about the functions of the different icons in the tool bar. It is activated when the mouse cursor rests a certain time over a specific icon. Several options of the 2D-view, in particular the selection of the elements (tracks, hits) of the display can be adjusted in the settings dialogue described below.

In addition to the (z, t) -view a 3-dimensional representation of the event showing the reconstructed or/and simulated particle tracks as well as the PMT hits can be generated. Reconstructed Cherenkov photons can be drawn in addition in this view. A change of the perspective and the zoom-level is possible via the mouse. The 3D-view is depicted in Figure A.3. It is also possible to generate an image file containing the 3D scene. Postscript or plain image formats like png are supported. Additionally an animation of the event can be stored in an animated GIF file. The t,r,w keys allow changing the rendering options of the 3D elements. Hits and tracks to be displayed can be selected in the settings dialogue.

The three most important and commonly used tools are the summary window, the settings dialogue, and the find dialogue. These are briefly described in the following. Event properties and reconstruction results are summarised in the display summary window. The event type as well as fit quality and further reconstruction parameters are displayed. A part of the summary window is depicted in Figure A.2. The (z, t) -view and the 3D-view can be configured via the settings dialogue, cf. Figure A.4. The dialogue can be activated in the main menu or by clicking on the settings icon (the wheel). Objects can be selected for being displayed and options like the colour scale for hit amplitudes can be set. The find dialogue provides the possibility of searching for events in the selected file. Triggercounter and frameindex of the event can be specified in the dialogue box. The program scans the file for the event and jumps to the location of the event in the file, if the event is found. The find dialogue window is depicted in Figure A.5.

A.3 Operation modes

Besides the use as a standalone program, the display can be started as a module in the KM3Tray chain (see Chapter 5). In this case, two different operation modes are supported. In the interactive mode, the user can interact with the display via the GUI. It is possible to stop and (re-)start the data processing in the chain. Conversely no display is invoked in the batch mode. In this mode the program can be used to dump images of selected events into image files. This operation mode is used in the online-display service, described in the following section. Several example scripts, demonstrating the different operation modes are available in the KM3Tray distribution.

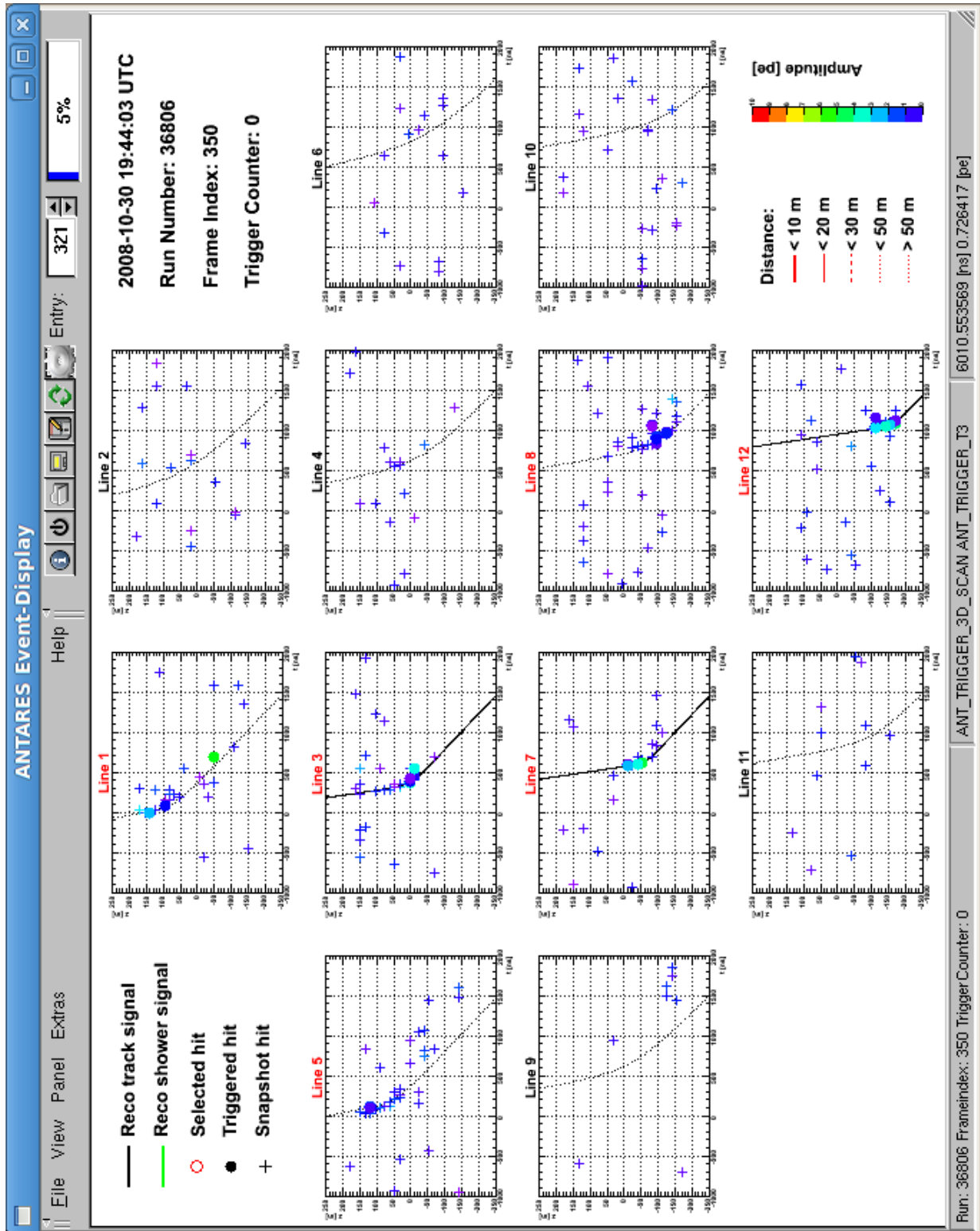
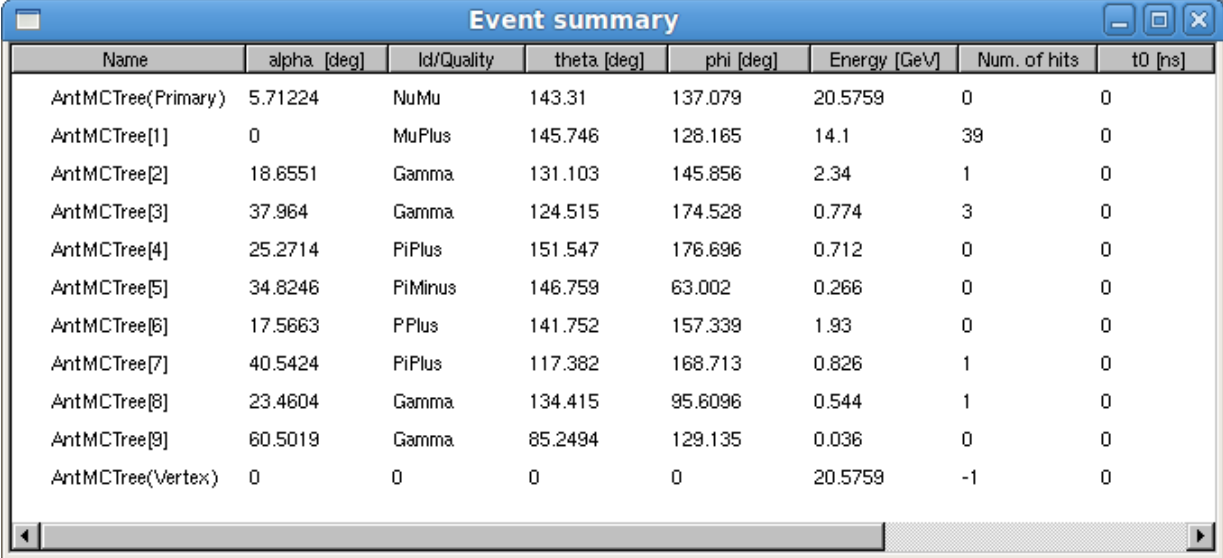


Figure A.1: The main window of the display (in the standalone mode) provides a (z, t) -graph with hits and track signatures for each line. See text for further information.



Name	alpha [deg]	Id/Quality	theta [deg]	phi [deg]	Energy [GeV]	Num. of hits	t0 [ns]
AntMCTree(Primary)	5.71224	NuMu	143.31	137.079	20.5759	0	0
AntMCTree[1]	0	MuPlus	145.746	128.165	14.1	39	0
AntMCTree[2]	18.6551	Gamma	131.103	145.856	2.34	1	0
AntMCTree[3]	37.964	Gamma	124.515	174.528	0.774	3	0
AntMCTree[4]	25.2714	PiPlus	151.547	176.696	0.712	0	0
AntMCTree[5]	34.8246	PiMinus	146.759	63.002	0.266	0	0
AntMCTree[6]	17.5663	PPlus	141.752	157.339	1.93	0	0
AntMCTree[7]	40.5424	PiPlus	117.382	168.713	0.826	1	0
AntMCTree[8]	23.4604	Gamma	134.415	95.6096	0.544	1	0
AntMCTree[9]	60.5019	Gamma	85.2494	129.135	0.036	0	0
AntMCTree(Vertex)	0	0	0	0	20.5759	-1	0

Figure A.2: The summary window provides information about the current event. Reconstruction parameters as well as information about Monte Carlo true values are listed.

A.4 Online display

The online display runs in the web browser of the user. It can be started by pointing the web browser to the following URL

www.pi1.physik.uni-erlangen.de/~antares/online-display/online-display.php
(password protected).

An AJAX script running on the client side and several PHP scripts on the server side generate updated images from the ANTARES live data stream. An archive of recorded special events (neutrino candidates) is available. Event rates in the live data stream can be monitored in the rate-monitor view of the display. See Chapter 5 for more information about the online-display service.

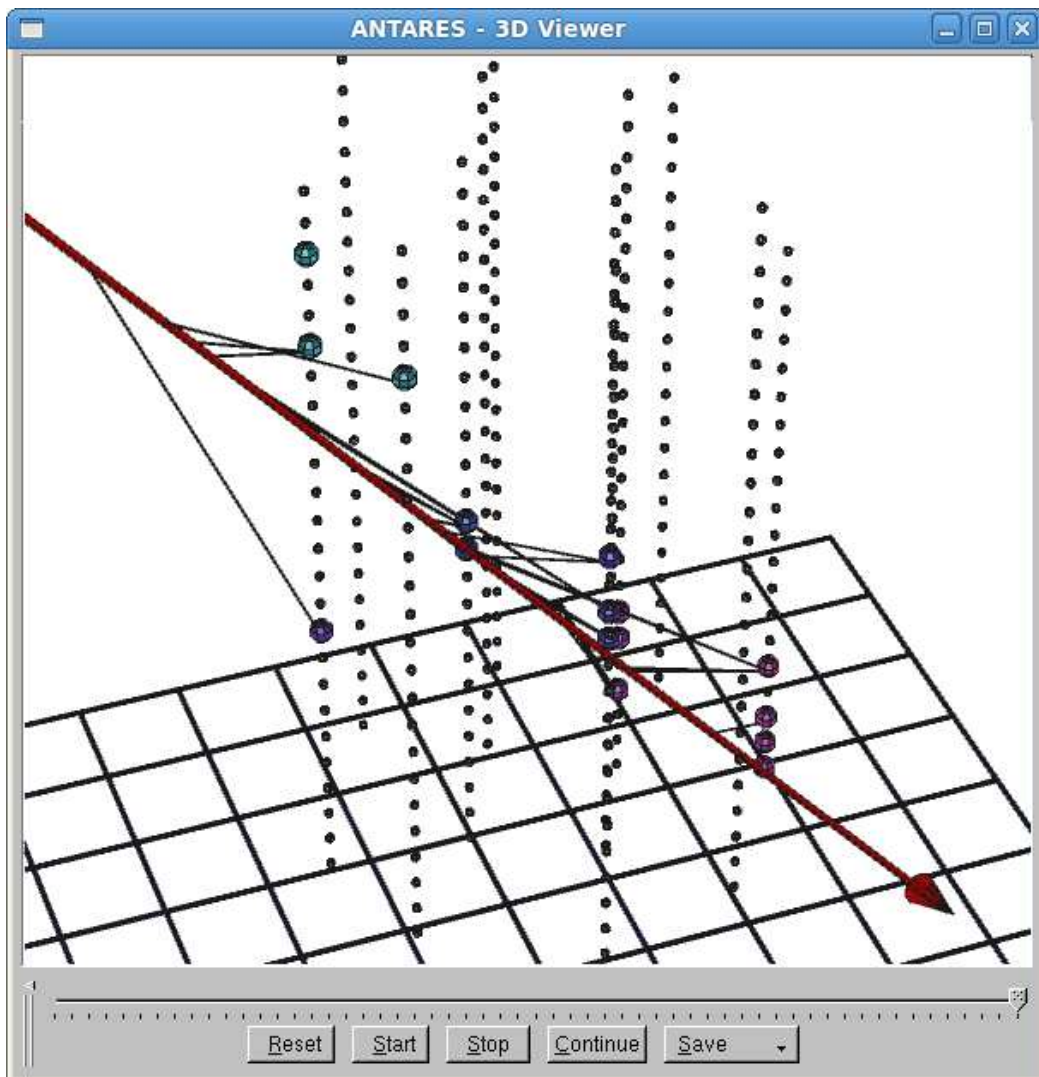
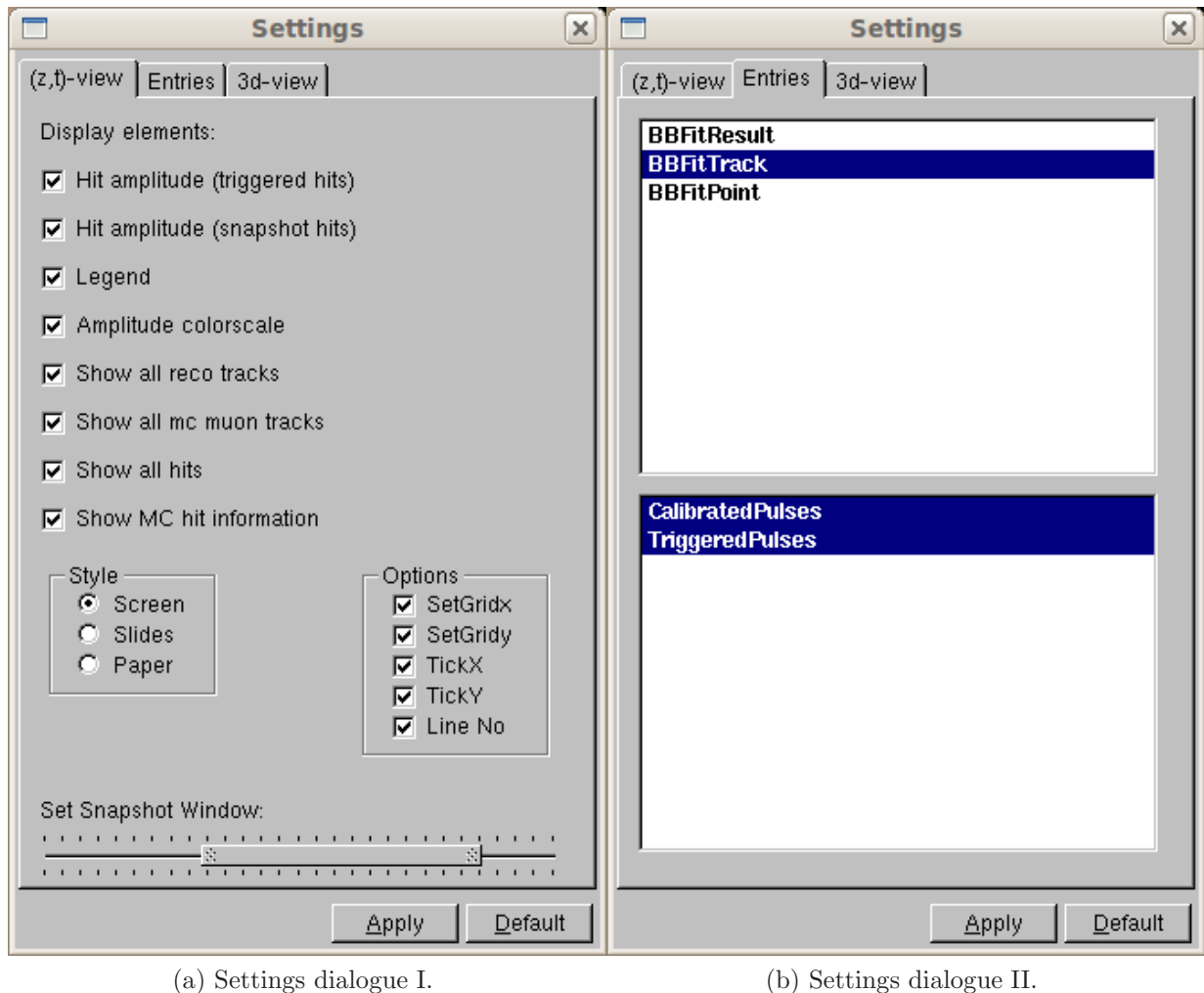


Figure A.3: *The 3D view of the ANTARES display. A 3D representation of selected tracks, OMs and photon lines is shown in this view. A grid is drawn to indicate the sea floor. The corresponding time can be adjusted via the slider bar. A simple animation can be replayed and recorded into an animated GIF file.*



(a) Settings dialog I.

(b) Settings dialog II.

Figure A.4: The display settings dialogue. This dialogue allows adjusting the display configuration. Elements (separated into hits and tracks/showers) can be activated or deactivated via the list-boxes in the “Entries” tab of the dialogue.

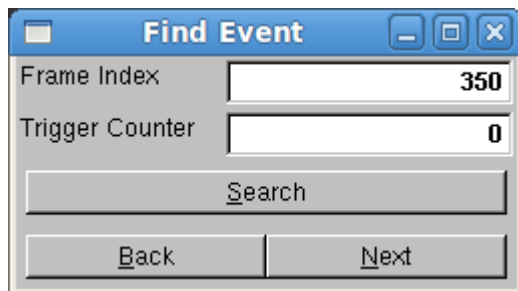


Figure A.5: The find dialogue of the ANTARES display permits one of searching for events by specifying values for frame index and trigger counter. This allows identifying and displaying specific events in the data file. (E.g. neutrino candidates.) The back and next buttons can be used to browse in the data file. The dialogue can be activated via the main menu or the tool bar.

Appendix B

Derivation of the two dimensional event signatures

A handy tool for evaluating reconstruction quality is given by the (z, t) -diagram. In this diagram, the altitude (z -coordinate) of the hit PMT is plotted against the light arrival time t , thus time residuals are immediately visible. In this appendix, the expected (z, t) -relations are derived for Cherenkov light emitted from tracks or bright points (showers).

B.1 Track signal in the (z, t) -diagram

A (muon) track T traversing the detector can be described by a straight line

$$\mathbf{r}(t) = \mathbf{r}_0 + \mathbf{v}(t - t_0), \quad (\text{B.1})$$

where \mathbf{r}_0 is the muon position at time t_0 and \mathbf{v} denotes the velocity vector of the track. The Cherenkov cone of the emitted light at time t with opening angle 2α is given by the set of points \mathbf{x} which fulfill (with $\hat{\mathbf{v}} = \mathbf{v}/\|\mathbf{v}\|$)

$$\hat{\mathbf{v}} \cdot \frac{\mathbf{r}(t) - \mathbf{x}}{\|\mathbf{r}(t) - \mathbf{x}\|} = \cos \alpha. \quad (\text{B.2})$$

In order to derive the two dimensional signature, we exploit the geometry and set without loss of generality $\hat{\mathbf{v}} = (\sin \theta, 0, \cos \theta)$, $\mathbf{r}_0 = (0, d_0, z_0)$ and $\mathbf{x} = (0, 0, z)$. Then, Equation B.2 can be rewritten as

$$v(t - t_0) - (z - z_0) \cdot \cos \theta = \cos \alpha \|\mathbf{r}(t) - \mathbf{x}\|. \quad (\text{B.3})$$

Now the right hand side of Equation B.3 is just the length of the projection of the vector $\mathbf{r}(t) - \mathbf{x}$ onto the track, and since $\cos \alpha = \sin \alpha / \tan \alpha$, this can be written as $1/\tan \alpha$ times the distance of the point \mathbf{x} to the track. This distance is simply

$$d(\mathbf{x}, T) = \sqrt{d_0^2 + (z - z_0)^2 \sin^2 \theta}. \quad (\text{B.4})$$

Finally, using $\tan \alpha = n/\sqrt{1+n^2} = 1/\tan \theta_C$ with the refraction index n , we arrive at

$$v(t - t_0) = (z - z_0) \cos \theta + \tan \theta_C \sqrt{d_0^2 + (z - z_0)^2 \sin^2 \theta} \quad (\text{B.5})$$

which is a **hyperbola** in the (z, t) -diagram. The (z, t) -relations for tracks with different zenith angles θ are shown in Figure B.1.

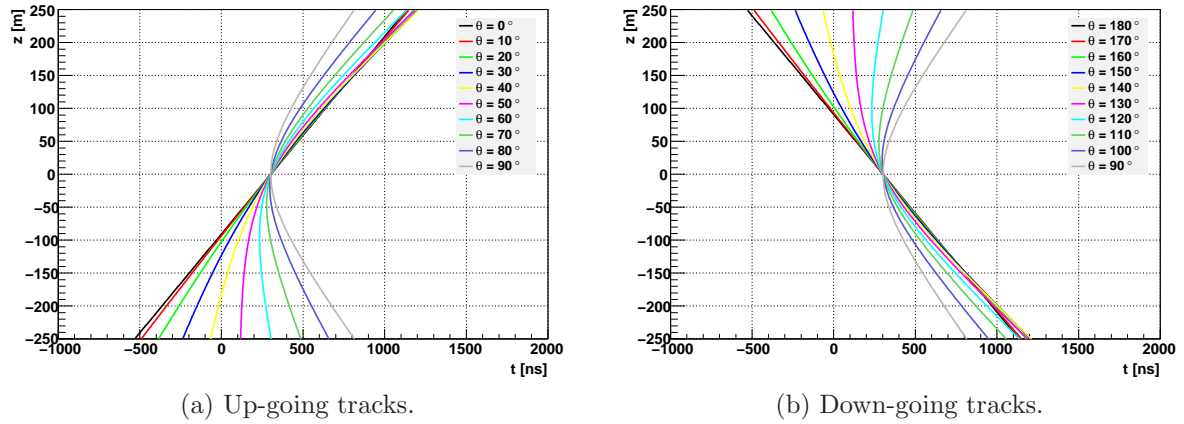


Figure B.1: The (z, t) -diagram for tracks with different zenith angles θ . Up-going tracks are shown on the left, down-going tracks on the right.

B.2 Signal of a bright point in the (z, t) -diagram

Light originating from a point \mathbf{r}_0 at time t_0 is measured at a point \mathbf{x} at time

$$t = t_0 + \frac{\|\mathbf{r}_0 - \mathbf{x}\|}{c}. \quad (\text{B.6})$$

Exploiting the symmetry of the problem and setting $\mathbf{r}_0 = (0, d_0, z_0)$ and $\mathbf{x} = (0, 0, z)$ we arrive without loss of generality at

$$c^2(t - t_0)^2 = d_0^2 + (z - z_0)^2, \quad (\text{B.7})$$

which corresponds to a **parabola** in the (z, t) -diagram.

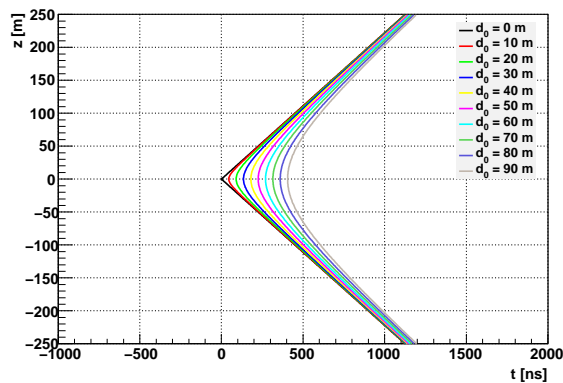


Figure B.2: A (z, t) -diagram for bright-point events occurring at different distances d_0 to the detection string at $z_0 = 0$. The solutions are described by parabolas, except for $d_0 = 0$, in which case the solution degenerates to a straight line.

Appendix C

ANTARES example events

The following figures present an illustrative selection of example events which have been measured by the ANTARES 12-string detector and were reconstructed using the online reconstruction algorithm. For each event, a 3D representation of the reconstructed signature (track or shower) is depicted. The storeys contributing hits for the reconstruction are marked by enlarged spheres. Reconstructed photon lines are drawn in addition. The time of the photon emission is calculated under the assumption that the photon travels with the group velocity. The emission angle is not constrained in this calculation. The angles can be compared with the Cherenkov angle as a consistency check. In some cases (delayed photons, due to scattering) a valid solution does not exist. Therefore no photon line is attached to these hits. The 2D (z, t) -diagrams, as described in Appendix B, are given in addition.

- Figure C.1 depicts an especially bright **neutrino candidate event**, which can be reconstructed with high quality.
- Figure C.2 gives an example of a down-going track event. This event is unambiguously reconstructed as down-going and is therefore most likely an **atmospheric muon event**.
- A possible **shower candidate event** is visualised in Figure C.3. In this case, the bright-point fit has a better quality than the track fit. The bright point corresponding to the shower vertex is reconstructed within the central, lower part of the detector. No track signal is visible in the upper part of the detector. It is therefore unlikely that the event is due to an electromagnetic shower along an atmospheric muon track. The event could be due to a cascade, although a detailed analysis is necessary for a definite conclusion.

The events depicted in Figure C.1 and Figure C.2 were created with the standalone version of the ANTARES display program from the off-line reconstruction for the Moonshadow analysis in this thesis. Figure C.3 is an edited version of a snapshot from the online event display service. The neutrino candidate event was marked as a special event by the online analysis chain and can also be found in the archive of the online event display.

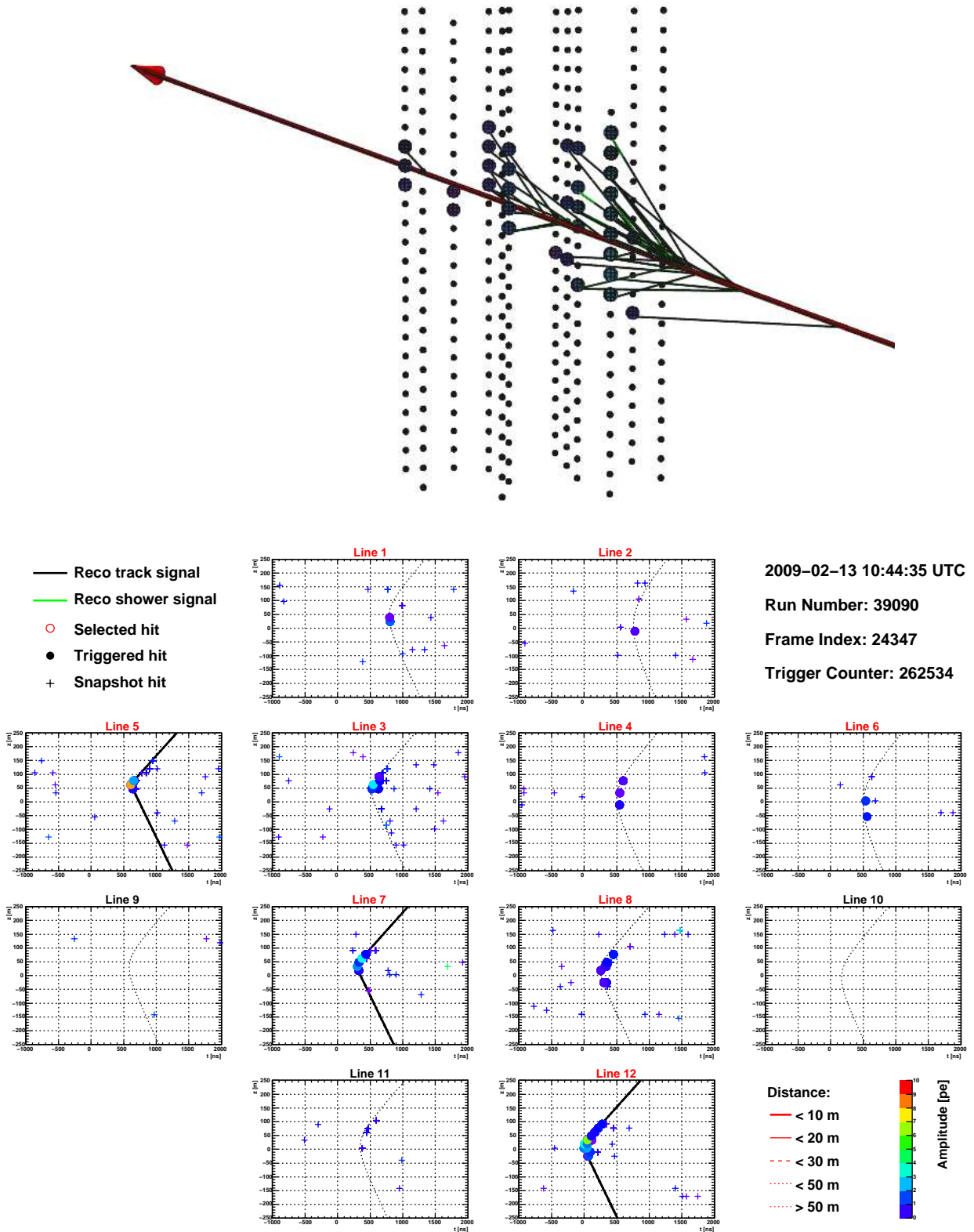


Figure C.1: A neutrino candidate event, registered with the ANTARES detector.

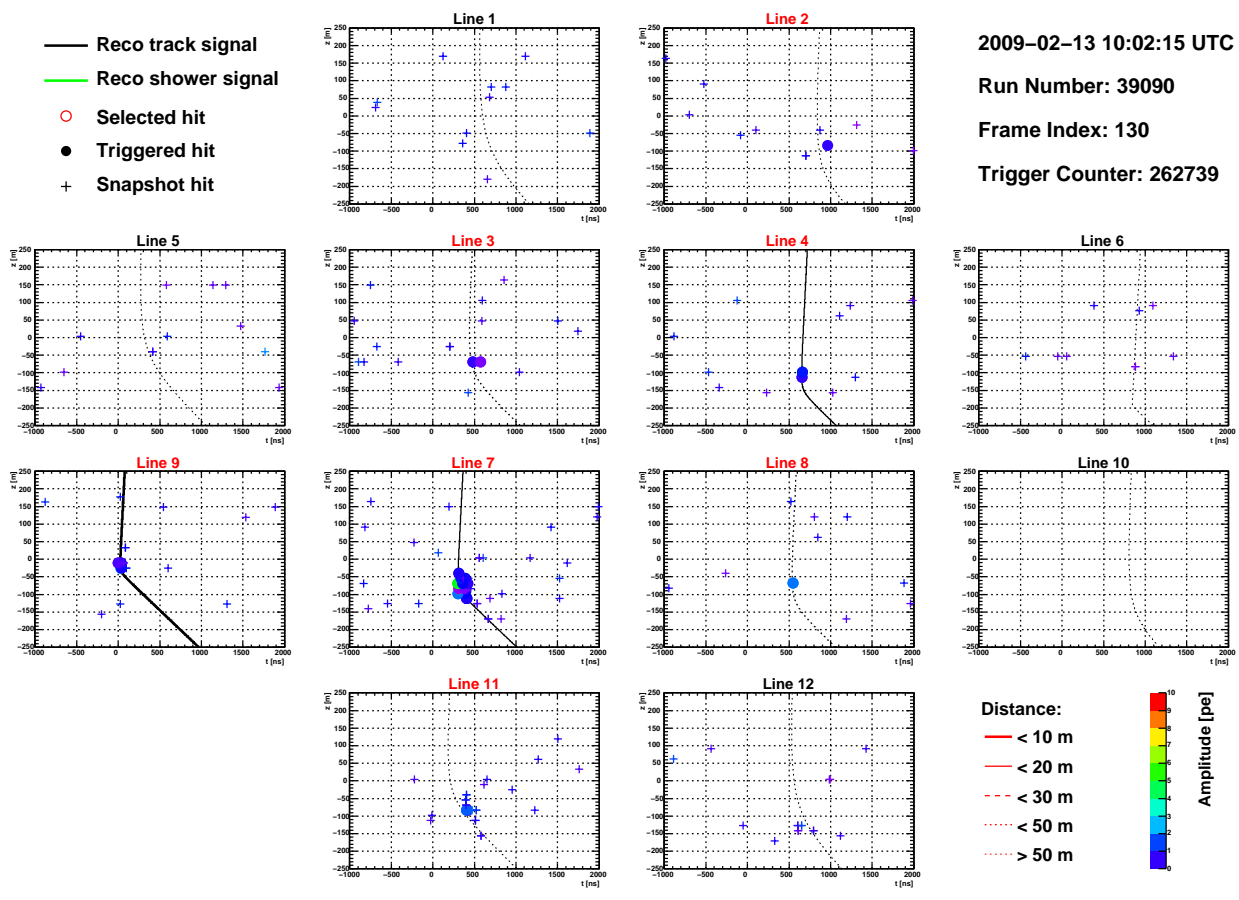
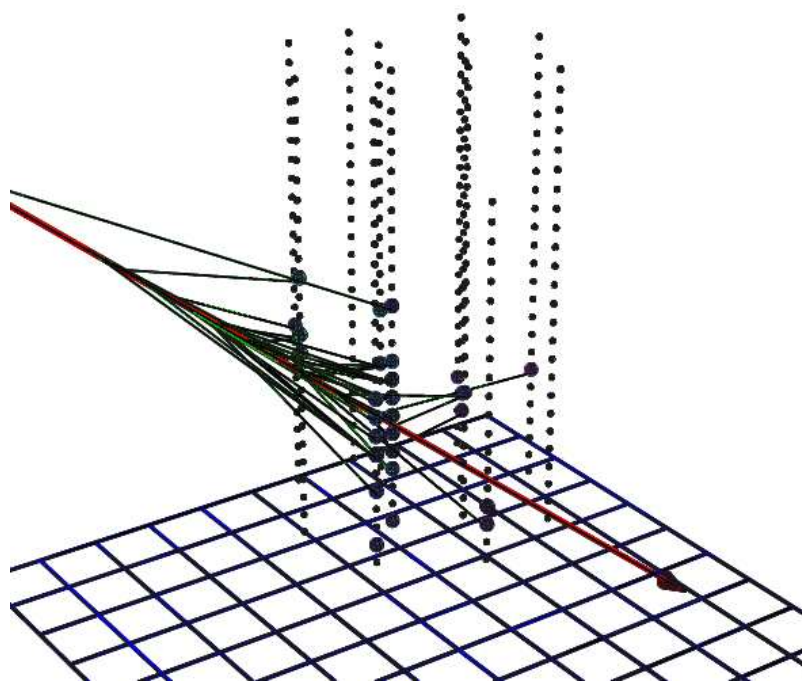


Figure C.2: An atmospheric muon event, measured with the ANTARES detector.

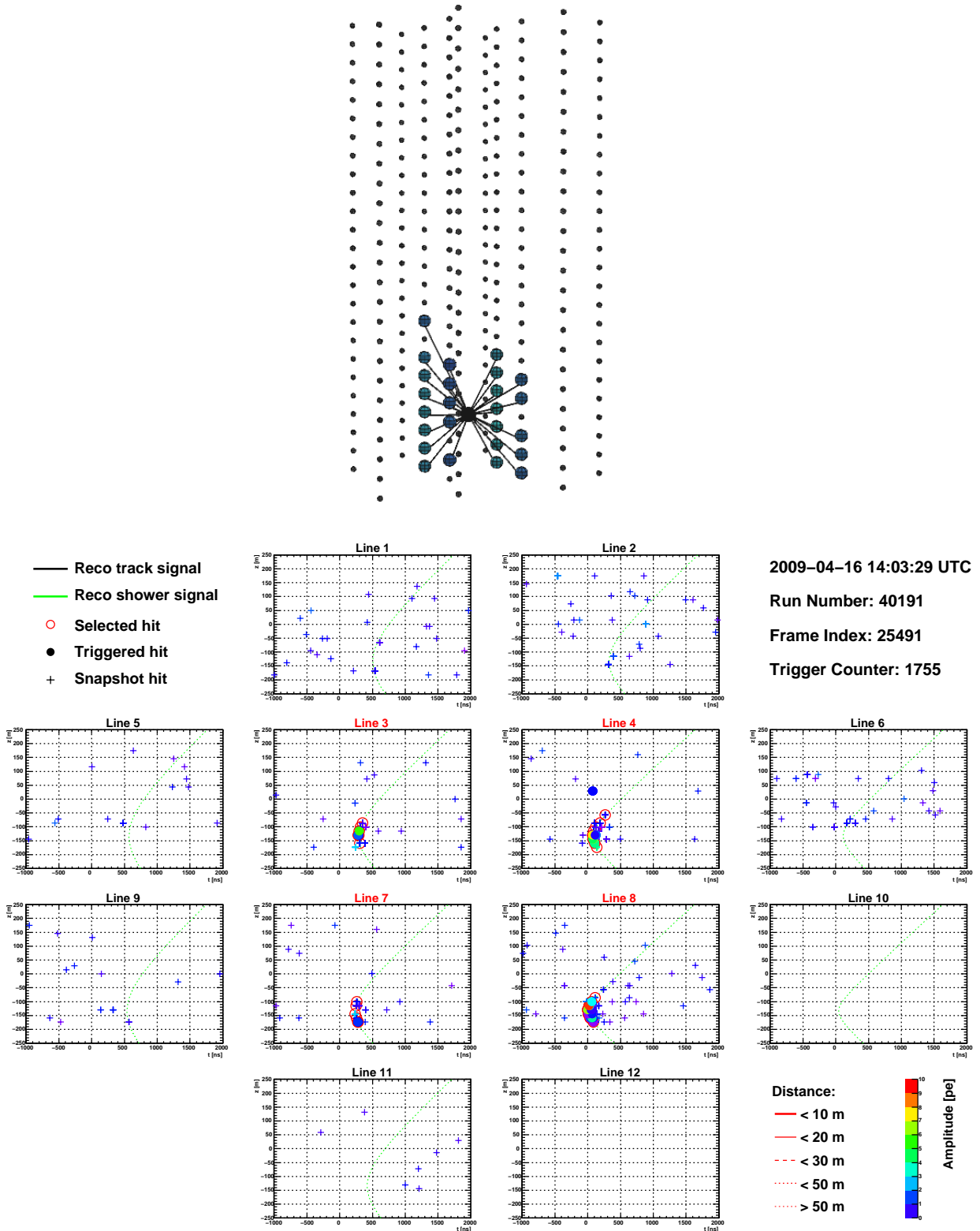


Figure C.3: A shower candidate event, recorded with the ANTARES detector. The bright point is reconstructed within the lower part of the detector and no track signal is visible in the upper part.

Bibliography

- [1] L.A. Seneca, “Epistulae morales ad Lucilium, 104 26,” ca. 62-65.
- [2] V.F. Hess, “Durchdringende Strahlung bei sieben Freiballonfahrten,” *Phys.Zeitschr. XIII*, p. 1084, 1912.
- [3] Y. Fukuda et al., “Evidence for Oscillation of Atmospheric Neutrinos,” *Phys. Rev. Lett.*, vol. 81, pp. 1562–1567, Aug 1998.
- [4] D. Clowe et al., “A direct empirical proof of the existence of dark matter,” *Astrophysical Journal Letters*, pp. 109–113, September 2006.
- [5] C.D. Anderson, “The apparent existence of easily deflectable positives,” *Science*, vol. 76, no. 1967, pp. 238–239, 1932.
- [6] S.H. Neddermeyer and C.D. Anderson, “Note on the Nature of Cosmic-Ray Particles,” *Phys. Rev.*, vol. 51, pp. 884–886, May 1937.
- [7] D.H. Perkins *Nature*, no. 159, pp. 126–127, 1947.
- [8] G.P.S. Occhialini and C.F. Powell, “Nuclear Disintegrations Produced by Slow Charged Particles of Small Mass,” *Nature*, no. 159, pp. 186–190, 1947.
- [9] C.M.G. Lattes, G.P.S. Occhialini and C.F. Powell, “Observations on the Tracks of Slow Mesons in Photographic Emulsions,” *Nature*, no. 160, pp. 453–456, 1947.
- [10] G.D. Rochester and C.C. Butler, “Evidence for the Existence of New Unstable Elementary Particles,” *Nature*, no. 160, p. 855, 1947.
- [11] C. Cowan, “Detection of the free neutrino: A confirmation,” *Science* 124, p. 103, 1956.
- [12] R. Davis, “Solar neutrinos. II: Experimental,” *Phys. Rev. Lett.*, vol. 12, pp. 303–305, 1964.
- [13] J. Davis, Raymond, D. S. Harmer, and K. C. Hoffman, “Search for neutrinos from the sun,” *Phys. Rev. Lett.*, vol. 20, pp. 1205–1209, 1968.
- [14] B. T. Cleveland *et al.*, “Measurement of the solar electron neutrino flux with the Homestake chlorine detector,” *Astrophys. J.*, vol. 496, pp. 505–526, 1998.

- [15] K. S. Hirata *et al.*, “Observation of B-8 Solar Neutrinos in the Kamiokande-II Detector,” *Phys. Rev. Lett.*, vol. 63, p. 16, 1989.
- [16] K. S. Hirata *et al.*, “Results from one thousand days of real-time, directional solar-neutrino data,” *Phys. Rev. Lett.*, vol. 65, pp. 1297–1300, 1990.
- [17] K. S. Hirata *et al.*, “Observation of a Neutrino Burst from the Supernova SN 1987a,” *Phys. Rev. Lett.*, vol. 58, pp. 1490–1493, 1987.
- [18] K. S. Hirata *et al.*, “Observation in the Kamiokande-II Detector of the Neutrino Burst from Supernova SN 1987a,” *Phys. Rev.*, vol. D38, pp. 448–458, 1988.
- [19] C. Amsler *et al.* (Particle Data Group) *Physics Letters*, vol. 667, 2008.
- [20] K. Greisen, “End to the cosmic ray spectrum?,” *Phys.Rev.Lett*, vol. 16, p. 748, 1966.
- [21] G. Zatsepin and V. Kuz’min, “Upper limit of the spectrum of cosmic rays,” *JETP Lett.*, vol. 4, p. 78, 1966.
- [22] J. Hörandel, “Models of the Knee in the Energy Spectrum of Cosmic Rays,” *Astropart. Phys.*, vol. 21, p. 241, 2004.
- [23] E. Fermi, “On the origin of cosmic rays,” *Phys.Rev.*, vol. 75(8), p. 1169, 1949.
- [24] E. Fermi, “Galactic magnetic fields and the origin of cosmic radiation,” *Astrophys. J.*, vol. 119, 1954.
- [25] J. Learned and K. Mannheim, “High-energy neutrino astrophysics,” *Ann. Rev. Nucl. Part. Sci.*, vol. 50, 2000.
- [26] P. Gorham, “In International Workshop on the Saldome Shower Array (SalSA),” *SLAC (US)*, 2005.
- [27] J. Cronin, “The highest energy cosmic rays,” 2004.
- [28] A. Hillas, “The origin of ultra-high energy cosmic rays,” *Annual Review of Astronomy and Astrophysics*, vol. 22, p. 425, 1984.
- [29] F.W. Stecker and M.H. Salamon, “High energy neutrinos from quasars,” *Space Sci. Rev.*, vol. 75, p. 341, 1996.
- [30] E. Waxmann and J. Bahcall, “High energy neutrinos from cosmological gamma-ray burst fireballs,” *Phys.Rev.Lett.*, vol. 78, pp. 2292–2295, 1997.
- [31] M. Vietri *Phys.Rev.Lett.*, vol. 80, p. 3690, 1998.
- [32] M. Botcher and C. Dermer *Astrophys. J.*, vol. 574, p. 65, 2002.

-
- [33] C. Distefano, D. Guetta, E. Waxman, and A. Levinson, “Neutrino flux predictions for known galactic microquasars,” *Astrophys. J.*, vol. 575, pp. 378–383, 2002.
- [34] A. Balenzano, F. Burgio and T. Montaruli *ANTARES Internal Note, ANTARES-PHYS-2003-006*, 2003.
- [35] R. Engel, D. Seckel and T. Stanev *Phys.Rev.D.*, vol. 64, p. 093010, 2001.
- [36] H. Muraishi et al., “Evidence for TeV γ -rays from SNR RX J1713.7-3946,” *Astron. & Astrophys.*, p. 354:L57, 2000.
- [37] F. Aharonian et al., “A detailed spectral and morphological study of the gamma-ray supernova remnant RX J1713.7-3946 with H.E.S.S.,” *Astron. & Astrophys.*, p. 354:L57, 2006.
- [38] E. Thrane, “Search for Astrophysical Neutrino Point Sources at Super-Kamiokande,” 2009.
- [39] The Pierre Auger Collaboration, “Correlation of the highest energy cosmic rays with nearby extragalactic objects,” *Science*, vol. 318, p. 939, 2007.
- [40] S. Eidelman et al., “Review of Particle Physics,” *Physics Letters B*, vol. 592, 2004.
- [41] J.G. Learned and S. Pakvasa *Astropart. Phys.*, vol. 3, p. 267, 1995.
- [42] R. Ghandi et al, “Ultrahigh-energy Neutrino Interactions,” *Astropart. Phys.*, vol. 5, p. 81, 1996.
- [43] Particle Data Group, “Passage of Particle through Matter,” *European Physics Journal C*, vol. 3, p. 144, 1998.
- [44] S. Klimushin et al., “Precise parameterizations of muon energy losses in water,” *Proceedings of ICRC*, 2001.
- [45] A. Heijboer, “Track reconstruction and point source searches with antares,” *PhD thesis, NIKHEF, Amsterdam*, 2004.
- [46] F. Bernard *Ph.D. Thesis, Univerity of Marseille, CPPM-T-2000-02*, 2000.
- [47] P. Cherenkov, “Visible radiation produced by electrons moving in a medium with velocities exceeding that of light,” *Phys. Rev.*, vol. 52, p. 378, 1937.
- [48] J. Jackson, *Classical Electrodynamics*. John Wiley and Sons, Inc., 1998.
- [49] M.A. Markov *Proc. Int. Conf. on High-Energy Physics, Rochester*, p. 578, 1960.
- [50] K. Greisen *Ann. Rev. Nucl. Science*, vol. 10, p. 63, 1960.

- [51] Hanada, H. et al., “A highly sensitive optical detector for use in deep underwater,” *Nucl. Instrum. Meth.*, vol. A408, pp. 425–437, 1998.
- [52] The Baikal Collaboration, “The Baikal neutrino project: Status report,” *Nucl. Phys. B (Proc. Suppl.)*, vol. 91, p. 438, 2001.
- [53] M. Kowalski *In Proceedings of the 28th International Cosmic Ray Conference*, 2003.
- [54] A. Achterberg, “Five years of searches for point sources of astrophysical neutrinos with the amanda-ii neutrino telescope,” *Physical Review D*, vol. 75, p. 102001, 2007.
- [55] J. Ahrens et al., “The IceCube Detector,” *Proc. of the 27th International Cosmic Ray Conference, Hamburg Germany*, p. 1237, 2001.
- [56] The IceCube collaboration, “The IceCube collaboration: contributions to the 30th International Cosmic Ray Conference (ICRC 2007),” 2007.
- [57] G. Aggouras et al. *Nucl. Phys. Proc. Suppl.*, vol. 151, p. 279, 2006.
- [58] The NESTOR collaboration, “The NESTOR homepage.” <http://www.nestor.org.gr>, 2009.
- [59] G. Aggouras et al. *Astropart. Phys.*, vol. 23, p. 377, 2005.
- [60] C. Distefano, “Detection of point-like neutrino sources with the NEMO-km3 telescope,” *Astrophys. Space Sci.*, vol. 309, pp. 415–420, 2007.
- [61] C. Distefano, “Sensitivity and pointing accuracy of the NEMO km3 telescope,” *Nucl. Instrum. Meth.*, vol. A567, pp. 495–497, 2006.
- [62] U. F. Katz, “Neutrino telescopy in the Mediterranean sea,” *Prog. Part. Nucl. Phys.*, vol. 57, pp. 273–282, 2006.
- [63] U. F. Katz, “KM3NeT: Towards a km3 Mediterranean neutrino telescope,” *Nucl. Instrum. Meth.*, vol. A567, pp. 457–461, 2006.
- [64] The KM3NeT consortium, “The KM3NeT homepage.” <http://www.km3net.org>, 2006.
- [65] G.A. Askariyan, “Excess negative charge of an electron-photon shower and its coherent radio emission,” *Sov. Phys. JETP.*, vol. 14, pp. 441–443, 1962.
- [66] G.A. Askariyan, B.A. Dolgoshein et al., “Acoustic detection of high energy particle showers in water,” *Nucl. Instrum. Methods*, vol. 164, p. 267, 1979.
- [67] The Antares Collaboration, *Conceptual design report*.
- [68] The Antares Collaboration, *Technical design report*.

-
- [69] The KM3NeT Consortium, *Conceptual design report*.
- [70] F. Montanet, “ANTARES 3D virtual pictures produced with POV-ray.” <http://antares.in2p3.fr/Gallery/3D/index.html>, 2009.
- [71] F. Fehr, “ANTARES 3D Online Event Display.” <http://www.pi1.physik.uni-erlangen.de/~antares/online-display/online-display.php>, 2009.
- [72] P. Amram *et al.*, “The ANTARES optical module,” *Nucl. Instrum. Meth.*, vol. A484, pp. 369–383, 2002.
- [73] K. Graf, “Experimental Studies within ANTARES towards Acoustic Detection of Ultra-High Energy Neutrinos in the Deep-Sea,” *Ph.D. thesis, University Erlangen-Nuremberg*, 2008.
- [74] S. Vecchio, “Analysis of the optical background sources in the antares experiment and preliminary studies related to a larger scale detector,” Dissertation, Università di Pisa, 2004.
- [75] J. Brunner, “Upgrade on K40 simulation,” *ANTARES Internal Note, ANTARES-PHYS-2006-005*, 2006.
- [76] S. Escoffier, “Bioluminescence studies with the ANTARES Prototype Sector Line,” *ANTARES Internal Note, ANTARES-SITE-2005-001*, 2005.
- [77] J. A. Aguilar, “The data acquisition system for the antares neutrino telescope,” *Nucl. Instrum. Meth.*, vol. A570, pp. 107–116, 2007.
- [78] P. Lucas, “An object-oriented language system for implementing concurrent, hierarchical, finite state machines.,” *Technical Report UIUCDCS-R-94-1868, University of Illinois at Urbana-Champaign*, 1994.
- [79] R. van Wijk. http://www.nikhef.nl/~ruud/HTML/choo_manual.html.
- [80] R. Gurin and A. Maslennikov, “ControlHost: Package for Distributed Data Handling,” *CASPUR Inter-Universitij Computing Consortium Rome*, 1995.
- [81] M. Bouwhuis, “Detection of neutrinos from gamma-ray bursts.,” *PhD thesis, Universiteit van Amsterdam*, 2005.
- [82] B.A.P. van Rens, “The Software Trigger in ANTARES,” *ANTARES Internal Note, ANTARES-SOFT-2004-001*, 2004.
- [83] M. de Jong, “The ANTARES Trigger Software,” *ANTARES Internal Note, ANTARES-SOFT-2005-005*, 2005.

- [84] J. Carr et al., “Proposition for an alternative trigger based on the T3 cluster trigger,” *ANTARES Internal Note, ANTARES-SOFT-2007-016*, 2007.
- [85] S. Escoffier, “Performance of the T3 Triggers on MC Data,” *ANTARES Internal Note, ANTARES-SOFT-2008-009*, 2008.
- [86] J. Brunner, “The BBfit Reconstruction Algorithm,” *ANTARES Internal Note, ANTARES-SOFT-2009-003*, 2009.
- [87] F. Fehr, “Calibration systems and methods for the ANTARES neutrino telescope,” *In Proceedings of the 30th International Cosmic Ray Conference, Merida, Mexico*, 2007.
- [88] J. A. Aguilar *et al.*, “Transmission of light in deep sea water at the site of the antares neutrino telescope,” *Astropart. Phys.*, vol. 23, pp. 131–155, 2005.
- [89] M. Ageron, “The antares optical beacon system,” 2007.
- [90] A. Brown, “Positioning system of the ANTARES neutrino telescope,” *Proc. of the 31th International Cosmic Ray Conference, Lodz Poland*, 2009.
- [91] The ANTARES collaboration, “Antares physics analysis plan,” 2009.
- [92] A. Margiotta, “Monte Carlo simulation of atmospheric muons,” *ANTARES Internal Note, ANTARES-SOFT-2008-005*, 2008.
- [93] D. Heck et al. *REPORT FZKA, Forschungszentrum Karlsruhe*, vol. 6019, 1998.
- [94] D. Heck and J. Knapp *REPORT FZKA, Forschungszentrum Karlsruhe*, vol. 6097, 1998.
- [95] P. Antonioli et al. *Astrop. Phys.*, vol. 7, p. 357, 1997.
- [96] Y. Becherini et al., “A parameterisation of single and multiple muons in deep water or ice,” *Astropart. Phys.*, vol. 25, 2006.
- [97] G. Carminati et al., “Atmospheric MUons from PArametric formulas: A fast GEnerator for neutrino telescopes (MUPAGE),” 2008.
- [98] G. Carminati et al., “MUPAGE User Guide,” *ANTARES Internal Note, ANTARES-SOFT-2007-004*, 2007.
- [99] D.J.L. Bailey, “Genhen: Extension of ”genneu” for high energy neutrino interactions,” *ANTARES Internal Note, ANTARES-SOFT-2000-5*, 2000.
- [100] D.J.L. Bailey, “Monte Carlo Tools and Analysis Methods for Understanding the ANTARES Experiment and Predicting Its Sensitivity to Dark Matter,” *Ph.D. Thesis, Wolfson College, Oxford*, 2002.

-
- [101] K. Kuzmin, T. Montaruli, I. Sokalski, “GENHEN v6r3: Implementation of the Glashow resonance and of MUSIC transport code,” *ANTARES Internal Note, ANTARES-SOFT-2004-012*, 2004.
- [102] G. Ingelman, A. Edin and J. Rathsman, “LEPTO 6.5 - A Monte Carlo generator for deep inelastic scattering,” *Comput. Phys. Commun.*, vol. 101, p. 108, 1997.
- [103] G. Barr, “The separation of signals and background in a nucleon decay experiment,” *Ph.D. Thesis, Keble College, University of Oxford*, 1987.
- [104] H.L. Lai et al., “Global QCD analysis and the CTEQ parton distributions,” *Phys.Rev.*, vol. D51, p. 4763, 1995.
- [105] T. Sjöstrand, “High-energy physics event generation with PYTHIA 5.7 and JET-SET 7.4,” *Compt. Phys. Commun.*, vol. 82, p. 74, 1994.
- [106] S. Navas and L. Thompson, “KM3 User Guide and Reference Manual,” *ANTARES Internal Note, ANTARES-SOFT-1999-011*, 1999.
- [107] J. Brunner, “GEASIM.”
<http://antares.in2p3.fr/internal/software/geasim.html>, 2000.
- [108] Application Software Group, “GEANT - Detector Description and Simulation Tool,” *CERN Program Library Long Writeup*, vol. W5013, 1993.
- [109] G. Riccobene, “Overview over Mediterranean Optical Properties,” *VLVnT Workshop, NIKHEF Amsterdam*, 2003.
- [110] A. Margiotta, “Study of the effects of water properties on Monte Carlo simulation of the atmospheric muon flux,” *ANTARES Internal Note, ANTARES-SOFT-2007-006*, 2007.
- [111] M. Anghinolfi, “New measurement of the angular acceptance of the Antares Optical Module,” *ANTARES Internal Note, ANTARES-OPMO-2008-011*, 2008.
- [112] M. de Jong, “The Summary Timeslice Writer program,” *ANTARES Internal Note, ANTARES-SOFT-2005-006*, 2005.
- [113] F. Feinstein, “The analogue ring sampler: A front-end chip for antares,” *Nucl. Instrum. Meth.*, vol. A504, pp. 258–261, 2003.
- [114] E. Delagnes et al., “ARS: tests, settings and performances for physics,” *ANTARES Internal Note, ANTARES-ELEC-2004-001*, 2004.
- [115] A. Kouchner, “Topics on ARS calibration,” *Talk at the ANTARES collaboration meeting, CERN December 2006*, 2006.

- [116] A. Kouchner, “On the linearity response of the ARS charge channels,” *ANTARES Internal Note, ANTARES-CALIB-2007-005*, 2007.
- [117] S. Loucatos, “Correction of the differential non-linearity of the ADCs,” *ANTARES Internal Note, ANTARES-ELEC-2005-002*, 2005.
- [118] M. de Jong, “The ARS AVC calibration,” *ANTARES Internal Note, ANTARES-CALI-2005-002*, 2005.
- [119] C. Colnard, “Ultra-high energy neutrino simulations,” *Ph.D. Thesis, University of Amsterdam*, 2009.
- [120] M. de Jong, “The TriggerEfficiency program,” *ANTARES Internal Note, ANTARES-SOFT-2009-001*, 2009.
- [121] F. Cassol, “Reconstruction reorganisation: RECO version 2.0,” *ANTARES Internal Note, ANTARES-SOFT-1999-004*, 1999.
- [122] F. Cassol, “RECO version 2.1: code and scripts,” *ANTARES Internal Note, ANTARES-SOFT-1999-005*, 1999.
- [123] A. Romeyer and T. Stolarczyk, “Reconstruction algorithms: a handbook for developers,” *ANTARES Internal Note, ANTARES-SOFT-2001-001*, 2001.
- [124] Y. Becherini et al., “Offline reconstruction and analysis software v1r6,” *ANTARES Internal Note, ANTARES-SOFT-2008-008*, 2008.
- [125] C. Kopper, “A software framework for KM3NeT,” *Nucl. Instrum. Meth.*, vol. A602, pp. 107–110, 2009.
- [126] R. Brun and F. Rademakers, “ROOT: An object oriented data analysis framework,” *Nucl. Instrum. Meth.*, vol. A389, pp. 81–86, 1997.
- [127] CMAKE Cross Platform Make. <http://www.cmake.org>, 2009.
- [128] Tigris.org Open Source Software Engineering Tools. <http://subversion.tigris.org>, 2009.
- [129] T. Eberl, “The KM3Tray software framework,” *ANTARES Internal Note, ANTARES-SOFT-2009*, 2009.
- [130] B. Stroustrup, *The C++ Programming Language (Special Edition)*. Addison Wesley. Reading Mass. USA, 2000. ISBN-0-201-70073-5.
- [131] G. van Rossum and J. F.L. Drake, *The Python Language Reference Manual*. Network Theory LTD, 2006. ISBN-0-9541617-8-5.
- [132] The HDF group. <http://www.hdfgroup.org/HDF5>, 2009.

- [133] C. Kopper. Ph.D. thesis in preparation.
- [134] R. Auer. Ph.D. thesis in preparation.
- [135] M. de Jong, “Antares data formats,” *ANTARES Internal Note, ANTARES-SOFT-2004-006*, 2005.
- [136] World Wide Web Consortium. <http://www.w3.org/XML>, 2009.
- [137] M. Bouwhuis, “Search for gamma-ray bursts with the Antares neutrino telescope,” *Proceedings of the 31st ICRC, Lodz, Poland*, 2009.
- [138] R. Shanidze, 2009.
- [139] C. Kopper, 2009.
- [140] B. Eckels, *C++ Thinking in Patterns*. Mind-View, 2005.
- [141] C. Reed, “CalReal Update,” *Talk at the Antares Collaboration Meeting, Paris 17th June 2008*, 2008.
- [142] S. Meyers, *Effective C++ (Third Edition)*. Addison-Wesley, 2005. ISBN-0-321-33487-6.
- [143] BOOST C++ libraries. <http://www.boost.org>, 2009.
- [144] R. Bruijn, “The Antares Neutrino Telescope: Performance studies and analysis of first data,” *Ph.D. thesis, University Amsterdam*.
- [145] F. Fehr, “The Making of ANTARES Display,” *Talk at the Erlangen KM3Tray software workshop*, 2008.
- [146] F. Fehr, “BETA version of AntDisplay v2r0 at Lyon.” ANTARES-ANALYSIS eLog Id 222, <http://ireswww.in2p3.fr/eelog/ANALYSIS/222>, 2008.
- [147] OpenGL. <http://www.opengl.org>, 2009.
- [148] PHP Documentation Group, “PHP Manual.” <http://www.php-center.de/en-html-manual>, 2009.
- [149] J.J. Garrett, “Ajax: A New Approach to Web Applications,” *Adaptive Path LLC*, 2005.
- [150] Internal documentation (Wiki), “The SGA batch system.” https://config.p11.physik.uni-erlangen.de/wiki/index.php/SGE:_Batch_System_, 2009.

- [151] B. Hartmann, “Reconstruction of neutrino induced hadronic and electromagnetic showers with the ANTARES experiment,” *Ph.D. thesis, University Erlangen-Nuremberg*, 2006.
- [152] S. Kuch, “Design studies for the KM3NeT Neutrino Telescope,” *Ph.D. thesis, University Erlangen-Nuremberg*, 2007.
- [153] M. de Jong, “Partial linearisation of the track fit problem,” *ANTARES Internal Note, ANTARES-SOFT-2007-01*, 2007.
- [154] E. Carmona, “Study of the event reconstruction and expected performances for point-like sources of the future ANTARES neutrino telescope,”
- [155] F. Fehr, “Muon reconstruction,” *Talk at the ANTARES-PAW meeting, Colmar*, 2007.
- [156] K. Lyons, “Analytical muon-track prefit techniques,” *Talk at the ANTARES-PAW meeting, Colmar*, 2007.
- [157] M. de Jong, “Linear prefit revisited,” *Talk at the ANTARES collaboration meeting, Bari*, 2007.
- [158] Bronstein, Semendjajew, Musiol and Mühlig, *Taschenbuch der Mathematik*. Harri Deutsch, 4th ed., 1999.
- [159] K.F. Riley, M.P. Hobson and S.J. Bence, *Mathematical methods for physics and engineering*. Cambridge University Press, 2nd ed., 2002.
- [160] S. Kirkpatrick, C.D. Gelatt, and M.P. Vecchi *Science*, vol. 220, p. 671, 1983.
- [161] A.K. Hartmann and H. Rieger, *Optimization Algorithms in Physics*. Wiley-VCH, 2002. ISBN-3-527-40307-8.
- [162] X.-F. Xie et al., “A Dissipative Particle Swarm Optimization,” *Proceedings of Congress on Evolutionary Computation, Hawaii, USA*, pp. 1456–1461, 2002.
- [163] M. Millinger, “Entwicklung und Vergleich von Strategien zur Rekonstruktion von Myonspuren mit dem ANTARES-Neutrino-Teleskop,” *Diploma thesis, University Erlangen-Nuremberg*, 2007.
- [164] W. Goffe et al., “Simulated Annealing: An Initial Application in Econometrics,” *Computer Science in Economics & Management*, vol. 5, pp. 133–46, May 1992.
- [165] J.-P. Ernenwein, A. Tsirigotis, and S. Tzamarias, “Study of the calibration potential of HELYCON detectors with ANTARES,” *Nucl. Instrum. Meth.*, vol. A602, pp. 88–90, 2009.
- [166] A. Kouchner, 2003.

-
- [167] G.W. Clark, “Arrival Directions of Cosmic Ray Air Showers from the Northern Sky,” *Physical Review*, vol. 108, 1957.
- [168] D.E. Alexandreas et al., “Observation of shadowing of ultrahigh-energy cosmic rays by the Moon and the Sun,” *Phys. Rev. D*, vol. 43, pp. 1735–1738, Mar 1991.
- [169] A. Borione, et al., “Observation of the shadows of the Moon and Sun using 100 TeV cosmic rays,” *Phys. Rev. D*, vol. 49, no. 3, pp. 1171–1177, 1994.
- [170] M. Amenomori et al., “Cosmic-ray deficit from the direction of the Moon and the Sun detected with the Tibet air-shower array,” *Phys. Rev. D*, vol. 47, no. 7, pp. 2675–2681, 1993.
- [171] M. Amenomori et al., “Moon shadow by cosmic rays under the influence of geomagnetic field and search for antiprotons at multi-TeV energies,” *Astroparticle Physics*, vol. 28, no. 1, pp. 137–142, 2007.
- [172] B. Wang et al., “Preliminary results on the Moon shadow with ARGO-YBJ,” *Proceedings of the 30th ICRC*, 2007.
- [173] M. Merck *26th Intern. Conf. on High-Energy Physics, Dallas, USA*, 1992.
- [174] P. Achard et al., “Measurement of the shadowing of high-energy cosmic rays by the Moon: A search for TeV-energy antiprotons,” *Astroparticle Physics*, vol. 23, pp. 411–434, 2005.
- [175] J.H. Cobb et al., “Observation of the shadow of the Moon in the underground muon flux in the Soudan 2 detector,” *Phys. Rev. D*, vol. 61, no. 9, 2002.
- [176] E.W. Grashorn, “MINOS Observations of Shadowing in the Muon Flux Underground,” 2007.
- [177] M. Ambrosio et al., “Observation of the shadowing of cosmic rays by the Moon using a deep underground detector,” *Phys. Rev. D*, vol. 59, p. 012003, Nov 1998.
- [178] M. Ambrosio et al., “Moon and Sun shadowing effect in the MACRO detector,” *Astroparticle Physics*, vol. 20, no. 2, pp. 145–156, 2003.
- [179] F. Fehr, “Moon shadow analysis.” ANTARES-ANALYSIS eLog Id 203, <http://ireswww.in2p3.fr/elog/ANALYSIS/203>, 2008.
- [180] F. Fehr, “Update on the Moon shadow analysis,” *ANTARES collaboration meeting, Genova*, 2009.
- [181] C. Distefano *Talk at the ANTARES-COLL-2009-04, Marseille April 2009*, 2009.
- [182] J. Hörandel, “On the knee in the energy spectrum of cosmic rays.,” *Astropart. Phys.*, vol. 19, p. 193, 2003.

- [183] C. Distefano *Private communication*, 2009.
- [184] e.g. <http://www.ngdc.noaa.gov/IAGA/vmod/igrf.html>, 2009.
- [185] F. James, R. Cousins and G. Cowan, “Statistics,” *In Journal of Physics G*, vol. 33, no. 1, 2006.
- [186] J. Neyman, E. Pearson, “On the Problem of the Most Efficient Tests of Statistical Hypotheses,” *Philosophical Transactions of the Royal Society of London*, vol. A, no. 231, pp. 289–337, 1993.
- [187] J. Rice, *Mathematical Statistics and Data Analysis*. Duxbury Press, (Second ed.) ed., 1995.
- [188] G. Cowan, *Statistical Data Analysis*. Oxford University Press, 1 ed., 1998.
- [189] A. Oppelt, “Etude de la resolution angulaire du telescope a neutrinos,” *Ph.D. Thesis, Universite de la Mediterranee*, 2001.
- [190] A. Oppelt, “Detection of the Moon shadow,” *ANTARES Internal Note, ANTARES-SOFT-2001-012*, 2001.
- [191] A. Heijboer, “Detecting the Moon Shadow,” *ANTARES Internal Note, ANTARES-PHYS-2005-004*, 2005.
- [192] A. Roodman, “Blind Analysis in Particle Physics.” arXiv.org:physics/0312102, 2003.
- [193] J.R. Klein and A. Roodman, “Blind Analysis in Nuclear and Particle Physics,” *Annual Review of Nuclear and Particle Science*, vol. 55, no. 1, pp. 141–163, 2005.
- [194] Meeus, *l’Astronomie*. 1994.
- [195] SLALIB - Positional Astronomy Library.
<http://www.starlink.rl.ac.uk/star/docs/sun67.htx/sun67.html>, 2006.
- [196] Defense Mapping Agency, “The Universal Grids – Universal Transverse Mercator (UTM) and Universal Polar Stereographic (UPS).” DMA Technical Manual, DMATM 8358.2, 1989.
- [197] P. Vernin, “The UTM Grid,” *ANTARES Internal Note, ANTARES-SOFT-2008-002*, 2008.
- [198] D.J. Boersma et al., “Moon Shadow Observation by IceCuce,” *Proceedings of the 31st ICRC, Lodz*, 2009.
- [199] T. Pynchon, *Mason & Dixon*. Henry Holt, 1997.
- [200] G. Simmel, *Soziologie. Untersuchung über die Formen der Vergesellschaftung*. Duncker & Humblot Verlag, Berlin, 1. Auflage, 1908.

List of Figures

1.1	<i>Cosmic-ray all-particle spectrum.</i>	8
1.2	<i>Sketch of the shock acceleration mechanism.</i>	9
1.3	<i>Observable distance in megaparsec as a function of the proton (photon) energy.</i>	11
1.4	<i>Sample trajectories for protons in the intergalactic magnetic field.</i>	12
1.5	<i>Hillas diagram.</i>	14
1.6	<i>Schematic view of an active galactic nucleus.</i>	15
1.7	<i>Schematic view of a GRB according to the fireball model.</i>	16
1.8	<i>Measurement of gamma rays from RX J1713.7-3946.</i>	19
1.9	<i>Air-shower detection with the Pierre-Auger hybrid detector.</i>	20
1.10	<i>Sky map of high-energy events recorded with Auger.</i>	21
2.1	<i>Summary of the neutrino nucleon deep-inelastic scattering channels.</i>	24
2.2	<i>Topology of the “double-bang” event.</i>	25
2.3	<i>Neutrino nucleon cross section as function of the neutrino energy.</i>	26
2.4	<i>Energy loss and range for muons in water.</i>	27
2.5	<i>Illustration of the Cherenkov effect.</i>	28
2.6	<i>AMANDA neutrino sky map.</i>	30
2.7	<i>Neutrino sky map measured with the IC-09 detector.</i>	31
3.1	<i>Comparison of the field of view.</i>	36
3.2	<i>A map of the ANTARES site.</i>	36
3.4	<i>The ANTARES detector.</i>	37
3.3	<i>Optical storey of the telescope.</i>	37
3.7	<i>Signal and background for neutrino telescopes.</i>	38
3.5	<i>Layout of the ANTARES detector.</i>	39
3.6	<i>String anchor positions.</i>	39
3.8	<i>Median background rate monitored over four years of operation.</i>	41
3.9	<i>Data flow in the ANTARES detector.</i>	43
3.10	<i>Definition of a physics event recorded with ANTARES.</i>	45
3.11	<i>Active time of the ANTARES detector.</i>	51
3.12	<i>Number of muon triggers recorded with ANTARES.</i>	51
4.1	<i>PMT readout in the off-shore DAQ.</i>	56
4.2	<i>Architecture of the ARS chip.</i>	57
4.3	<i>Explanation of the differential-non-linearity.</i>	59
4.4	<i>Illustration of the DNL effect.</i>	60

4.5	<i>Example of an integrated photoelectron peak spectrum.</i>	62
4.6	<i>Example of an integrated pedestal spectrum.</i>	62
4.7	<i>Example of the crosstalk effect.</i>	63
4.8	<i>Example of the calibration user interface for the 1 pe and crosstalk fit.</i>	64
4.9	<i>The calibration monitor program.</i>	65
4.10	<i>Evolution of the charge pedestal.</i>	67
4.11	<i>Evolution of the photoelectron peak.</i>	67
4.12	<i>Example for a positive drift of the photoelectron peak.</i>	68
4.13	<i>Summary of the time evolution.</i>	68
5.1	<i>Illustration of the modular approach adopted in KM3Tray.</i>	73
5.2	<i>The ANTARES online event-display.</i>	80
5.3	<i>Data flow in the online event-display service.</i>	81
5.4	<i>The KM3Tray reconstruction chain used for data analysis.</i>	84
6.1	<i>Track- and shower-like events in ANTARES.</i>	86
6.2	<i>Schematic of the likelihood fit.</i>	88
6.3	<i>Example of a χ^2-landscape.</i>	89
6.4	<i>Visualisation of an example event.</i>	93
6.5	<i>Example one-dimensional χ^2 distributions.</i>	94
6.6	<i>Ghost solutions.</i>	95
7.1	<i>Deflection of the primary proton in the geomagnetic field versus energy.</i>	107
7.2	<i>Point-spread function at the final analysis level.</i>	108
7.3	<i>Shape of the Moon shadow.</i>	108
7.4	<i>Definition of significance and power.</i>	110
7.5	<i>Distribution of the test statistic.</i>	113
7.6	<i>Expected significance for the detection of the Moon-shadow effect.</i>	113
7.7	<i>Test characteristics for the detection of the shadow effect.</i>	114
7.8	<i>Expected significance for the observation of the Moon-shadow effect.</i>	114
7.9	<i>Optimisation of the quality parameter cut.</i>	115
7.10	<i>Impact of a misalignment on a point source.</i>	116
8.1	<i>The geocentric parallax.</i>	118
8.2	<i>Coordinate systems.</i>	119
8.3	<i>Distribution of the Moon positions in the detector system for 2008.</i>	120
8.4	<i>Comparison between the quality parameter distributions for data and simulation.</i>	122
8.5	<i>Azimuth and zenith angle distributions for event in the on-region.</i>	124
8.6	<i>Number of events versus solid angle.</i>	125
8.7	<i>Test statistics for the two hypotheses.</i>	125
A.1	<i>Main window of the display.</i>	139
A.2	<i>Summary window of the display.</i>	140
A.3	<i>The 3D view of the ANTARES display.</i>	141

A.4	<i>The display settings dialogue.</i>	142
A.5	<i>The display find dialogue.</i>	142
B.1	<i>(z,t)-diagram for muon tracks.</i>	144
B.2	<i>(z,t)-diagram for showers.</i>	144
C.1	<i>A neutrino candidate event.</i>	146
C.2	<i>An atmospheric muon event.</i>	147
C.3	<i>A shower candidate event.</i>	148

List of Tables

2.1	<i>Comparison of different high-energy neutrino detection techniques.</i>	33
5.1	<i>Non-exhaustive list of KM3Tray projects, used in this work.</i>	82
7.1	<i>Observation of the Moon shadow by different experiments.</i>	104
7.2	<i>Number of generated air showers in the CORSIKA Moon simulation.</i>	105
7.3	<i>Parameters of the Hörandel model used in the CORSIKA Moon simulation.</i>	106
7.4	<i>Probabilities for a 3σ detection of the Moon shadow.</i>	112

Acknowledgements

“For if each Star is little more a mathematical point, located upon the Hemisphere of heaven by Right Ascension and Declination, then all the Stars, taken together, tho’ innumerable, must like any other set of points, in turn represent some single gigantick Equation, to the mind of God as straightforward, as say, the Equation of a sphere, – to us unreadable, incalculable, a lonely, uncompensated, perhaps even impossible Task, – yet some of us must ever be seeking, I suppose.” [199]

The challenges which are faced by the scientist, who is engaged in fundamental research, are fittingly vocalised in the preceding passage taken from a novel written by Thomas Pynchon. Thus it appears that fundamental research is largely driven by curiosity, inquisitiveness about nature, not-yet-understood processes and the search for new phenomena - it is about discovering how things work; and in spite of all fascination, it’s certainly also true that it can be a tough venture and a lonely, unrewarded task. Therefore, at the end of the day [and this thesis, . . . which accidentally coincides], when all is said and done, it’s a particular pleasure to thank everybody who has supported me during the last few years.

First of all, I would like to thank Prof. Dr. Uli Katz very warmly for the opportunity of conducting research for this thesis in his group as well as for comments on this manuscript. I am also grateful to Prof. Dr. Christian Stegmann who kindly agreed to write a report on my work.

Working with experts is always a pleasure. I have to thank Claudio Kopper and Ralf Auer for doing a great job as system administrators at ECAP, which included resurrecting the batch farm for me over the week-end as well as installing new software packages for my analysis as late (or early) as 2:00am! I wish you all the best for the future.

I enjoyed working in a European collaboration and participating in such an intriguing project as ANTARES is. Starting off my work in the beginning of 2006, I could witness the construction of the telescope from the very first string to the solemnised finalisation of the detector in May 2008. For sure, I will never forget the great moment when first neutrino signals were recorded with ANTARES. Finishing the work for this thesis in mid 2009, I have had the chance and the privilege of analysing first data taken with the completed detector. I would like to express my gratitude to all ANTARES colleagues who have made this possible. Particular thanks go to Jürgen Brunner for helping when problems related to computing at Lyon came up, to Carla Distefano for the work on the Moon-shadow simula-

tion, and to Antoine Kouchner for helping me with the charge calibration. Special thanks also to Aart Heijboer who wrote a nice internal note on the Moon-shadow effect which has inspired me in my work.

I hope that I could contribute a little bit to this fascinating experiment. I wish all of my ANTARES colleagues many more neutrinos and success in the ultimate goal – neutrino astronomy.

A hearty thanks to all who have made my stay at Erlangen enjoyable and fun.

At ECAP, Thomas Eberl, Kay Graf, Bettina Hartmann, Alexander Kappes, Robert Lahmann, Friederike Schöck, and all the others have created a unique atmosphere. Thank you! To all Ph.D. students at ECAP good luck and “Bon courage!” for finishing their own theses.

I am indebted to Mechthild and Wolf-Dieter Finkelnburg for their cordiality and the possibility of residing at Sieglitzhof. Vielen herzlichen Dank!

Finally, I have to thank my family – for everything!

“Denn diesem nach kann es sich nur um Anfang und Wegweisung für einen unendlich langen Weg handeln, und jede systematisch abschließende Vollständigkeit wäre mindestens eine Selbsttäuschung. Vollständigkeit kann der Einzelne hier nur in dem subjektiven Sinne erreichen, dass er alles mitteilt, was ihm zu sehen gelungen ist.” [200]

GEORG SIMMEL